UNIVERSITAT POLITÈCNICA
DE CATALUNYA
BARCELONATECH

PhD program in Optical Engineering

DESIGN AND CONSTRUCTION OF A SNAPSHOT FULL-STOKES POLARIMETRIC CAMERA: SEEING THROUGH FOG

Doctoral Thesis by:
Sara Peña Gutiérrez

Thesis advisor:
Santiago Royo Royo

Centre for Sensors, Instruments and Systems Development (CD6-UPC)
Faculty of Optics and Optometry of Terrassa (FOOT)

UPC DOCTORAL
SCHOOL

2022

Series of dissertations submitted to the
Centro de Desarrollo de Sensores, Instrumentación y Sistemas, Universitat Politècnica de Catalunya
No. 1234

ISSN 1234-5678

"Como el ojo no puede ver sin la luz,
el hombre no puede obrar sobrenaturalmente
sin el auxilio de la gracia divina."
S. Agustín

Abstract

Polarization is one of the properties of light and it is often put aside. Human beings receive light beams and process only the intensity and wavelength information. Our optical system lacks the capability of 'seeing' polarization in comparison to other animals. The vectorial nature of polarization is uncorrelated to the intensity and colour information and this can unveil additional information for improving the current technology.

This Thesis aims to develop a camera capable of measuring the full polarization in a 2D scene. In particular, it focuses on the design and construction of a prototype that measures in the visible waveband the full-Stokes vector in a snapshot such that the acquisition time and noise equalization are balanced while reducing movement and registration artefacts.

The Thesis starts with the revision of the current state of the art in the polarimetric imaging field. Based on this, the optomechanical design of the polarimetric camera is developed ensuring a faster acquisition of polarization since it integrates optimum states to immunize the system from Gaussian and Poisson noise.

Accordingly, this Thesis proposes a general calibration methodology addressed to the radiometry of the sensor, the geometrical aberrations from optics and the polarization elements in the system to transform the intensity measurements into polarization information. Besides, this Thesis studies two imaging modes of polarization, Stokes imaging and Mueller matrix imaging, for different applications. The novelty of this system consists of the use of optimal polarization states in a division of aperture architecture for noise immunization.

Finally, this Thesis studies the application of the system to improve detection in the real-world problem of seeing through the fog. Polarization information can improve the range of detection due to the polarization memory effect. This system could be employed inside a multimodal system to ensure detection when others are hampered due to external conditions.

La polarización es una de las propiedades de la luz y de la que a menudo se prescinde. Los seres humanos percibimos los rayos de luz y solo procesamos la información proveniente de la intensidad y de las longitudes de onda de la luz. Nuestro sistema óptico carece de la capacidad de "ver" la polarización en comparación con otros animales. La naturaleza vectorial de la polarización no está correlacionada con la información aportada por la intensidad y el color, y esto puede desvelar información adicional para mejorar la tecnología actual.

Esta Tesis tiene como objetivo desarrollar una cámara para medir la polarización en una escena 2D. En particular, se centra en el diseño y construcción de un prototipo que mida en el espectro visible el vector de Stokes completo en un solo disparo de manera que el tiempo de adquisición y la ecualización del ruido estén compensados a la vez que se reduzcan los artefactos debidos al movimiento y al registro.

La Tesis comienza revisando el actual estado del arte en el campo de imagen polarimétrica. A partir de esto, se realiza el diseño optomecánico de la cámara polarimétrica garantizando una adquisición rápida ya que el diseño implementa unos estados óptimos de polarización para inmunizar el sistema del ruido de gaussiano y de Poisson.

Por consiguiente, esta Tesis propone una metodología general de calibración dirigida a la radiometría del sensor, a las aberraciones geométricas de la óptica y a los elementos de polarización en el sistema para transformar las medidas de intensidad en información polarimétrica. Además, esta Tesis estudia dos modos de imagen de la polarización, imagen de Stokes e imagen de la matriz de Mueller, para diferentes aplicaciones. La novedad de este sistema radica en la utilización de estados de polarización óptimos basándose en una arquitectura de división de apertura para la inmunización al ruido.

Finalmente, esta Tesis estudia las aplicaciones del sistema para mejorar la detección en un problema del mundo real como es ver a través de la niebla. La información de la polarización puede mejorar el rango de detección debido al efecto de memoria de la polarización. Este sistema podría utilizarse dentro de un sistema multimodal para asegurar la detección cuando el resto de sistemas están perjudicados por las condiciones externas.

La polarització és una de les propietats de la llum i que sovint es prescindeix d'ella. Els éssers humans reben els raigs de llum i únicament processen la informació provinent de la intensitat i la longitud d'ona de la llum. El nostre sistema òptic no té la capacitat de "veure" la polarització en comparació a altres animals. La natura vectorial de la polarització està no correlada amb la informació donada per la intensitat i el color, i això pot revelar informació addicional per millorar la tecnologia actual.

Aquesta Tesi té com a objectiu desenvolupar una càmera per mesurar la polarització d'una escena 2D. En particular, es centra en el disseny i construcció d'un prototip que mesuri a l'espectre visible el vector de Stokes complert en un sol tret de manera que el temps d'adquisició i la equalització del soroll siguin compensats a la vegada que es redueixen els artefactes causats pel moviment i pel registre.

La Tesi comença revisant l'actual estat de l'art en el camp de la imatge polarimètrica. Arran d'això, es realitza el disseny optomecànic de la càmera polarimétrica garantint una adquisició ràpida, ja que el disseny implementa uns estats òptims de polarització per immunitzar el sistema de soroll gaussià i de Poisson.

Per tant, aquesta Tesi proposa una metodologia general de calibratge dirigida a la radiometria del sensor, a les aberracions geomètriques de l'òptica i als elements de polarització en el sistema per transformar les mesures d'intensitat en informació polatimétrica. A més, aquesta Tesi estudia dues maneres d'imatge de la polarització, imatge de Stokes i imatge de la matriu de Mueller, per diferents aplicacions. La novetat d'aquest sistema radica en la utilització d'estats de polarització òptims basant-se en una arquitectura de divisió d'apertura per la immumització al soroll.

Finalment, aquesta tesi estudia les aplicacions del sistema per millorar la detecció en un problema del món real com és veure a través de la boira. La informació de la polarització pot millorar el rang de detecció degut a l'efecte de memòria de la polarització. Aquest sistema, doncs, podria utilitzar-se dins d'un altre sistema multimodal per assegurar la detecció quan la resta de sistemes estiguin perjudicats per les condicions externes.

Acknowledgements

Para todo aquel que quiso estar,
y estuvo.
Para todo aquel que pudo estar,
y estuvo.
Para todo aquel que hubo querido estar,
y no pudo.
Para todo aquel que hubo podido estar,
y no quiso.

Sara Peña Gutiérrez
Terrassa (Barcelona), November 2022

Contents

List of Figures

List of Tables

List of Acronyms

ϵ ellipticity.

3-OSC 3-parameters Orthogonal State Contrast.

AFOV Angular Field-of-View.

AL Achromatic Lens.

AOLP Angle of Linear Polarization.

AR Achromatic Retarder.

BCPN Balanced Condition of Poisson Noise.

BRIEF Binary Robust Independent Elementary Features.

CL Collimating Lens.

CMOS Complementary Metal-Oxide-Semiconductor.

CO Co-polarized.

CP Circular Polarizer.

CROSS Cross-polarized.

DoAmP Division of Amplitude Polarimeter.

DoAP Division of Aperture Polarimeter.

DoAPC Division of Aperture Polarimetric Camera.

DOCP Degree of Circular Polarization.

DoFP Division of Focal Plane.

DoG Difference of Gaussian.

DOLP Degree of Linear Polarization.

DOP Degree of Polarization.

DoTP Division of Time Polarimeter.

DRM Data Reduction Matrix.

ECM Eigenvalue Calibration Method.

EWV Equally Weighted Variance.

FAST Features from Accelerated Segment Test.

FOV Field-Of-View.

FPA Focal Plane Array.

FS Field Stop.

HL Horizontal linear.

HWP Half-wave plate.

LA Minilenses Array.

LC Left circular.

LCVR Liquid Crystal Variable Retarder.

LED Light Emitting Diode.

LP Linear Polarizer.

MM Mueller matrix.

MMI Mueller Matrix Imaging.

MSAC M-Estimator Sample Consensus.

MSE Mean Square Error.

NaN Not-a-Number.

OL Objective Lens.

ORB Oriented FAST and Rotated BRIEF.

OSC Orthogonal State Contrast.

PC Portable Computer.

PCA Principal Component Analysis.

PCM Polarizer Calibration Method.

PME Polarization Modulation Measurement.

PoCL Power over Camera Link.

PSA Polarization State Analyzer.

PSG Polarization State Generator.

QWP Quarter Waveplate.

RA Retarders Array.

RAD Reciprocal Absolute Determinant.

RC Right circular.

ROI Region-Of-Interest.

RPS Reference Polarization States.

RRFP Routable Retarder and Fixed Polarizer Polarimeter.

SIFT Scale Invariant Feature Transform.

SNR Signal-to-Noise-Ratio.

SoA State-of-the-Art.

SSIM Structural Similarity Index.

SURF Speeded Up Robust Features.

SVD Singular Value Decomposition.

ThI Tetrahedon I.

ThII Tetrahedon II.

TRE Target Registration Error.

VIS Visible Waveband.

VL Vertical linear.

VR Vortex Retarder.

VRFP Variable Retarders and a Fixed Linear Polarizer.

Chapter 1

Introduction

Motivation

The interaction of light with different types of materials has been always a subject of interest in Optics and Science. Legend says that Vikings used a ”sólarsteinn”, or sunstone, to help them navigate across the north Atlantic. It has been suggested that this sunstone could have been a piece of Icelandic spar [1] with a special property.

Nevertheless, the official first clues of polarization are attributed to Erasmus Bartholin in 1669 when discovered that those Iceland spar crystals (a variety of transparent calcite) refract light and produce a double image when objects are viewed through the crystals in transmitted light, although he was not aware of the phenomenon of polarization. Huygens interpreted the double refraction by assuming the different speeds of light inside the crystals and Thomas Young proved with the wave-particle duality of light that both split beams have different polarizations. Then, Etienne Louis Malus observed in 1808 that some images from reflected light from calcite crystals would occasionally disappear. He concluded that polarised light could be present in reflections from any transparent or opaque sample, except for polished metals. Once the electromagnetic theory was developed and the wave equation was demonstrated to be a consequence of Maxwell's theory [2], the research in polarization experimented a great progress, and so did the study of light-matter interaction.

The measurement of the primary physical quantities associated with the optical field such as intensity, wavelength, coherence and polarization provides different and complementary information about the nature of materials. In current image processing applications, including neural network training and deep learning, gathering as much information as possible becomes critical for each use case.

Conventional cameras measure the intensity of optical radiation over a discrete number of wavebands of interest. Spectral imagers appeared in order to measure the intensity in a variable number of wavebands, which can vary from one or two (with three being the well-known standard for a colour RGB camera) to multispectral systems that measure about 10 independent spectral bands, or hyperspectral systems that may measure 300 independent spectral channels, sometimes even more. Spectral sensors take advantage of the different behaviour of materials in different spectral bands to provide information about the distribution of the materials that compose a scene.

Polarimetry, however, provides a completely different source of information to get complementary data for computer vision applications. It consists in the measurement of the polarization state of the light beam, which has a vectorial nature that cannot be directly measured with a single image capture. Regarding

this, theoretical parameters have been developed to calculate through them the light state with a minimum of four independent intensity measurements. Polarization changes in a scene can give information on surface features, materials, shape, shading and roughness. This information tends to be largely uncorrelated with spectral and intensity images, making polarimetric images especially interesting due to the additional information content they may bring in.

Polarization imaging thus expands the dimensions of study from a point-to-point measurement of polarization to the evaluation of polarization in a 2D region of space. The polarization recovery can be done in two modes of acquisition: measuring the polarization states of light (Stokes imaging) or recovery of the matrix that contains all the polarization-related optical properties of the scene (Mueller matrix imaging). Both measurements are complementary since the Stokes vector arises from the application of the Mueller matrix of the sample to the light interacting with it. However, they need different times in acquisition, and different set-ups making them appropriate for different applications.

Consequently, polarimetry has emerged over the past decades as a powerful tool for image classification, and lately for computer vision and deep learning. Applications in imaging polarimetry have been found in remote sensing [3, 4], sensing through diffusive media like fog or smoke [5–7], aerosol characterisation [8], non-invasive cancer diagnostics [9, 10] or astrophysics [11–13], to mention a few.

This Thesis has, additionally, the particularity that it stands as the first work in polarimetry at CD6. This new line of research is complementary to other current active lines such as conventional imaging, spectral imaging, imaging through scattering media, and LiDAR imaging. Most of the applications in the field are evolving towards multi-modal sensory solutions, where polarimetric imaging is expected to provide a very relevant add-on,

Lately, applications have arisen in special in aspects related to vision through scattering media related to autonomous vehicles, where a big amount of energy is being devoted to improving perception of the environment of the vehicles in conditions where other imaging modes (intensity cameras, LiDAR) presented severely degraded performance.

Objectives of the Thesis

The main goal of this Thesis is to develop and optimize a snapshot polarimetric camera in the full VIS waveband, which maps the full state of polarization, including elliptical polarization states, across the scene of interest. Apart from different applications in material classification, such polarimetric imaging device could be applied to investigate imaging in scattering environments, in particular in fog.

Hence, the polarimetric camera developed in this Thesis is designed to extract specific polarization information by two main modes of imaging: Stokes imaging (under passive or active polarized illumination), and Mueller matrix imaging. This involves the development of a new hardware unit and the associated software algorithms required for the optimization of the obtained images. In particular,

this general objective requires a complete analysis of the methods used in modern polarimetry and of the state of the art of the technique.

To achieve this general objective, this Thesis has four consecutive specific objectives to accomplish. First specific objective is the detailed optomechanical design of the optimal polarimetric camera. Before performing the detailed optomechanical design, different configurations must be analysed to determine which is the most adequate approach to obtain a camera with a performance as good as possible. Priority will be given to acquire different polarimetric images with high speed while minimizing artifacts for applications in the detection of objects in movement.

Once the best configuration is chosen, the design and optimization of the prototype will be required using professional optical design programs such as Zemax OpticStudio. To do so, all the necessary optomechanical components to build the polarimetric camera onto an optical bench will be defined, from the components holding the optical components to the optical casing of the camera, adapted to real-world scenarios. Here we include decisions in the selection of how these components will be modified in the future use of the camera: passively (meaning by manually exchanging components when needed) or actively (using e.g. liquid crystals or other types of active devices), which types of components are needed including specific parameters, like polarimetric performance, the way of integration inside the set-up and the adequate illumination, detection and acquisition systems.

Our second specific objective will be developing the camera prototype designed, so it encompasses not only the correct mechanical assembly and optical performance, but also managing to communicate the hardware to the software for image acquisition and storage. The prototype pursues to set the basis for a robust and efficient camera with potential commercial and field use. Thus, it is necessary to register the polarimetric measurements, process them and quantify the viability as well as the main experimental factors that limit the performance of the system. This building process will include establishing the communication between components to acquire images, and also to implement the necessary calibration procedures of the system for the accurate recovery of polarization information.

This third specific objective allows the extraction of the final polarimetric images. After the system is built and calibrated, there is a need to develop detailed image processing algorithms to obtain the final polarimetric images from the measured intensity images. Two main modes of polarimetric imaging will be implemented, so different algorithms will be required for each one. Furthermore, the analysis of the obtained polarization information is expected to allow the calculation of inherent polarimetric parameters from the final images, simplifying the understanding of the polarimetric information. These parameters are easily displayed to an end user or introduced in a detection algorithm, depending on the final application.

Our final specific objective is to test and validate the performance of the polarimetric camera built in the Thesis. Once the polarimetric camera is correctly built so it displays accurately the polarimetric images, it is time to prove its

performance in two different scenarios. Firstly, the polarimetric camera will validate its performance in material inspection applications, testing its capability to differentiate materials. These experiments will increase in complexity starting from samples with known properties up to real-world scenarios, and will use both polarization modes of the camera are tested to demonstrate the capability of the system to retrieve any kind of polarization information. Both Stokes and Mueller matrix imaging modes will be used and its differences shown. Secondly, we intend to apply the prototype to investigate a real-world problem: imaging through diffusive media using active Stokes imaging. The study of contrast enhancement is particularly interesting when applied to image recovery through highly scattering media such as fog, smoke and other turbid media, such as tissue [14].

Structure of the thesis

This Thesis is structured in four parts corresponding to the main specific objectives described above which are coincident with the development stages of the polarimetric camera: State-of-the-Art (SoA), design and built-up, system calibration and polarization results. Each part is divided into chapters explaining in detail the different topics. This Thesis begins with Chapter 1 to motivate this work. The main and specific objectives are presented and they agree with the structure of the developed work and this dissertation.

Part I intends to present the general context of the polarization field directly related to this Thesis. This part only contains Chapter 2 where several topics related to polarimetric imaging are introduced to the reader. Polarization theory is briefly explained to provide the basis of the theoretical calculations later used in this dissertation. This sets a basis to detail the theory of polarimetric imaging introducing the different modes of imaging (Stokes and Mueller matrix imaging) together with the analysis in the literature about the theoretical optimization of the polarimetric devices. Thereafter, a second part of the chapter addresses experimental issues relevant to our development. Firstly, the existing configurations for the construction of a polarimetric device are presented with their advantages and disadvantages. Then, the different algorithms for calibrating these devices are gathered from the literature and discussed. Finally, an outline of reported applications of polarimetric imaging are given, with a special emphasis on the application of polarization detection in dispersive media.

Part II comprises Chapter 3, and becomes the inflection point from theoretical study to empirical work. It extends into the steps followed for the optomechanical design of the snapshot polarimetric camera and further improvements on the polarimetric device for various applications. It presents the final design and shows the built-up device. The hardware-software communication for the acquisition of the images is presented. Moreover, the chapter also presents the different illumination arrangements for the different imaging modes.

Part III describes in detail the methodology of calibration required for the correct performance of the polarimetric camera. In Chapter 4, the calibrations regarding the sensor itself and the optical elements are described. Every sensor

needs to be calibrated radiometrically for acquiring the correct intensity values during the experiments. On the other hand, optical elements may introduce aberrations in the light beam arriving at the sensor and a geometrical calibration accounts for these distortions. Chapter 5 explains the polarimetric calibration that allows the camera to transform the intensity values measured at the sensor into polarization information. Each mode of imaging has its own calibration algorithm. This chapter describes the algorithms used and shows the first quantitative results in polarization recovery.

Last Part IV gathers all the experimental results of this Thesis work. Imaging polarimetry has a very wide field of work, as mentioned in the motivation. Chapter 6 presents the polarization information recovered by our polarimetric camera using passive and active Stokes imaging and Mueller matrix imaging. Each mode lets us observe different information about the scene. Various samples are tested using both modes of imaging and the results are discussed. Finally, Chapter 7 develops the work carried out in a large-scale experiment where the ability of polarimetric imaging for object detection in dispersive media is analysed.

After the four parts of the work have been presented, global conclusions are given together with suggestions for future works related to the results of this Thesis.

Part I

State of the Art

Chapter 2

Polarimetric imaging

This chapter contextualizes the framework in which this project is conceived. In the beginning, a brief overview of polarization theory is presented. Then, the state-of-the-art related to polarimetric imaging is covered by a review of the different measurement strategies, calibration techniques and optimization methods. Finally, the different applications of the polarimetric cameras are listed, highlighting the applications pursued in imaging through diffusive media.

2.1 Polarization of light

The light was seen by Maxwell for the first time as an electromagnetic wave in 1865 [2, 15]. The electromagnetic theory states that light propagates in free space as a transverse electromagnetic wave, where the electric field $\vec{E}$ and magnetic field $\vec{H}$ oscillate in mutually perpendicular directions and in phase, for a monochromatic wave. For the light of angular frequency ω, wave number k and direction of propagation z, the electric field may oscillate in the xy plane such that it can be represented as a vector in Cartesian coordinates:

$$\begin{aligned}\vec{E}(z,t) &= E_x(z,t)\hat{x} + E_y(z,t)\hat{y} \\ &= E_{0x}\cos(kz - \omega t + \phi_x)\hat{x} + E_{0y}\cos(kz - \omega t + \phi_y)\hat{y}\end{aligned} \tag{2.1}$$

where t represents time, $\hat{x}$ and $\hat{y}$ are the unit vectors and E_{0x} and E_{0y} are the initial electric field amplitudes in x and y directions, respectively.

The polarization of light relates to the orientation of the electric field in the electromagnetic wave. The locus of the tip of the electric field vector (at fixed position z) generally describes an ellipse with a rotated axis defined by the following parametric equation:

$$\frac{E_x^2(t)}{{E_{0x}}^2} + \frac{E_y^2(t)}{{E_{0y}}^2} - 2cos\phi\frac{E_x(t)E_y(t)}{E_{0x}E_{0y}} = sin^2\phi \tag{2.2}$$

where $\phi = \phi_y - \phi_x$ is the phase difference between the x and y components of the electric field vector. Viewed along the direction of propagation of light, the tip of the electric field may rotate clockwise (or anti-clockwise) and it is called right-handed (left-handed) elliptical polarization.

Figure 2.1 displays the possible positions of the tip of the electric field vector that can be traced out in the xy plane for various ϕ values. The electric field rotates as the wave propagates, repeating its motion periodically with a spatial period of a wavelength λ.

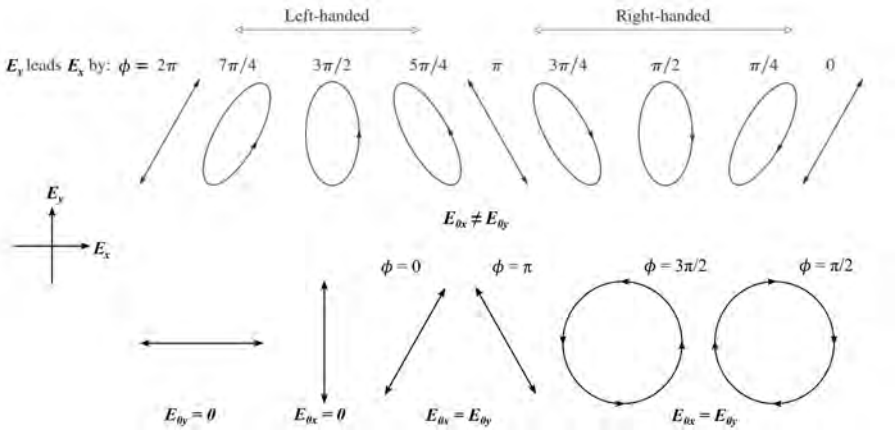

Figure 2.1: Various polarization configurations resulting from different values of phase difference ϕ and amplitudes E_{0x} and E_{0y}.

The shape of the ellipse determines the state of polarization of the wave. This shape depends on the ratio of amplitudes E_{0x}/E_{0y} and the phase difference ϕ and there exist two degenerate cases:

1. If one of the components vanishes: $E_{0x} = 0$ or $E_{0y} = 0$ or the phase difference is $\phi = m\pi$ ($m = 0, \pm1, \pm2, \dots$), the Equation (2.2) describes a straight line and the wave is said to be linearly polarized.

2. If $E_{0x} = E_{0y}$ and $\phi = 1/2m$ ($m = \pm1, \pm3, \pm5$), the resulting Equation (2.2) corresponds to the equation of a circle. The wave is said to be circularly polarized, with appropriate handedness.

To determine this ellipse, the amplitudes E_x and E_y and the phase difference ϕ must be identified. Since measuring directly these magnitudes is not possible, four parameters are identified to determine the ellipse experimentally and are known as Stokes vector, named after Stokes who first introduced them [16].

Stokes vector describes the state of polarization of light. In the case of a monochromatic wave, the amplitudes E_{0x} and E_{0y} and the phase difference ϕ are constants. Since the amplitudes E_x and E_y are implicitly time-dependent, it is necessary to average over a single period of vibration $\langle ... \rangle_T$. Therefore, the Stokes parameters provide the amplitudes of the electric field and the phase difference of both components using simple experiments that measure the time-averaged intensity of the waves. The four Stokes parameters for a monochromatic light are defined as follows [17]:

$$\vec{S} = \begin{cases} S_0 = 2\left\langle E_x^2 \right\rangle_T + 2\left\langle E_y^2 \right\rangle_T = E_{0x}^2 + E_{0y}^2 & \text{(2.3a)} \\ S_1 = 2\left\langle E_x^2 \right\rangle_T - 2\left\langle E_y^2 \right\rangle_T = E_{0x}^2 - E_{0y}^2 & \text{(2.3b)} \\ S_2 = 4\,\mathbb{R}\mathrm{e}\left\langle E_x E_y^* \right\rangle_T = 2E_{0x}E_{0y}\cos\phi & \text{(2.3c)} \\ S_3 = -4\,\mathbb{I}\mathrm{m}\left\langle E_x E_y^* \right\rangle_T = 2E_{0x}E_{0y}\sin\phi & \text{(2.3d)} \end{cases}$$

Note only three of these parameters are independent, since $S_1^2 + S_2^2 + S_3^2 = S_0^2$ for fully polarized monochromatic light.

In the 1940s, two separate theories of treating polarized light arose by the hand of Jones (1941) and Mueller (1943) [18]. Each one developed a matrix calculus to describe the linear interaction of polarized light but from a different basis. Jones calculus works in the space of two-dimensional complex vectors that represent the electric field and accounts for the absolute phase. The Jones vector for a general fully polarized light (elliptically polarized state) is written by omitting the space and time-varying phase factor $kz - \omega t$:

$$\vec{E} = \begin{pmatrix} E_x \\ E_y \end{pmatrix} = \begin{pmatrix} E_{0x} \\ E_{0y}e^{i\phi} \end{pmatrix} \tag{2.4}$$

The interaction of light with a non-depolarizing birefringent material is represented by a 2x2 complex matrix. Jones calculus does not allow the description of partially polarized light or depolarized light since the light is described as a deterministic transverse wave. It does not consider incoherent light, either.

On the other hand, Mueller calculus describes the linear interaction of the polarized light with an optically anisotropic medium, and it is based on the intensity rather than on the electric field as Jones calculus, neglecting the phase information. Under this approach, any fully polarized, partially polarized or depolarized light beam can be represented as a Stokes vector and any physically realisable optical element can be represented by a 4x4 Mueller matrix with real-valued elements:

$$\mathbf{M} = \begin{pmatrix} m_{00} & m_{01} & m_{02} & m_{03} \\ m_{10} & m_{11} & m_{12} & m_{13} \\ m_{20} & m_{21} & m_{22} & m_{23} \\ m_{30} & m_{31} & m_{32} & m_{33} \end{pmatrix} \tag{2.5}$$

Then, the Mueller matrix of a system is defined as the matrix $\mathbf{M}$ which transforms an incident Stokes vector $\vec{S}_{in}$ into the exiting (reflected, transmitted or scattered) Stokes vector $\vec{S}_{out}$

$$\vec{S}_{out} = \mathbf{M} \cdot \vec{S}_{in} \tag{2.6}$$

Both formalisms are useful in diverse situations due to their features [2, 19]. When measuring a polarization state it is best to use Mueller-Stokes formalism, as a certain degree of unpolarized light will be present. Nevertheless, when doing

theoretical calculations, full polarization is assumed and it can be advantageous to consider the Jones formalism with the absolute phase of the light.

A very useful tool for visualizing the effects of optical elements such as polarizers or retarders, on a polarized beam is the Poincaré sphere. It can be understood as a 3-dimensional plot of the Stokes vector, where the Cartesian coordinates correspond to the Stokes parameters, as depicted in Figure 2.2. Hence, any polarization state can be represented as a point on the unity-radius sphere. The points on the surface correspond to fully polarized states, while partially polarized states lie inside the Poincaré sphere at a distance $P = \sqrt{S_1^2 + S_2^2 + S_3^2}$ from the origin. Totally unpolarized light will be represented by a point at the origin of coordinates. The equator represents all linear polarization states since the S_3 parameter is null and no ellipticity is present. The "north" and "south" poles of the sphere represent purely right- and left-circular polarization, respectively. Any point lying between the equator and the poles corresponds to an elliptically polarized state. The angle of the ellipticity (ξ) depends on the angle along the equator and the azimuth angle (ψ) accounts for the angle between S_1 and S_2 axes.

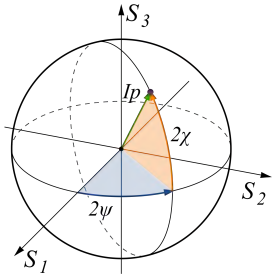

Figure 2.2: Poincaré sphere where the three Stokes parameters (S_1, S_2, S_3) are plotted in Cartesian coordinates. IP denotes the radius of the point of the specific polarization state. Ξ corresponds to the ellipticity angle and Ψ denotes the azimuth angle

2.2 Polarimetric imaging: theoretical background

Polarimetry is the science of measuring polarization, as already introduced. The polarization properties of the light beam or the samples are detected by employing polarimeters. They can be subdivided into two main categories: light-measuring or Stokes polarimeters and sample-measuring or Mueller matrix polarimeters. In this Thesis, the imaging polarimeters are explained since they provided 2-dimensional spatial information.

The polarimeters operate by acquiring intensity measurements with a set of polarization state analyzers and a set of polarization state generators. A polarization analyzer (PSA) is a configuration of polarization elements, optical elements and a detector whose detected intensity is proportional to the content of a specific polarization state in the incident beam [20]. Similarly, a polarization generator (PSG) consists of a light source, optical elements and polarization

elements that produce a specific and known polarization state. They are used in Mueller matrix retrieval and the calibration of imaging polarimeters.

Along with this Thesis, the Mueller-Stokes calculus is used for describing the irradiance-measuring models of the different polarimeters.

2.2.1 Stokes imaging

The Stokes parameters determine the polarization state of a light beam or some of its polarization characteristics. In order to do that, they use a set of polarization elements placed in the light beam path in front of a radiometer. That means the input light beam from the scene is analyzed by a series of polarization state analyzers and the Stokes vector of the input light can be retrieved from those measurements after calibration.

A full-Stokes camera provides four-dimensional images corresponding to the Stokes vector $\vec{S} = (S_0, S_1, S_2, S_3)$. As the Stokes vector comes from the measurement of the resulting intensities, its values depend on the wavelength, the position of the object, and the light's direction of emission or scatter. Therefore, the measured Stokes vector is average over the area, the solid angle and the wavelength, as it happens in any radiometric measurement [20]. The Stokes parameters have four degrees of freedom, and thus, they can be obtained by taking at least four different measurements [21]. In some cases, the Stokes parameter can be calculated directly by subtracting the intensities of six distinct images of the scene at each pixel [15, 22]:

$$\vec{S} = \begin{pmatrix} S_0 \\ S_1 \\ S_2 \\ S_3 \end{pmatrix} = \begin{pmatrix} I_x + I_y \\ I_x - I_y \\ I_{45^o} - I_{-45^o} \\ I_R - I_L \end{pmatrix} \tag{2.7}$$

where I_x is the image obtained using a polarizer with its axis parallel to x axis, I_y the image using a polarizer parallel to y axis, I_{45^o} and I_{-45^o} the images taken with polarizers oriented at $\pm 45^o$ and I_R, $I_L$are intensity images of the scene obtained using right and left circular polarizer, respectively.

The image of the Stokes vector is a stack of four different images that provides the Stokes vector of the scene at each pixel. Normally, these multiple images are reduced to a single scalar image to be displayed to an end-user or introduced in a detection algorithm. This scalar parameter can be the degree of polarization (DOP) or the orthogonal-states contrast (OSC) parameter, depending on the final application.

The DOP image informs about the fraction of the intensity attributable to polarized light states [2, 20]. Mathematically, it is expressed in terms of the Stokes parameters in the following manner:

$$DOP = \frac{\sqrt{S_1^2 + S_2^2 + S_3^2}}{S_0} \tag{2.8}$$

This polarimetric parameter may allow distinguishing between materials that have the same reflectivity but present different polarimetric properties [21]. DOP

imaging has been used widely in various fields of polarimetry such as industrial machine vision [23], biomedical imaging for the diagnosis of skin pathology [24] and for tissue imaging [14].

Apart from the DOP parameter, the fraction of polarized light can be split into two more specific parameters depending on the type of polarization: the degree of linear polarization (DOLP) and the degree of circular polarization (DOCP):

$$DOLP = \frac{\sqrt{S_1^2 + S_2^2}}{S_0} \tag{2.9}$$

$$DOCP = \frac{S_3}{S_0} \tag{2.10}$$

These parameters allow enhancing the contrast where such polarizations appear, for example, the DOCP may allow distinguishing between dielectric and metal materials under linear polarized light [21].

Regarding the OSC image, it is analogous to DOP when the birefringent materials being part of the image can be neglected, under active illumination with linear polarization along x and y directions. It is obtained by measuring a partial Stokes vector:

$$OSC = \frac{S_1}{S_0} \tag{2.11}$$

Other advanced parameters can be extracted from the Stokes parameters images like the angle of linear polarization (azimuth) and the ellipticity [2, 19, 20].

$$\alpha = \frac{1}{2}\arctan(\frac{S_2}{S_1}), \qquad 0 \leq \alpha \leq \pi \tag{2.12}$$

$$\epsilon = \frac{1}{2}\arcsin(\frac{S_3}{S_0}), \qquad -\frac{\pi}{4} \leq \epsilon \leq \frac{\pi}{4} \tag{2.13}$$

Stokes vector and related parameters for a light beam are calculated from the measurement of the flux transmitted through a set of polarization state analyzers (PSA). The polarization of the incident beam is projected onto each analyzer determining the proportional flux arriving at the detector. This PSA must be calibrated to recover the polarization information, as will be explained in the following Section 2.4.3. The behaviour of the whole PSA of N analyzers is characterized in the instrument matrix $\mathbf{A}$, which is composed by stacking vertically the first row of the Mueller matrix of each analyzer [19, 25]:

$$\mathbf{A} = \begin{pmatrix} a_{0,0} & a_{0,0} & a_{0,0} & a_{0,0} \\ a_{1,0} & a_{1,0} & a_{1,0} & a_{1,0} \\ \vdots & \vdots & \vdots & \vdots \\ a_{N-1,0} & a_{N-1,0} & a_{N-1,0} & a_{N-1,0} \end{pmatrix} \tag{2.14}$$

Hence, the intensity vector $\vec{I}$ detected in after the PSA is calculated by applying the instrument matrix to the incident Stokes vector $\vec{S}_{in}$. This is expressed by the polarimetric measurement equation:

$$\vec{I} = \mathbf{A} \cdot \vec{S}_{in} \tag{2.15}$$

If $\mathbf{A}$ is known, the Equation (2.15) can be inverted to solve the incident Stokes vector. The main objective of the polarimetric calibration consists of determining the instrument matrix $\mathbf{A}$ containing the real information of the PSA. It should be convenient to state that there will be always differences between the calibrated matrix and the actual instrument matrix due to systematic errors.

Finally, the Stokes vector of a scene ($\vec{S}_{rec}$) can be obtained by applying the inverse of the instrument matrix ($\mathbf{W} = \mathbf{A}^{-1}$) to the intensity values projected from the PSA at the detector:

$$\vec{S}_{rec} = \mathbf{W} \cdot \vec{I} \tag{2.16}$$

As stated before, the simplest recovery of the Stokes vector occurs when the PSA is composed of four linearly independent analyzers. In this case, the rank of $\mathbf{A} = 4$ and the instrument matrix $\mathbf{A}$ is not singular, proving the existence and uniqueness of $\mathbf{W}$ [2, 26].

2.2.2 Mueller matrix imaging

Mueller matrix polarimeters retrieve the relationship between the input and output polarization states for a sample. The measurements are acquired using a PSG to generate the input polarized beams into the scene of interest and a PSA to detect the output polarized beams from the sample.

Recalling the Mueller matrix (MM), it is a four-by-four matrix with real elements. It models the effects of an optical component on any polarization state and it can be used for characterizing polarization measurements since it contains all polarization properties: diattenuation, retardance and depolarization.

The MM allows to know the output polarization state ($\vec{S}_{out}$) of an arbitrary input polarization state ($\vec{S}_{in}$). When a beam interacts with several polarization elements through its path, the MM can be expressed as the right-to-left product of the individual matrices ($\mathbf{M}_i$, $i = 1, 2..., Q$):

$$\vec{S}_{out} = \mathbf{M}_Q \cdot \mathbf{M}_{Q-1} \cdots \mathbf{M}_2 \cdot \mathbf{M}_1 \cdot \vec{S}_{in} \tag{2.17}$$

A rotation by θ, without changing the angle of incidence, of a polarization element with Mueller matrix $\mathbf{M}$ can be represented by the rotation Mueller matrix $\mathbf{M}(\theta)$:

$$\mathbf{M}(\theta) = \mathbf{R}_M(\theta)\mathbf{M}\mathbf{R}_M(-\theta) \tag{2.18}$$

where $\mathbf{R}_M$ is the rotational change of basis in the Mueller-Stokes formalism:

$$\mathbf{R}_M(\theta) = \begin{pmatrix} 1 & 0 & 0 & 0 \\ 0 & \cos(2\theta) & -\sin(2\theta) & 0 \\ 0 & \sin(2\theta) & \cos(2\theta) & 0 \\ 0 & 0 & 0 & 1 \end{pmatrix} \tag{2.19}$$

Materials can show diattenuation, where the intensity transmittance of the output light beam depends on the incident polarization state, or retardance, where a polarization-dependent phase change is introduced depending on the input polarization state. Generally, polarization elements are non-ideal and a combination of both properties can occur simultaneously. Equation (2.20) shows the MM associated with this non-ideal sample which can act like a linear-diattenuator and/or a linear-retarder [2, 27].

$$\mathbf{M}_{gen}(\tau, \Psi, \delta) = \tau \cdot \begin{pmatrix} 1 & -\cos 2\Psi & 0 & 0 \\ -\cos 2\Psi & 0 & 0 & 0 \\ 0 & 0 & \sin 2\Psi \cos\delta & \sin 2\Psi \sin\delta \\ 0 & 0 & -\sin 2\Psi \sin\delta & \sin 2\Psi \cos\delta \end{pmatrix} \tag{2.20}$$

where τ is the total intensity transmittance, δ is the retardance of the sample and Ψ is the elliptic angle between the electric field components.

$$\tau = \sqrt{\tau_{\parallel}^2 + \tau_{\perp}^2} \tag{2.21a}$$

$$\tan\Psi = \sqrt{\frac{\tau_{\parallel}}{\tau_{\perp}}} \tag{2.21b}$$

The general MM of a non-ideal polarization element can be done by applying a rotation of angle θ to the $\mathbf{M}_{gen}$ matrix using Equation (2.19).

The MM can be determined following the same procedure as in Stokes imaging. Several polarimetric measurements are performed to calculate the elements of the matrix $q = 0, 1, ..., Q-1$. In this case, for each qth measurement, the PSG generates the polarization state which is incident on the sample $\vec{S}_q$. The output Stokes vector from the sample corresponds to $\mathbf{M}\vec{S}_q$. This state is analyzed by the qth analyzer of the PSA. The flux measured at the detector is $\vec{I}_q = \vec{A}_q^T \mathbf{M} \vec{S}_q$.

Each measured flux $\vec{I}_q$ is a linear function of the elements of the MM. Performing a set of polarimetric measurements, at least 16, allows us to solve the matrix system for the MM. Therefore, the complete matrix system consists of the fluxes $\mathbf{I}_{QxN}$ coming from the M generated polarization states ($\mathbf{G}$) which have been measured by each of the N analyzers composing the PSA ($\mathbf{A}$):

$$\mathbf{I}_{NxQ} = \mathbf{A}_{Nx4} \mathbf{M}_{4x4} \mathbf{G}_{4xQ} \tag{2.22}$$

This method requires the PSG ($\mathbf{G}$) and PSA ($\mathbf{A}$) to be well characterized through calibration for an accurate MM measurement. Once both matrices are

obtained by applying the calibration methods explained in Section 2.4.3, the MM can be estimated by solving the previous linear system:

$$\mathbf{M} = \mathbf{A}^{-1}\mathbf{I}\mathbf{G}^{-1} = \mathbf{W}\mathbf{I}\mathbf{G}^{-1} \tag{2.23}$$

The MM fully characterizes a polarization element. As previously said, despite that the three polarization properties are contained in the MM description, their determination is a complex process.

The MM elements can be related to a certain property, though they are intrinsically related [20, 28]:

$$\begin{pmatrix} 0 & a & b & c \\ a & 0 & -d & -e \\ b & d & 0 & -f \\ c & e & f & 0 \end{pmatrix} \tag{2.24}$$

The following properties are related to the specified elements:

a - linear diattenuation oriented at 0^o or 90^o

b - linear diattenuation oriented at 45^o or 135^o

c - circular diattenuation

d - linear retardance oriented at 0^o or 90^o

e - linear retardance oriented at 0^o or 90^o

f - circular retardance

Other degrees of freedom in the MM in the diagonal and the rest of the components indicate the presence of depolarization and inhomogeneity.

The diattenuation $\mathbf{D}(\mathbf{M})$ of a MM measures the variation of intensity transmittance with incident polarization state. An index of the diattenuation presence can be calculated as:

$$\mathbf{D}(\mathbf{M}) = \frac{\sqrt{m_{01}^2 + m_{02}^2 + m_{03}^2}}{m_{00}} \tag{2.25}$$

If $\mathbf{D} = 1$, the sample is an ideal analyzer. Moreover, if there is no depolarization, its MM represents a polarizer. If $\mathbf{D} = 0$, the incident and output states will have the same intensity.

Depolarization is the transformation of polarized light into unpolarized light. This happens when the output DOP is less than one. Depolarization is closely related to scattering and normally has its origin in retardance or diattenuation which varies rapidly in time, space or wavelength [20]. An index of depolarization can show how close a MM is to the non-depolarizing Mueller matrix [29]:

$$\mathbf{Dep}(\mathbf{M}) = 1 - \frac{\sqrt{(\sum_{i,j} m_{ij}^2) - m_{00}^2}}{\sqrt{3} m_{00}} \tag{2.26}$$

On contrary, when having a complex sample (like in an anisotropic medium), distinguishing the polarization properties from the MM is not so straightforward since it may happen that several polarization behaviours simultaneously. As consequence, a solution to this problem can be found by using various methods of decomposing a macroscopic MM into a product of several matrices. Nowadays, this topic is becoming very relevant since there is a growing interest in the applications of polarimetric characterization techniques. Mueller matrix decomposition is a key role to study and interpret the experimental data in a proper manner [30–33].

Several Mueller matrix decompositions have been proposed. Three main decompositions stand out among the others and they are based on different approaches. Cloude decomposition is a sum-based decomposition that enables the description of the predominant polarizing optical behavior of a certain sample, as well as characterizing its depolarizing properties [34, 35]. Despite this, it cannot separate all the optical effects and account for them. Lu-Chipman polar decomposition [30, 36] generalized the polar decomposition for depolarizing media. It is the most widely used method in experimental Mueller matrix applications, see Section 2.5. The differential decomposition [28, 31, 37] is especially suited for analyzing media with simultaneously occurring effects. Other interesting decompositions are the normal form decomposition [38] and the symmetric decomposition [39, 40], being the latter comparatively easier to obtain and interpret.

Despite the different studies on decompositions, there are still some difficulties that usually arise when experimentally measuring and analyzing samples. First of all, the order in which the effects take place in the sample may not be known *a priori*, and therefore the results are subjected to entail some errors. And secondly, there are media in which the effects are produced in a distributed way, homogeneously, and not in a sequential fashion. In this case, product decompositions are about to fail [31].

2.2.3 Optimization of imaging polarimeters

The intensity measurement of any signal consists of the detection of the desired signal itself in addition to different noises. This is a general known which applies to the (imaging) polarimeter devices. All the polarimeters are formed by a set of optics and a no-polarization sensitive sensor. The three main sources of noise are random intensity fluctuations, systematic errors from misalignment and non-ideal components.

Stokes (imaging) polarimeters: figures of merit

Polarimeters measure the intensities in order to get the polarization signature by means of estimating the Stokes parameters, $\vec{S}$, that is by the measurement matrix $\mathbf{A}$.

$$\vec{I} = \mathbf{A} \cdot \vec{S} \Rightarrow \vec{S} = \mathbf{W} \cdot \vec{I} \tag{2.27}$$

If the intensity signal contains noise, as stated, the estimated Stokes parameters will be retrieved with noise contamination.

$$\vec{S} = \mathbf{W} \cdot (\vec{I} + \Delta\vec{n}) = \mathbf{W} \cdot \vec{I} + \mathbf{W} \cdot \Delta\vec{n} \tag{2.28}$$

Several studies have been carried out during the last twenty years about how to reduce the noise interference in the retrieved signal and thus, improve the detection accuracy of the polarization signature of the scene. Tyo [41, 42] develop a figure of merit to improve detection by means of choosing the correct polarization states of measurement. This figure was the condition number based on the metric p (κ_p) of the measurement matrix, **A**:

$$\kappa_p = \|A\|_p^{-1} \cdot \|A\|_p \tag{2.29}$$

For an optimal polarimeter, it was demonstrated to be $\kappa_2 = \sqrt{3}$ [42]. This is equivalent to a polarimeter whose polarization states form a geometrical figure with the maximum volume when represented in the Poincaré sphere, which corresponds to moving the **A** matrix away from a singularity ($|A| \neq 0$). Simultaneously, Sabatke [43] studied two parameters based on singular value decomposition of the measurement matrix: reciprocal absolute determinant (RAD) and equally weighted variance (EWV). The RAD is the determinant of **A** and its geometrical interpretation lies in maximizing the volume by minimizing the determinant. On the other hand, the second figure of merit studies the variation of the polarization signal by analysing the variation sum of variances of the Stokes vector. Firstly, he did some assumptions such as the variances of the different Stokes parameters were equal under the condition of the noise is signal-independent and the S_0 component is larger than S_i, under signal-dependent noise. He arrived at the same conclusion as Tyo, since the equally weighted variance (EWV):

$$EWV = \sum_{i=0}^{3}\sum_{j=0}^{N-1}(\mathbf{W}^+)_{i,j}^2 = Tr[(\mathbf{W}^+)^T\mathbf{W}^+] = \sum_{j=0}^{N-1}\frac{1}{\sigma_j^2} \tag{2.30}$$

is optimized when the locus of the Stokes vectors of **A** form a regular polyhedron with maximum volume. In the formula, W^+ is the Moore-Penrose pseudoinverse matrix (when $N \neq 4$) and σ_j^2 are the singular values of W^+. The optimal value when the noise fulfils the aforementioned conditions is EWV = 10. Since $N = 4$ is the minimum number of measurements, he also demonstrated it is not necessary to oversample with more than the 4 optimal ones since the mere repetition of them (or performing a large exposition at each acquisition) leads to the same results.

Another figure of merit, more applied to astronomical polarimeter design, is the polarization modulation measurement (PME). It was first introduced by Del Toro and Collados [44]. This parameter helps to compare polarimeters with a different number of polarization states. They define the concept of global variance as the accumulation of the variance at each measurement (σ_j^2) through

a complete cycle $\bar{\sigma}_i^2 = n \cdot \sigma_i^2$. They introduce the PME as a factor that represents the efficiency of the modulation scheme when obtaining ($\bar{\sigma}_j^2$):

$$\epsilon_i = (n \sum_{j=1}^{N} \mathbf{A}_{i,j}^2)^{-\frac{1}{2}} \tag{2.31a}$$

$$\bar{\sigma}_j^2 = \frac{\sigma^2}{\epsilon_i^2} \tag{2.31b}$$

Two modulation schemes of equal efficiency will have equal contributions to the total variance of the cycle, and the larger n, the smaller σ_j^2 is.

The PME allows obtaining the maximum (optimum) efficiency numbers by calculating:

$$\mathbf{O} = \mathbf{A}^T \cdot \mathbf{A} \tag{2.32}$$

where $\mathbf{A}$ is the measurement matrix. The matrix $\mathbf{O}$ has the form:

$$\mathbf{O} = \frac{N}{4} \begin{pmatrix} \epsilon_{max,1} & 0 & 0 & 0 \\ 0 & \epsilon_{max,2} & 0 & 0 \\ 0 & 0 & \epsilon_{max,3} & 0 \\ 0 & 0 & 0 & \epsilon_{max,4} \end{pmatrix} \tag{2.33}$$

where N is the number of the polarization states measurements in the cycle and $\epsilon_(max, i)^2$ are the squared singular values of $\mathbf{O}$ matrix, the adjoint operator of $\mathbf{A}$. The conditions of this matrix are $\epsilon_{max,1}^2 = 1$ and $\sum_{j=1}^{N} \epsilon_{max,i}^2 \leqslant 1$ [44].

Last presented figures (κ_2, EWV and PME), when at their optimum value, are equivalent to reaching the maximum SNR. This happens when the rows of the matrix $\mathbf{A}$ are a combination similar to $\{1, \sqrt{3}, \sqrt{3}, \sqrt{3}\}$, whose correspondent singular values are $[1, 1/\sqrt{3}, 1/\sqrt{3}, 1/\sqrt{3}]$ [41, 44, 45]. This condition for N = 4 leads to the optimum measurement matrix $\mathbf{A}_{opt}$ be:

$$\mathbf{A}_{opt} = \frac{1}{2} \begin{pmatrix} 1 & -\frac{1}{\sqrt{3}} & -\frac{1}{\sqrt{3}} & -\frac{1}{\sqrt{3}} \\ 1 & -\frac{1}{\sqrt{3}} & +\frac{1}{\sqrt{3}} & +\frac{1}{\sqrt{3}} \\ 1 & +\frac{1}{\sqrt{3}} & +\frac{1}{\sqrt{3}} & -\frac{1}{\sqrt{3}} \\ 1 & +\frac{1}{\sqrt{3}} & -\frac{1}{\sqrt{3}} & +\frac{1}{\sqrt{3}} \end{pmatrix} \tag{2.34a}$$

$$\mathbf{A}_{opt} = \frac{1}{2} \begin{pmatrix} 1 & +\frac{1}{\sqrt{3}} & +\frac{1}{\sqrt{3}} & +\frac{1}{\sqrt{3}} \\ 1 & +\frac{1}{\sqrt{3}} & -\frac{1}{\sqrt{3}} & -\frac{1}{\sqrt{3}} \\ 1 & -\frac{1}{\sqrt{3}} & -\frac{1}{\sqrt{3}} & +\frac{1}{\sqrt{3}} \\ 1 & -\frac{1}{\sqrt{3}} & +\frac{1}{\sqrt{3}} & -\frac{1}{\sqrt{3}} \end{pmatrix} \tag{2.34b}$$

As it may be appreciated, the relation between the EWV and the PME is straightforward. The former is the sum of the inversed components of the latter. Hence, achieving the maximum efficiency means having the lowest variation in the estimation of the Stokes components.

Among the previous parameters, EWV was felt as an important parameter in polarimeter design and it was further studied. Peinado *et al.* [46] threw the conclusions that, as previously highlighted, the polarization analysers that equal the vertexes of the so-called Platonic Solids, the regular polyhedrons that achieve maximum volume in the Poincaré sphere, have optimal minimum κ_2 and EWV. However, there is a global family, known as spherical t-design (in specific for $t \geq 2$), that contains them and fulfils simultaneously the optimization for κ_2 and EWV making them minimum [47].

In addition, it is especially remarkable the work of Goudail [45] who studied the behaviour of the EWV under the presence of Poisson shot noise. He applied the work of Sabatke [43] employing estimators for the Stokes parameters and covariance theory. The estimator $\hat{S} = \mathbf{W}^{+}\vec{I}$ when $N > 4$ it is shown that W^{+} is the maximum-likelihood estimator in the presence of Gaussian noise. In the presence of Poisson shot noise, it is a closed-form algorithm [45]. Furthermore, it is unbiased since $\left\langle \hat{S} \right\rangle = \mathbf{W}^{+} \left\langle \vec{I} \right\rangle = \vec{S}$ and the estimation performance of the estimator $\hat{S}$ relies on its covariance matrix:

$$\Gamma^{\hat{S}} = \mathbf{W}^{+} \cdot \Gamma^{\mathbf{I}} \cdot (\mathbf{W}^{+})^{T} \tag{2.35}$$

where Γ^{I} is the covariance matrix of the intensity matrix $\mathbf{I}$.

Defining the properties of $\Gamma^{\mathbf{I}}$ under the presence of Gaussian or Poisson shot noise, the covariance matrix $\Gamma^{\hat{S}}$ expresses the variances on each component. From [48], it can be seen that the covariance matrix under Gaussian noise is written as:

$$\Gamma_{G}^{\hat{S}} = \sigma^{2}(\mathbf{A}^{T} \cdot \mathbf{A})^{-1} \tag{2.36}$$

where σ^2 is the Gaussian noise variance. As it can be appreciated, the covariance matrix under Gaussian noise is the inverse matrix of the adjoint operator of $\mathbf{A}$, previously presented in the PME. Substituting in the inverse of Equation (2.33) the condition of the singular values above mentioned, the covariance matrix is:

$$\Gamma_{G}^{\hat{S}} = \frac{4\sigma^{2}}{N} \begin{pmatrix} 1 & 0 & 0 & 0 \\ 0 & 3 & 0 & 0 \\ 0 & 0 & 3 & 0 \\ 0 & 0 & 0 & 3 \end{pmatrix} \tag{2.37}$$

The EWV is calculated from the covariance matrix as explained in [43] and it agrees with the expression derived from [47]:

$$EWV_{G} = Tr[\Gamma_{G}^{\hat{S}}] = \frac{4\sigma^{2}}{N} \tag{2.38}$$

However, this is not complete since Poisson shot noise must be introduced. Due to the shot noise properties, each intensity measurement is independent of the other and $\left\langle \vec{I} \right\rangle = \mathbf{W} \cdot \vec{S}$, which denotes that its mean and variance are both equal to $\vec{I}$. From these conditions, the covariance matrix under Poisson noise is

[45]:

$$\Gamma^{\hat{S}}_{P_{i,j}} = \sum_{k=0}^{3} S_k \sum_{n=1}^{N} \mathbf{W}^{+}_{in}\mathbf{W}^{+}_{jn}\mathbf{W}_{nk} \tag{2.39}$$

The variances on each component of the Stokes vector $\hat{S}$ are:

$$\gamma_i = \Gamma^{\hat{S}}_{P_{i,j}} = \sum_{k=0}^{3} Q_{ik} \cdot S_k = I_0(Q_{i0} + P\vec{q}^{\,i} \cdot \vec{s}) \tag{2.40}$$

where $Q_{ik} = \sum_{n=1}^{N}(\mathbf{W}^{+}_{in})^2\mathbf{W}_{nk}$, $\vec{u}^{\,i} = (Q_{i1}, Q_{i2}, Q_{i3})$, I_0 is the first component of the Stokes vector (S_0), P is the degree of polarization and $\vec{s} = (S_1, S_2, S_3)$.

The EWV, which has to be optimized, is:

$$EWV_P = Tr[\Gamma^{\hat{S}}_{P}] = \sum_{i=0}^{3} \gamma_i = I_0(q_{i0} + P\vec{q} \cdot \vec{s}) \tag{2.41}$$

where $q_{ik} = \sum_{k=0}^{3} Q_{ik}$ and $\vec{q} = (q_1, q_2, q_3)$.

The EWV_P (and thus the variance of $\vec{s}$) is independent of the input Stokes vector $\vec{s}$ when $\|\vec{q}\| = 0$, especially if q_k, $\forall k = \{0, 1, 2, 3\}$. The $\mathbf{A}_{opt}$ is a spherical t-design matrix, maximizing the volume of the inscribed in the Poincaré sphere. Together with the characteristic of $Q_{k0} = 3Q_{00}$, $\forall k = \{1, 2, 3\}$, regarding these special geometrical shapes, these conditions conform the Balanced Condition of Poisson Noise (BCPN) [45, 49].

The total variance of the measurements under additive noise and Poisson shot noise is:

$$EWV_T = EWV_G + EWV_P \tag{2.42}$$

being independent of the input polarization state ($\vec{s}$) if BCPN is met.

If N=4 (the minimum measurements needed for $\vec{S}$ estimation), the geometrical shape of $\mathbf{A}$ is a spherical 2-design, in particular a regular tetrahedron, which has this minimal EWV. However, the equalization of the last three variances γ_i ($i = 1, 2, 3$) under Poisson noise only happens at two specific orientations where $\mathbf{A} = \mathbf{A}_{opt}$ (Equation (2.34)) [48, 50]. When employing a spherical 3-design ($N = 6$, regular octahedron), it is demonstrated that EWV is minimal and variances are equalized in the presence of Poisson noise, being $\mathbf{A} = \mathbf{A}_{opt}$, whatever its orientation [48, 50].

Other polarimetric metrics which may be of interest are the variances of the DOP, AOLP and ellipticity. The reason is they are the final products of polarization detection since they are more understandable and may be a starting point to maximize contrast. Therefore, calculating the error associated with noise corruption may be of assistance for evaluating the imaging polarimeter designs depending on their final goal. J. Dai *et al.* [48, 50] have derived closed-form expressions for their variances from the EWV formula, the small perturbations theory and the covariance matrix of the system. Moreover, they have applied them to study some designs.

In addition, they obtained the full expression of the EWV by using the parametrization of the Stokes parameter in the previously derived expressions [45, 49]:

$$\vec{S} = S_0 \begin{pmatrix} 1 \\ P\cos(2\alpha)\cos(2\epsilon) \\ P\sin(2\alpha)\cos(2\epsilon) \\ P\sin(2\epsilon) \end{pmatrix} \tag{2.43a}$$

$$EWV = [\sigma^2 + \frac{S_0}{2}]\sum_{i=0}^{3}\delta_{ii} + S_0 P(\beta_1\cos(2\alpha)\cos(2\epsilon) + \beta_2\sin(2\alpha)\cos(2\epsilon) + \beta_3\sin(2\epsilon)) \tag{2.43b}$$

with $\delta_{ii} = [(\mathbf{A}^T\mathbf{A})^{-1}]_{ii}$ and $\beta_{ii} = \sum_{i=0}^{3} Q_{ik}$. This expression can be reduced to $EWV = \frac{40}{N}[\sigma^2 + S_0/2]$ for a spherical $t \geq 3$ [49].

Stokes (imaging) polarimeters: optimized designs

Several studies have been performed in order to obtain full Stokes polarimeter designs which perform with optimal figures of merit [41, 43, 51–55]. The first systems based on routable retarder and fixed polarizer polarimeter (RRFP) were studied. By minimizing the condition number of **A** matrix, Ambirajan and Look [51, 52] proposed four optimal rotation angles $(-45^o, 0^o, 30^o, 60^o)$ for the RRFP with a standard quarter-wave plate (QWP). Sabatke *et al.* [43] found that the RRFP with a 132^o retarder and a principal axis set $(-51.7^o, -15.1^o, 15.1^o, 51.7^o)$ is more robust to the signal-independent Gaussian additive noise, and Goudail [45, 50] asserts that is partial optimum for minimizing Poisson noise but without independence of input polarization. Shibata *et al.* [53] adapted a standard 0-45-90-135 configuration DoFP linear Stokes polarimeter to full Stokes polarimetry by inserting a rotating QWP in front and rotating to two azimuth angle (θ) positions.

The next generation of full Stokes polarimeters is built on two variable retarders and a fixed linear polarizer (VRFP). Tyo [41] proposed a noise-equalization VRFP system that uses two liquid crystal variable retarders with fixed angular positions and variable retardance. The angular positions of the two variable retarders are fixed at 22.5^o and 45^o, and a set of optimum retardance is $(-158^o, 50.6^o)$, $(127^o, -178^o)$, $(47^o, -16.9^o)$, $(0.66^o, 126^o)$. Zallat *et al.* [55] found that for a VRFP with two standard QWPs and a set of optimum angular positions $(-20.3^o, -41.14^o)$, $(-20.3^o, 41.14^o)$, $(20.3^o, -41.14^o)$, $(20.3^o, 41.14^o)$ the noises in raw image data also can be reduced and propagated equally to the Stokes channels under Gaussian noise although it does not hold the BCPN.

Goudail *et al.* [45, 50] theoretically demonstrated that the fulfilment of κ_2, EWV and BCPN leads to the measurement matrix $\mathbf{A} = \mathbf{A}_{opt}$, they do not provide an experimental configuration though. Mu *et al.* have been working on looking for designs, which perform full Stokes in $N = 4$ measurements, holding the κ_2, EWV and BCPN optimum values [56–58]. Two spherical 2-designs stand out. Their figures are presented in Table 2.1. The first design is compounded by one retarder at two specific retardances (δ_1, δ_2) each one at two different orientation angles. The second one is formed by two QWP at four different orientations [57]. Both designs are followed by a fixed polarizer at 0^o.

Config.	Retardance	Azimuth	EWV
(I)	102.2°	±71.9°	10.0000
	142.1°	±34.95°	
(II)	(102°, 110.1°)	(±63.53°, ∓7.09°)	10.0000
	(63.8°, 154.2°)	(±80.73°, ±56.45°)	
(III)	(90°, 90°)	(±70.15°, ±87.84°)	10.0000
		(±42.82°, ±19.14°)	

Table 2.1: Retardance and azimuth values of two retarders for an optimum 2-design of a full-Stokes polarimeter [57].

Apart from these two possible configurations, a very straightforward configuration of interest is the one provided by the definition used by many authors of the Stokes parameters. The use of $N = 6$ measurements which are linear polarizations at $0^o, 45^o, 90^o$ and 135^o, together with the right and left circular polarizations compose a regular octahedron in the Poincaré sphere, thus being an optimal spherical 3-design [46, 49, 50]. Mu *et al.* built a DoAP full-Stokes camera based on this configuration using Wollaston prisms and a 480 nm bandpass filter [56].

In addition, several groups have developed achromatic polarimeters useful in real conditions where the available light is broadband [58, 59].

Once the different performance metrics for measuring the fluctuations in the intensity and the available systems for full Stokes polarimetry have been presented, it is preferable to highlight some reviews about performance comparison among all these devices and metrics [50, 60].

Mueller matrix (imaging) polarimeters

Apart from full-Stokes polarimeters, another task to optimize is the study of error propagation and the optimization in Mueller polarimetry. The devices measure the full Mueller matrix of the scene, requiring active illumination and a Stokes polarimeter as the sensor. Several studies have been carried out to analyse the required number of illumination states, as well as, the detection states. The conclusion is that, as extracted from Stokes polarimetry, the minimum number of illumination and detection states is 4 for each, being a total of 16 measurements,

to solve the 16 unknowns of the matrix. As before, optimization metrics are currently being studied [61–65]. They extend the EWV and covariance matrix study to analyse the error propagation in the presence of additive and shot noise. Also, they state that due to the symmetry of the system, the optimal configurations for the PSA are equally correct for the PSG.

Systematic errors: alignment & real nominal parameters

Another source of error of interest is the systematic error from alignment error of the elements or the own deviations from nominal values in retardance, for example. Some studies have been carried out by Tyo referring to these errors [42, 66] where the main conclusion is the optimized system to be immune to noise will not be immune to systematic errors. Also, some theoretical error propagation about the previously explain systems have been simulated by Mu *et al.* [57, 67] regarding the tolerance of the system when having deviations in alignment or retardance.

In specific, regarding DoFP polarimeters, some studies about the κ_2, EWV and possible misalignment errors are theoretically treated giving by a glance at the change in the nominal retardance due to thickness variation from manufacturer [68].

2.3 Polarimetric imaging: devices

To retrieve the different polarization information, polarimetric cameras generally intend to measure the Stokes vector or the Mueller matrix at each pixel of the image, using different strategies. This section reviews the different imaging architectures for developing polarimetric cameras. As seen in Section 2.2, multiple intensity images are required to measure polarization. All conventional polarimetric cameras use polarization-sensitive optical filters to obtain the images for the Stokes vector estimation at each pixel, as explained in the previous section. Hence, rotating polarizers [69], Savart plates [70], polarization gratings [71] or liquid crystal variable retarders (LCVRs) [72] have been used in different designs to obtain the images sequentially. To have a snapshot imaging polarimeter, approaches based on micro-grid polarizers, Wollaston prisms or lens arrays have proved to be efficient and capable of accomplishing real-time polarimetric images of a scenario. In addition, some alternative approaches to measuring polarization have been proposed taking advantage of very different ideas, which are mentioned at the end of the section.

Polarization polarimeters generally are based on four established architectures: Division of Time, Division of Amplitude, Division of Focal-Plane array and Division of Aperture. In the following, the principle of each architecture is briefly explained and some examples of devices from literature, especially commercial ones, are provided. In addition, trade-offs among the conventional configurations, as well as, issues of cost and complexity of fabrication and integration are listed in Table 2.2 [3] for a global vision.

Table 1. Polarization Phenomenology and Effects from the Visible to the LWIR

	Advantages	Disadvantages
Visible, NIR, SWIR Typical signal: 1%–60% Sensor resolution: >1%–2%	• Sun is a strong source • High dynamic range of polarization signatures • Sensors cheaper, easier to build and calibrate	• Strongly dependent on geometry • High dynamic range of signatures • Inconsistent signatures • Small well size for FPAs limits polarimetric resolution • No night operation
MWIR Typical signal: 0.1%–25% Sensor resolution: >0.2%	• Good signatures for hot targets • Night operation • Large well sizes for FPA for better sensitivity	• Signatures combination of emissive and reflective • Sensors require cooling • Sensors more expensive and difficult to build and calibrate
LWIR Typical signal: 0.1%–20% Sensor resolution: <0.1%	• Signatures dominated by emission • Less dynamic range for polarization signatures • Large well sizes for FPA for better sensitivity • Night operation	• Sensors require cooling • Sensors most expensive and difficult to build and calibrate

Table 2.2: Schematic resume of the trade-offs among the conventional architectures for imaging polarimeters. [3]

Division of Time Polarimeter (DoTP)

One of the simplest approaches is just to take different images sequentially while rotating polarization elements in front of a focal plane array (FPA). It is relatively straightforward for the system design and the data treatment. Nevertheless, the main drawback is that both scene and platform must be stationary to avoid motion artefacts. To acquire real-time images, the rotation rate must be fast enough to acquire the required four images while avoiding such movement artefacts. A LCVR can be used instead of a rotating polarizer to speed up the system. [72]. Commercial cameras based on this architecture are popular and in improvement [69, 73]. Bossa Nova Technologies is a company that has started developing two polarimetric cameras Samba and Salsa. The Samba camera is a difference polarization camera, which only measures two crossed-polarized states, meanwhile, the Salsa camera is a full-Stokes camera. This latter uses a patented polarization filter based on ferroelectric liquid crystals to achieve up to 12 fps (at maximum resolution) at a bandwidth of 520-550 nm. It shows you the Stokes vector maps and DOP maps (see Figure 2.3 (a)).

Division of Amplitude Polarimeter (DoAmP)

It was first suggested by Garlick *et al.* [74] for a two-channel system, but it was again taken into account for full-Stokes imaging. This type of imaging polarimeter consists of two or more separate FPA. The incoming beam of light is divided by specialized prisms such as Wollaston prism or polarizing beam splitters, passing through polarization optics (if needed) and relay lenses to produce a real-time polarimetric image. Special care must be taken in alignment. In addition, postprocessing is required to coregister the different images since the relay lenses may introduce different aberrations at each channel. When a full spatial resolution is desired and the size and cost of components are less of an issue, this architecture is very suitable. Commercial cameras are available based on this design [75, 76]. Flux Data company has developed the linear-

Stokes FD-1665P camera. It uses beamsplitters that split the incoming beam into three channels, which are independently analysed by linear polarizers at different angles, and recorded on three synchronised FPAs (see Figure 2.3 (b)). Its maximum frame ratio at maximum resolution is 32 fps and the bandwidth depends on the implemented Sony sensor. Since the camera only shows you the intensity maps at the three channels, the Stokes vectors recovery must be performed manually.

Division of Focal-Plane array Polarimeter (DoFP)

This configuration integrates micro-optical polarization elements directly onto the sensor. Every four or more pixels form a superpixel, which estimates the Stokes vector, dividing the focal plane. The micro-optical polarizers tend to be nano-wire polarizers that change at each pixel its orientation axis. This method is similar to the Bayer filter patterns used in colour cameras where the wavelength filters are located in a specific pattern to obtain a colour image at each superpixel. Owing to this, real-time polarimetric images can be acquired yet some disadvantages appear. DoFP systems need to trade off spatial resolution in exchange for polarization information, as well as a non-uniformity in optical properties of the nano-wire polarizers is present, which can vary as much as 20% [77, 78]. Lucid Vision Labs has released two linear–Stokes models to the market: Phoenix 5.0 MP Polarization Model and Triton 5.0 MP Polarization Model, see Figure 2.3 (c) and (d). They have redesigned their cameras by just simply featuring the Sony's IMX250MZR CMOS Polarsens™ (monochrome) or IMX250MYR CMOS Polarsens™ (colour) polarized sensors [79]. Their frame rate is up to 24 fps (at maximum resolution) and the bandwidth depends on the Sony's sensors ranging from 400 nm up to 600 nm. Their Arena SDK enables users to compute both the intensity and colour (colour model only) information as well as the angle and degree of polarization for each pixel. This last year Sony commercialised the new IMX250MZR / MYR corresponding to a 1.1" FPA with a higher number of available pixels [80].

Division of Aperture Polarimeter (DoAP)

This methodology employs a reimaging system to project multiple images onto a unique FPA accurately aligned preserving the field of view for all polarization channels [81]. Compared to DoAmP, once this architecture is aligned and fixed is shown to be stable in time. This configuration allows the performing real-time acquisition of polarimetric images. Different polarization elements have been tested from polarizer sheets to Wollaston prisms in visible [56] and MWIR [81–83].

Alternative non-conventional approaches

Two other approaches for polarimetric imaging, which are worth mentioning, have been reported in the literature during the last decade. One interesting approach is called channelled polarimetry. It is a technique that measures the

polarimetric information by encoding and decoding the incident light in spectral, temporal or spatial domains. Modulated polarimeters were first introduced by Oka and Kato [84] and then extended to get single-shot polarimetric images [84–88]. They are based on polarization elements designed to modulate the incident light beam in spatial, temporal or spectral domains. Its main drawback is that they surpass the temporal limitation of conventional polarimeters at the expense of limiting the domain where the modulation is performed. For example, [85] presents a wavelength polarization coding which has the restriction of working in a very narrow spectrum range ($\Delta\lambda \approx 10$nm). Recently, a new design for a full-Stokes polarimetric camera is presented based on metasurfaces—subwavelength arrays [89–91]. This type of design is based on diffraction gratings that can excite eigenmodes of the nanoresonators, thus displaying a unique diffraction pattern for retrieving full-Stokes information. The gratings are composed of arrays of subwavelength-scale pillar elements having birefringence. The resulting diffraction pattern can be designed so each order of diffraction can act as an analyser sensitive to a selected polarization state. These devices are compact cameras retrieving in a snapshot the Stokes information. However, they are restricted to work in the design wavelength of the metasurfaces.

Figure 2.3: Commercial polarimetric cameras based on different architectures. (a) Salsa camera of Bossa Nova Vision [73]. (b) FD-1665P of Flux Data [76]. (c) Phoenix 5.0 MP Polarization Model of Lucid Vision Labs [79].

2.4 Polarimetric imaging: calibrations

Polarimetry is the science of measuring polarization and can be thought of as simply as radiometry with polarization elements. To perform accurate polarimetry, all the issues necessary for careful radiometry must be addressed, together with the extra polarization issues. Hence, a polarimetric device that detects the polarization state of light needs at least two types of calibrations: radiometric and polarimetric calibration.

Radiometric calibration is a common factor for any “electronic sensor”. The sensor itself, for example, a CMOS, may introduce errors to the measurements such as dark current noise, also generating a background offset, saturation, and fixed noise patterns due to the pixels [92, 93].

The polarimetric calibration consists in deriving the linear transformation, which lets the measured intensities be understood as Stokes vectors. This linear operator is known as the instrumentation or measurement matrix and several procedures have been developed to its precise obtaining [3]. This is a crucial step for passing from an intensity-sensitive device to a polarization-sensitive device.

In some cases, the acquisition is conditioned to the optical configuration and could require more than one optical path. Consequently, a geometrical calibration is necessary for the correct registration of the images, even more, if a post-processing step may merge or compare them.

All three calibrations are needed and crucial for recovering accurate polarimetric information and, in specific, in a DoAP polarimetric camera. In the following points, these distinct calibrations are addressed.

2.4.1 Radiometric calibration

The radiometric calibration consists in studying wether the sensor is working in the linear regime, avoiding the saturation, getting rid of the dark effects, no uniformity of the gain, and removal of the dead and hot pixels of the sensor. Despite this, the radiometric calibration also addresses the removal of background effects of the system components, especially present when there are more than one optical path and the components, deviating from the ideal behaviour, may introduce some differences in the intensities.

This calibration is performed using a very basic set-up. The only thing needed is a spatially uniform unpolarized light source and device. This type of source can be obtained by employing a xenon lamp, a laser source coupled to an integrating sphere, which ensures the total loss of any polarization residual and homogeneous output light.

Two modifications may be done to the raw image: subtracting the fixed dark pattern (I_{offset}) and the gain non-uniformity pattern (I_{GNU}). The former is calculated by averaging over several dark frames acquired in total darkness. The latter is obtained by illuminating with uniform unpolarized light and recording the resulting pattern. This image is normalized by the mean grey level.

The corrected image can be systematically obtained using [6]:

$$I_corr = \frac{I_{raw} - I_{offset}}{I_{GNU}} \tag{2.44}$$

As a reminder, it is also necessary to check for any transmission asymmetry in the sub-images. Just taking the averaged ratio of the images by the selected as a reference will be enough to correct the asymmetry.

2.4.2 Geometric calibration

Similar methodologies have been developed to overcome these problems [6, 56, 81, 94, 95]. In the case of a Division of Aperture Polarimeter (DoAP), the misregistration of the sub-images mainly is due to distortion of the minilenses located at the aperture. The deviation of the lens centre from the optical axis

will induce different distortions to the subimages, as well as, misregistration in the entire FOV. These effects must be characterized and corrected via software. Pezzaniti *et al.* [81] propose a selective image registration method where a reference spot array object is required. A. Bénière *et al.* [96] propose to use a two-dimensional polynomial transformation of order 4 to fit a spot array as [6, 81] but they measure the efficiency by using a chart of concentric black and white discs to see final deformation.

It has to be noted that this correction will affect the speed of the acquisition and estimation of the Stokes vector. Hence, it must be studied which methods will be applied if a real-time acquisition is performed [6].

It is worth mentioning some sub-pixel image registration algorithms can be employed for this task, for example, Scale Intensity Feature Transformation SIFT [97] and Speed-Up Robust Features SURF [98, 99]. These algorithms have been used in plenty of vision applications and are optimized for high-speed applications. They are based on the sub-pixel edge estimation technique which is used to generate a high-resolution edge map from the low-resolution image, and then the high-resolution edge map is used to guide the interpolation of the low-resolution image to the final high-resolution version [100].

SIFT: Scale Invariant Feature Transform

SIFT is an algorithm proposed by Lowe which solves the image scale and rotation, distortion, 3D viewpoint, and illumination change in matching features by taking them to be invariant under these transformations [97].

This algorithm has four basic steps in order to determine the highly distinctive features. Firstly, the scale space extreme is computed by using the Difference of Gaussian (DoG). This gives a close approximation to the scale-normalized Laplacian of Gaussian, producing the most stable image features compared to the gradient, Hessian or Harris corner function. Secondly, the feature key point location is determined by applying the gradient of DoG and comparing that pixel to its neighbours. This method can be improved by applying the method introduced by Brown *et al.* [101] where a 3D quadratic function is fitted to the local sample to determine the interpolated location of the maximum. Thirdly, there is an orientation assignment for the key point. This is done by forming an orientation histogram from the gradient orientations of sample points within a region around the ke ypoint. Each sample of the histogram is weighted by its gradient magnitude and by a Gaussian-weighted circular window. Peaks in the orientation histogram correspond to dominant orientations.

Lastly, the feature descriptor is generated. In order to do so, the image gradient magnitudes and orientations are sampled around the keypoint location. These are weighted by a Gaussian window, so as to not have sudden changes in the descriptor when having small changes in the position window. Then, the samples are accumulated into an orientation histogram, allowing a significant shift in gradient positions. To avoid boundary effects, trilinear interpolation is applied in the orientation histogram.

The descriptor is formed from a vector containing the values of all the orientations of the histogram entries (4x4 array x 8 orientations = 128 elements). In order to reduce the effects of illumination change, the feature vector is normalized.

The matching stages consist in finding the nearest neighbour in the database of key points form the training set. In order to match images with the fewest number of features, clusters of at least 3 features are first identified that agree on an object and its pose, as these clusters have a much higher probability of being correct than individual feature matches. Then, each cluster is checked by performing a detailed geometric fit to the model, and the result is used to accept or reject the interpretation.

SURF: Speeded Up Robust Features

This method is proposed by H. Bay *et al.* [98] and it improves the repeatability, distinctiveness and robustness that come from pushing further the previous state-of-the-art methods. It employs a Fast-Hessian detector to detect the interest points due to its good performance in computation time and accuracy. It relies on the determinant of the Hessian matrix that is calculated from integral images and box filters, which are the approximation of the second-order Gaussian derivatives. The scale space is analysed by up-scaling the filter size rather than iteratively reducing the image size. Since the relative weights applied to the rectangular regions are kept simple and balanced for computational efficiency and the filter responses are normalized with respect to the mask size, they are already scale normalized. To find the interest points in the image and over the scales, the maxima of the determinant of the Hessian matrix are interpolated in scale and image space with the method explained by Brown *et al.* [101].

The descriptor of the features used here is the SURF descriptor. It is based on similar properties to SIFT but it is fastest and more distinctive. Firstly, a reproducible orientation of the interest points is identified in order to be rotation invariant. Therefore, the Haar-wavelet responses in the x and y directions are computed in a circular neighbourhood around the interest point. These calculations are implemented using integral images for fast filtering. Then, the responses are weighted with a Gaussian centred at the interesting point and they are represented as vectors that are summed. The longest such vector indicates the orientation of the point of interest. To extract the descriptor, a square region centred at the interesting point and oriented along the orientation selected before. The region is split into smaller 4x4 square subregions, each one having a four-dimensional descriptor vector consisting of the vertical/horizontal Harr-wavelet responses and the sum of the absolute vertical/horizontal Haar-wavelet responses.

In the matching stage, an interesting point in the test image is compared to an interest point in the reference image by calculating the Euclidean distance between their descriptor vectors. A matching pair is detected when its distance is closer than 0.7 times the distance of the second nearest neighbour. In addition,

for fast indexing while matching, the sign of the Laplacian is calculated just to compare the features that have the same type of contrast.

SURF adds a lot of features to improve the speed in every step. Analysis shows it is 3 times faster than SIFT while performance is comparable to SIFT [98, 102]. SURF is good at handling images with blurring and rotation, but not good at handling viewpoint change and illumination change.

Previous algorithms (SIFT and SURF) are robust, although they have a large computational cost to apply them in real-time applications. Therefore, some other algorithms are developed like the Features from Accelerated Segment Test (FAST), the Binary Robust Independent Elementary Features (BRIEF) and the Oriented FAST and Rotated BRIEF (ORB).

FAST: Features from Accelerated Segment Test

This algorithm was proposed by Edward Rosten and Tom Drummond in 2006 to have a high-speed features detector [103]. It uses a small patch of an image to see if it looks like a corner using machine learning, and finally deriving a feature detector. The segment test criterion operates by considering a circle of 16 pixels around the corner candidate p. Then, the improved approach uses a decision tree which can correctly classify all corners seen in the training set and correctly fulfils the rules of the chosen FAST.

It is several times faster than other existing corner detectors. However, it is not robust to high levels of noise and it does not have any orientation component. It is dependent on a threshold.

BRIEF: Binary Robust Independent Elementary Features

SIFT and SURF create descriptors that occupy a lot of memory and maybe not all are needed for actual matching. Therefore, these methods need to compress the information and select which is uncorrelated by using Principal Component Analysis (PCA), for example.

BRIEF provides a fast-speed matching by computing difference tests to represent an image patch as a binary string without training phase [104]. The results of the test are used to train classification trees or a Naïve Bayesian classifier to recognise patches seen from different viewpoints. When creating the descriptor, the test responses must have been smoothed in order to reduce the sensitivity to noise. It also provides a high recognition rate unless there is a large in-plane rotation.

ORB: Oriented FAST and Rotated BRIEF

This algorithm was brought up by Ethan Rublee *et al.* in 2011 [105]. ORB is a fusion of FAST keypoint detector and BRIEF descriptor with many modifications to enhance the performance.

Firstly, it uses FAST to find key points and then applies the Harris corner measure to find the top N points among them. It also uses a scale pyramid to

produce multiscale features. However, FAST does not include the orientation operator. The orientation is introduced by the intensity centroid technique, which gives a single dominant result. Comparing this method to some gradient-based measures (like SIFT algorithm), it is shown that the centroid gives a uniformly good orientation, even under large image noise.

Regarding the descriptors, ORB uses BRIEF descriptors but "steering" them in the principal orientation of the key points making it invariant to in-plane rotation. BRIEF has an important property that each bit feature has a large variance and a mean near 0.5. However, once it is oriented along the key point direction, it loses this property and becomes more distributed. To resolve all these, ORB searches among all possible binary tests to find the ones that have both high variance and means close to 0.5, as well as being uncorrelated.

Some efforts have been made to improve ORB performance when matching with large databases [106].

2.4.3 Polarimetric calibration

After providing reliable intensity information and subpixel image registration, the next action is to determine the measurement matrix $\mathbf{A}$ of the system to estimate the polarization state. As exposed in the previous Section 2.2.3, performing a preliminary optimization during the system design may help to get better results when dealing with noise after the calibration.

Fourier-based calibration methods were first developed for Mueller and Jones matrix estimation doing non-imaging measurements of polarized and partially polarized light, and also for ellipsometric measurements [107, 108]. Despite they are more commonly used for polarimeters with rotating parts such as linear polarizers and retarders [109], they have been applied to other architectures [83].

In this approach, a series of images are taken meanwhile the elements of the PSA of the polarimetric camera are varied harmonically. The incident polarization is encoded onto the harmonics of the detected signal. Thus, the Stokes vector components are recovered through a Fourier transform of the measurement data set. In this strategy of polarization imaging, the Stokes vector is computed independently at each pixel. The chief disadvantage of this method is that the MM of the system needs to be accurately known. As a consequence, this requires perfect polarization elements where polarizers contain no retardance and retarders contain no diattenuation.

Apart from these, several types of polarimetric calibrations have been derived over the years [6], including those related to a solution for a particular system [83, 110–114], a specific calibration method to partially Stokes polarimetry [95, 115], or both features such as DoFP microgrid cameras [116, 117]. Among them, three main methods can be highlighted whose principal advantage is the system-independent procedure: Data Reduction Matrix method (DRM) [118], and Eigenvalue Calibration Method (ECM) [119], and the recently Polarizer Calibration Method (PCM) [120]. Each of the previously mentioned calibration methods relies on a different physical or mathematical approach and various studies have been addressed to study their performance [121–123].

Data Reduction Matrix (DRM)

This strategy is mainly used for calibrating a PSA which measures the Stokes vector. The Stokes elements could be recovered at each pixel following the linear matrix form of Equation (2.16). Recall that $\vec{I}$ contains the intensities measured at the different PSA states, $\vec{S}_{rec}$ is the Stokes vector to be recovered and $\mathbf{W}$ is referred to as the data reduction matrix. This latter matrix is not unique. Owing to this, several studies for optimization of this matrix have been made and have been briefly explained in Section 2.2.3.

Normally, the calibration method to acquire the Stokes vector consisted in performing N measurements corresponding to N configurations of the polarization elements of the PSA [20, 25] of known input $\vec{S}$. As explained in Section 2.2.1, having the $\vec{I}$ from the N measurements, finding $\mathbf{W}$ is straightforward just by solving Equation (2.15) for $\vec{S}$, that is, by performing the pseudoinverse of $\mathbf{I}$. However, this method requires $\mathbf{A}$ to be known. This needs the polarization elements composing the PSA to be fully characterized, or high-quality components, which increases their price.

Following the conventional method, an improved method was presented by Boulbry *et al.* [118] without requiring an *a priori* knowledge of the details of the PSA components. The details about this calibration procedure are provided in detail in the introductory theory of Chapter 5.

The possible sources of errors during calibration are three [118]: those which are associated with uncertainties in the reference Stokes vectors, those which are associated with errors in the polarimeter, and those associated with the subsequent measurements.

Since matrix $\mathbf{A}$ depends on the input Stokes vectors, these must be chosen carefully in order to prevent error propagation when inverting $\mathbf{A}$. If the optimal states, already discussed in Section 2.2.3, are implemented, the calibration error might be reduced. This method allows calibrating the system without *a priori* knowledge of the PSA with the advantage of considering the higher-order effects such as multiple reflections between or within the optical devices, imperfect analysers, composed by polarizers and retarders, and residual birefringence.

Eigenvalue Calibration Method (ECM)

This method is mainly aimed at calibrating Mueller polarimeters. It was developed by Compain *et al.* [119, 124] and consists in extending the use of the matrix formalism to the global experimental set-up to be calibrated. The PSG and the PSA are described by two matrices $\mathbf{G}$ and $\mathbf{A}$. They use reference samples ($\mathbf{M}$) to determine the coefficients of matrices $\mathbf{G}$ and $\mathbf{A}$.

The basic measurement of the active device, under matrix formalism, is:

$$\mathbf{I} = \mathbf{A} \cdot \mathbf{M} \cdot \mathbf{G} \tag{2.45}$$

where $\mathbf{I}$ is compound by 16 coefficients. Certain polarization states illuminate the reference sample through the calculation of eigenvalues of the intensity matrix instead of using its pseudoinverse for the recovery of both calibration matrices. $\mathbf{G}$

and **A** are calculated at the same time by introducing the recovered eigenvalues in the corresponding Mueller matrix model and the cost function is optimized to get the calibration matrices. A brief scheme of the ECM algorithm is depicted in Figure 2.4. The complete insights of the procedure are explained in Chapter 5.

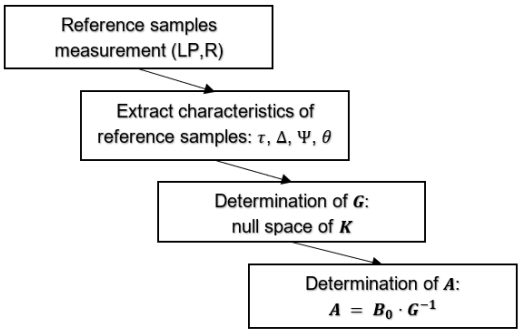

Figure 2.4: Scheme of the ECM algorithm.

The advantages of this method are:

- No assumption has to be made about the system, except that it is complete (full-Stokes). No first-order approximation is needed, the procedure is universal depending on the choice of reference samples.

- The characteristics of the elements of the set-up do not need to be known *a priori*. The inherent defects of the optical elements that compound the PSG and the PSA are automatically considered they are determined during calibration.

- There is no need for precise orientation/alignment between the various elements.

- The accuracy of the calibration procedure can be evaluated.

The reference samples should be smooth, isotropic as the matrix **G** of the PSG and the matrix **A** of the PSA must be invertible. At least, a dichroic sample and a retarder, are needed for a unique calibration. Consequently, linear polarizers (dichroic sheet polarizers are not allowed) and a QWP are employed.

During the procedure, Mueller matrices of the reference samples (**M**) are assumed to be perfectly known. The model of the MM should be defined for calculations. Some authors consider the ideal MM of the samples, whereas others prefer to employ the general dichroic retarder MM in Equation (2.20) [125, 126]. Both types of MM should take into account the rotation of the matrices: $\mathbf{M}_{gen}(\tau, \Psi, \delta, \theta) = \mathbf{R}_M(\theta) \cdot \mathbf{M}_{gen}(\tau, \Psi, \delta) \cdot \mathbf{R}_M(-\theta)$.

Polarizer Calibration Method (PCM)

This calibration method is a variation of the ECM where only a linear polarizer sample is employed. PCM [120] does not introduce any retarder or air samples to calculate the two instrument matrices of the system simultaneously, **G** and **A**. The algorithm dispenses with the retarder so as to be free of the principal errors which appear when they are used like chromatic effects and misalignment errors. In contrast, it requires the complete polarization model of the system under calibration for a complete calculation of the matrices

PCM relies on treating the Mueller matrix of the polarizer as a projector's product. Hence, the basis of all the mathematical derivations is to find the projectors that are the eigenvectors of certain intensity-related matrices. Since all the measurements are performed with a polarizer, PCM directly recovers from the intensity data the components of the instrument matrices that are associated with linear polarization. Consequently, the circular-related components of the calibration matrices are derived through the polarization model of the system under calibration.

2.5 Polarimetric imaging: applications

Polarimetry encompasses a wide range of applications in very different fields, as stated in the introduction. The fields can range from atmospheric remote sensing to biomedical diagnostics, passing by many different fields that need very sensitive polarization detection.

Remote sensing has adopted polarimetric imaging as an important technique since it provides additional information to the spectrometric techniques. Polarimetry is employed for the characterization of aerosol particles [8, 127, 128] in the atmosphere since the sunlight comes unpolarized but the scattering events in the atmosphere make it acquire a large degree of polarization depending on the present particles. It also can be applied to object detection

For target detection field [3, 4], polarimetric imaging can be applied in various applications from machine vision for the industry, road inspection, profilometry [69], and metrology oriented towards material identification [23] are examples of the potential of imaging polarimetry. Fresnel theory explains how dielectric media generally reflects partially polarized light [129]. Measuring reflected light allows us to distinguish between a wet and dry road or between dielectric and metal materials [130, 131]. Polarization has been also used in measuring the refractive index and recovering the 3D surface of an object [132, 133]. Another interesting application is measuring the polarization properties of speckle [134, 135].

Astronomy has an interest in polarimetry since polarization gives astronomical bodies information about their physical state that usually cannot be acquired by any other form. It can be used for revealing circumstellar structures [4] or determining solar magnetic fields [136].

Spectropolarimetry is another field which takes advantage of polarization for characterizing chemical samples in both spectral and polarimetric dimensions.

Here, inherent material properties can be only measured using polarization: optical activity and photoelasticity.

Any material which makes the electrical field of light rotate is said to be optically active. Many other substances like benzyl and quartz only exhibit this property in crystals form. On the other hand, many organic compounds like sugar and turpentine can be optically active in a solution. In these cases, the rotatory power of solutions varies with the concentration. This fact is particularly helpful in determining, for example, the amount of sugar present in a urine sample or a commercial sugar syrup [129]. Much other research is oriented to study the properties of *d-glucose* and different approaches to achieve a noninvasive detection [137–142].

Photoelasticity is the phenomenon that makes normally transparent isotropic substances optically anisotropic by applying mechanical stress [129]. It serves for studying the stresses in transparent and opaque mechanical structures. Under compression, the material exhibits induced birefringence proportional to this stress [86].

Finally, the medical field is a very broad field where polarimetric imaging can be employed as a relatively simple and economical detection scheme. Biological tissues are complex samples that show all possible optical properties like diattenuation, depolarization and retardance. They can be measured through Stokes and Mueller matrix imaging adding more information for medical diagnosis. In addition, tissues behave like a dispersive medium and signal is lost very rapidly due to the scattering. A lot of research is conducted on very diverse topics such as tissue imaging [14, 143–145], tissue characterization [146, 147] and improvement in cancer diagnosis [9, 10, 148–151].

2.5.1 Turbid media imaging

In recent years, many researchers have noticed the associated problems of see-through highly scattering media raised in navigation, medical imaging, transportation, and surveillance. Light travelling through a complex medium with randomly distributed positions and refractive indices undergoes absorption and random scattering and loses the spatial and temporal information of its source [152]. The majority of photons that undergo such multiple scattering events have lost the information related to their source and are called diffusive photons. A very small fraction of the total photons, called ballistic photons, undergo very few forward scattering events before they reach the detector, retaining the information of their source (direction, polarization state, modulation...). This latter type of photons is of interest in imaging through turbid media since they are key to enhancing the resolution, but require time-resolved, sensitive detectors, as most of the photons will undergo diffuse trajectories where essentially all information on coherence and polarization is lost, leaving just radiometric information.

In typical diffusive conditions (e.g. in non-transparent body tissues, underwater media, fog, smog or smoke), the light propagation is largely diffusive rather than ballistic. Due to the interest in the topic, several techniques have been developed in the last few decades to image in such media. Diffuse Optical

Tomography [153] uses image reconstruction strategies based on the inverse-source algorithm to recover the hidden objects from the scattered detected photons. The first category of ballistic imaging is based on time-gating techniques [154], which employ a pulse light source to illuminate the scattering medium and a time-gated detector to measure the ballistic photons that are not delayed by multiple scattering, unlike diffusive photons. In addition, imaging ballistic photons are also attempted with continuous-wave approaches, using either polarization of light [155, 156], or intensity modulation techniques [7]. The use of polarized light and polarization imaging has been long used for image contrast in other applications. Consequently, combining the capability of polarization to enhance contrast and the fact that ballistic photons conserve their initial properties, including their polarization state, offers a very interesting approach to exploiting the properties of polarization imaging in turbid media.

Theoretical simulations have analyzed the behaviour of polarized light in forward scattering, and despite ideal conditions, the main conclusion was that the behaviour depends on the input polarization state [157–159]. Other authors have experimentally proven the results given by simulations; specifically, that the depolarization of the beam during the propagation is proportional to the optical depth, although this result is restricted to linear polarization[6, 160]. Apart from imaging in diffusive media, several efforts are made towards the implementation of active polarization imaging for the development of dehazing methods oriented to visibility enhancement through fog [161] or turbid water [162]. Some studies are also being carried out discussing the influence under various polarization conditions [163, 164]. Results show that orthogonal detection supplies the best resolution compared with other polarization directions in turbid water and the performance of the circular polarization method is better than the linear process due to the polarization memory effect [162, 165, 166].

Part II

Design and Built-up

The main objective of this thesis is to develop a polarimetric camera capable of measuring the complete polarization information in a scene in the lowest time possible with the highest accuracy. To do this, the optical design of the system should be studied and decide which type of architecture must be employed, which optical components are suitable for the application, as well as, the mechanical assembling and the hardware connections.

About the first query, the DoAP architecture is selected since the polarimetric camera is desired to acquire in a single shot the full polarization information of the scene. As described in Section 2.3, DoAP lets the system to have a real time parallel acquisition rate and the ability to avoid temporal registration errors (artifacts) between channels. Regarding the spatial registration errors, they can be are corrected through calibration. Using this design, the beam can be split in the desired number of sub-images and the system shares optics and sensor, making this choice more economical respect to others. After a careful analysis, the system is set to divide the beam into the minimum number of paths for recovering the polarization, thus $N = 4$, in order to balance the speed of polarization calculation with preserving the spatial resolution in the sub-images.

The rest of inquiries related to the camera design are addressed in the following chapter. Chapter 3 is the first chapter describing the own work directed to the development of the polarimetric camera. The opto-mechanical design is described in detail, as well as the key parts regarding polarization measurement.

Chapter 3

Design and built-up of DoAP system

This chapter presents the optomechanical design of our full-Stokes Division of Aperture Polarimetric Camera (DoAPC). The initial requirements for the system are to measure full-Stokes images in the VIS range, in a single snapshot for faster acquisition enabling the capture of targets in movement and to be immune to Gaussian and Poisson noise. Based on these preconditions, the optomechanical design was developed. Thereafter, the final mechanical assembly is explained together with the hardware connections to link the camera to the PC and the software needed for the acquisition of images. In the last sections, the active illumination design is addressed followed by the mechanical solution for introducing the DoAPC in turbid media.

3.1 Optical design of the system

As already discussed, the DoAPC employs the DoAP architecture to acquire in a single shot the four images necessary for retrieving the full-Stokes vector of the incoming light. Therefore, the main issue in the optomechanical design is how to split the beam into four equal parts.

Preliminary optical designs

Three different ways to separate the incoming light beam have been studied using the professional optical design software Zemax OpticStudio. The main element of interest was initially a pyramid prism, but it had very strict tolerances for its fabrication and positioning. Owing to this, two additional optical elements were contemplated to substitute the ideal pyramid prism: a double roof prism system and a minilens array, which consists of a 2x2 array of small lenses properly positioned. They are more accessible find and their construction tolerances are easier to meet by manufacturers making them more economic alternatives.

The ideal optical element initially considered for dividing the beam consisted of a pyramid prism with four sides, equivalent to the ones used as pyramid wavefront sensors in adaptive optics in the past [167, 168]. The beam must be focused onto the vertex of the prism so four equal beams will arise after passing through the pyramid. This technique is very well known in wavefront sensing in astronomy [169]. The angle of divergence between the four beams will depend on the angle of the vertex of the pyramid. In Figure 3.1, a picture of the prism is presented. Such a division of amplitude is ideal for the development of an imaging polarimeter, as the pupil is divided in four equal subpupils which diverge

according to the prismatic power of the sides of the pyramid prism, so this would be the natural first choice for our design. In this approach, we are implementing the first lens to focus the beam at the vertex that is placed at the aperture of the system and a second lens to re-image the four beams onto the sensor. Its main drawbacks are the high sensitivity of the system to displacements of the pyramid prism itself (seen to be lower than a tenth of a millimetre) and the micrometric tolerances in the pyramid construction referred to in literature [56, 170], not surprisingly, this resulted in the impossibility to find a manufacturer, not even a customized one, for sourcing the pyramid. If the beam is not precisely focused on the vertex, the output beams will not be divided equally . This is the reason why it is so useful in wavefront sensing, where its vertex is precisely positioned to measure the incoming wavefront using relative measures of intensity of the four channels split at the vertex.

Figure 3.1: The glass pyramid used on the William Herschel telescope [170]. Note that its diameter is no more than 15 mm.

Consequently, the use of a double roof prism was analysed as an alternative. A roof prism is an optical element such that any two faces of glass meet at ninety degrees (not the roof angle) (see Figure 3.2 (left)). This design results in the beam entering from the side opposite to the roof, so it is split into two beams as the light exits the prism. By combining two roof prisms and aligning them such that their peaks point towards each other and being orthogonal, the light will pass through the first prism creating two beams that will be doubled as they pass through the second prism and finally projected by a second imaging lens at the sensor plane (Figure 3.2). Here, the beam must be focused in the space between both prisms to get the four beams. In addition, the parameter which conditions the angular separation of the beams is the roof angle (α) of the prisms. Four roof prisms can be used to remove any chromatic aberrations by carefully selecting the glasses (two sets of prisms glued back-to-back), although it is not necessarily an optimal design.

The experiment is simulated in Figure 3.2 (middle) using a collimated light beam, a focusing lens before the prisms and an imaging lens after them. The roof prisms specifications are 25 mm x 25 mm, a thickness of 10 mm, fused silica material with an anti-reflecting coat and a roof angle α of 1.887^o (Figure 3.2 (left)). As in the previous case, the prisms must be very precisely aligned as

a misalignment of just 0.1 mm in any direction will cause the beams not to be separated. Thus, the system becomes very limited regarding positioning tolerances both for manufacturing and in field use.

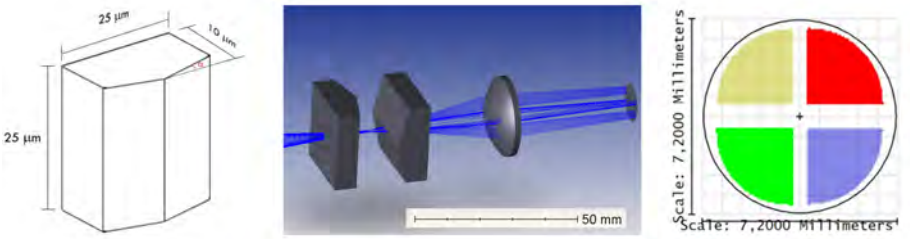

Figure 3.2: (Left) Schematic and parameters of two glued roof prisms. (Middle) Zoom of the optical design using Zemax professional software at the separating plane of the beam. (Right) Image plane with the four divided images.

Despite its better construction conditions regarding manufacturability of the components, the good alignment of the double roof prism implies the introduction of two more variables when compared to the pyramid design, such as the relative position of the two prisms and the perfect orthogonality required between them, which act as constraints on the system.

Hence, a third simpler alternative was contemplated. Using an array of 2x2 lenses of small diameter, which we called minilenses (as they are a few millimeters in diameter, so cannot be named microlenses), the beam will be divided into four beams without the limitations associated with highly precise positioning. This array should be placed in the aperture of the system so that the beam is splitted into four sub-rays. The diameter of the minilenses and the separation between them are the key variables in the optimization of the four sub-images formed at the sensor plane. Manufacturers offer various diameters of minilenses and the distance between lenses can be adjusted in the mechanical design.

Out of these three initial concepts, the minilens array stands out as the best option, as it is the one which better meets the initial design conditions. The pyramid is discarded since it is not so easy to source due to the strict parameters required for its manufacturing. The roof prisms are adequate in cost and fabrication feasibility, but their tight tolerances regarding misalignment make them not suitable for their use in order to subdivide the pupil into four separate images.

Final optical design

The final optical design of the DoAPC is depicted in Figure 3.3. The system was optimized regarding curvatures and positions of the elements until a good enough configuration matching with an available hardware sensor and lenses was found. Only the final results are shown for compactness of the Thesis, despite a number of alternative configurations for imaging were considered.

Firstly, the target is imaged by an objective lens (OL) onto the intermediate plane, known as the field plane. Here, a field stop (FS) is located to limit the Field-Of-View (FOV) of the system up to $\pm 5^o$ preventing the superposition of larger fields in the different sub-images in the sensor. Afterwards, the polarization analyser set (composed of a set of retarders and a polarizer) is located. Right before the minilens array (LA), the array of retarders (RA) is placed to have uniform illumination from the incident rays coming with small slope within the angle of acceptance range. The linear polarizer (LP) follows the LA. The combination of the RA and the LP gives an analyser array composed of four different elliptical polarization states. This analyzer will project the incoming polarization state to the camera into intensity levels for estimating the polarization parameters together with the calibration matrices. The corresponding retardance and azimuth (δ, θ) of each RA is $(102^o, 72^o)$, $(102^o, -72^o)$, $(142^o, 35^o)$ and $(142^o, 35^o)$. Then, the light is focused as a quadrant image onto the active area of the CMOS. The total dimensions of the DoAPC are 415 x 60 x 60 mm.

The OL is a commercial Canon EF lens of 85 mm, f/1.4. The LA is formed by 2x2 achromatic lenses of Edmund #49312 with a focal length of 60 mm with a VIS-NIR coating. The RA are custom designed from Meadowlark with the previous values of the retardance and with the same azimuth angles in the working range of 400-700 nm. The dimensions of the retarders are optimized to fit in the final optical design. The LP is an off-the-shelf linear polarizer from Edmund Optics #47316. The sensor is a mono CMOS camera (JAI, #SP-20000-PMCL).

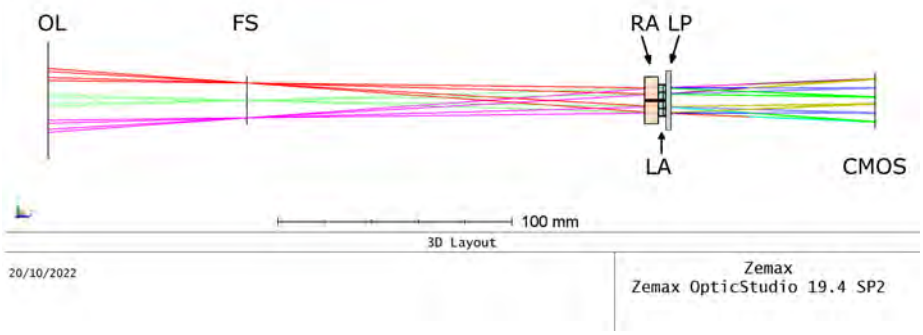

Figure 3.3: Optical design using Zemax OpticStudio professional software. OL collects the incoming light and projects it into the RA while being spatially filtered by the FS. The LA splits the beam into four and then they pass through the LP until reach the CMOS surface.

Another critical aspect to consider is the spatial resolution of the sensor, as long as we will divide the pupil aperture into four different images, which, in the optimal case, will have only 25% of the initial spatial resolution of the sensor. Thus, the spatial resolution of the system relies on the size of the sensor, so small pixels in large arrays are desirable, pushing the limits of the optical design.

In this case, the sensor is composed of big square 6.4 μm pixels. The aberrations of field curvature, distortion and lateral colour are studied for the optical design to see the quality of the design.

Figure 3.4 displays the field curvature and the distortion of the system. The field curvature describes the amount in which the image plane curves due to the curvature in the lens design. It varies with the wavelength and with the angle of the field. The curvature reaches 0.2 mm for green and red wavelengths at 5^o and the maximum is 0.33 mm at 7^o. Blue wavelength experiments the lower curvature in the rays. Distortion is a monochromatic optical aberration describing how the magnification in an image changes across the FOV at a fixed working distance. The maximum distortion of the system is 0.65%, being below 1.0%. This means that the changes in distortion can pass unnoticeable in comparison with the other aberrations.

The system is intended to work in the visible spectrum so chromatic aberration needs be considered. Lateral colour error accounts for the failure of a lens to focus all colours to the same point caused by dispersion. Figure 3.5 displays the computed lateral colour error taking as reference the primary wavelength (587 nm). The maximum error is observed at the blue wavelength (0.4861 nm) where it is 4.38 μm at a field of 0^o and 5.16 μm at a field of 5^o. Despite this, the colour aberration is inferior to the pixel size of the sensor.

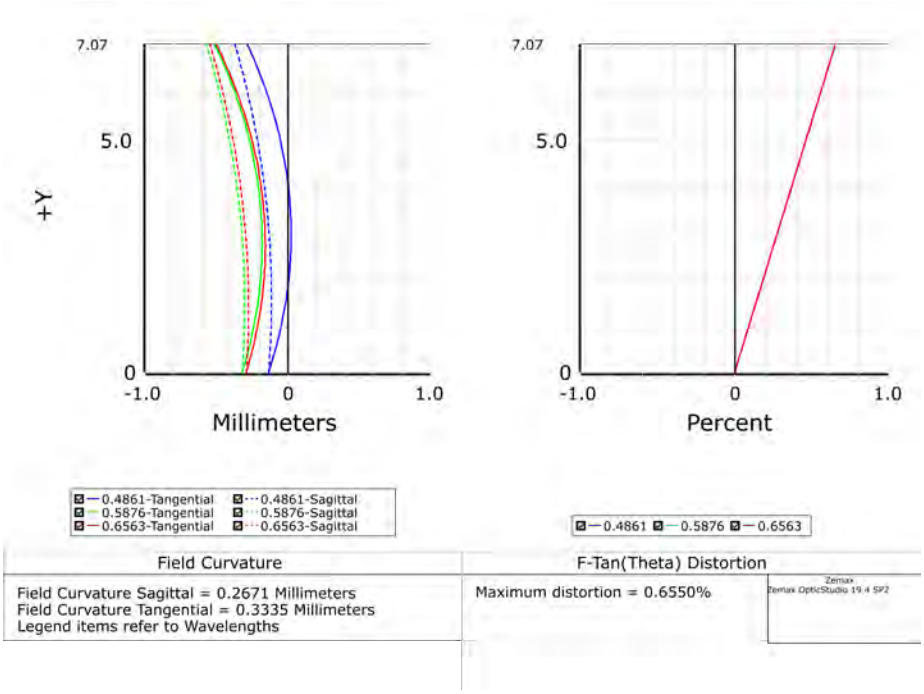

Figure 3.4: Field curvature (left) and distortion (right) of the optical design using Zemax OpticStudio professional software.

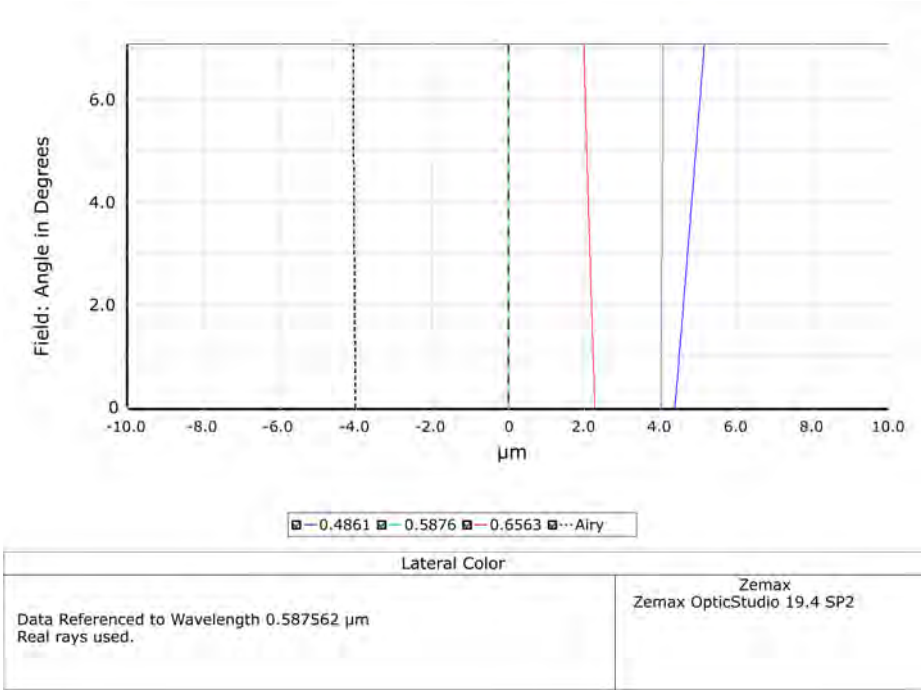

Figure 3.5: Lateral colour aberration of the final optical system using Zemax OpticStudio professional software.

Minilens array

The minilens array is modelled in Zemax by using a 2x2 array of small lenses decentered from the optical axis in order to get images at different points of the sensor. It is thus possible to perform in an equivalent manner to the behaviour of a pyramid prism, defining four configurations referring to the decentering, see Figure 3.6 (left). The parameter of the diameter and the accuracy of decentering are the main constraints of this design, although they are acceptable to main manufacturers.

A tolerance study based on the two constraints were done in order to find the combination that achieves the lower colour and curvature aberrations meanwhile taking advantage of the maximum active sensor area. The final design include lenses with a diameter of 6.25 mm placed on a black holder with a distance between them of 3.37 mm from the optical axis of each lens. The lenses re-image the pupil plane into the sensor surface producing four sub-images as shown in Figure 3.6 (right).

Polarization components

The array of 2x2 retarders is located right before the LA, in order to be uniform and fully illuminated. As mentioned in Section 2.2.3 in Table 2.1 **(I)**, the nominal

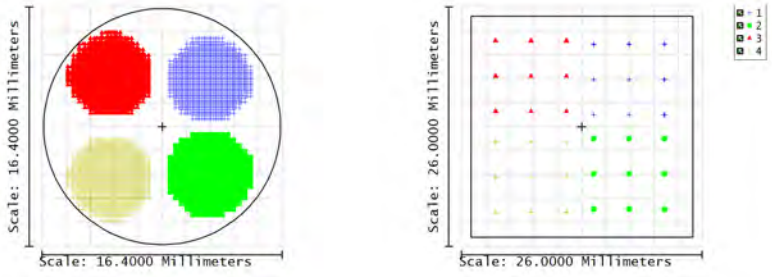

Figure 3.6: (Left) Divided images placed as a 2x2 array after the LA plane. (Right) Divided images at the plane of the sensor. Each colour corresponds to a different lens.

optimal retardance and azimuths of RA is $(102^o, 72^o)$, $(102^o, -72^o)$, $(142^o, 35^o)$ and $(142^o, 35^o)$. This combination of values allows the system to be immunized to Gaussian and Poisson noise.

Following the LA, a fixed LP is placed to project the polarization modified by the retarders to have their related intensity values at the corresponding sub-images in the CMOS sensitive area.

The retarders are pieces of birefringent, uniaxial material in which the ordinary and extraordinary rays travel at different velocities, thus presenting different refractive indexes. So, there is a relative retardation between the path of the two output rays $N\lambda$ [171]:

$$N\lambda = \pm d(n_e - n_o) \tag{3.1}$$

Where n_o is the refractive index of the ordinary ray, n_e is the refractive index of the extraordinary ray, d is the physical thickness of the plate and λ is the wavelength.

N can thus be considered as the retardation of the plate in terms of the fraction of wavelength. The phase difference between the rays passing through the birefringent material is $2\pi/\lambda$ times the path difference:

$$\delta = \pm 2\pi d(n_e - n_o)/\lambda \tag{3.2}$$

$\pi/2$ and $\pi/4$ correspond to the retardances of the most commonly used retarder plates: the half-wave (HWP) and the quarter-wave plates (QWP), respectively. Their characteristic property is in the former case the input linear polarization state is rotated θ, while the latter one converts the linear polarization into circular polarization, and vice versa.

The retarders are usually built from crystals which are cut so that the optical axis lies in a plane parallel to the face of the plate. Typical materials for waveplates are mica, stretched polyvinyl alcohol, and quartz, although some other plastics can also be used [26].

Waveplates are usually sensitive to temperature changes and to the variation of their performance depending on the angle of incidence, and thus are affected by the FOV. This last feature is important since the design may not have a

collimated incident beam on the retarder plate, and a variation of a maximum of 5^o would be expected due to tolerances in positioning, tilt, and divergence of the incoming light rays. In [171], it is shown that the change in the phase retardation with an angle of incidence, $2\pi(\Delta N)_\theta$, is proportional to the total thickness of the plate (which is incorporated into N) and the square of the angle of incidence when the rotation is about an axis parallel to the optical axis.

To perform the estimation of the Stokes parameters of a measured scene, the Mueller matrix of the polarimetric system (let us understand it as the polarization state analyser) must be constant over the operational range in order to consider the system achromatic, and thus invariant under different wavelengths. Polarizers have an equivalent behaviour in the VIS range, so the weakest point in the PSA would be the variation of the retarder plates. Hence, it is important to ensure the best possible level of achromaticity in the retarder plates used in the final system.

Achromatic retardation plates are, obviously, those for which phase retardation is independent of wavelength. There exist several manners to obtain an achromatic waveplate. The most used are those based on the principle of the Fresnel rhomb, in which phase retardation occurs due to internal reflections. A material with appropriate wavelength variation can be employed. Composite plates, consisting of two or more plates of the same material whose axes are oriented at appropriate angles can also provide an achromatic retarder plate.

The main interest of the imaging polarimetric camera is to perform imaging detection under different scenes, including dispersive media. Therefore, an analysis of the optimum analysing states of the PSA is performed. According to several studies presented in Section 2.2, the optimum behaviour of the system under Gaussian and Poisson noises is using one retarder followed by a linear polarizer. The retardance and the orientation of the retarder vary in the four measurements, being the set gathered in Table 3.1 from [45, 57].

Retardance (δ)	Angle of fast axis (θ)
102^o	$\pm 71.9^o$
142^o	$\pm 35.1^o$

Table 3.1: Optimum values of the retardance and fast axis angle of the retarders compounding the RA.

Retarders are a key component of the design since they allow the system to be immune to Gaussian and Poisson noise, thus being equalized. These values of retardance are not commonly employed, and they must be custom designed and built. The custom waveplate is acquired based on a composite of plates since the geometry of the system does not accept beam deviation or displacement and the space available is restricted. The conditions required for the retarders are their retardance (102^o and 142^o), their broadband achromaticity in the VIS range (400-700nm), their high retardance accuracy ($\lambda/100$) and a suitable angle of acceptance ($\pm 4^o$).

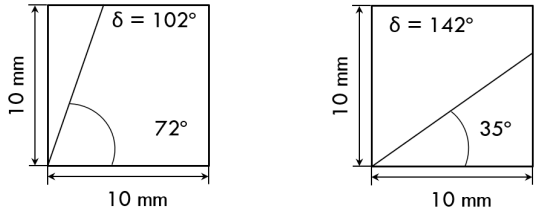

Figure 3.7: Scheme of the desired retarder plates (left) retarder of retardance $\delta = 102^o$ and fast axis at 72^o and (right) retarder of retardance $\delta = 142^o$ and fast axis at 35^o.

Several distributors/designers were asked to meet these requirements and only one of them managed to do it properly. Meadowlark is an American company dedicated to producing all types of polarization-sensitive components. The specifications of the retarders they constructed are shown in Figure 3.8.

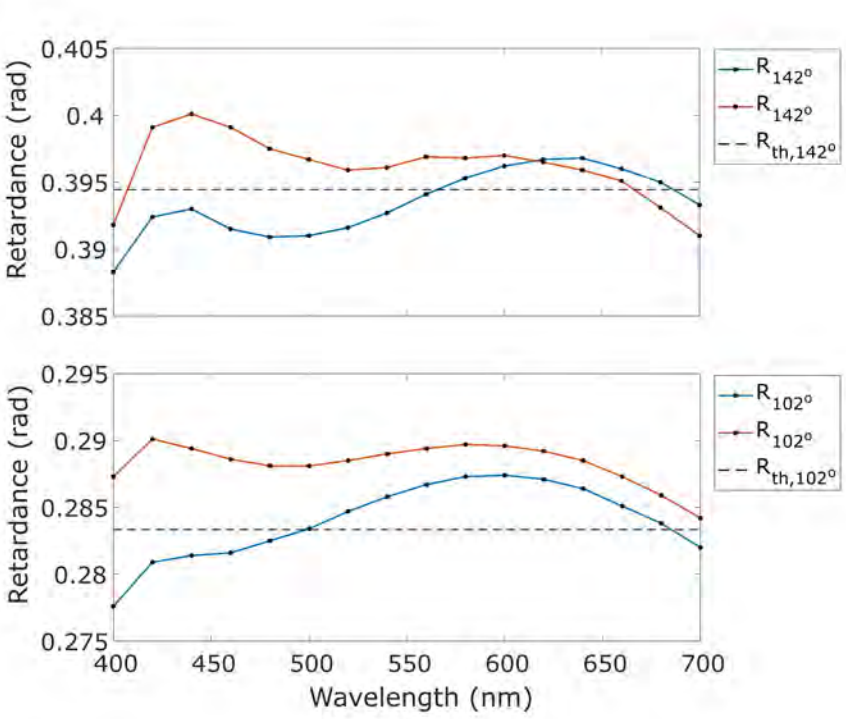

Figure 3.8: (Top) Retardance curves of the two retarders of 142^o and (Bottom) the two retarders of 102^o to show their achromaticity in the VIS range.

The nominal retardances of the plates varies across the VIS spectrum with an error of less than $\pm 2^o$ and its angle of incidence can be up to 10^o. The

dimensions of the crystals are 10 mm x 10 mm x 5.57 mm with a deviation in size of ±0.51 mm.

Finally, the LP is added after the RA and LA. It is a high-performance polarizer made of B270 glass. It features an extinction ratio of 10,000:1 and a transmission of 25% for unpolarized light over the waveband of 400 - 700 nm, across a FOV of $> \pm 10^o$. Its working waveband is thus equivaletnt to that of the system. Furthermore, differences in the polarization response through the sensor area are avoided since the LP is fixed at 0^o and an covers all the sensing area. The large extinction ratio of the LP contributes to the achievement of noise immunity.

CMOS sensor

The monochromatic CMOS sensor (JAI, #SP-20000-PMCL) consists of a large format 20 MP global shutter imager. It is powered over Mini Camera Link connectors (PMCL). It is selected as it provides a high dynamic range of 12-bit digital output to account for the photons in low illumination conditions, and a large enough number of pixels to maintain a reasonable image resolution as the aperture is divided into four images . Its maximum quantum efficiency is 65% and it ranges between 40% and 65%, as shown in Figure 3.9. Its dark noise is 8.6 e^- and the full-well capacity is $10,505$ e^-, one order of magnitude less than typical astronomical sensors. It has a frame rate of 30 fps at full resolution. The resolution of the sensor is 5120 x 3840 pixels with a pixel size of 6.4 μm. The four sub-images do not cover the complete area, so the total effective area is a ROI of 3500 x 3500 pixels.

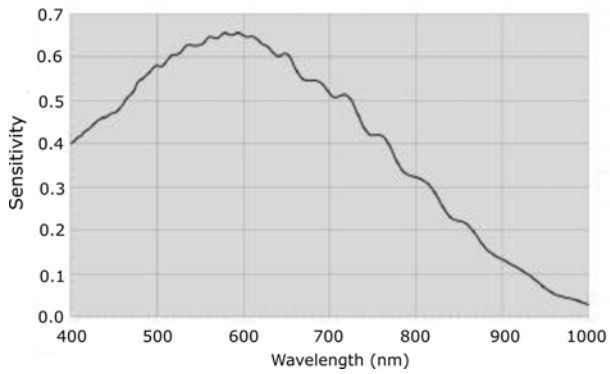

Figure 3.9: Quantum efficiency of the CMOS sensor in the JAI #SP-20000-PMCL.

3.2 Construction of the system

This section comprises the descripiton of the activities on mechanical assembly of the optomechanical design and the software configuration in order to have a

functional polarimetric camera.

Mechanical assembly

Once the optical design is completed, it is necessary to do the optomechanical design to ensure that all pieces remain properly placed and fixed to avoid modifications during the measurement, in case of external movements, or in presence of reasonable amounts of shock or vibration. Figure 3.10 shows the mechanical design and the system once assembled. The lens rests on a ad-hoc metallic piece to fix it in a specific position. PVC plastic tubes are used as connections between the OL and the piece containing the polarization elements and the minilenses. These tubes are black and prevent non-desired light from entering the system. Further, they help to locate the stack containing the arrays at a fixed position from the OL and the sensor area. A detail of the piece containing the RA, LA and the LP is shown in displayed in Figure 3.11.

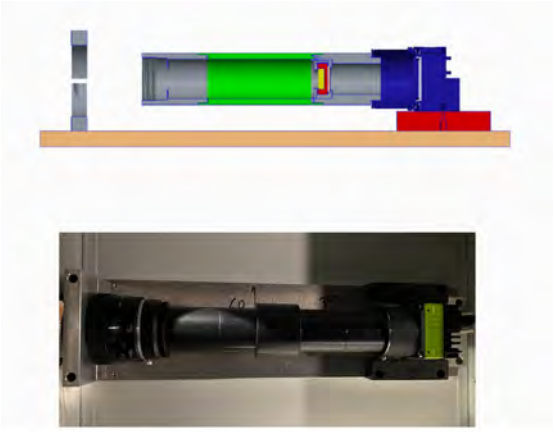

Figure 3.10: (Top) Profile of the mechanical design and (bottom) picture of the assembled system.

Once the stack of RA, LA and the LP piece has been assembled in the aperture of the system, its final behaviour is characterized experimentally. The set-up to carry out these measurements is made up of white LED lighting, a diffuser, the piece RA-LA-LP located in reverse, with the quadrant to be measured free and the rest covered with optical tape, followed finally by the Thorlabs VIS range polarimeter (PAX1000VIS), see Figure 3.12.

The piece is then illuminated with unpolarized light and the Stokes vector generated by the LP and the uncovered RA is measured by the polarimeter. The Stokes vector components should be $\frac{1}{\sqrt{3}}$ 0.577 with the corresponding signs. The

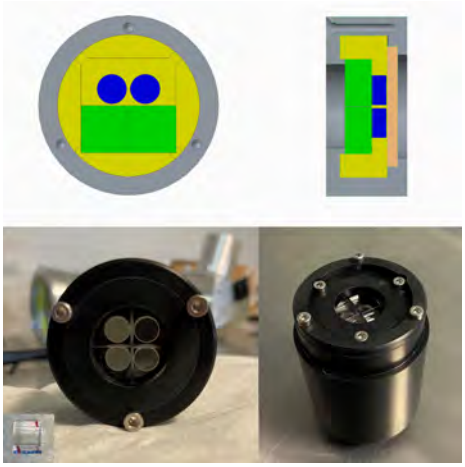

Figure 3.11: (Top) Mechanical design of the stack at two different views. The green rectangle corresponds to the retarder, the blue colour stands for the minilens and the orange surface corresponds to the LP. (Bottom) The picture on the left shows the assembled system with the RA, LA and the LP. In the bottom corner of the image on the left, a photograph of a retarder of 10mm-size is shown. The picture on the right displays the polarization stack inside the tube connecting it to the sensor.

Figure 3.12: Picture of the set-up of the characterization of the piece composed by the RA, LA and the LP.

final measured matrix of the system is:

$$\mathbf{A_{PSA}} = \frac{1}{2}\begin{pmatrix} 1.00 & -0.64 & -0.54 & -0.55 \\ 1.00 & -44 & +0.78 & +0.44 \\ 1.00 & +0.63 & +0.71 & -0.33 \\ 1.00 & +0.42 & -0.55 & +0.72 \end{pmatrix} \tag{3.3}$$

The matrix $\mathbf{A_{PSA}}$ is very close to the optimum PSA matrix presented in Equation (2.34). (Note: The signs of S_1, S_2 and S_3 are the opposite since they were measured in reverse order), This shows the appropriateness of the procedures applied and confirms the validity of the constructed setup.

Software requirements

One of the main complexities of the system setup has been that the camera sensor accepts only Mini Camera Link connectors (PMCL), which transport the power and the signal together. Consequently, a frame grabber is required to convert the Camera Link camera into a native USB 3.0 Vision camera. The camera provider recommended the external frame grabber iPORT CL-U3 (Pleora Technologies) to do so. This model comes with the option of power over Camera Link (PoCL) to provide the needed voltage to the sensor (12V to 24V DC ± 10%). It requires an external power supply GPIO connector to do so. It also works as a receiver from the sensor and sends the signal to the PC through a USB 3.0 cable. Both connections between the camera and the frame grabber are depicted in Figure 3.13. The PC to control the DoAPC has a processor Intel Core i5-8250U 1.6GHz, and an NVIDIA GeForce MX150 board with 8GB of RAM.

Figure 3.13: (Left) Camera Link connectors (PMCL). (Right) iPORT CL-UB3 frame grabber with the PCML coming from the sensor on the left side and the USB 3.0 on the right side to connect to the PC.

The frame grabber is controlled with the eBUS Player professional software (Pleora Technologies). The parameters of the camera cannot be modified using its software, instead, orders must be sent using the frame grabber software. The acquisitions by the DoAPC are made in the following steps:

a The frame grabber should be connected to the power supply and then connected through the PMCL to the sensor and the USB 3.0 to the PC. Figure 3.14 displays the device menu to select the frame grabber.

b Selection of the image format parameters of the frame grabber to be sent to the sensor for the acquisition as shown in Figure 3.15. The ROI of interest is specified here.

c The configuration of the sensor (e.g. the exposure time or the dynamic range) is set via serial communication with the sensor and the frame grabber, see Figure 3.16.

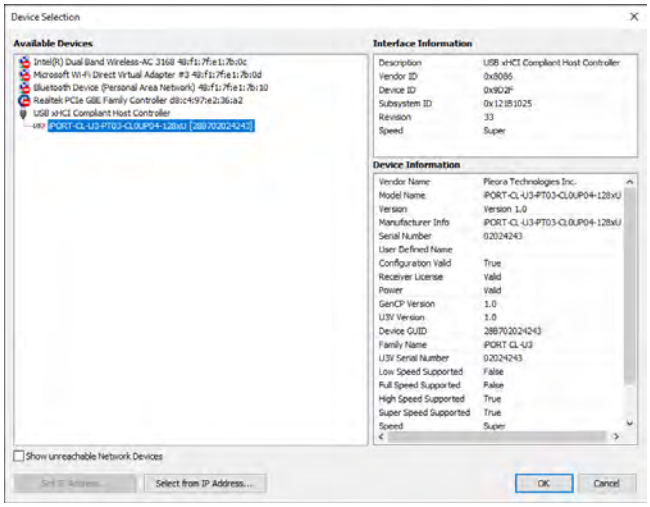

Figure 3.14: Frame grabber software: device selection menu of the eBUS Player.

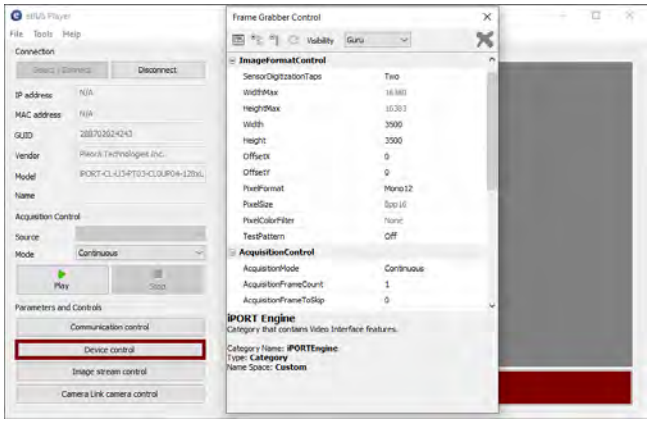

Figure 3.15: Frame grabber software: device control menu of the eBUS Player to specify the image format of the acquisitions.

d Figure 3.17 shows the visualization of the acquisition of the raw intensity images. Four sub-images are distinguished in the sensor area corresponding to the different configurations of the retarders in the RA of the optical design. Each sub-image has a size of 1324 x 1324 pixels.

After the acquisition of the images using the eBUSPlayer, the raw images must be processed to obtain the polarization information from the 4 sub-images measured in a single shot. The different calibration algorithms together with the image processing ones to generate the polarization maps (Stokes vector, advanced parameters and Mueller matrix) are self-developed algorithms using MATLAB MATLAB 2019 using the raw images from the DoAPC.

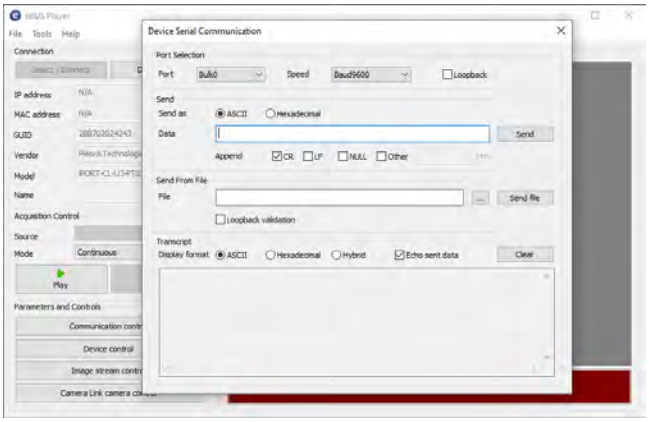

Figure 3.16: Frame grabber software: serial communication menu of the eBUS Player to set the configuration of the CMOS.

Figure 3.17: Frame grabber software: visualization menu of the eBUS Player to see the raw acquisitions. Four sub-images are distinguished corresponding to the four configurations of the retarders in the RA.

Mechanical modifications: turbid media application

After the construction of the DoAPC, a final modification is required to perform the experiments presented in Chapter 7. The camera needs to be introduced in a high-humidity environment for making fog experiments. In order to preserve the metallic and electronic components of the system from water, the system is encapsulated using a mild steel box (RS PRO #775-5805) of dimensions 500x400x150mm guaranteeing IP66 protection. Figure 3.18 displays the final mechanical design of the set-up with the system inside the metallic box. Next, the final mounting of the system is shown in the laboratory.

To perform the measurements with the camera inside the box an aperture is created and an N-BK7 window is fixed with silicone to have it completely sealed.

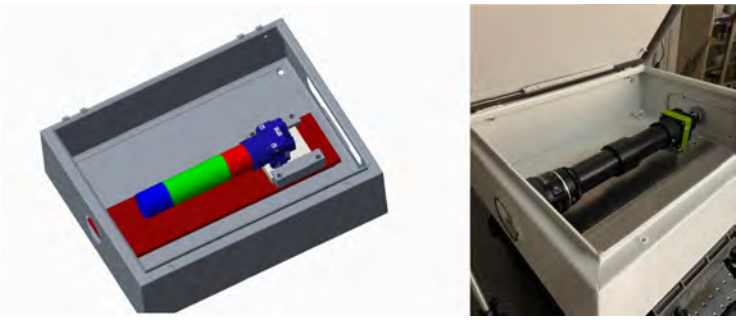

Figure 3.18: (Left) Mechanical design of the complete DoAPC inside the IP66 steel box. (Right) Picture of the encapsulated DoAPC.

The window is characterised under different polarized light states to test if some deviation is introduced in the polarization states passing through it. Figure 3.19 presents the results of a specific case. It shows the polarization measured in the presence and absence of the window. The input light is left-circularly polarized and, as it can be appreciated, the behaviour of the outgoing polarization in both cases is nearly identical. The S_3 channel is maintained at values around -1.0, showing its independence to the window. The input light value of S_1 and S_2 parameters is 0.0, while the experimental mean values of S_1 and S_2 channels oscillate between 0.02 and -0.025 (without window) and 0.04 and 0.033 (with the window), respectively. The variance of all values is below 10^{-2} allowing to consider irrelevant the effect of the added window in the polarization states measured. Equivalent results were obtained in the different polarization states tested. The states encompassed the full sphere of Poincaré, from the linear states passing through the elliptical to the circular states.

3.3 Active imaging: illumination

The DoAPC can be employed to measure the Stokes vector in passive or in active mode, this is, without or with an additional light source illuminating the sample under observation with a known polarization state. In addition, the system requires an active mode to retrieve the Mueller matrix of the scene. Previous to all these modes of operation, a polarimetric calibration, explained in Chapter 5, will be required to deliver controlled polarization states, which needs a polarization state generator PSG.

In first instance, a white light integrating sphere was employed as the light source for calibration, since it was supposed to give homogeneous and uniform unpolarized illumination. Our first calibration trials were performed with this type of illumination, but the results did not agree with the expected values. When revised, the integration sphere was found to have a very large angle of divergence, which surpassed the acceptance angles of the polarization elements of the PSG and the DoAPC, thus making the input polarized light to include a

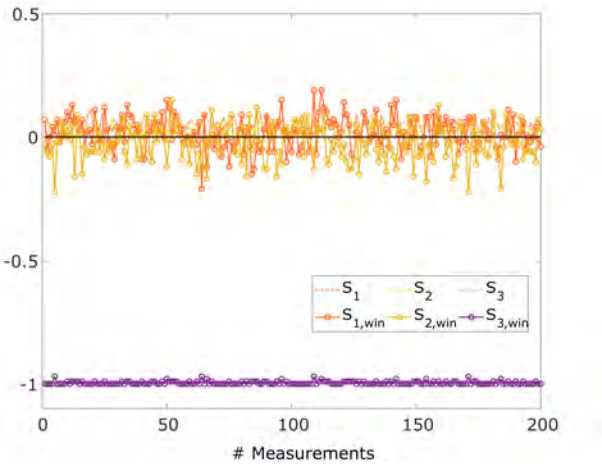

Figure 3.19: Analysis of the polarization stability after adding an N-BK7 window to the housing. The Stokes parameters after passing the window ($S_{i,win}$) and without the window (S_i) are compared and shown to be equivalent.

significant percentage of non-polarized light originating from the rays out of the acceptance angle range.

Thus, we modified our source by designing and building a light source based on LEDs with the aim to use it in the polarization state generator for the calibration of the system, as well as the active Stokes imaging and Mueller matrix imaging. As it will be seen in Chapter 5, this light source is more appropriate to this application than the former presented.

Due to the need to achieve a degree of incidence of less than 10^o on the polarization elements (retarders and polarizer), an array of 4 high-power white LEDs has been used. This type of LED array also has plastic microlenses designed and characterized already embedded. Figure 3.20 presents photographs and information on the LED array used (Luxeon Rebel LXML-PWC2).

Figure 3.20: (Left) Picture of the white LEDs array. (Right) Image from the datasheet of the plastic lenses that collimate the light emitted by the LEDs

The Zemax OpticStudio optical layout of the light source using the information from these components and its illuminated area at 1m are presented

in Figure 3.21. The full angle of divergence of the light source is 11.3^o.

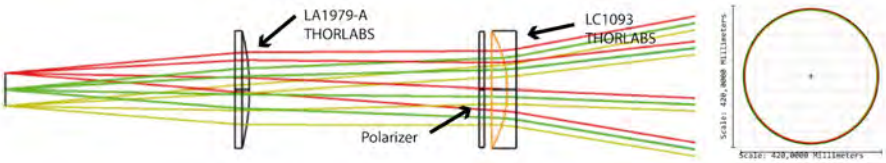

Figure 3.21: The image on the left shows the Zemax OpticStudio design of the light source. On the right, the area of illumination at one meter.

The selected high-power LEDs selected as source for the illumination system need to be cooled to ensure their stability and robustness. Heatsinks designed specifically for this LED source have been incorporated into the mechanical system (as shown in the mechanical layout of Figure 3.22).

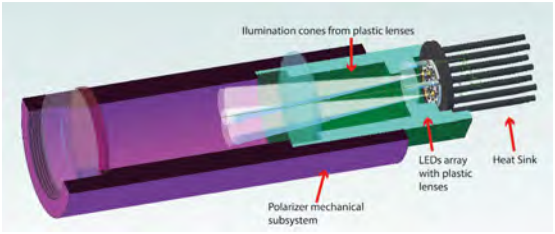

Figure 3.22: Image of the mechanical design of a single light source.

The final application of our system consists of performing active Stokes imaging in turbid media, as presented in Chapter 7. As a consequence, we decide to build a system with cylindrical symmetry in order to be able to rotate the illuminating element to align the axis when introducing polarizers as quickly as possible, when required, during the turbid media tests. The LP used in these tests is EO #19-013 and the circular polarizer CP is EO#88-100. In addition, it was decided to build four equivalent light sources to be able to produce a homogeneous illumination distribution in a significant area by emitting the polarized light at four points equidistant from the optical axis of the polarimetric camera, arranged in a 2x2 array. The final unit for these experiments is depicted in Figure 3.23.

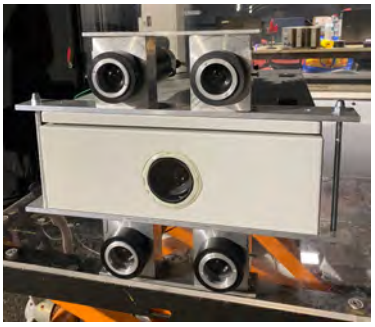

Figure 3.23: Photography of the encapsulated DoAPC together with the illumination array for active Stokes imaging.

Part III

System Calibration

Any device used for quantitative measurement requires precise calibration. In specific, a polarization-sensitive device needs at least two types of calibration: radiometric and polarimetric calibration.

The radiometric calibration is a common factor for any "electronic sensor". For example, a CMOS, which is formed by an array of pixels, may introduce errors to the measurement such as dark current noise and also generate background offset, saturation, and fixed noise patterns due to the different responses of the pixels [92].

The polarimetric calibration consists in deriving the linear transformation that lets the measured intensities be understood as polarization information. This linear operator is known as the instrumentation or measurement matrix and several procedures have been developed for its precise obtaining, as explained in Section 2.4.3. This is a crucial step for passing from an intensity-sensitive device to the desired polarization-sensitive device.

In some cases, the acquisition could require more than one simultaneous optical path (like in DoAP architecture), and thus, a geometrical calibration is necessary for the correct registration of the images, even more, if a post-processing step may merge or compare them.

In this case, since our system is a DoAP polarimetric camera, all three calibrations are needed and essential for recovering accurate polarimetric information. In the following Chapter 4 and Chapter 5, these distinct calibrations are addressed and extended.

Chapter 4

Radiometric and Geometric calibrations

In this chapter, the steps formerly to polarization recovery are addressed. Initially, the radiometric calibration is addressed in Section 4.1 since it is basic to know the characteristics of the sensor to prepare the data for its processing. Later, the geometric calibration goal is reviewed in Section 4.2 together with the different techniques for its application and the metrics for its quantitative evaluation. The results obtained after these processes are presented in each section for a detailed analysis of the DoAP performance. After this pre-processing step, we will continue the final step for polarization recovery in Chapter 6.

4.1 Radiometric calibration

The radiometric calibration consists in studying whether the sensor is working in the linear regime, by avoiding the saturation and getting rid of the dark noise effects, the lack of uniformity of the gain, and the dead and hot pixels of the sensor [93], in our case a CMOS-based camera. Moreover, the radiometric calibration addresses the removal of background effects of the system components especially present when there is more than one optical path and the components may introduce some differences in the intensities due to non-idealities.

The set-up for this calibration is very basic. Only a spatially uniform unpolarized light source together with the device to be calibrated are needed. In our calibration, a xenon lamp coupled to an integrating sphere compose the light source. It ensures the total loss of any polarization residual and provides spatially homogeneous output light. The camera is placed next to the light source, as shown in Figure 4.1.

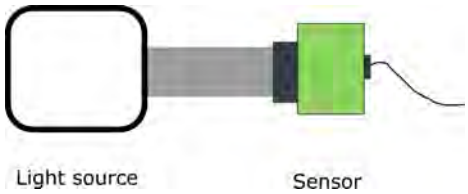

Figure 4.1: Scheme of the radiometric calibration set-up. The light coming from the light source comes into the bare sensor surface for calculating the I_{GNU}.

Two operations must be done to the raw image for correction: subtracting the fixed dark pattern (I_{dark}) and the gain non-uniformity pattern (I_{GNU}). For that reason, several dark frames are acquired in total darkness with the camera and

averaged to get the I_{dark}. For the second pattern, the light source illuminates the bare sensor of the camera with uniform unpolarized light and the resulting pattern normalized by its mean grey level is saved. This is done several times to improve the accuracy of the calibration. From the previous measurements, the corrected image (I_{corr}) can be systematically obtained using the equation[6]:

$$I_{corr} = \frac{I_{raw} - I_{dark}}{I_{GNU}} \tag{4.1}$$

In our case, the dark noise pattern I_{dark} is calibrated for different exposure times of the camera ranging from 50 to 120 ms to assure the best results during measurements. Figure 4.2 shows the histograms and fitted Gaussian distributions of the dark noise present in the sensor. The mean values are around 2100 in the dynamic range of the camera at 16 bits. By subtracting this noise, the images are compensated for the inhomogeneity of the sensor chip.

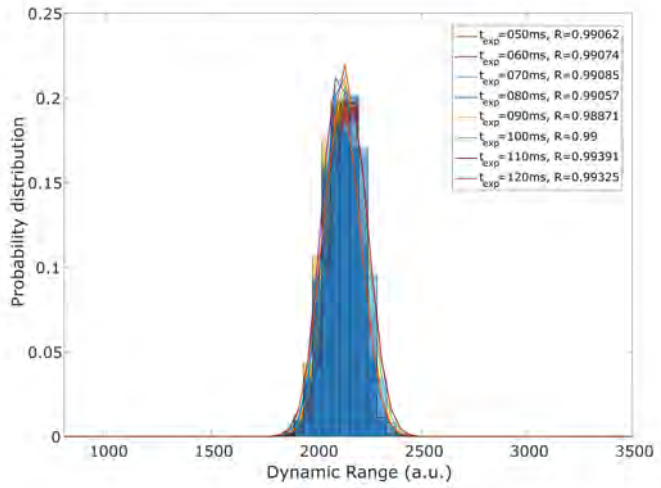

Figure 4.2: Dark noise fixed pattern I_{dark} distributions of exposure times of the camera between 50 and 120 ms.

In the same trend, the flat field pattern is evaluated in the same range of exposure times to see the performance of the sensor. It is observed in Figure 4.3 that there exists skewness in the Gaussian distributions in the histograms when being illuminated at the 75% of the saturation value (2^{16}). This demonstrates the need of applying this correction to eliminate the intensity falloff towards the edges. The resulting images show uniform brightness over the entire FOV.

Since our system has more than one optical path in the PSA, different components are placed in the distinct paths. This can generate asymmetry in the light transmission of the resulting sub-images due to the tolerances of fabrication of the optical elements and must be calibrated. To do this, the same light source is used and the complete DoAP camera is located in front of it, see Figure 4.4.

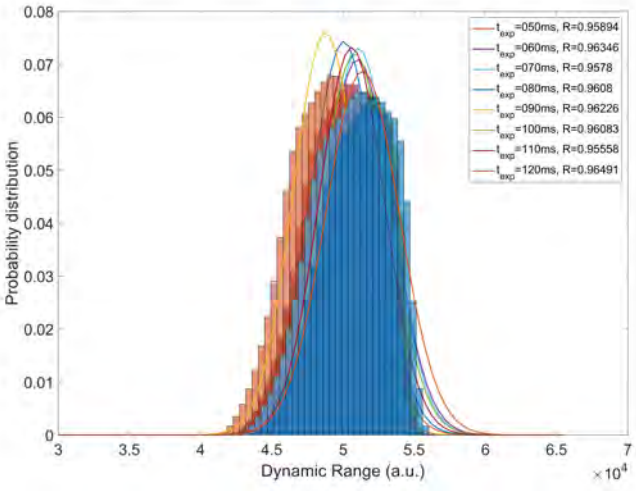

Figure 4.3: Distributions of the flat fixed pattern I_{GNU} of exposure times of the camera between 50 and 120 ms.

The light entering the system is granted to be unpolarized and uniform due to the integrating sphere. After illuminating the aperture of the OL, the sub-images are averaged and the ratios between them calculated to correct the asymmetry.

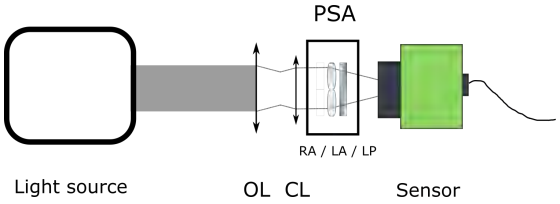

Figure 4.4: Scheme of the radiometric calibration set-up to correct the difference of the transmissions between channels. The illumination from the light source comes into the camera through the objective lens (OL), the collimating lens (CL), the PSA formed by the achromatic retarder (AR), the achromatic lenses (AL) and the LP up to the sensor.

4.2 Geometric calibration

Once the first step is accomplished and the intensity is correctly computed, the next action is to correct the possible misregistration presumably caused by image distortion, magnification error and alignment error [56, 81]. In the DoAP camera, four intensity sub-images will be used for the estimation of the polarimetric parameters. Therefore, any misregistration among these sub-images may result in a false polarization signature due to small differences within the manufacturing tolerance of the different components of the system.

Each sub-image is affected by its distortion across the FOV due to the minilenses decentering from the optical axis and possible irregularities of the respective AR. This calibration must be performed via software to characterize the errors of each sub-aperture. The reference sample is placed in front of the camera to match the position of the detected landmark points of the images, such as corners. Then, several sub-pixel image registration algorithms are studied to see which one fits better our requirements: good registration in real scenes and enough speed to perform real-time acquisition.

As presented in Section 2.4.2, many methodologies have been developed to tackle this problem. Some algorithms seem to fit the previous requirements such as SIFT and SURF. They arise as powerful tools to perform sub-pixel registration that take into account not only intensity-based features but local feature detection. In this section, different registration algorithms are tested on the system and their results are presented and discussed.

Apart from custom interpolation algorithms based on intensity patterns, the local feature detection algorithms do not only allow performing image registration but object detection and classification, tracking and motion estimation. They search for anchor points, like blobs, corners and edge pixels, to correlate two different images or reconstruct them in 3D. These local features come from local gradient computation and let find image correspondence without segmenting the image regardless of occlusion, changes in viewing conditions and presence of clutter. Here, the SURF [REF] and ORB [REF] algorithms together with the combinations of FAST-SURF [REF] and SURF- ORB are studied for the DoAP system. Although SIFT method [REF] is the basis where SURF is developed, it has a higher computational cost and is not included in the study.

During the registration algorithm, only a pair of detector-descriptor is needed to obtain the features for calculating the geometric transformation. This pair can be composed of the mentioned algorithms. Their properties vary among them due to their scheme detection-description of the features giving them the ability to be invariant to intensity, rotations or scaling, as formerly explained in Section 2.4.2. SURF can be used in the detection and description of the features and its characteristic points are based on blobs. This algorithm is invariant to intensity changes, rotations and even to different scales. FAST is a corner detector and is invariant to intensity changes but not to scale. It can be implemented together with SURF to describe more types of points for calculating the transformation. ORB is used in both modes detecting and extracting the features. It employs the Oriented FAST and rotated BRIEF [103]. It is faster than SURF but it is not invariant to different scales. It can be also combined with SURF to expand the classes of detected points.

The measurements are taken using a reference sample, in this case, a chess board, and the DoAP camera, as displayed in Figure 4.5. The acquisitions consisted in several positions of the reference sample under different illumination conditions to see the stability of the algorithms. The DoAP camera has four sub-images and channel 2 is chosen as the reference image since it is less affected by distortion. Before geometric calibration, previous steps are mandatory:

a Ensure the non-existence of dead and hot pixels, substituting them by 0, NaN or the mean of adjacent pixels.

b Apply the radiometric calibration with the respective exposure time.

c Normalise reference and raw images before the registration algorithms.

Once the data is pre-processed, the features have to be found by the detector and then extracted by the descriptor. As previously said, four possibilities are studied for our system: SURF and ORB algorithms and the combinations of FAST-SURF and SURF-ORB. Firstly, the SURF and ORB are used as detector-descriptor alone and, then FAST-SURF and SURF-ORB as detector-descriptor pairs. After acquiring the features, the points should be checked to be outliers or inliers. The latter are those that when performing the transformation from the point in image B to image A, its distance from the corresponding point in image A is within the specified threshold. This is done by the MSAC algorithm (MATLAB R2019b, Computer Vision Toolbox) that estimates the geometric transformation and separates the inliers matching points. This registration workflow is represented in Figure 4.6 for better comprehension.

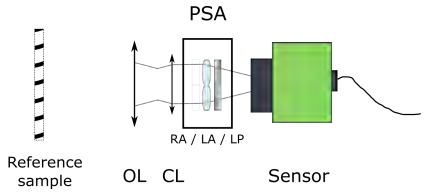

Figure 4.5: Scheme of the geometric calibration set-up. The reference sample (chess board) is illuminated by homogeneous light and imaged by the DoAP.

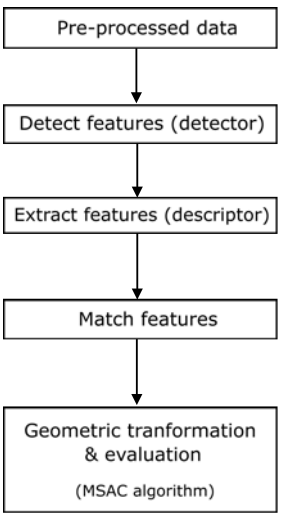

Figure 4.6: Workflow for registering a raw image to the reference image.

To analyse and evaluate the quality of the registration, three error metrics are defined and the computation time is saved. The Mean Square Error (MSE) measures the average squared difference between the registered (x_i) and the reference (x_i^*) images. Since it is derived from the square of Euclidean distance, it is always a positive value that decreases as the error approaches zero.

$$MSE = \frac{1}{n}\sum_{i=1}^{n}(x_i - x_i^*)^2 \tag{4.2}$$

The Structural Similarity Index (SSIM) is an image quality metric that assesses the visual impact of three characteristics of an image: luminance $l(x, y)$, contrast $c(x, y)$ and structure $s(x, y)$ [172]:

$$SSIM(x, y) = [l(x, y)]^{\alpha} \cdot [c(x, y)]^{\beta} \cdot [s(x, y)]^{\gamma} \tag{4.3}$$

The value of SSIM is typically in the range [0, 1]. The value 1 indicates the highest quality and occurs when raw and reference images are equivalent. Smaller values correspond to poorer quality.

Finally, the Target Registration Error (TRE) is the distance after registration between corresponding points not used in calculating the registration transform [173]. It is calculated from the Euclidean distance and divided by the length of the image diagonal. This metric tends to zero as the registered (x_i) and the reference (x_i^*) images approach.

$$TRE = \frac{||x_i - x_i^*||}{d} \tag{4.4}$$

Results and discussion

The presented algorithms are evaluated to derive which one fulfills the desired conditions of good registration and high speed. Several acquisitions of the reference table in different positions and illumination conditions are measured. The four channels shown in Figure 4.7 have different FOV and distortions. Channel 2 is considered the reference channel to apply the registration algorithms. In this subsection, the images of one method are displayed for each sample and the evaluation metrics, including the computation time, are gathered in a table for all methods.

The samples used for testing the registration algorithms are based on the reference sample, the chess board, with different elements on it. All of them are displayed in Figure 4.7. Sample 1 is close to the camera position, normal to the camera and includes a LP in the middle. Sample 2 is located further away from the camera, continues in normal position and includes more stickers around the LP. Sample 3 is the same as sample 2 but including a rotation of the chessboard and lower illumination. All of them have the LP included in order to see the influence of different PSA states in the intensity of the four channels and, thus, in the registration results. A last sample, sample 4, is studied to see the ability of the algorithms using only the chess board without additional elements with a rotation and low illumination.

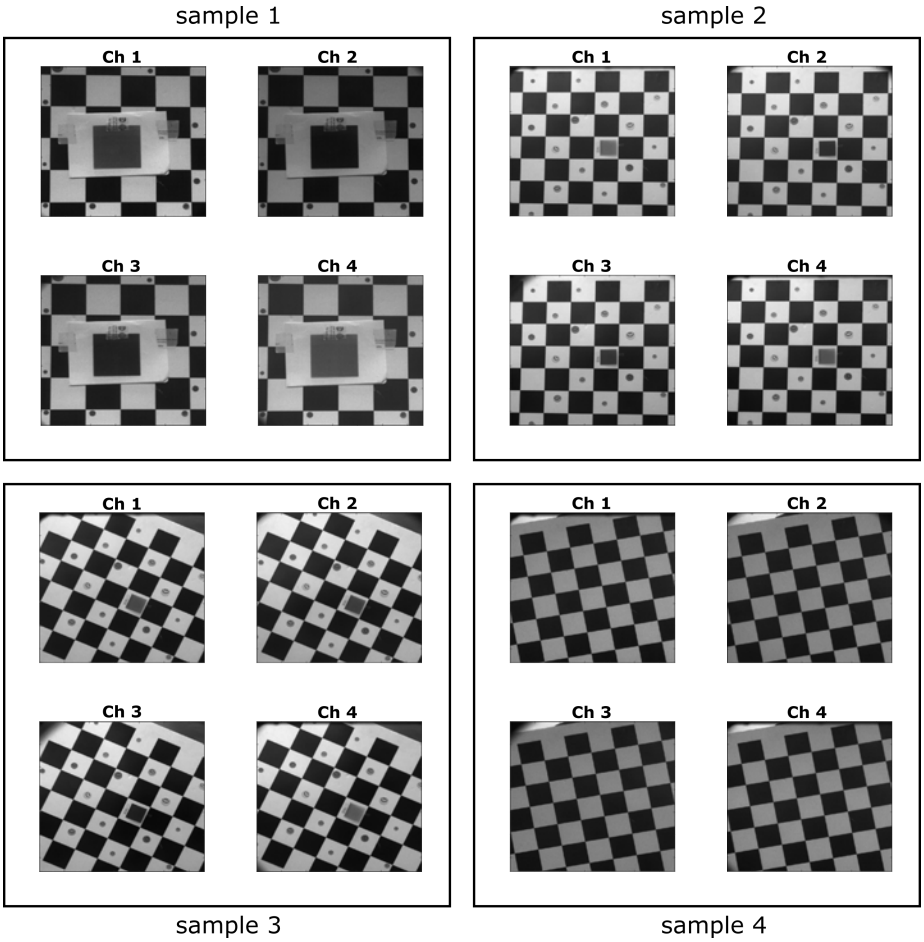

Figure 4.7: Intensity images at each channel of the samples before their registration. Each sample changes the position, illumination and elements of the reference sample.

The comparison of sample 1 between the pre-registered channels 1,3 and 4 versus the reference channel 2 is done in Figure 4.8 (top). It displays the superposition of respective channels with channel 2 and the misalignment between them is shown in false colour for a better contrast. Channel 3 shows the highest deviation from channel 2 and the LP intensity differs between the channels. This variation denotes the polarization-dependence of our system. Sample 1 shows several matching points between the different channels and the reference. Figure 4.8 (center) shows the points detected by SURF method. ORB method does acquire similar results with fewer detected points and the registration has the same error values in less time, as shown in Table 4.1. Mixing SURF with FAST/ ORB does not affect any metric but increases in calculation time. The subtraction images between registered channels and channel 2 displayed in

Figure 4.8 (bottom) indicate that the algorithm registers correctly the images despite the intensity variation at the LP. The MSE, TRE and SSIM values are correlated to the difference image. The better the registration, the lower MSE, TRE and higher SSIM indicating a higher resemblance. The SSIM is around 70% since the difference between the intensity of LP and the insufficient matching in the corners decreases the metric from 1.0 to 0.7.

Following the previous analysis, Figure 4.9 compiles all the steps in the registration of channels 1, 3 and 4 for sample 2. At the top, differences between images can be appreciated. The 3rd channel shows again the highest deviation from reference. In the middle, the matching points between the channels and the reference are detected using SURF. In this case, the number of points is higher than sample 1 due to the stickers. Finally, the difference between registration in channels and reference is shown. In this case, the LP is set in the same axis orientation as previously, and thus the intensity variation is remarkable in channels 1 and 4 once more. Table 4.2 agrees with Figure 4.9(bottom) showing that the errors are minimum. Performing the geometric calibration with sample 2 leads to analogous computation times to sample 1. The MSE and TRE are decreased and SSIM is improved with respect to sample 1. This is due to the availability of a higher number of inliers to calculate the transformation. The minimal changes do not influence the registration result when the distance of objects varies from the device.

Sample 3 lets us study the influence of rotations and lower illumination conditions. Since this sample is oblique to the normal of the camera, the misalignment between channels and reference is more notorious in all of them, Figure 4.10 (top). In addition, the number of matching points is larger than in any other method, as displayed for SURF in Figure 4.10 (middle). The recovered images after applying the geometric transformation show lower errors than in sample 2. It is congruent with the quantitative error evaluation in Table 4.3 where MSE and TRE are decreased besides SSIM being maintained. This demonstrates that using different positions of the sample can help to improve pixel-matching.

Sample 4 consists of placing the bare reference sample in front of the camera rotated and slightly tilted. At first sight from Figure 4.11 (top), there is not a large deviation from the reference channel. On the contrary, the SURF and the combination of FAST-SURF do not detect enough inliers (minimum 3 matching points) to proceed with the calculation of the geometric transformation. This is reflected in Table 4.4, where no metrics are retrieved from the transformation. Therefore, Figure 4.11 (middle) displays the very few inliers detected with ORB. This points are matched using the SURF descriptor and the final registration is shown in Figure 4.11 (bottom). All the channels are badly registered and these results are quantified in Table 4.4. The MSE and TRE are increased around six times. The SSIM drops from 80% values to 10% meaning that the calibrated image does share very few characteristics, proving the bad registration using ORB and SURF-ORB. The time triggered in performing the transformation is higher than normal showing the additional work of the algorithm to find a suitable transformation when a low number of matching points is detected.

When these problems arise during registration time, a possible solution can be to apply a previously calculated transformation. This is tried in sample 4, where the inliers points were insufficient and the registration was not possible or very poor. Taking the geometric transformation recovered at each channel using sample 2, the resulting registration is Figure 4.12 (bottom). The calibrated channels are correctly registered and the comparison between metrics is gathered in Table 4.5. In both cases, the same method is employed but the computation times differ. When applying the previously calculated transformation, the time is reduced since it is only applied to each channel. The MSE and TRE returns to normal values when applying the transformation of sample 2 . The SSIM reflects this passing from 0.10 to 0.83, meaning the registration is correct. This solution results to be a good procedure to tackle misregistrations when there is a lack of inliers.

Method	**Ch #**	**MSE**	**SSIM**	**TRE**	t_{comp}
SURF	Ch 1	0.019	0.73	0.012	0.33 s
	Ch 3	0.016	0.73	0.053	0.35 s
	Ch 4	0.020	0.71	0.004	0.34 s
ORB	Ch 1	0.019	0.72	0.006	0.17 s
	Ch 3	0.016	0.73	0.016	0.14 s
	Ch 4	0.020	0.69	0.003	0.12 s
FAST-SURF	Ch 1	0.019	0.73	0.012	0.36 s
	Ch 3	0.016	0.73	0.051	0.35 s
	Ch 4	0.020	0.71	0.004	0.37 s
SURF-ORB	Ch 1	0.019	0.73	0.013	0.43 s
	Ch 3	0.016	0.73	0.050	0.42 s
	Ch 4	0.020	0.71	0.005	0.41 s

Table 4.1: Registration metrics of each channel when applying SURF, ORB, FAST-SURF and SURF-ORB methods on sample 1, taking as reference channel 2.

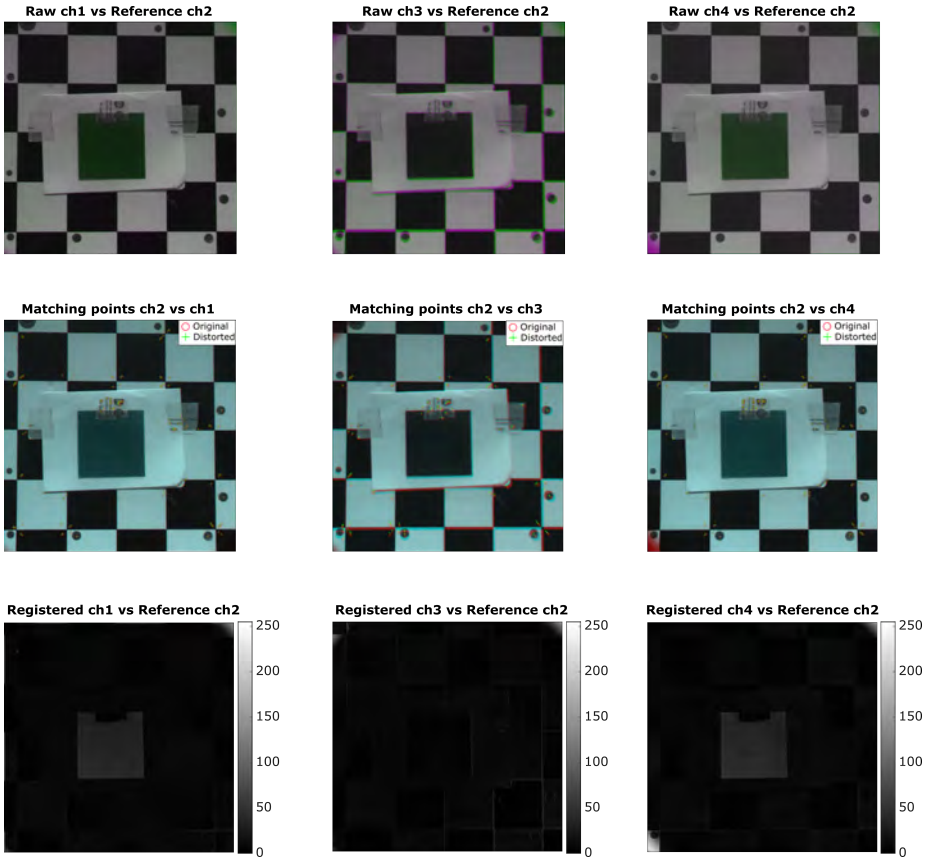

Figure 4.8: Registration of sample 1. (Top) Before registration: False colour comparison between the pre-calibrated intensity images of channels 1,3 and 4 and the reference channel 2. (Middle) During registration: Extracted matching points (inliers) between the reference channel 2 and channels 1,3 and 4 were extracted using the SURF detector. (Bottom) After registration: Difference between the registered images using the SURF descriptor and reference channel 2.

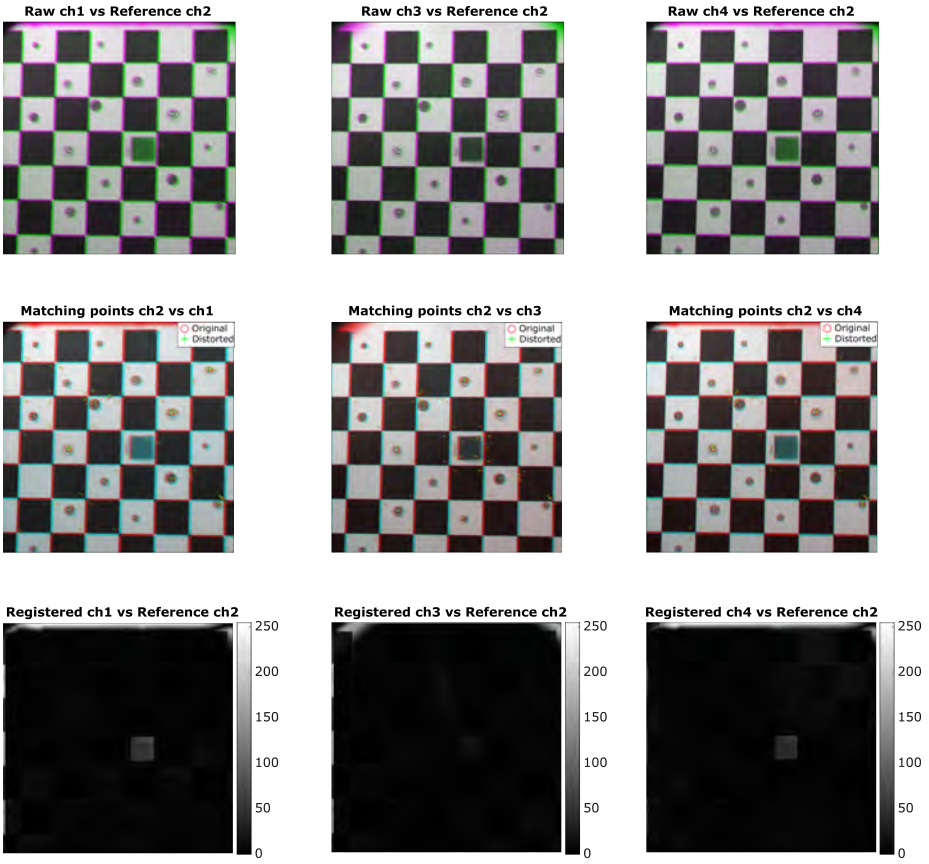

Figure 4.9: Registration of sample 2. (Top) Before registration: False colour comparison between the pre-calibrated intensity images of channels 1,3 and 4 and the reference channel 2. (Middle) During registration: Extracted matching points (inliers) between the reference channel 2 and channels 1,3 and 4 were extracted using the SURF detector. (Bottom) After registration: Difference between the registered images using the SURF descriptor and reference channel 2.

Method	**Ch #**	**MSE**	**SSIM**	**TRE**	t_{comp}
SURF	Ch 1	0.013	0.83	0.082	0.36 s
	Ch 3	0.006	0.85	0.068	0.36 s
	Ch 4	0.011	0.84	0.05	0.34 s
ORB	Ch 1	0.013	0.83	0.044	0.17 s
	Ch 3	0.006	0.84	0.041	0.26 s
	Ch 4	0.011	0.83	0.025	0.20 s
FAST-SURF	Ch 1	0.013	0.83	0.082	0.38 s
	Ch 3	0.006	0.84	0.067	0.37 s
	Ch 4	0.011	0.84	0.050	0.37 s
SURF-ORB	Ch 1	0.013	0.83	0.092	0.45 s
	Ch 3	0.006	0.85	0.079	0.49 s
	Ch 4	0.011	0.84	0.056	0.42 s

Table 4.2: Registration metrics of each channel when applying SURF, ORB, FAST-SURF and SURF-ORB methods on sample 2, taking as reference channel 2.

Method	**Ch #**	**MSE**	**SSIM**	**TRE**	t_{comp}
SURF	Ch 1	0.008	0.82	0.086	0.36 s
	Ch 3	0.007	0.83	0.063	0.35 s
	Ch 4	0.007	0.82	0.045	0.34 s
ORB	Ch 1	0.009	0.82	0.054	0.11 s
	Ch 3	0.007	0.82	0.035	0.11 s
	Ch 4	0.007	0.82	0.022	0.17 s
FAST-SURF	Ch 1	0.008	0.82	0.086	0.40 s
	Ch 3	0.007	0.82	0.063	0.37 s
	Ch 4	0.007	0.82	0.046	0.37 s
SURF-ORB	Ch 1	0.009	0.82	0.101	0.44 s
	Ch 3	0.007	0.83	0.072	0.43 s
	Ch 4	0.007	0.82	0.051	0.47 s

Table 4.3: Registration metrics of each channel when applying SURF, ORB, FAST-SURF and SURF-ORB methods on sample 3, taking as reference channel 2.

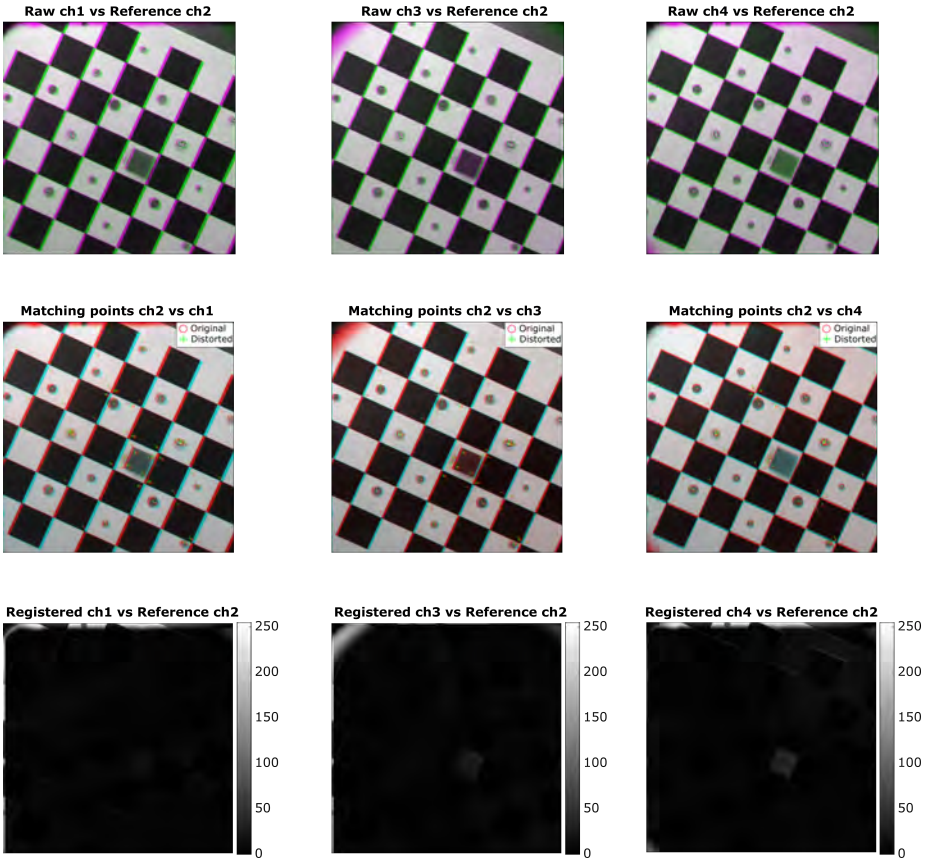

Figure 4.10: Registration of sample 3. (Top) Before registration: False colour comparison between the pre-calibrated intensity images of channels 1,3 and 4 and the reference channel 2. (Middle) During registration: Extracted matching points (inliers) between the reference channel 2 and channels 1,3 and 4 were extracted using the SURF detector. (Bottom) After registration: Difference between the registered images using the SURF descriptor and reference channel 2.

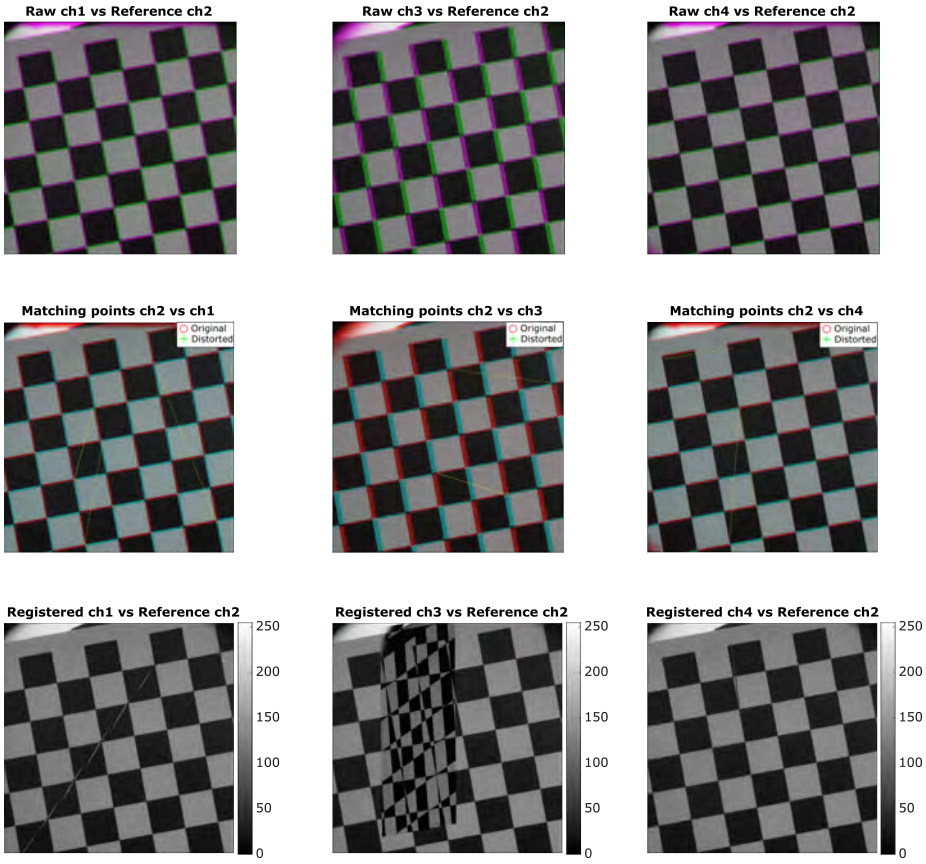

Figure 4.11: Registration of sample 4. (Top) Before registration: False colour comparison between the pre-calibrated intensity images of channels 1,3 and 4 and the reference channel 2. (Middle) During registration: Extracted matching points (inliers) between the reference channel 2 and channels 1,3 and 4 were extracted using the SURF detector. (Bottom) After registration: Difference between the registered images using the ORB descriptor and reference channel 2.

Method	Ch #	MSE	SSIM	TRE	t_{comp}
ORB	Ch 1	0.100	0.38	0.531	0.35 s
	Ch 3	0.137	0.07	0.636	0.33 s
	Ch 4	0.129	0.13	0.103	0.34 s
SURF-ORB	Ch 1	0.147	0.01	0.653	0.63 s
	Ch 3	0.126	0.12	0.429	0.64 s
	Ch 4	0.146	0.01	0.575	0.57 s

Table 4.4: Registration metrics of each channel when applying ORB, and SURF-ORB methods on sample 4, taking as reference channel 2.

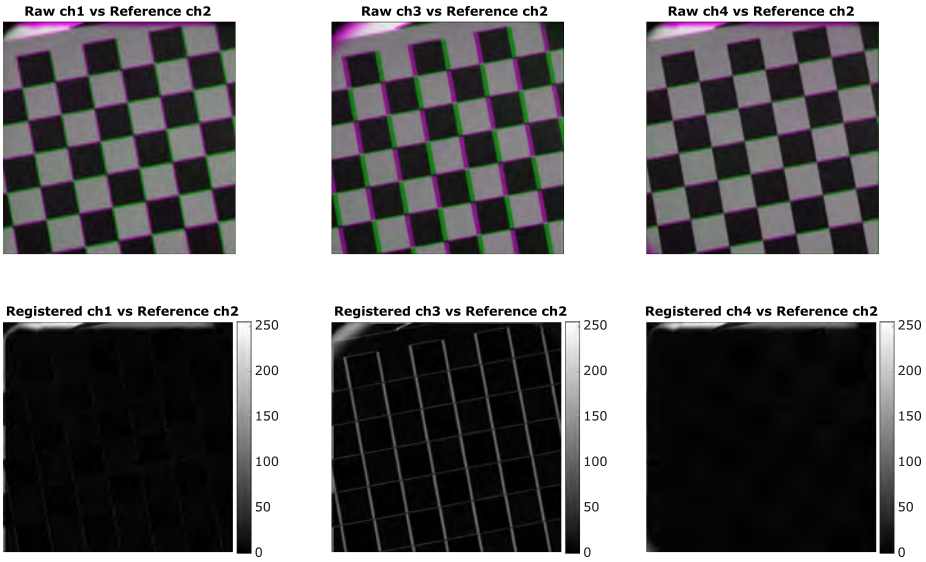

Figure 4.12: Registration of sample 4 using geometric transformation of sample 2. (Top) Before registration: False colour comparison between the pre-calibrated intensity images of channels 1,3 and 4 and the reference channel 2. (Bottom) After registration: Difference between the registered images using the transformation of sample 2 and reference channel 2.

Method	Ch #	MSE	SSIM	TRE	t_{comp}
SURF-ORB (Own transformation)	Ch 1	0.147	0.01	0.0653	0.63 s
	Ch 3	0.126	0.12	0.429	0.64 s
	Ch 4	0.146	0.01	0.575	0.57 s
SURF-ORB (Sample 2 transformation)	Ch 1	0.013	0.83	0.092	0.45 s
	Ch 3	0.006	0.85	0.079	0.49 s
	Ch 4	0.011	0.84	0.055	0.42 s

Table 4.5: Registration metrics of each channel, taking as reference channel 2, when applying SURF-ORB methods on sample 4 using the own geometric transformation and applying the calculated one in sample 2.

Conclusions

After presenting the complete study of methods for the geometric calibration, the following conclusions are extracted.

a Four methods are checked to be invariant to rotations, tilts and changes in scale and illumination.

b SURF detects more inliers than ORB despite it spends triple time in computation.

c SURF and ORB detect different types of characteristics complementing themselves when the registration process fails when applying them alone.

From these conclusions, the SURF-ORB combination is going to be employed for the geometrical calibration of the DoAP system. The best metrics are obtained with it when the registration fails on the object and a previously saved transformation from a reference sample is applied.

Chapter 5

Polarimetric calibration of the DoAP camera

5.1 Introduction

Polarization recovery needs specific calibration methods to get accurate polarization results. Initially, the sensor of the system only detects the intensity of the channels ($\vec{I}$), since it is not sensitive to polarization. When placing the polarization-sensitive components in front of the sensor, the detected intensity now depends on both the input polarization states ($\vec{S}_{in}$) and the measurement matrix ($\mathbf{A}$) of the polarization components in the sensor, following the equation:

$$\vec{I} = \mathbf{A} \cdot \vec{S}_{in} \tag{5.1}$$

Consequently, the intensity measurements ($\vec{I}$) together with their associated $\vec{S}_{in}$ reference polarization states (RPS) are the two basic ingredients to get the instrument matrix ($\mathbf{W}$) of a polarimetric system. This matrix $\mathbf{W}$ gathers the detector system's characteristics in polarization and transforms the input intensity signals into polarization states ($\vec{S}_{out}$) according to the following linear equation:

$$\vec{S}_{out} = \mathbf{W} \cdot \vec{I} \tag{5.2}$$

This instrument matrix $\mathbf{W}$ is calculated by means of a polarimetric calibration. It can be understood as the transfer function matrix of the DoAP system for converting the intensity into a polarization signal. It is influenced by two sets of RPS: the PSA states which compound the measurement matrix ($\mathbf{A}$) and the input polarized illumination set ($\vec{S}_{in}$) generated by the PSG for calibration, as depicted in Figure 5.1. Since the $\mathbf{W}$ matrix is not unique, it is important to study which RPS sets make it optimum to decrease the propagation uncertainties during the polarization recovery. The former analysis related to the PSA states has been already performed and explained in Chapter 3 (optimization of PSA states). The analysis of $\vec{S}_{in}$ set is performed during the calibration procedure and its results are presented in this chapter.

Several polarimetric calibration methods exist based on different physical approaches such as the Fourier transform, the least-square method, and the search for eigenvalues and singular values, as introduced in Chapter 2, Section 2.4.3. Depending on the system architecture, it is necessary to investigate the most appropriate method.

In this chapter, the different calibration methods implemented for the DoAP system are presented. The employed $\vec{S}_{in}$ during calibration will affect the final

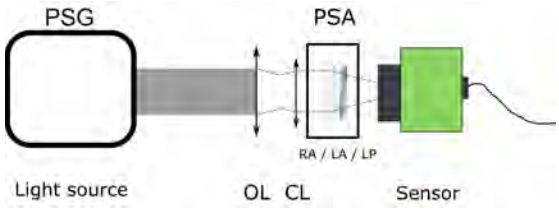

Figure 5.1: Scheme of a standard polarimetric calibration set-up using with the DoAPC. The PSA comprises the OL, RA, LA and LP and the sensor. The PSG contains the light source and the polarization optics necessary to generate the desired RPS.

result (**W**) so their optimization will improve the performance of the system in polarization recovery. For that reason, different sets of RPS were studied for a proper Stokes recovery besides the calibration methods implementation. Likewise to the PSA optimization, two main figures of merit for polarimeter optimization, the condition number (κ) and the equally weighted variance (EWV) are calculated and compared between the sets and the calibration methods.

Originally, the device was conceived as a white light 2D Stokes imaging polarimeter and the DRM calibration was applied. Despite being implemented for monochromatic punctual-detection Stokes polarimeters in past, we expand its application to broadband 2D polarimetric imaging. In addition, we study the influence of the RPS number (N) generated in the illumination during calibration. We conclude that performing the calibration using an illumination based on optimal states with N = 4 gives similar results to using N = 20, providing a faster procedure. This calibration let us recover the Stokes vectors of a scene with low errors.

After thinking about the possible functionalities of the device, Mueller Matrix imaging (MMI) arises as a promising field of application. For this reason, other calibration methods emerged as more suitable than the DRM for MMI. Their implementation started from the analysis in DRM which stated the optimal illumination RPS are the ones with N = 4. Unlike the DRM, the ECM needs to employ two samples in the procedure: an achromatic retarder, for preserving the broadband application, and an LP. In the ECM, the best sample combination was examined to be applied for optimal calibration of the DoAP system. The results show that this calibration works better for MMI applications than the DRM. Finally, a third calibration proposal is worthy of being implemented. The PCM uses a unique sample, an LP, and relies on the knowledge of the polarization model of the system to be calibrated. This allows having a cheaper calibration set-up because the retarder is discarded together with its possible chromatic aberrations. The calibration is performed using the optimal illumination RPS set and its results are compared with the two antecedent methods. In the case of the DoAP system, the DRM and the ECM have shown to be the most convenient calibrations for Stokes imaging and MMI applications, respectively.

5.2 Stokes imaging calibration

Stokes parameters and their related advanced parameters (DOP, DOLP, DOCP, LP) can be mapped using a polarization-sensitive sensor, in our case the DoAP system, and its intrinsic instrument matrix **W**, following Equation (5.2). The calibration method more suitable and faster for Stokes imaging polarimeters is the Data Reduction Method (DRM).

Data Reduction Matrix calibration

The DRM has been used for calibrating punctual Stokes polarimeters and, as already explained in Chapter 2, consists in finding the $\mathbf{W}_{DRM}$ matrix directly solving Equation (5.2) using the M intensities of the optimized input RPS $\vec{S}_{in}$ measured with the PSA basis of the DoAPC (N = 4) [20]. The Stokes vectors of these input RPS are already known $\vec{S}_{in}$ $(i = 0, 1, \ldots, M)$ and the only remaining parameter to be calculated is $\mathbf{W}_{DRM}$. From this, Equation (5.2) can be written in matrix form as:

$$\mathbf{S} = \mathbf{W}_{DRM} \cdot \mathbf{I} \tag{5.3}$$

where **S** is a 4 x M matrix, **I** is an NxM matrix and $\mathbf{W}_{DRM}$ has dimensions of 4 x N. The data reduction matrix W_{DRM} is determined by performing the right pseudo-inverse of **I**:

$$\mathbf{W}_{DRM} = \mathbf{S} \cdot \mathbf{I}^{+} = \mathbf{S} \cdot \mathbf{I}^{T} \cdot (\mathbf{I} \cdot \mathbf{I}^{T})^{-1} \tag{5.4}$$

The pseudoinverse of $\mathbf{I}^{+}$ requires calculating the matrix $(\mathbf{I} \cdot \mathbf{I}^{T})^{-1}$ that may not be well-conditioned and can lead to errors in the calculation of $\mathbf{W}_{DRM}$. A solution to this problem, as stated in [118], is to apply the singular value decomposition (SVD) method to obtain the pseudoinverse of **I**. Since the Stokes vector has four degrees of freedom, the range of solutions of **I** should have four dimensions, and thus, only four single values. They recommend using the truncated pseudoinverse by setting to zero all those single values smaller than the fourth major single value. They demonstrate that truncating the pseudoinverse involves a data reduction matrix more stable, optimized and less susceptible to errors. In addition to the truncated SVD, another strategy recommended for optimizing the estimation of the Stokes vector is the careful selection of both RPS sets. In this case, the ones used in the DRM calibration and the PSA basis of the DoAP.

Once the $\mathbf{W}_{DRM}$ matrix is calculated from the calibration, the system is prepared for recovering correctly the Stokes vectors of the images by solving the Equation (5.2) pixel-wisely.

DRM set-up

The DRM calibration set-up comprises the PSG and the DoAP system, as seen in Figure 5.2 (left). The PSG is compounded by a fixed high contrast LP (EO #47316) and two achromatic QWPs (AQWP10M-580) in the visible range (400 – 700 nm) placed in a rotating mounting. The PSA of the DoAP system is compounded by four fixed custom achromatic retarders in the visible range followed by a high contrast LP (EO #47316). The LPs are high-end polarizers in order to decrease the noise and improve filtering.

The calibrations are carried out in the broadband range of the visible spectrum. The light source illuminating the PSG provides white light coming from an integrating sphere to ensure a uniform and fully non-polarized illumination. The measurements are performed in dark conditions.

The DoAP system generates four different intensity images on the sensor surface for each input RPS as displayed in Figure 5.2 (right). This comes from the projection of the input RPS into the basis compound by the four polarization states of the fixed achromatic retarders of the PSA. The PSA basis is calculated and presented as optimum in Chapter 3. This configuration provides the minimum number of states in the PSA (N = 4) to recover the full Stokes vector from the intensities by operating the instrument matrix obtained during the calibration.

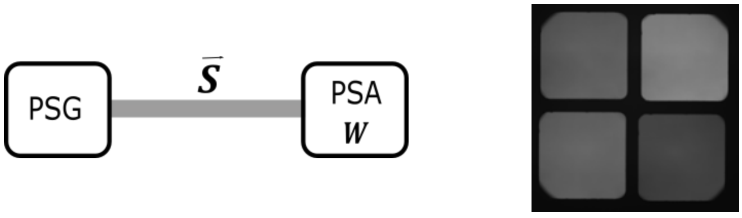

Figure 5.2: (Left) Scheme of the PSA system's calibration for the calculation of the instrument matrix $\mathbf{W}$ using DRM. The input RPS $\tilde{\mathbf{S}}$ are generated by the PSG. (Right) Intensity image of an input RPS acquired in a snapshot by the DoAP system. Each sub-aperture corresponds to a different optimal polarization state of the PSA (N=4).

Since the best possible calibration is required, several calibration cycles are performed using sets of different sizes N of RPS for the PSG. These RPS are separated into two groups, optimal configurations and non-optimal configurations, to analyse their influence on the resulting instrument matrix after applying the DRM algorithm. The optimal RPS sets are shown in Table 5.1 and the non-optimal sets are gathered in Table 5.2. The non-optimal sets have the same number of RPS to make a clear comparison.

Each RPS set of Table 5.1 corresponds to a spatial configuration that occupies the maximum volume inside the Poincaré sphere, coinciding with the platonic solids. They represent the optimum values for a set of N RPS. Figure 5.3 shows the associated Platonic solids for N = 4, 6, 8, and 20. On the contrary, the non-optimal RPS sets with $N = 4, 6, 8$ and 18 are gathered in Table 5.2. These

Configuration of RPS (N)	$(\theta_{LP}, \theta_{QWP1}, \theta_{QWP2})^o$
Tetrahedron I (N = 4)	$(0.0, \mp 64.66, \pm 58.18)$, $(0.0, \pm 70.86, \pm 47.18)$
Tetrahedron II (N = 4)	$(0.0, \pm 19.14, \pm 42.82)$, $(0.0, \pm 87.84, \pm 70.15)$
Octahedron (N = 6)	$(0.0, \pm 45.0, -20.0)$, $(0.0, \pm 45.0, +25)$, $(0.0, 0.0, \pm 45.0)$
Cube (N = 8)	$(0.0, \pm 45.0, \pm 22.0)$, $(0.0, \pm 45.0, \mp 22.0)$, $(0.0, \pm 12.6, \mp 45.0)$, $(0.0, \pm 12.7, \mp 45.0)$
Dodecahedron (N = 20)	Vertex of dodecahedron over a unitary sphere.

Table 5.1: List of the parameters to generate the optimal RPS sets with the PSG during the DRM. The polarization parameters of the PSG components are displayed in order: the azimuth angle of the LP (θ_{LP}), the first QWP (θ_{QWP1}) and the second QWP (θ_{QWP2}).

Configuration of RPS (N)	$(\theta_{\mathbf{LP}}, \theta_{\mathbf{QWP1}}, \theta_{\mathbf{QWP2}})^{\mathbf{o}}$
N = 4	$(0,0,0)$, $(0,0,70)$, $(0,0,120)$, $(0,0,140)$
N = 6	$(0,0,0)$, $(0,0,10)$, $(0,0,20)$, $(0,0,100)$, $(0,0,120)$, $(0,0,140)$
N = 8	$(0,0,10)$, $(0,0,30)$, $(0,0,50)$, $(0,0,70)$, $(0,0,90)$, $(0,0,110)$, $(0,0,130)$, $(0,0,150)$
N = 18	$(0,0,[0,180])$ (θ_{QWP2} rotates in steps of 10^o)

Table 5.2: List of the non-optimal RPS sets generated by the PSG during the DRM. The polarization parameters of the PSG components are displayed in order: the azimuth angle of the LP (θ_{LP}), the first QWP (θ_{QWP1}) and the second QWP (θ_{QWP2}).

configurations are represented over the Poincaré sphere and it is demonstrated that their volumes do not provide the maximum one, see Figure 5.4.

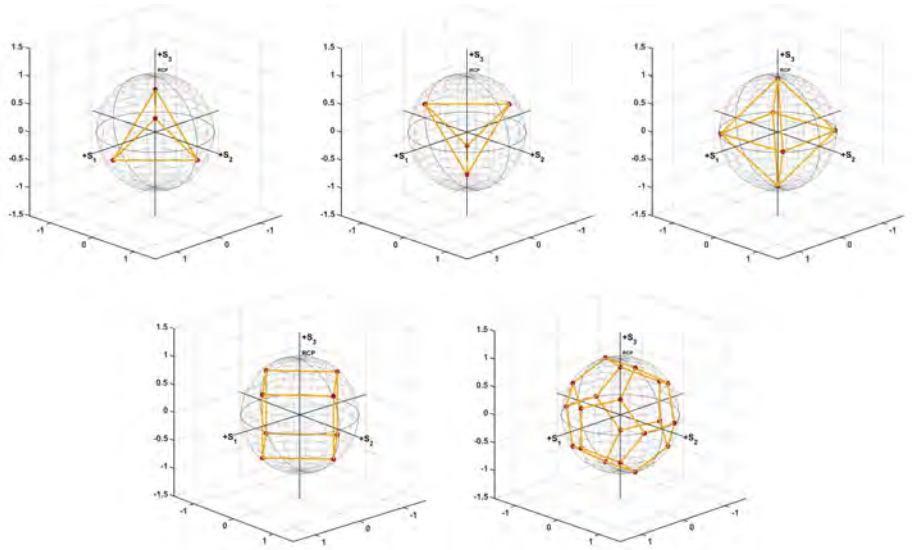

Figure 5.3: Spatial distribution of the optimal configurations of Table 5.1 over the Poincaré sphere. From left to right in increasing number of vertices: (up) tetrahedron I (N = 4), tetrahedron II (N = 4), octahedron (N = 6), (bottom) cube (N = 8) and dodecahedron (N = 20).

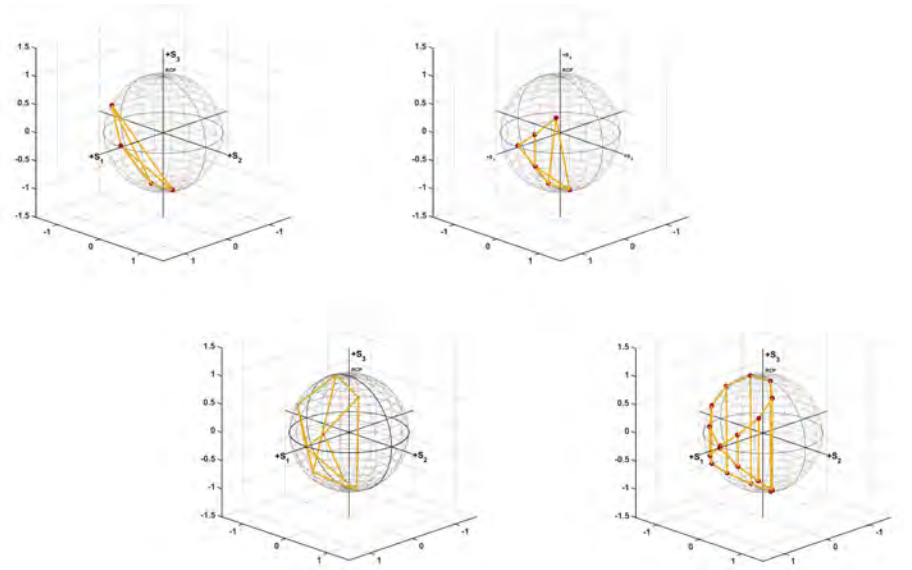

Figure 5.4: Spatial distribution of the non-optimal configurations of Table 5.2 over the Poincaré sphere. From left to right in increasing number of vertices: (up) N = 4, N = 6, (bottom) N = 8 and N = 18.

5.3 Mueller matrix imaging calibration

Retrieving the Mueller matrix of materials in a scene lets the complete knowledge of their polarization properties. Ellipsometry measures the complete Mueller matrix using monochromatic light and a punctual detector. In this thesis, the Mueller matrix is acquired by performing Mueller matrix imaging (MMI), which expands the previous work of the ellipsometry and acquires the Mueller matrix of a whole scene. This imaging technique provides the 4x4 matrix at each pixel of the 2D image taking advantage of the intensity array sensors and the knowledge acquired through the design of Stokes imaging polarimeters. To do so, the PSG matrix ($\mathbf{G}$) and the PSA matrix ($\mathbf{A}$) are needed to be calibrated. The Eigenvalue Calibration Method (ECM) and the Polarizer Calibration Method (PCM) are two methods of polarization calibration that let calibrate both matrices simultaneously.

Eigenvalue Calibration Method (ECM)

The ECM uses the matrix formalism for the global calibration of the set-up [119], which means calibrating together the PSG and the PSA. This approach is applied to Mueller polarimeters and, in this context, is also applied to calibrate the DoAP device. Recalling Equation (5.1), one could write the intensity measurement of the device, under the matrix formalism, as:

$$\mathbf{I} = \mathbf{A} \cdot \mathbf{M} \cdot \mathbf{G} \tag{5.5}$$

where $\mathbf{A}$ is the measurement matrix of the PSA, $\mathbf{G}$ is the transpose of the corresponding measurement matrix of the PSG (compound by the illumination RPS) and $\mathbf{M}$ is the Mueller matrix of the sample.

Unlike the DRM, ECM requires employing different calibrations samples consisting of suitable dichroic retarders for determining the $\mathbf{A}$ and $\mathbf{G}$ matrices. The essential steps of the procedure are described in the following.

Firstly, a measurement without any sample (air) giving the unitary matrix $\mathbf{B_0}$ is necessary:

$$\mathbf{B_0} = \mathbf{A} \cdot \mathbf{G} \tag{5.6}$$

Next measurements are performed using different samples (such as a linear polarizer, a quarter waveplate, etc.) yielding the intensity matrices $\mathbf{B_i}$:

$$\mathbf{B_i} = \mathbf{A} \cdot \mathbf{M_i} \cdot \mathbf{G}\ (i = 1, \ldots, n) \tag{5.7}$$

where n is the number of the known calibration samples in the set and $\mathbf{M_i}$ stands for the Mueller matrix for the ith calibration sample of the set whose azimuthal angle is ϕ_i:

$$\mathbf{M_i} = \mathbf{R}(-\phi_i) \cdot \mathbf{M_i}(\tau_i, \psi_i, \Delta_i) \cdot \mathbf{R}(\phi_i) \tag{5.8}$$

where $\mathbf{R}(\phi_i)$ is the rotation matrix by an angle ϕ_i about the z-axis and $\mathbf{M_i}(\tau_i, \psi_i, \Delta_i)$ refers to the Mueller matrix of a dichroic retarder in its principal axes.

From these measured data $\mathbf{B_i}$, the matrices $\mathbf{C_i}$ are calculated:

$$\mathbf{C_i} = \mathbf{B_0^{-1}B_i} = \mathbf{G^{-1}} \cdot \mathbf{M_i} \cdot \mathbf{G} \tag{5.9}$$

From the definition the matrices $\mathbf{C_i}$ maintain the same eigenvalues as $\mathbf{M_i}$:

$$\lambda_{R_1} = 2\tau_i \sin^2(\psi_i) \tag{5.10a}$$
$$\lambda_{R_2} = 2\tau_i \cos^2(\psi_i) \tag{5.10b}$$
$$\lambda_{C_1} = \tau_i \cos(2\psi_i) e_i^{-i\delta_i} \tag{5.10c}$$
$$\lambda_{C_2} = \tau_i \cos(2\psi_i) e_i^{i\delta_i} \tag{5.10d}$$

where ψ_i and Δ_i are the ellipsometric angles and τ_i refers to the transmission of the calibration sample i. These eigenvalues of$\mathbf{M_i}$ are independent of the orientation of the dichroic retarder. Thus, $\mathbf{C_i}$ provide the values of $(\tau_i, \psi_i, \Delta_i)$.

Then, $\mathbf{G}$ can be derived from the null space of the set of equations:

$$\mathbf{M_i G} - \mathbf{G C_i} = 0 \tag{5.11}$$

Vectorising the previous equation, it can be simplified to the following one:

$$\mathbf{H_i}\vec{G} = \vec{0} \tag{5.12}$$

where the error function $\mathbf{H_i} = \mathbf{I} \otimes \mathbf{M_i} - \mathbf{C_i}^T \otimes \mathbf{I}$ is a 16 real matrix, $\mathbf{I}$ is the identity matrix and $\vec{G}$ is a 16x1 linear vector. The $\mathbf{H_i}$ represents the experimental errors and it would be null if the system was ideal. This function can be built from the previously calculated $\mathbf{C_i}$ and the $\mathbf{M_i}$ derived from the parameters using the eigenvalues in Equation (5.10) (except the orientation of the dichroic retarder ϕ_i). The polarimetric characteristics of a Mueller matrix are the transmission (τ), the elliptical angle (ψ) and the retardance (Δ):

$$\tau = 0.5 \cdot (\lambda_{R_1} + \lambda_{R_2}) \tag{5.13a}$$
$$\psi = \arctan(\sqrt{\lambda_{R_1}/\lambda_{R_2}}) \tag{5.13b}$$
$$\Delta = \arg(\sqrt{\lambda_{C_1}/\lambda_{C_2}}) \tag{5.13c}$$

There are two different models for the Mueller matrix that can be employed in the ECM. The ideal method assumes that all the samples behave ideally. Therefore, the Mueller matrices for an LP and a QWP with horizontal optical axis are:

$$\mathbf{M}_{LP} = \frac{1}{2}\begin{pmatrix} 1 & 1 & 0 & 0 \\ 1 & 1 & 0 & 0 \\ 0 & 0 & 0 & 0 \\ 0 & 0 & 0 & 0 \end{pmatrix} \tag{5.14a}$$

$$\mathbf{M}_{QWP} = \begin{pmatrix} 1 & 0 & 0 & 0 \\ 0 & 1 & 0 & 0 \\ 0 & 0 & 0 & 1 \\ 0 & 0 & -1 & 0 \end{pmatrix} \tag{5.14b}$$

On the contrary, the general model of a Mueller matrix assumes that all samples follow the same matrix form of a dichroic retarder and introduces all the polarimetric characteristics, allowing having non-ideal polarizers or retarders. The Mueller matrix of a dichroic retarder with optical axis at 0^o is:

$$\mathbf{M}_{gen}(\tau,\Psi,\delta) = \tau \cdot \begin{pmatrix} 1 & -\cos 2\Psi & 0 & 0 \\ -\cos 2\Psi & 0 & 0 & 0 \\ 0 & 0 & \sin 2\Psi \cos\delta & \sin 2\Psi \sin\delta \\ 0 & 0 & -\sin 2\Psi \sin\delta & \sin 2\Psi \cos\delta \end{pmatrix} \tag{5.15}$$

where τ is the transmission coefficient, Ψ and Δ correspond to the ellipsometric angles related to the Fresnel coefficients. The Mueller matrices of the previous samples at different angles of the optical axis should be rotated by applying the rotational change of the basis matrix $\mathbf{R}(\phi)$.

$$\mathbf{M}_{final} = \mathbf{R}(\phi)\mathbf{M}\mathbf{R}(-\phi) \tag{5.16a}$$

$$\mathbf{R}_M(\phi) = \begin{pmatrix} 1 & 0 & 0 & 0 \\ 0 & \cos(\phi) & -\sin(2\phi) & 0 \\ 0 & \sin(\phi) & \cos(2\phi) & 0 \\ 0 & 0 & 0 & 1 \end{pmatrix} \tag{5.16b}$$

The solution to the overdetermined linear system Equation (5.12) is obtained by the least-square method:

$$\mathbf{K}(\vec{\phi})\vec{G} = \vec{0} \tag{5.17}$$

where $\mathbf{K}(\vec{\phi}) = \sum_{i=1}^{n} \mathbf{H_i^T}(\vec{\phi})\mathbf{H_i}(\vec{\phi})$. $\mathbf{K}$ depends on the azimuth angle of each sample of the set $\vec{\phi} = (\phi_1, \cdots, \phi_i, \cdots, \phi_n)$. In addition, it is a positive symmetric real matrix, and thus, it is diagonalizable. Since Equation (5.17) can never be exactly solved due to the limitation in experimental precision of $\mathbf{C_i}$, the eigenvalues $(\lambda_1(\vec{\phi}), \cdots, \lambda_{16}(\vec{\phi}))$ of $\mathbf{K}(\vec{\phi})$ are all different from zero except the smallest one, λ_{16}, which should be null although it is close to zero in measurements. The solution vector $\vec{G}$ is the eigenvector of $\mathbf{K}(\vec{\phi})$ associated with this null eigenvalue $\lambda_{16}(\vec{\phi})$.

The optimum $\vec{G}$ is finally derived when calculating the remaining parameter of the sample set, the azimuthal angle $\vec{\phi}$. It can be retrieved from matrix $\mathbf{K}(\vec{\phi})$ by optimising the azimuthal angle ϕ_i of each $\mathbf{M_i}$ matrix, which verifies the condition:

$$\frac{\lambda_{16}(\vec{\phi})}{\lambda_{15}(\vec{\phi})} \to 0 \tag{5.18}$$

Finally, $\vec{G}$ is written back as a square 4 x 4 matrix $\mathbf{G}$ and $\mathbf{A}$ matrix is obtained directly solving Equation (5.6):

$$\mathbf{A} = \mathbf{B_0}\mathbf{G^{-1}} \tag{5.19}$$

To perform the Stokes vector recovery, the instrument matrix $\mathbf{W}_{ECM}$ is calculated as the inverse of $\mathbf{A}$ and introduced in Equation (5.2). Otherwise, the Mueller matrix can be calculated through Equation (5.5). The conditioning of $\mathbf{K}$ is affected by $\mathbf{A}$ and $\mathbf{G}$, and the calibration can be less accurate if these matrices are ill-conditioned from the beginning. Therefore, we performed a previous study to choose the desired RPS sets.

Polarizer Calibration Method (PCM)

Finally, a third calibration method has been tested for the DoAP device, the PCM. It is a variation of the former explained ECM where only a linear polarizer sample is used instead. The retarder is avoided to speed up the calibration process, get rid of its associated errors such as chromaticity or misalignment and obtain a more affordable set-up.

The complete recovery of the calibration matrix is achieved under the following assumption: the polarization states are totally polarized, that is the device does not depolarize [120].

The present Mueller matrix along the calibration corresponds to an LP. The Mueller matrix of the LP ($\mathbf{P}$) can be represented as the multiplication of projectors ($\vec{p}$), where α stands for the azimuth angle of the principal axis of the polarizer:

$$\mathbf{P} = \frac{1}{2}\vec{p}\cdot\vec{p}^{T}\begin{pmatrix}1\\ \cos\alpha\\ \sin\alpha\\ 0\end{pmatrix}\cdot(1\ \cos\alpha\ \sin\alpha\ 0) \tag{5.20}$$

Hence, the intensity matrix $\mathbf{B}$ can be rewritten following this projectors notation:

$$\mathbf{B} = \frac{1}{2}\vec{b}\cdot\vec{c}^{T} \tag{5.21}$$

where $\vec{b}$ and $\vec{c}$ are known vectors and can be acquired from the columns and rows of $\mathbf{A}$ and $\mathbf{G}$ together with $\vec{p}$, respectively.

To calculate this decomposition, the two symmetric matrices $\mathbf{BB^T}$ and $\mathbf{B^TB}$ must be computed to identify $\vec{b}$ and $\vec{c}$, sequentially. These matrices are projectors and, thus, each one has a unique non-vanishing eigenvalue. These vectors coincide with the eigenvector associated with the largest eigenvalue of the corresponding matrix.

Vectorising the matrices of the PSG and the PSA derives the following linear systems:

$$\begin{pmatrix}c^{(2)}\vec{p}^{T}-c^{(1)}\vec{p}^{T}\vec{0}^{T}\vec{0}^{T}\\ \vec{0}^{T}c^{(3)}\vec{p}^{T}-c^{(2)}\vec{p}^{T}\vec{0}^{T}\\ \vec{0}^{T}\vec{0}^{T}c^{(4)}\vec{p}^{T}-c^{(3)}\vec{p}^{T}\end{pmatrix}\begin{pmatrix}\vec{g}_1\\ \vec{g}_2\\ \vec{g}_3\\ \vec{g}_4\end{pmatrix}=\mathbf{P}_{\tilde{\mathbf{c}}}\vec{g} \tag{5.22a}$$

$$\begin{pmatrix}b^{(2)}\vec{p}^{T}-b^{(1)}\vec{p}^{T}\vec{0}^{T}\vec{0}^{T}\\ \vec{0}^{T}b^{(3)}\vec{p}^{T}-b^{(2)}\vec{p}^{T}\vec{0}^{T}\\ \vec{0}^{T}\vec{0}^{T}b^{(4)}\vec{p}^{T}-b^{(3)}\vec{p}^{T}\end{pmatrix}\begin{pmatrix}\vec{a}_1\\ \vec{a}_2\\ \vec{a}_3\\ \vec{a}_4\end{pmatrix}=\mathbf{P}_{\tilde{\mathbf{b}}}\vec{a} \tag{5.22b}$$

Where the null vector is $\vec{0}^{T}=(0,0,0,0)^{T}$ and $u^{((j))}$ notation stands for the jth component of the vector $\vec{u}$. In this case, $\vec{g}$ is a 16-component vector from vectorising $\mathbf{G}$ and equally $\vec{g}$ from $\mathbf{A}^{T}$. The resulting matrices $\mathbf{P}_{\tilde{\mathbf{c}}}$ and $\mathbf{P}_{\tilde{\mathbf{b}}}$ have a dimension of 3x16. It is worth mentioning that the following decomposition assumes the PSG and the PSA of the system generate and measure the minimum necessary number of RPS (n=4).

These linear systems Equation (5.22) must be completely overdetermined by stacking the different n calibration measurements ($\mathbf{P}_{\tilde{\mathbf{c}}}$ and $\mathbf{P}_{\tilde{\mathbf{b}}}$) by rotating

the linear polarizer to n azimuth angles α_i, resulting $3nx16$ linear homogeneous equations:

$$\begin{pmatrix} \mathbf{P}_{\tilde{\mathbf{c}}^{(1)}} \\ \mathbf{P}_{\tilde{\mathbf{c}}^{(2)}} \\ \cdots \\ \mathbf{P}_{\tilde{\mathbf{c}}^{(n)}} \end{pmatrix} \vec{g} = \mathbf{P}_{\mathbf{n}\tilde{\mathbf{c}}}\vec{g} = \vec{0} \qquad (5.23a) \qquad \begin{pmatrix} \mathbf{P}_{\tilde{\mathbf{b}}^{(1)}} \\ \mathbf{P}_{\tilde{\mathbf{b}}^{(2)}} \\ \cdots \\ \mathbf{P}_{\tilde{\mathbf{b}}^{(n)}} \end{pmatrix} \vec{a} = \mathbf{P}_{\mathbf{n}\tilde{\mathbf{b}}}\vec{a} = \vec{0} \qquad (5.23b)$$

Since there is no retarder sample in the calibration set that could provide the circular polarization component, the 4jth columns of the previous stacked matrices ($\mathbf{P}_{\mathbf{n}\tilde{\mathbf{c}}}$ and $\mathbf{P}_{\mathbf{n}\tilde{\mathbf{b}}}$) must be removed ($\mathbf{P}_{\mathbf{n}\tilde{\mathbf{c}}}{}^{r}$ and $\mathbf{P}_{\mathbf{n}\tilde{\mathbf{b}}}{}^{r}$). The remaining system can be solved by determining the reduced vectors ($\vec{g}^{r}$) and ($\vec{a}^{r}$) corresponding to the eigenvectors of the smallest eigenvalue of the matrices $\mathbf{P}_{\mathbf{n}\tilde{\mathbf{c}}}{}^{rT}\mathbf{P}_{\mathbf{n}\tilde{\mathbf{c}}}{}^{r}$ and $\mathbf{P}_{\mathbf{n}\tilde{\mathbf{b}}}{}^{rT}\mathbf{P}_{\mathbf{n}\tilde{\mathbf{b}}}{}^{r}$, respectively. As consequence, 12 out of 16 components of the vectors are recovered from the reduced systems.

The 4jth components of the vectors $\vec{g}$ and $\vec{a}$ can be recovered because the Stokes vectors comprising the PSG and the PSA matrices are assumed to be totally polarized. The circular-related component is calculated by using the relation between fully-polarized Stokes components.

$$g_{4j} = \epsilon_G^{(j)} \sqrt{(g_{4j-3}^2 - g_{4j-2}^2 - g_{4j-1}^2} \qquad (5.24a)$$

$$a_{4j} = \epsilon_A^{(j)} \sqrt{(a_{4j-3}^2 - a_{4j-2}^2 - a_{4j-1}^2} \qquad (5.24b)$$

where $\epsilon_{G/A}^{(j)} = \pm 1$ and $j = 1, 2, 3, 4$. The signs of $\epsilon_(G/A)^{(j)}$ are adjusted accordingly to the Mueller matrix model of the system.

To conclude, the $\mathbf{G}$ and $\mathbf{A}$ matrices can be recovered by reorganizing the $\vec{g}$ and $\vec{a}$ vectors in matrix notation. It has to be noted that one of the matrices must be rescaled so that Equation (5.5) is fulfilled. Likewise in ECM, the instrument matrix $\mathbf{W}_{PCM}$ comes from the inverse of $\mathbf{A}$, the Stokes vector is recovered from Equation (5.2) and the Mueller matrix can be calculated by solving Equation (5.5).

Set-up for ECM and PCM

The ECM and the PCM require the same materials for illumination as the DRM: broadband white light, an integrating sphere, and dark environment conditions. The calibration is also performed through direct transmission. The main difference in the setup resides in the introduction of samples in the optical path of the PSG and the DoAP system, as shown in Fig. Figure 5.5.

It can be noticed that the first measurement of the ECM ($\mathbf{B}_0$) consists of doing a DRM with the desired $\mathbf{G}$ matrix. Afterwards, the samples are introduced to the optical path. Each sample comes from one of these groups: a dichroic sample or a retarder sample. In specific, an LP (Thorlabs WP25M-VIS)) and an achromatic QWP (Thorlabs AQWP10M-580)) are employed in the ECM.

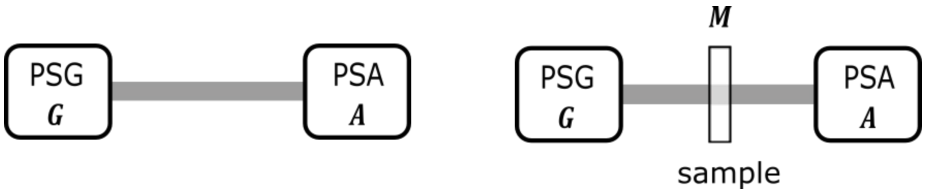

Figure 5.5: (Left) Direct transmission measurement through the air. (Right) Direct transmission measurement with a sample with Mueller matrix **M**. For the ECM, the samples are an LP and an achromatic QWP. For the PCM, only an LP is necessary.

Although the samples needn't be ideal, the LP is a high-contrast polarizer to reduce noise as has been done in the PSG design.

For the ECM experiment, the best configuration for PSG with N = 4 of Table 5.1 is chosen for illumination since the ECM is applied for calibrating Mueller polarimeters and a fast calibration is desired. Based on the theory, using N = 4 already provides the minimum number of RPS to obtain the calibration matrix. Besides, tetrahedron I (ThI) and tetrahedron II (ThII) are optimal configurations for having good conditioning in the **G** matrix, as confirmed in DRM results. The ECM requires at least two measurements from the LP and one measurement with the QWP. From the literature, some theoretical studies have been performed regarding the optimization of the polarization parameters of the samples to achieve a good calibration result. The optimum azimuths for the LP are the pairs $\theta_{LP} = (0^o, 90^o), (+45^o, -45^o)$ and for the retarder the angles $\theta_{QWP} = 30^o$ and 90^o, under the constraint the retarder is a QWP ($\delta = 90^o$) [119]. In the experiment, the possible combinations between them, listed in Table 5.3, are studied to select the best combination for an optimum calibration result.

Sample sets	$(\theta_{LP}, \theta_{LP}, \theta_{QWP})/^o$
Set I	$(0, 90, 30)$
Set II	$(0, 90, 90)$
Set III	$(+45, -45, 30)$
Set IV	$(+45, -45, 90)$

Table 5.3: List of the combinations of the samples for the ECM.

For the PCM, the set-up is maintained from the ECM (Figure 5.5) but the QWP sample is dismissed. The LP sample is the only sample and each measurement corresponds to a different α_i. The LP is the high-end polarizer to reduce the measured noise intensity signal by improving filtering. In this case, two sets are generated varying the number of azimuth positions, see Table 5.4. Just like in the ECM, the PSG generates the optimal tetrahedron configuration for simplification of the calibration process and comparison of its performance.

Aside from the DoAP device, an interesting contribution of this thesis in

LP azimuth sets	$(\theta_{LP})/^o$
Set I (N = 4)	$(0, 30, 60, 90)$
Set II (N = 6)	$(0, 30, +45, 60, -45)$

Table 5.4: List of the azimuth angle positions of the LP during the PCM.

the calibration procedure is to tune the PCM through the implementation of the polarization model of our PSA. As explained in Section 5.3, the $4jth$ components of **G** and **A** matrices come from applying the operations described in Equation (5.24a) and Equation (5.24b) together with the polarization model of the system. Since the model was already computed, for optimization purposes of the studies presented in Chapter 3, the verification of the correct recovery of these components are done using this polarization model, explained in Section 3.2. The signs of the components were correctly implemented and the relationships inside the matrix were properly maintained.

5.4 Calibration results

The calibration results from the described methods are presented and discussed in the following subsections. The acquisition conditions of the images are maintained for the three methods. The intensity images have a dynamic range of 12 bits and their size is 3500 x 3500 pixels. The sensor was set to 120 ms of time exposition and the number of repetitions for each generated input RPS is 200 images.

5.4.1 Stokes imaging calibration

The DRM is performed following the algorithm and employing the set-up described in Section 5.2. Concurrently, the influence of having more available states in the PSG in the final results is analyzed. The aim is to find the ideal number of RPS that allows a fast and simple calibration, as well as, a good recovery of the Stokes parameters.

The optimal sets of RPS, gathered in Table 5.1, were implemented for performing the calibration. The experimental PSA matrix $\mathbf{W}_{PSA}$ is directly measured through the Stokes vector of each configuration in the PSA. It corresponds to the ideal instrument matrix $\mathbf{W_{PSA}}$ which equals the minimum theoretical condition number $\kappa(\mathbf{W_{PSA}}) = 1.73$.

To compare the configurations, the condition number $\kappa(\mathbf{W_{DRM}})$, the associated theoretical and the experimental EWV of $\mathbf{W_{DRM}}$ were calculated. These figures of merit were employed to find the optimum RPS for the PSA, see Section 2.2.3. Just to remind, the minimization of $\kappa(\mathbf{W_{DRM}})$ maximizes system stability and lowers noise propagation for the recovery of the Stokes vector. On the other hand, the EWV shows the estimation of the global error amplification in the solution vector $\vec{S}$ from the noisy intensity measurement vector $\vec{I}$.

These figures of merit are collected in Table 5.5. The theoretical EWV is obtained by means of Equation (2.30) using the corresponding $\mathbf{W_{DRM}}$ matrix and assuming the $\sigma_G = 1.0$. The experimental EWV is calculated following the definition of EWV by summing up all the Stokes parameters variances ($\delta(S_i)^2$) from the recovery process of an incident polarization state. Additionally, the condition number of the matrix compound by the RPS of the PSG ($\mathbf{S_{PSG}}$) is given if this parameter can affect the obtained calibration matrix.

Configuration of RPS (N)	$\kappa(\mathbf{W_{DRM}})$	$\mathbf{EWV_{th}}$	$\mathbf{EWV_{exp}}$	$\kappa(\mathbf{S_{PSG}})$
Th I (N = 4)	5.12	36.91	0.099	1.77
Th II (N = 4)	5.07	36.42	0.098	1.74
Octahedron (N = 6)	4.46	32.91	0.1	1.71
Cube (N = 8)	4.75	33.94	0.1	1.77
Dodecahedron (N = 20)	4.78	34.11	0.1	1.74
Theoretical	1.73	[10.0, 6.7, 5.0, 2.0]	-	1.73

Table 5.5: List of the figures of merit ($\kappa(\mathbf{W_{DRM}})$, EWV_{th}, EWV_{exp}, $\kappa(S_{PSG})$) for the analysis of the obtained $\mathbf{W_{DRM}}$ for optimal configurations of the RPS generated by the PSG in the DRM.

It can be appreciated that the $\kappa(\mathbf{W_{DRM}})$ does not strongly depend on the number of RPS used in the calibration. Since the $\mathbf{W_{DRM}}$ is the inverse of the PSA matrix, the results agree with the fact the PSA of the DoAPC remains constant throughout the different calibration cycles. The theoretical EWV shows a decreasing tendency for error propagation from the intensity measurements when having more RPS available. Although the magnitudes are very similar, an increase in experimental errors in the generation of the RPS is appreciated which can be due to alignment errors when generating more states (N=20). The experimental EWV seems to be equal under the different illumination sets. From the EWV results, we can conclude that the contribution of using a higher number of RPS does not add enough advantages over higher time spent on the calibration.

The same study is done for non-optimal RPS, see Table 5.6. The obtained calibration matrices have slightly higher condition numbers $\mathbf{W_{DRM}}$ than the optimal cases. The theoretical EWV parameter with the same intensity signal variance as before is not improved by having more states in illumination. Neither there is no variation in the experimental EWV. This means the calibration matrix seems to be not affected by the disposition of the RPS of the PSG.

Recovery of the Stokes vector

Once the analysis of the instrument matrix $\mathbf{W_{DRM}}$ is done, the Stokes vector recovery results are shown. The experiment consists in illuminating an LP sample and recovering the Stokes vector pixel-wisely.

Configuration of RPS (N)	$\kappa(\mathbf{W_{DRM}})$	$\mathbf{EWV_{th}}$	$\mathbf{EWV_{exp}}$	$\kappa(\mathbf{S_{PSG}})$
N = 4	5.69	34.89	0.099	10.71
N = 6	5.41	34.91	0.1	7.12
N = 8	5.20	36.57	0.1	3.64
N = 20	5.22	36.59	0.1	3.65
Theoretical	1.73	[10.0, 6.7, 5.0, 2.0]	-	1.73

Table 5.6: List of the figures of merit ($\kappa(\mathbf{W_{DRM}})$, EWV_{th}, EWV_{exp}, $\kappa(S_{PSG})$) for the analysis of the obtained $\mathbf{W_{DRM}}$ for non-optimal RPS sets generated by the PSG in the DRM.

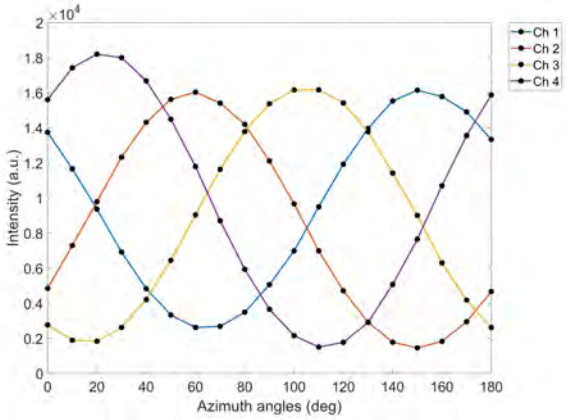

Figure 5.6: Average measured intensity from an LP rotated from 0^o to 180^o in steps of 10^o in each of the four channels of the PSA.

In order to evaluate the ability of the system of working as a Stokes polarimeter, an LP is rotated from 0^o to 180^o in steps of 10^o for its polarization recovery. The sample is illuminated with the same white light source and the same camera settings for the acquisition as in the calibration process. The average Stokes vector together with the parameters DOLP, DOCP and AOLP are recovered by testing the different obtained calibration matrices from the intensity measurement of Figure 5.6. Figure 5.7 shows the Stokes vector averaged over the central region, marked in the maps of Figure 5.8, for each channel of the PSA. For the sake of brevity, only the Stokes curve of the best configuration is displayed. The errors and variances of the optimal configurations are gathered in Table 5.7. The best instrument matrix ($\mathbf{W_{DRM}}$) stands for the ThI configuration. It can be appreciated in Figure 5.7 that the maximum error in the Stokes parameters is around the 0.05 upper limit. The DOLP error is below the 0.01 error, meanwhile, the DOCP shows a residual three times higher than the linear counterpart. The AOLP error is close to 1.5^o, which provides good confidence in the results and

its variance is 7.00^o, as presented in Table 5.7. Some general comments are addressed for the other configuration errors shown in Table 5.7. The maximum error in the Stokes parameters is lower than the 0.05 limit except in the Octagon configuration for the circular parameter. The errors for the rest of the parameters are similar to the ones in ThI. Regarding the variances, they are almost negligible except for the case of the AOLP parameter where the variance range is 7^o. It can be concluded that using the minimum number of polarization states in illumination provides similar results in the final matrix than a higher number of RPS, as well as, a more agile calibration process.

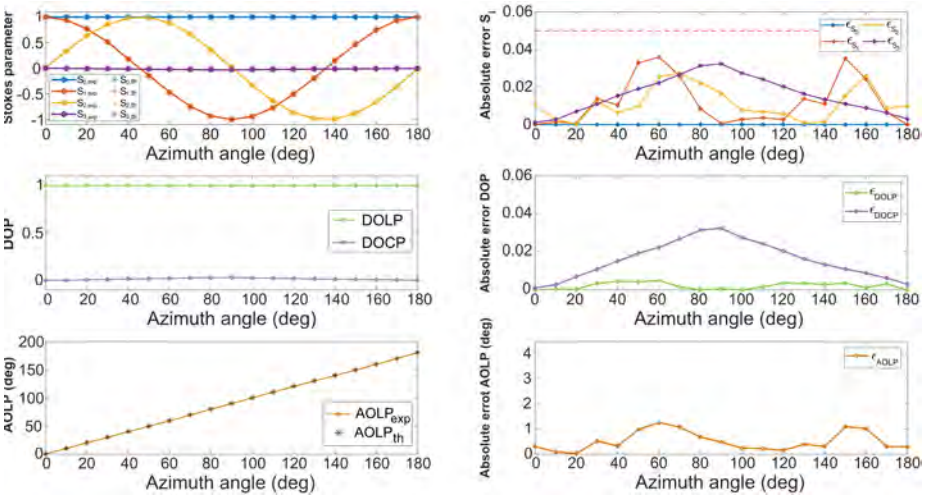

Figure 5.7: (Left) Average recovered Stokes vector, DOLP, DOCP and AOLP corresponding to a rotation of an LP between $[0, 180]^o$ using the ThI configuration. (Right) Related errors of the previous parameters.

RPS sets	ϵ_{S_1}	ϵ_{S_2}	ϵ_{S_3}	$\epsilon_{DOLP,DOCP}$	ϵ_{AOLP}	δ_{S_1}	δ_{S_2}	δ_{S_3}	$\delta_{DOLP,DOCP}$	δ_{AOLP}
Th I	**0.036**	**0.026**	**0.032**	**5e-3, 0.032**	**1.26°**	**4.4e-3**	**4.9e-3**	**6.1e-3**	**1.2e-5, 0.002**	**7.66°**
Th II	0.036	0.060	0.028	5e-3, 0.028	1.84°	4.1e-3	4.4e-3	5.9e-3	1.1e-5, 0.0019	7.00°
Octahedron	0.036	0.020	0.093	7e-3, 0.093	1.09°	3.8e-3	4.9e-3	9.4e-3	6.25e-6, 0.0045	7.21°
Cube	0.045	0.047	0.033	5e-3, 0.033	1.61°	4.2e-3	4.7e-3	7.9e-3	3.49e-5, 0.0034	7.37°
Dodecahedron	0.035	0.042	0.024	5e-3, 0.024	1.24°	4.2e-3	4.7e-3	7.5e-3	2.37e-5, 0.0028	7.37°

Table 5.7: Maximum errors and standard deviations of the Stokes parameters S_1, S_2, S_3, and the advanced parameters DOLP, DOCP, and AOLP during the recovery of an LP rotated from 0^o to 180^o in steps of 10^o using the $\mathbf{W_{DRM}}$ of optimal RPS in the PSG.

In a parallel analysis, the results of the recovery applying the calibration

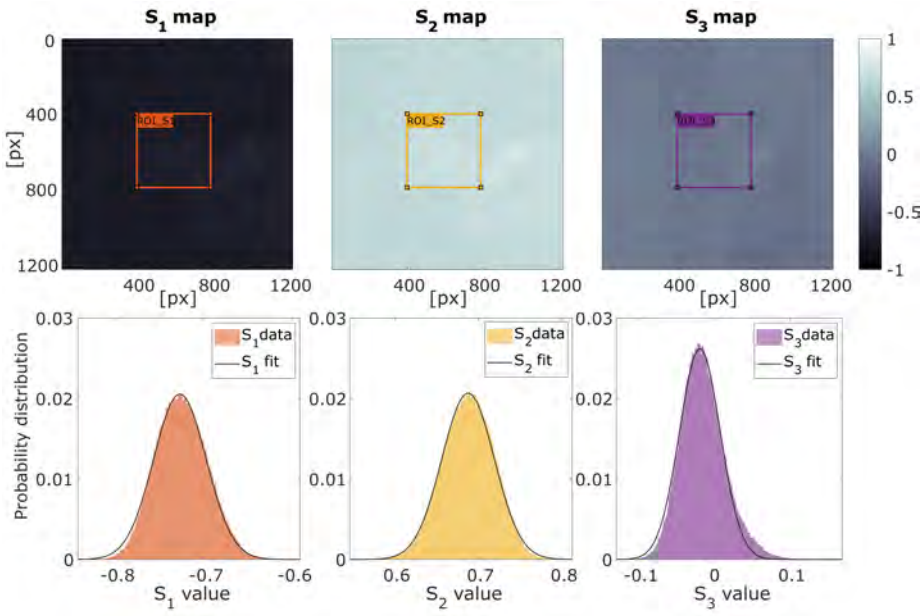

Figure 5.8: (Top) Recovered maps of the Stokes vector parameters corresponding to an LP with an axis at 70^o using the ThI configuration. (Bottom) Related histograms over the central region of the previous parameters.

matrices from non-optimal RPS are discussed. In order to compare them with the previous results, the non-optimal configuration with N = 4 is displayed in Figure 5.9. The condition numbers of the resulting matrices are very similar to the previous ones. However, looking at the Stokes recovery in Figure 5.9, the behaviours are very distant. The Stokes errors are far from the 0.05 limit and the DOCP is affected. The maximum AOLP error is 10^o, which indicated very low confidence in the recovery results. Nevertheless, the variances show similar behaviour as in the optimal configurations.

General comments for the results of non-optimal configurations are derived from the errors shown in Table 5.8. When increasing the number of RPS, the magnitude of all errors decreases and the variances show no change. However, the configuration with the largest number of RPS N = 18 still exhibits two times bigger errors than the optimal configuration of ThI with N = 4. This leads to conclude that the illumination RPS should be chosen wisely, so as to reduce the effect of error propagation in the recovery of the Stokes vectors.

Final recovery of the Stokes vector

Once the calibration for Stokes vectors recovery was finished, a new set-up was designed for measuring the Mueller matrix from these calibration results. The white light was changed by an array of custom white LEDs collimated and matching the entrance aperture of the PSG to have a more compact illumination

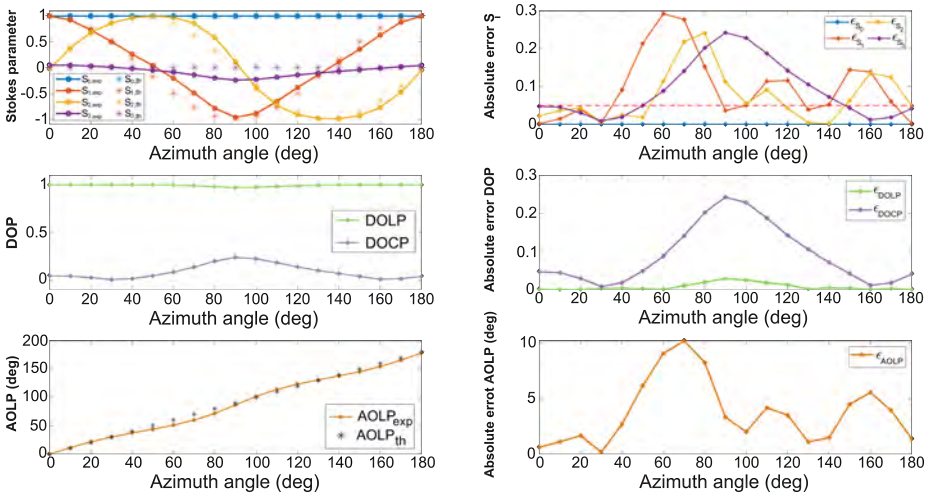

Figure 5.9: (Left) Average recovered Stokes vector, DOLP, DOCP and AOLP corresponding to a rotation of an LP between $[0, 180]^o$ using the N = 4 non-optimal configuration. (Right) Related errors of the previous parameters.

RPS sets	ϵ_{S_1}	ϵ_{S_2}	ϵ_{S_3}	$\epsilon_{DOLP,DOCP}$	ϵ_{AOLP}	δ_{S_1}	δ_{S_2}	δ_{S_3}	$\delta_{DOLP,DOCP}$	δ_{AOLP}
N = 4	0.293	0.242	0.242	3e-2, 0.242	10.21°	6.6e-3	2.1e-3	7e-3	6.6e-5, 0.0046	7.28°
N = 6	0.149	0.111	0.216	2.4e-2, 0.216	4.48°	6.5e-3	4.8e-3	6.8e-3	7.7e-5, 0.005	9.14°
N = 8	0.072	0.064	0.023	5e-3, 0.023	2.53°	4.8e-3	4.4e-3	8.2e-3	3.25e-5, 0.0034	7.63°
N = 18	**0.078**	**0.071**	**0.029**	**5e-3, 0.029**	**2.76°**	**4.9e-3**	**4.4e-3**	**8.4e-3**	**2.87e-5, 0.0031**	**7.65°**

Table 5.8: Maximum errors and standard deviations of the Stokes parameters S_1, S_2, S_3, and the advanced parameters DOLP, DOCP, and AOLP during the recovery of an LP rotated from [0, 180]^o in steps of 10^o using the $\mathbf{W_{DRM}}$ of non-optimal RPS in the PSG.

system. New calibrations were done using the optimal states with N = 4 (ThI and ThII configurations) to see the influence of the new illumination system. The results shown to were significant changes in the calibration matrices, improving the previous figures of merit. Therefore, the new results are presented and the next calibration method were performed using this new illumination set-up.

The figures of merit regarding the new $\mathbf{W_{DRM}}$ matrices for ThI and ThII configurations are displayed in Table 5.9. Here, the condition numbers of both matrices are closer to the theoretical one than the former calibration. Since the EWV is related to the $\kappa(\mathbf{W_{DRM}})$, it is also reduced to nearly the ideal value. The generated RPS by the PSG are the same as in the previous analysis demonstrating the PSG generates good polarization states. The major difference between results stands for the value disposition in the matrix. They come from

the inversion of the **I** matrix, as seen in Equation (5.4). Their values maintain the same trend but an offset is observed when comparing the measurements of both illuminations. The prior measurement shows an intensity offset indicating a non-desired unpolarized light was being introduced into the system during calibration.

Configuration of RPS (N)	$\kappa(\mathbf{W_{DRM}})$	$\mathbf{EWV_{th}}$	$\mathbf{EWV_{exp}}$	$\kappa(\mathbf{S_{PSG}})$
Th I (N = 4)	2.07	10.71	0.0944	1.77
Th II (N = 4)	2.14	10.97	0.0953	1.74
Theoretical	1.73	10.0	-	1.73

Table 5.9: List of the figures of merit ($\kappa(\mathbf{W_{DRM}})$, EWV_{th}, EWV_{exp}, $\kappa(S_{PSG})$) for the analysis of the obtained $\mathbf{W_{DRM}}$ for the optimal configurations with N = 4 generated by the PSG during the DRM calibration with the new set-up.

Despite the differences in the figures of merit, the Stokes results were recovered with the same accuracy as in the former analysis. Hence, the pieces of evidence extracted during the study of the optimal number of RPS in illumination and the study of influence under optimal or non-optimal RPS in the PSG are considered equally legitimate. The Stokes curves and the advanced parameters are shown in Figure 5.10. for ThII configuration. Figure 5.11 show the Stokes maps for the specific state of an LP at 70^o. It can be seen in the histograms that there is no longer the skewness in the distributions being gaussian.

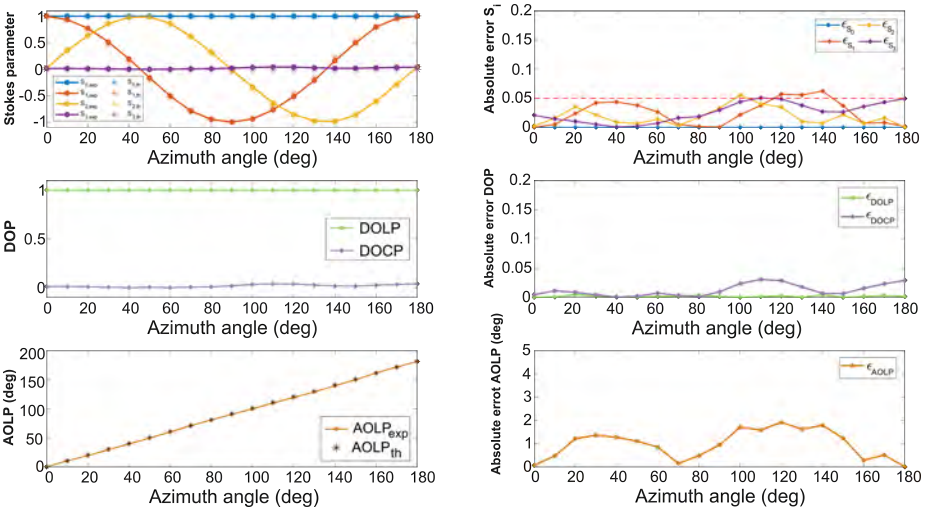

Figure 5.10: (Left) Average recovered Stokes vector, DOLP, DOCP and AOLP corresponding to a rotation of an LP between $[0, 180]^o$ using ThII configuration. (Right) Related errors of the previous parameters.

Table 5.10 gathers the maximum errors in the recovery of both configurations together with the variances. ThI shows higher errors in parameters and a lower

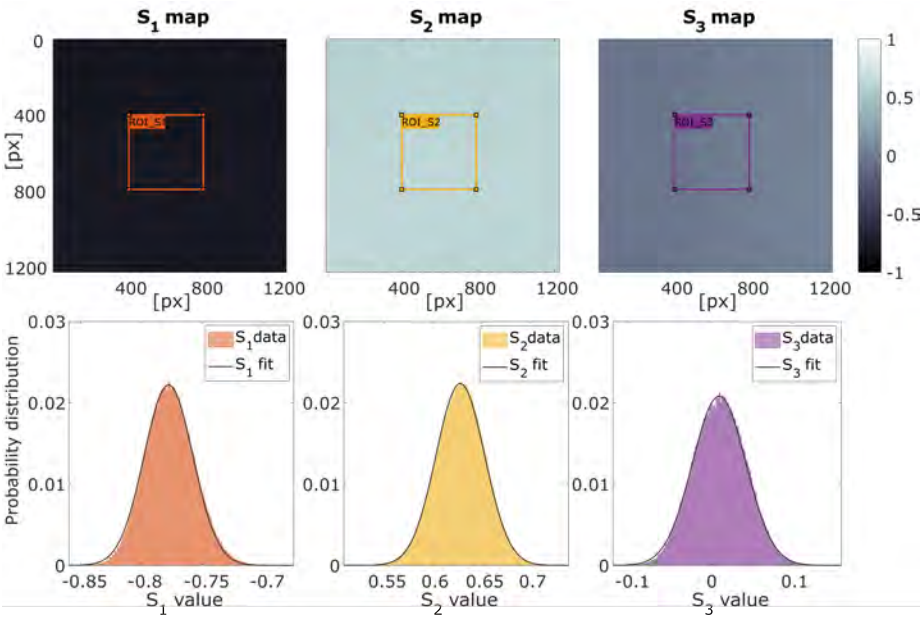

Figure 5.11: (Top) Recovered maps of the Stokes vector parameters corresponding to an LP with an axis at 70^o using the ThII configuration. (Bottom) Related histograms over the central region of the previous parameters.

RPS sets	ϵ_{S_1}	ϵ_{S_2}	ϵ_{S_3}	$\epsilon_{DOLP,DOCP}$	ϵ_{AOLP}	δ_{S_1}	δ_{S_2}	δ_{S_3}	$\delta_{DOLP,DOC}$	δ_{AOLP}
Th I	0.050	0.068	0.067	7e-3, 6.7e-2	1.95º	2.4e-3	3.4e-3	4.7e-3	1.72e-5, 2.4e-3	4.87º
Th II	**0.055**	**0.062**	**0.050**	**4e-3, 0.038**	**1.91º**	**2.3e-3**	**3.7e-3**	**5.4e-3**	**9.73e-6, 1.8e-3**	**4.96º**

Table 5.10: Maximum errors and standard deviations of the Stokes parameters S_1, S_2, S_3, and the advanced parameters DOLP, DOCP, and AOLP during the recovery of an LP rotated from 0^o to 180^o in steps of 10^o using the $\mathbf{W_{DRM}}$ of the optimal RPS with N = 4 in the PSG.

variance in the maps. ThII exhibits the best performance although the difference between the two configurations is low. Comparing these results with Table 5.8, they are observed to behave similarly in the Stokes parameters being around the 0.05 boundary, the DOLP, DOCP and AOLP errors have increased slightly. On the other hand, both configurations show a half variance from prior results.

Conclusions

The study of calibration presented in this section led to three main conclusions. It is shown that a higher number of RPS in the PSG decreases the variance of the recovered Stokes vectors but the condition number of the matrices remains

constant, in accordance with previous studies [46]. It is demonstrated that choosing carefully the RPS reduces the errors and the variances of the Stokes vector, as seen in the comparison of the optimal vs non-optimal RPS. Using the minimum number of N = 4 for the PSG provides the same errors as greater sets and a faster and simpler calibration. It is shown that the light source takes its part in the calibration process and its design must be optimised.

And finally, the best configuration which fulfils the trade-off between simplicity of calibration and precision in recovery is the tetrahedron II and it will be applied for the Stokes imaging experiments.

5.4.2 Mueller matrix imaging calibration (ECM)

The ECM was implemented following the algorithm and utilizing the set-up described in Section 5.3. In this experiment, we seek to elucidate which sample set is the best for our calibration results. Recalling the set-up of ECM, three samples are employed: an LP at two different azimuth angles and a retarder, in this case, a QWP.

The possible sets of samples for the calibration are gathered in Table 5.3. All of them fulfil the conditions explicit in [119] for a correct calibration process. Considering the conclusions in the DRM calibration, the PSG is set to generate the ThII during the ECM calibration process using the illumination source matching the aperture.

The ECM provides two outputs: the PSG matrix $\mathbf{G_{ECM}}$ and the system matrix of the PSA $\mathbf{A_{ECM}}$. The instrument matrix for recovering the Stokes vector corresponds to the inverse: $\mathbf{W_{ECM}} = \mathbf{A_{ECM}}^{-1}$. Likewise in the DRM, the figures of merit $\kappa(\mathbf{W_{ECM}})$, $\kappa(\mathbf{G_{ECM}})$, the theoretical EWV and the experimental EWV are calculated in the same manner using the corresponding $\mathbf{W_{ECM}}$ for each sample set.

During the ECM algorithm, the polarization parameters of the samples are recovered from a specific MM model Section 5.3. Depending on the choice, the output matrices vary together with their associated $\kappa(\mathbf{W_{ECM}})$ and EWV. Following the first paper on ECM [119], they provided the ideal MM for each sample type, meanwhile, other posterior authors [REFs] applied a general dichroic retarder model for all the samples.

Comparing Tables 5.11 and 5.12, the $\kappa(\mathbf{W_{ECM}})$ of the PSA remains constant for both models except in set III for the ideal model. Since the theoretical EWV comes from the instrument matrix, the calibration matrices based on the ideal and general model of MM should have similar theoretical and experimental EWV values around the DRM range. The latter EWV behaviour means the intensity noise of the system is common to all the calibration cycles since we have the same PSA and sensor.

The $\kappa(\mathbf{G_{ECM}})$ of the PSG changes also depending on the model due to the assumptions made by each model of MM. Imposing the ideal model makes the calibration samples be considered perfect polarizers or retarders through Equation (5.14), though the sample attributes needn't be known as they are derived from measurements during ECM. Therefore, the condition numbers of

Sample sets	$\kappa(\mathbf{W_{ECM}})$	$\mathbf{EWV_{th}}$	$\mathbf{EWV_{exp}}$	$\kappa(\mathbf{G_{ECM}})$
Set I	1.90	10.90	0.1002	1.99
Set II	2.66	5.15	0.0931	4.45
Set III	41.12	9.70	0.0985	72.26
Set IV	1.87	55.70	0.0934	2.17
Theoretical	1.73	10.0	-	1.73

Table 5.11: List of the figures of merit ($\kappa(\mathbf{W_{ECM}})$, EWV_{th}, EWV_{exp}, $\kappa(G_{ECM})$) for the analysis of the obtained $\mathbf{W_{ECM}}$ for each sample set applying the ideal model of MM during the ECM using the ThII RPS.

Sample sets	$\kappa(\mathbf{W_{ECM}})$	$\mathbf{EWV_{th}}$	$\mathbf{EWV_{exp}}$	$\kappa(\mathbf{G_{ECM}})$
Set I	2.04	11.74	0.0973	1.89
Set II	1.96	8.66	0.1016	2.62
Set III	2.24	13.04	0.0957	1.88
Set IV	2.19	13.01	0.0955	1.83
Theoretical	1.73	10.0	-	1.73

Table 5.12: List of the figures of merit ($\kappa(\mathbf{W_{ECM}})$, EWV_{th}, EWV_{exp}, $\kappa(G_{ECM})$) for the analysis of the obtained $\mathbf{W_{ECM}}$ for each sample set applying the general model of MM during the ECM calibration using the ThII RPS.

the PSA and PSG show the existence of errors coming from non-idealities of samples. On the other hand, applying the general model allows the sample matrices to have non-perfect values and the resulting condition numbers tend to be the theoretical value.

Recovery of the Stokes vector

From the previous results, the different sets of samples show very similar behaviour. Consequently, another evaluation of the instrument matrices' performance is done by recovering the incident Stokes vectors. To maintain the coherence, the same linear Stokes vectors validated in the DRM are recovered using ECM matrices and the intensities of Figure 5.6.

The optimal sample set for the ECM is Set I with the general model of MM. Figure 5.12 shows its averaged estimated Stokes vectors and the advanced parameters averaged over the central region for each channel of the PSA. Besides, the histogram for each Stokes parameter map is calculated and fitted with a Gaussian distribution. The maximum errors of all sets and the variances are gathered in Table 5.13. The maps are not displayed since the Gaussian distributions are the same as the ThII of DRM. All the calibration matrices are applied over the same intensity distribution in the sensor, so the resulting distributions will be equal but have different mean values associated with the accuracy of the method. The specific combination of samples of Set I (the LP

at 0^o and 90^o and the QWP at 30^o) shows the best precision in recovering the polarization signature. Its Stokes parameters errors are nearby the 0.05 boundary as achieved in DRM calibration. Its respective variances remain the same as in DRM. The DOLP and DOCP show low error and the mean AOLP one is around 2^o along with the complete rotation of the LP.

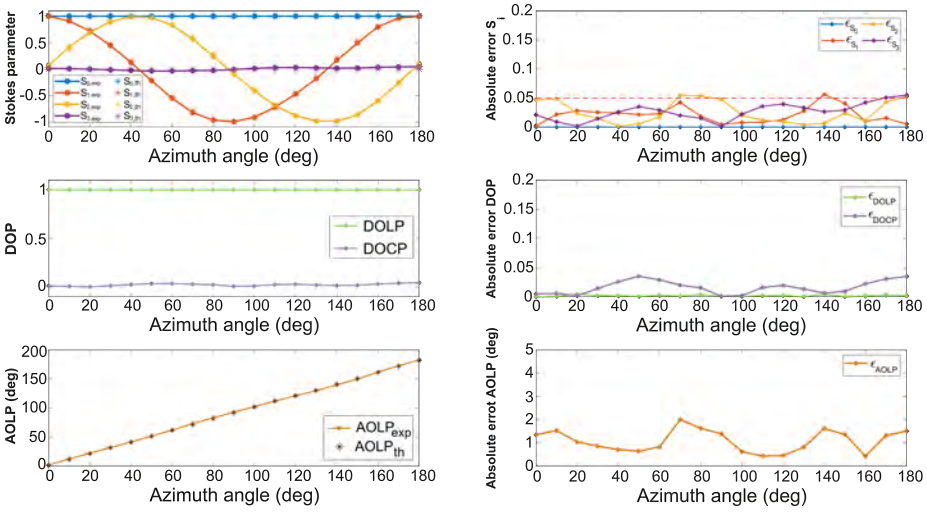

Figure 5.12: (Left) Average recovered Stokes vector, DOLP, DOCP and AOLP corresponding to a rotation of an LP between $[0, 180]^o$ using the Set I, the general model of MM and the ThII illumination during the ECM. (Right) Related errors of the previous parameters.

Sets II and IV, where the QWP axis is at 90^o, show worse performance than their counterparts whose QWP is at 0^o. Their Stokes parameter errors are equal to or higher than the 10% of error as displayed in Table 5.13. The AOLP errors are higher than 2^o. This allows concluding that the optimal sets can be compounded by the LP combinations together with the QWP axis being 0^o since Set I and Set III have lower calculation errors.

Recovery of the Mueller matrix

As previously mentioned, the ECM gives two matrices that let calculate the MM from the measured intensities of the sample, solving Equation (5.5). A third test of the capability of this calibration method is done by recovering the MM of the same sample displayed in the maps in Stokes imaging, an LP at 70^o. For its evaluation, the Mueller deviation matrix ($\mathbf{\Delta M}$), which contains all the non-ideal effects of the system in a single MM, the mean absolute error ($\epsilon_{\mathbf{M}}$) of the MM and the percentage average error per coefficient ($\mathbf{\Delta}_{\mathbf{M}}$) are extracted. Besides, two figures related to variance are extracted: the mean-variance ($\delta_{\mathbf{M}}$) and the percentage standard deviation per coefficient ($\sigma_{\mathbf{M}}$).

Sample sets	ϵ_{S_1}	ϵ_{S_2}	ϵ_{S_3}	$\epsilon_{DOLP,DOCP}$	ϵ_{AOLP}	δ_{S_1}	δ_{S_2}	δ_{S_3}	$\delta_{DOLP,DOCP}$	δ_{AOLP}
Set I	**0.056**	**0.055**	**0.055**	**4.8e-3, 0.035**	**1.99º**	**2.2e-3**	**4.1e-3**	**7.2e-3**	**1.38e-3, 2.1e-3**	**5.20º**
Set II	0.251	0.166	0.143	1.17e-2, 1.40e-2	7.62º	3.9e-3	4.4e-3	9.5e-3	7.86e-3, 5.1e-3	6.66º
Set III	0.063	0.063	0.045	5.3e-3, 0.033	1.94º	1.7e-3	3e-3	7.1e-3	1.43e-5, 2.2e-3	3.94º
Set IV	0.092	0.117	0.058	4e-3, 0.038	3.46º	1.6e-3	3.8e-3	6.3e-3	1.21e-3, 2e-3	4.51º

Table 5.13: Maximum errors and standard deviations of the Stokes parameters S_1, S_2, S_3, and the advanced parameters DOLP, DOCP, and AOLP during the recovery of an LP rotated from 0^o to 180^o in steps of 10^o using the corresponding instrument matrices $\mathbf{W_{ECM}}$ of the sets obtained during the ECM using the ThII illumination.

Figure 5.13 shows the images MM of the ideal (left) and the experimental measurement (right) using calibration matrices ($\mathbf{W_{ECM}}$, $\mathbf{G_{ECM}}$) from Set I. Table 5.14 collects the statistical parameters to quantify the difference between the ideal and experimental MM. From a visual analysis, it can be appreciated that the recovered MM appearance is close to the ideal matrix although some spatial noise is present.

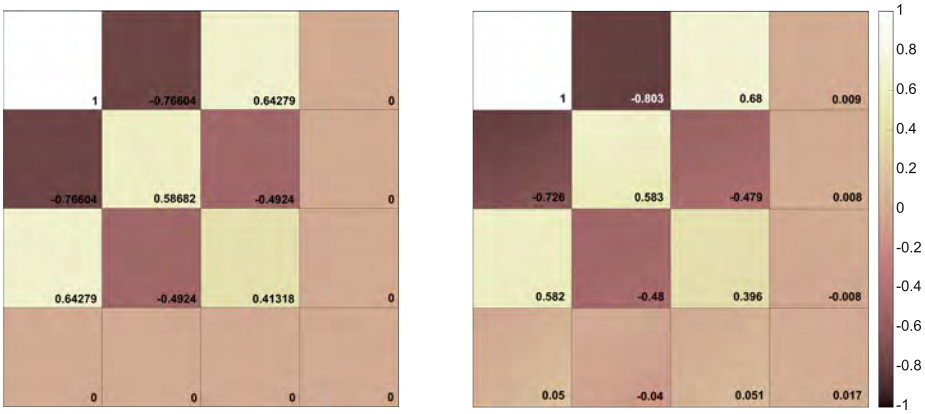

Figure 5.13: (Left) Ideal Mueller matrix image of an LP with axis at 70^o. (Right) Recovered MM image of the LP with axis at 70^o by the ECM using the instrument matrices from Set I.

As formerly concluded in Stokes imaging, Set I proves the lower error when calculating the MM. In general, the two sets corresponding to the QWP at 90^o (Set II and Set IV) have the highest errors as in the Stokes imaging reconstruction.

Sample sets	ΔM	$\epsilon_{\mathbf{M}}$	$\Delta_{\mathbf{M}}$	δ_M	σ_M
Set I	$\begin{pmatrix} 0.965 & 0.019 & 0.080 & 0.016 \\ 0.101 & 0.900 & -0.083 & -0.083 \\ 0.006 & 0.112 & 0.920 & 0.075 \\ 0.035 & -0.062 & 0.077 & 0.972 \end{pmatrix}$	**0.034**	**0.90%**	**9.71e-9**	**3.31e-7%**
Set II	$\begin{pmatrix} 1.045 & -0.135 & 0.095 & -0.011 \\ -0.045 & 0.983 & -0.224 & -0.077 \\ -0.012 & 0.188 & 1.157 & -0.014 \\ 0.044 & -0.066 & 0.227 & 1.138 \end{pmatrix}$	0.068	1.96%	1.11e-8	4.36e-7%
Set III	$\begin{pmatrix} 0.963 & 0.005 & 0.067 & 0.008 \\ 0.090 & 0.837 & -0.036 & -0.198 \\ -0.020 & 0.169 & 0.926 & 0.085 \\ 0.046 & -0.019 & 0.057 & 0.8826 \end{pmatrix}$	0.037	1.02%	1.11e-8	4.29e-7%
Set IV	$\begin{pmatrix} 0.958 & -0.013 & 0.061 & -0.014 \\ 0.087 & 0.801 & -0.021 & -0.051 \\ -0.024 & 0.084 & 0.924 & 0.101 \\ 0.038 & -0.066 & 0.059 & 0.929 \end{pmatrix}$	0.04	1.08%	1.13e-8	4.35e-7%

Table 5.14: Mueller deviation matrix ($\mathbf{\Delta M}$), mean absolute error ($\epsilon_{\mathbf{M}}$), percentage average error per coefficient ($\mathbf{\Delta}_{\mathbf{M}}$), mean-variance ($\delta_{\mathbf{M}}$) and percentage standard deviation per coefficient ($\sigma_{\mathbf{M}}$) of the Mueller matrix of an LP with an axis at 70^o. The MM is calculated using the calibration matrices ($\mathbf{W_{ECM}}$, $\mathbf{G_{ECM}}$) of the different sets in ECM.

Conclusions

It is demonstrated that the election of the MM model of the samples influences the results of the calibration. Comparing the results between the ideal and the general model, the condition numbers of $\mathbf{W_{ECM}}$ and $\mathbf{G_{ECM}}$ of the former are not as good as the latter because it does not take into account possible no-idealities from the samples or the set-up in the calibration process.

It is shown that Set I provides the best recovery of the polarization state in comparison with the other proposed sets for ECM, despite being also valid the sets comprising the QWP at 0^o. Its $\mathbf{W_{ECM}}$ exhibits the lower condition number. Its results in the Stokes recovery present the same accuracy as the DRM.

For the Mueller matrix imaging, Set I exhibits the best results showing the capability of the ECM to calibrate the system for performing MMI experiments. The images of ideal and experimental MM are almost identical and the errors show a discrepancy of less than 2%. This opens the door to performing some experiments where the measurement of the MM is an improvement.

5.4.3 Mueller matrix imaging calibration (PCM)

The alternative PCM is implemented to test it for MMI to compare its performance with the well-established ECM. The algorithm is explained in detail

in Section 5.3 and the setup, shared with the ECM with a modification. Since the motivation of this calibration is to investigate its application to the DoAP system and study its performance, two sets of samples are utilized differing in their size, see Table 5.4. Following a parallel structure of the previous MM calibration method, the PCM uses the ThII configuration of the PSG for illumination.

The PCM returns also simultaneously the PSG and PSA matrices $\mathbf{G_{PCM}}$ and $\mathbf{A_{PCM}}$. The instrument matrix $\mathbf{W_{PCM}}$ for recovering the Stokes vector is obtained through the inverse of $\mathbf{A_{PCM}}$. Following the established scheme of discussion, the figures of merit $\kappa(\mathbf{W_{PCM}})$, $\kappa(\mathbf{G_{PCM}})$, the theoretical EWV and the experimental EWV are shown in Table 5.15. The theoretical condition number of the implemented PSA in our DoAP device has an ideal instrument matrix $\kappa(\mathbf{A_{PSA}}) = 1.73$. The $\kappa(\mathbf{W_{PCM}})$ and the $\kappa(\mathbf{G_{PCM}})$ for both sets of samples are equivalent and in the order of the DRM calibration matrices. The values of both EWV are similar to DRM results.

Sample sets	$\kappa(\mathbf{W_{PCM}})$	$\mathbf{EWV_{th}}$	$\mathbf{EWV_{exp}}$	$\kappa(\mathbf{G_{PCM}})$
Set I (N = 4)	2.07	10.81	0.0959	1.98
Set II (N = 6)	2.06	10.42	0.0961	1.93
Theoretical	1.73	[10.0, 6.7]	-	1.73

Table 5.15: List of the figures of merit ($\kappa(\mathbf{W_{PCM}})$, EWV_{th}, EWV_{exp}, $\kappa(G_{PCM})$) for the analysis of the obtained $\mathbf{W_{PCM}}$ for the two sample sets during the PCM.

Recovery of the Stokes vector

For testing the PCM in Stokes vector measurement, the same proceeding of earlier subsections is done. The Stokes vectors are recovered by using the $\mathbf{W_{PCM}}$ matrix from the two sets of the PCM of Table 5.4 together with the intensity measurement of Figure 5.6. The curves of all Stokes vectors and their advanced parameters calculated with Set I are presented in Figure 5.14. The error of the plotted parameters and their associate standard deviations are compiled in Table 5.16. The higher precision of measuring the input full polarization state is achieved using Set I, although the differences between sets are small. The errors and deviation evolution with higher N states induces the thinking that searching optimal states at higher N is decisive to decrease them. Despite this, their orders of magnitude are the greatest among the three calibration methods where the Stokes parameters maximum error is near 0.14 and the AOLP error is 4.83^o.

Recovery of the Mueller matrix

As before, the PCM capability of recovering the MM of an LP at 70^o is evaluated. The MM is recovered by illuminating the sample with the ThII configuration and solving the Eq.(4) using the calibration matrices ($\mathbf{W_{PCM}}$,$\mathbf{G_{PCM}}$). The ideal and the experimental MM are depicted in Figure 5.15. The former is obtained

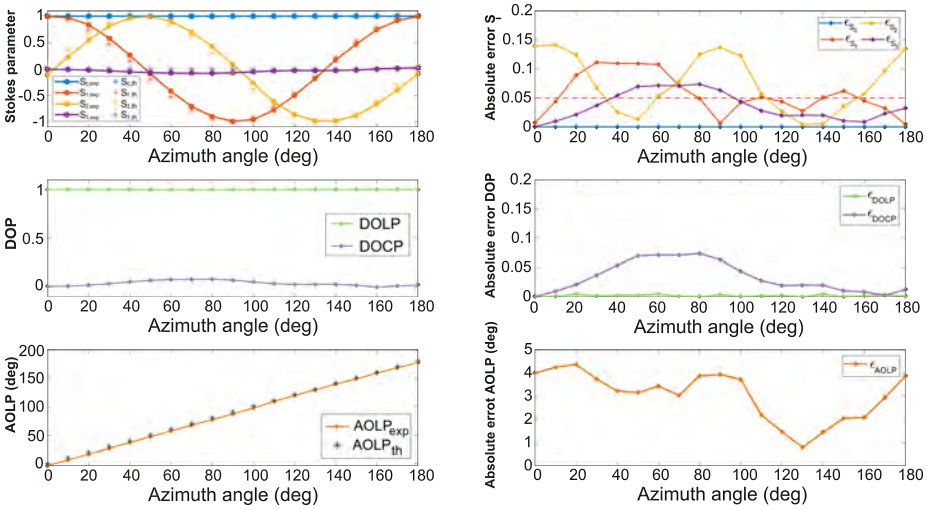

Figure 5.14: (Left) Average recovered Stokes vector, DOLP, DOCP and AOLP corresponding to a rotation of an LP between $[0, 180]^o$ using the Set I, the general model of MM and the ThII illumination during the PCM. (Right) Related errors of the previous parameters.

Sample sets (N)	ϵ_{S_1}	ϵ_{S_2}	ϵ_{S_3}	$\epsilon_{DOLP,DOCP}$	ϵ_{AOLP}	δ_{S_1}	δ_{S_2}	δ_{S_3}	$\delta_{DOLP,DOCP}$	δ_{AOLP}
Set I (N = 4)	**0.113**	**0.141**	**0.074**	**4.8e-3, 0.074**	**4.3°**	**2.9e-3**	**2.5e-3**	**6.5e-3**	**3.6e-5, 3.4e-3**	**4.51°**
Set II (N = 6)	0.247	0.248	0.061	4.6e-3, 0.06	7.81°	3.8e-3	1.9e-3	6.6e-3	2.4e-5, 2.8e-3	4.61°

Table 5.16: Maximum errors and standard deviations of the Stokes parameters S_1, S_2, S_3, and the advanced parameters DOLP, DOCP, and AOLP during the recovery of an LP rotated from 0^o to 180^o in steps of 10^o using the corresponding instrument matrices $\mathbf{W_{PCM}}$ of the sets obtained during the PCM using the ThII illumination.

using the calibration matrices of Set I for coherence with ECM. Just by looking at the colour variation, it can be noticed that there exist differences between the ideal matrix (Figure 5.15 (left)) and the experimental one (Figure 5.15 (right)). This does not happen in the ECM, where the colours matched the ideal matrix ones.

The errors and the variance-related parameters are compiled in Table 5.17. Likewise in Stokes vector recovery, the errors show a huge variation between theoretical and recovered values. Set I shows errors of 6% and contrast with Set II, whose error is more than 3%.

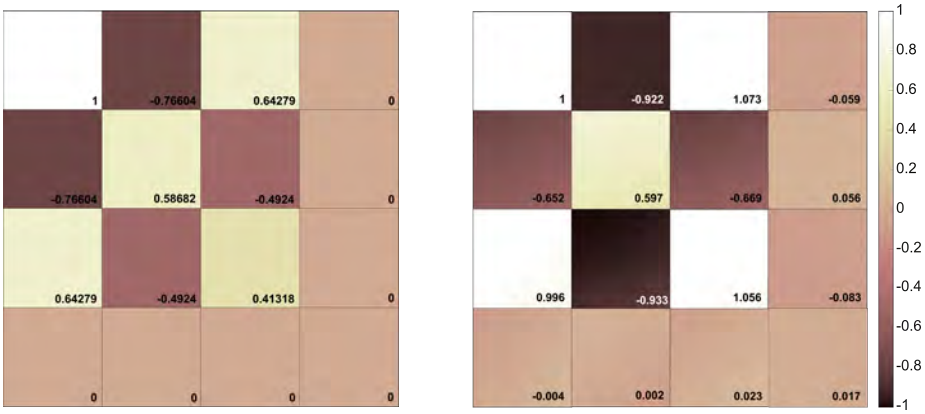

Figure 5.15: (Left) Ideal Mueller matrix image of an LP with axis at 70^o. (Right) Recovered MM image of the LP with axis at 70^o by the PCM using the instrument matrices from Set I.

Sample sets	ΔM	$\epsilon_{\mathbf{M}}$	$\Delta_{\mathbf{M}}$	δ_M	σ_M
Set I	$\begin{pmatrix} 0.986 & -0.083 & 0.104 & -0.022 \\ 0.018 & 0.861 & -0.154 & -0.154 \\ -0.086 & 0.354 & 0.853 & 0.121 \\ 0.081 & -0.072 & 0.073 & 1.102 \end{pmatrix}$	0.17	6.14%	4.28e-8	1.71e-6%
Set II	$\begin{pmatrix} 1.003 & -0.064 & 0.051 & -0.008 \\ -0.014 & 0.925 & -0.211 & -0.084 \\ -0.079 & 0.348 & 0.931 & 0.055 \\ 0.070 & -0.084 & 0.066 & 1.050 \end{pmatrix}$	**0.11**	**3.17%**	**1.48e-8**	**3.47e-7%**

Table 5.17: Mueller deviation matrix ($\mathbf{\Delta M}$), mean absolute error ($\epsilon_{\mathbf{M}}$), percentage average error per coefficient ($\mathbf{\Delta}_{\mathbf{M}}$), mean-variance ($\delta_{\mathbf{M}}$) and percentage standard deviation per coefficient ($\sigma_{\mathbf{M}}$) of the Mueller matrix of an LP with an axis at 70^o. The MM is calculated using the calibration matrices ($\mathbf{W_{PCM}}$, $\mathbf{G_{PCM}}$) of the different sets in PCM.

Conclusions

The PCM was proposed as a possible method where the speed, complexity and cost of the calibration set-up and process were affordable. However, as observed from the previous results, the polarization calculation based on the PCM calibration exhibits lower accuracy than the DRM and ECM, as presented in Stokes imaging of an LP.

It is shown that the best sample set for PCM is Set I for Stokes imaging whereas Set II distinguishes in MMI, although there is no great difference between the two presented sets.

Set I of PCM will be used in the following for a proper comparison of effectiveness in polarization measurement between DRM, ECM and PCM. Thus,

they will employ the same illumination states (ThII configuration) and the same number of samples (N = 4).

5.5 Full-Stokes vector recovery: comparison of methods

Formerly, the different calibration methods were presented, as well as their results in Stokes and MM imaging. In this subsection, a complete comparison is addressed recovering full polarization states, including elliptical ones. In addition, conclusions about the performance of each method are provided.

The best instrument matrices ($\mathbf{W}$) of the calibration methods are gathered in Table 5.18 for better comprehension. All matrices used ThII illumination and are compounded by sets of N = 4.

Calibration method	$\kappa(\mathbf{W})$	$\mathbf{EWV_{th}}$	$\mathbf{EWV_{exp}}$	$\kappa(\mathbf{G})$
DRM (ThII)	2.14	10.97	0.0953	1.74
ECM (Set I)	2.04	11.74	0.0973	1.89
PCM (Set I)	2.07	10.81	0.0959	1.98
Theoretical	1.73	10.0	-	1.73

Table 5.18: List of the figures of merit ($\kappa(\mathbf{W})$, EWV_{th}, EWV_{exp}, $\kappa(G)$) for the analysis of the best $\mathbf{W}$ obtained in each calibration method: DRM, ECM and PCM.

Recovery of the Stokes vector

In the previous analysis, the generated polarization states from a rotating linear polarizer were studied. In this case, the polarization detected by the DoAP system comes from an LP at 0^o followed by a rotating QWP whose principal axis varies from 0^o to 180^o in steps of 10^o. The presence of the QWP introduces a phase shift between the components of the electric field coming out from the LP and transforms it into an elliptically polarized field. The intensity measured by the four channels of the PSA (see Figure 5.16) shows a different modulation at each step, as appreciated in Figure 5.6. Therefore, a full polarization state should be retrieved and the three available methods are tested in full Stokes imaging.

From this intensity in Figure 5.16, the Stokes vector and the advanced parameters of DOP, DOLP, DOCP and AOLP are estimated by applying the derived instruments matrices of Figures 5.17-19 show the recovered full polarization states of the DRM, ECM and PCM, respectively. It can be appreciated that the S_3 parameter is no longer zero introducing elliptical states, as expected. Here, the DoAP system must recover the complete polarization state, including the elliptical ones. Analysing the curves, the recovery of non-linear states involves higher errors in the recovery. DRM curves show very similar behaviour, though the AOLP has an outlier at 7.23^o. ECM curves suffer a general increase in calculation error, as well as the PCM curves. The maximum errors and the standard deviations of each recovery are illustrated in Table 5.19.

As already observed in the curves, the DRM achieves the best polarization reconstruction. Its maximum error is 0.08 in the Stokes parameters and 7.23^o

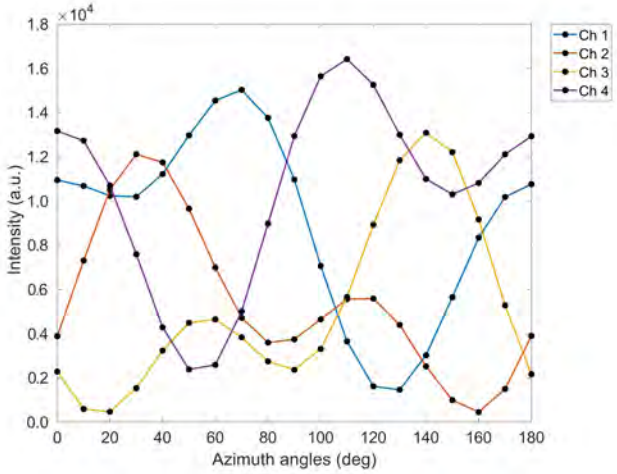

Figure 5.16: Average measured intensity in the four channels of the PSA from a fixed LP at 0^o followed by a rotating achromatic QWP from 0^o to 180^o in steps of 10^o.

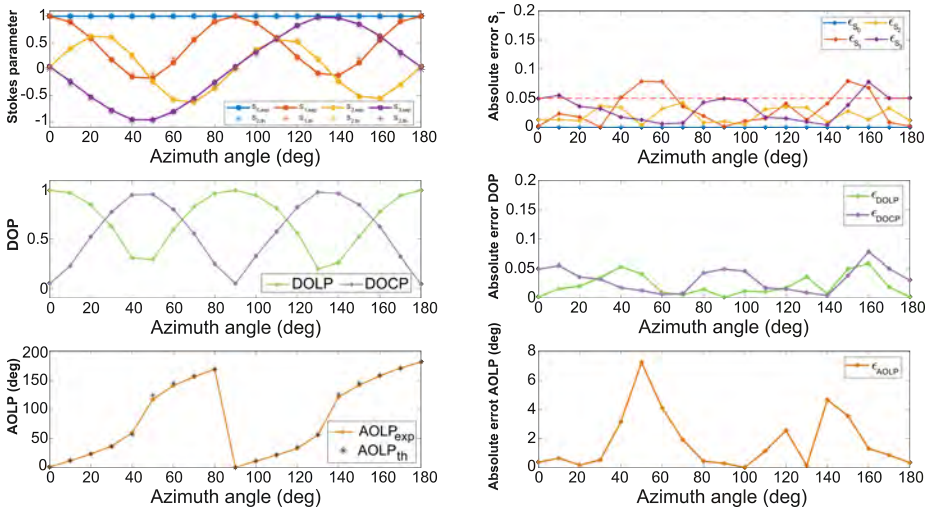

Figure 5.17: (Left) Average recovered Stokes vector, DOLP, DOCP and AOLP corresponding to a fixed LP at 0^o followed by a rotating achromatic QWP from 0^o to 180^o in steps of 10^o applying the $\mathbf{W_{DRM}}$ of ThII configuration of DRM. (Right) Related errors of the previous parameters.

in the AOLP along the complete rotation of the QWP. The other two methods show similar accuracy between them in the elliptical polarization measurement.

Method	ϵ_{S_1}	ϵ_{S_2}	ϵ_{S_3}	$\epsilon_{DOLP,DOCP}$	ϵ_{AOLP}	δ_{S_1}	δ_{S_2}	δ_{S_3}	$\delta_{DOLP,DOCP}$	δ_{AOLP}
DRM	**0.080**	**0.042**	**0.078**	**0.059, 0.078**	**7.23º**	**7.1e-3**	**3.3e-3**	**5.9e-3**	**2.5e-3, 6.0e-3**	**9.89º**
ECM	0.071	0.111	0.143	0.116, 0.143	8.10º	7.2e-3	3.4e-3	5.8e-3	5.63e-2, 5.8e-3	10.34º
PCM	0.152	0.098	0.077	0.070, 0.077	5.66º	5.3e-3	2.2e-3	5.1e-3	2.3e-3, 5.1e-3	6.59º

Table 5.19: Maximum errors and standard deviations of the Stokes parameters S_1, S_2, S_3, and the advanced parameters DOLP, DOCP, and AOLP during the recovery of a fixed LP at 0^o followed by a rotating achromatic QWP from 0^o to 180^o in steps of 10^o using the best instrument matrices $\mathbf{W}$ for each calibration method.

Recovery of the Mueller matrix

A second test is done with the two calibration methods that recover the MM of a scene. The samples used in the calibrations are Set I, in the case of ECM, and set of N = 4, in the case of PCM. The sample test consists of a horizontal LP followed by an achromatic QWP whose optical axis is at 70^o. As in Stokes imaging, the presence of the QWP introduces the elliptical states. This allows studying the ability of the methods to retrieve the components of the last row and column that now are different from zero.

In the specific case of the QWP at 70^o, the theoretical matrix is displayed in the top line of Figure 5.20. In the bottom line of Figure 5.20, the experimental

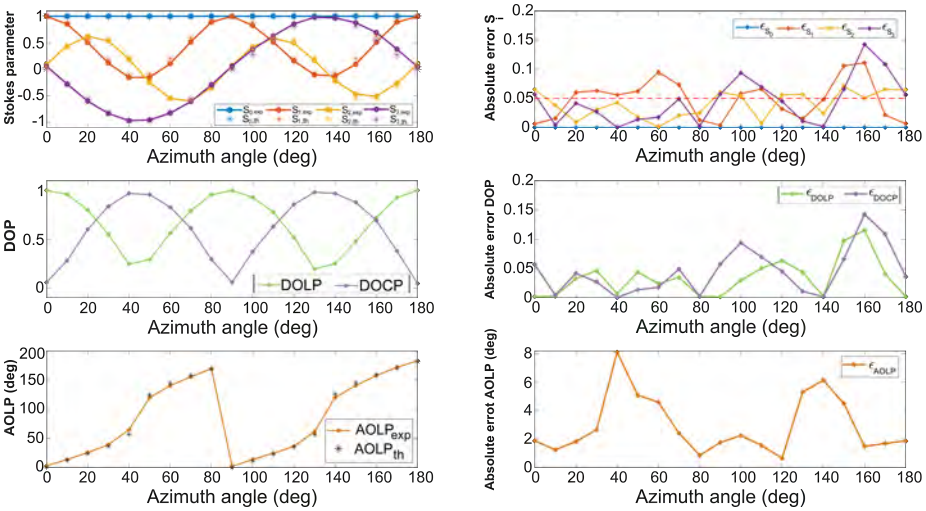

Figure 5.18: (Left) Average recovered Stokes vector, DOLP, DOCP and AOLP corresponding to a fixed LP at 0^o followed by a rotating achromatic QWP from 0^o to 180^o in steps of 10^o applying the $\mathbf{W_{ECM}}$ of Set I in ECM with ThII illumination. (Right) Related errors of the previous parameters.

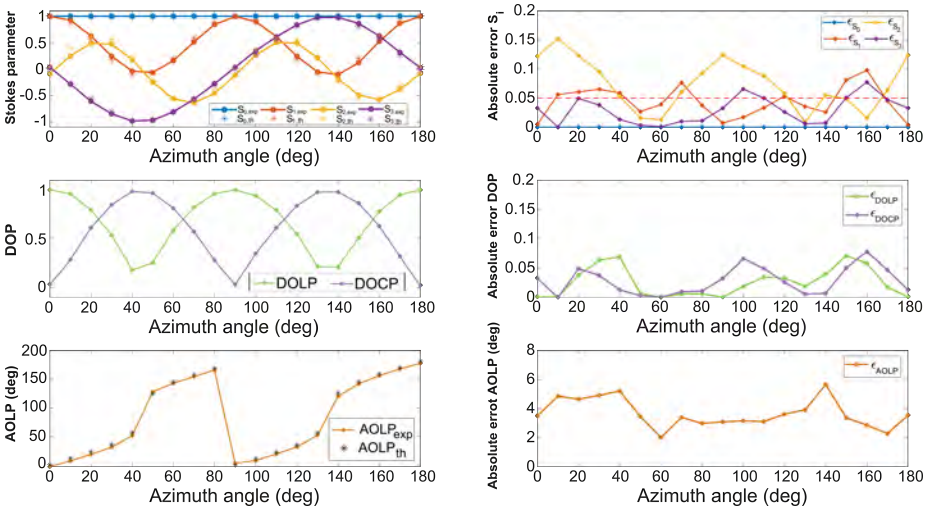

Figure 5.19: (Left) Average recovered Stokes vector, DOLP, DOCP and AOLP corresponding to a fixed LP at 0^o followed by a rotating achromatic QWP from 0^o to 180^o in steps of 10^o applying the $\mathbf{W_{PCM}}$ of Set I in PCM with ThII illumination. (Right) Related errors of the previous parameters.

MM applying the ECM (left) and the PCM (right) are displayed. *A priori* by visual inspection, the MM of ECM shows more coincidence in colours than the counterpart of PCM. The mean value of each Mueller matrix coefficient in each of the maps is presented for a quantitative comparison.

Table 5.20 shows the Mueller deviation matrix ($\mathbf{\Delta M}$), mean absolute error ($\epsilon_{\mathbf{M}}$), percentage average error per coefficient ($\mathbf{\Delta_M}$), mean-variance ($\delta_{\mathbf{M}}$) and percentage standard deviation per coefficient ($\sigma_{\mathbf{M}}$) of the Mueller matrix for both methods. It demonstrates that the ECM outperforms PCM with lower global mean error and percentage error per coefficient. The ECM results have the best precision when calculating the MM with and $\mathbf{\Delta_M}$) around 1.5%. $\mathbf{\Delta M}$ parameter of ECM method is closer to the identity matrix sustaining the conclusion the ECM works better. The same is observed in the variance parameter $\delta_{\mathbf{M}}$ proving that the PCM matrices propagate more noise in the recovery process.

These results depicted a specific elliptical state for a more conscious analysis of the Mueller matrix components maps. In subsequent, a complete study of the evolution of the Mueller matrix when the fast axis of a single achromatic QWP (THORLABS AQWP10M-580) is rotated between 0^o and 180^o is performed for both calibration methods. This intends to generate more coverage of the Mueller matrix elements and test if they really differ in performance.

Since the sample surface is uniform, each mean value and its variance are plotted for all components of the MM in Figure 5.21 applying the calibration matrices of ECM. The theoretical values agree with the experimental data from the DoAP system using the ECM matrices. The error bars are higher in the circular-related components but below the 10% of error (except in the m_{44}

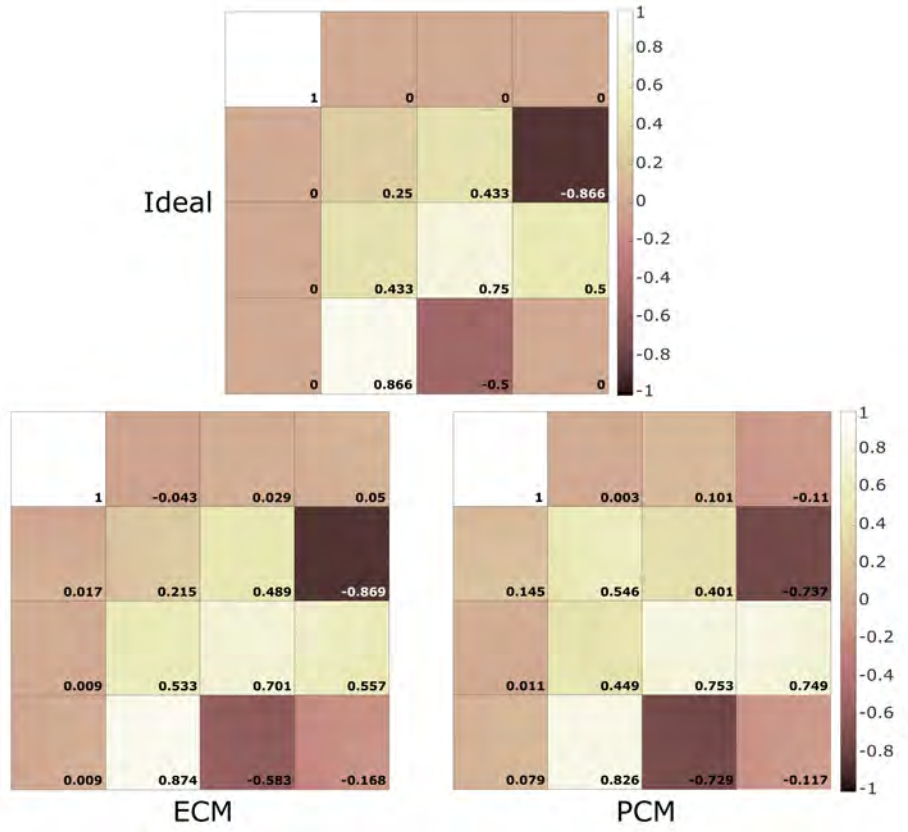

Figure 5.20: (Left) Theoretical Mueller matrix image of an LP, with an optical axis at 0^o, followed by an achromatic QWP with a fast axis at 70^o. (Right) Recovered MM image of the an LP, with an optical axis at 0^o, followed by an achromatic QWP with a fast axis at 70^o by the ECM (left) and PCM (right) using the instrument matrices of their best set.

component), aligning with the errors shown in Table 5.20. Results also agree with the ones obtained in MM systems of the SoA [174]. When employing the calibration matrices recovered from the PCM, the experimental Mueller matrix exhibits a more unstable recovery, as depicted in Figure 5.22. The errors are larger than the ones in ECM proving the superiority of the ECM for the calibration of a MMI system. PCM essentially pushes noise amplification into the circular-related polarization reconstruction in the inversion of the matrices. This could be improved by finding the optimal set of angles of the LP sample for the PCM procedure.

Calibration method	ΔM	ϵ_M	Δ_M	δ_M	σ_M
ECM	$\begin{pmatrix} \mathbf{0.970} & \mathbf{0.019} & \mathbf{0.080} & \mathbf{0.016} \\ \mathbf{0.100} & \mathbf{0.900} & \mathbf{-0.083} & \mathbf{-0.083} \\ \mathbf{0.006} & \mathbf{0.112} & \mathbf{0.920} & \mathbf{0.075} \\ \mathbf{0.035} & \mathbf{-0.062} & \mathbf{0.077} & \mathbf{0.972} \end{pmatrix}$	**0.051**	**1.54%**	**6.08e-8**	**2.32e-06%**
PCM	$\begin{pmatrix} 0.986 & -0.083 & 0.104 & -0.022 \\ 0.018 & 0.861 & -0.154 & -0.154 \\ -0.086 & 0.354 & 0.853 & 0.121 \\ 0.081 & -0.072 & 0.073 & 1.102 \end{pmatrix}$	0.067	1.92%	3.0e-8	1.14e-06%

Table 5.20: Mueller deviation matrix ($\mathbf{\Delta M}$), mean absolute error (ϵ_M), percentage average error per coefficient ($\mathbf{\Delta}_M$), mean-variance (δ_M) and percentage standard deviation per coefficient (σ_M) of the Mueller matrix of an LP, with an optical axis at 0^o, followed by an achromatic QWP with a fast axis at 70^o. The MM is calculated using the calibration matrices ($\mathbf{W}$, $\mathbf{G}$) of the best set for each method.

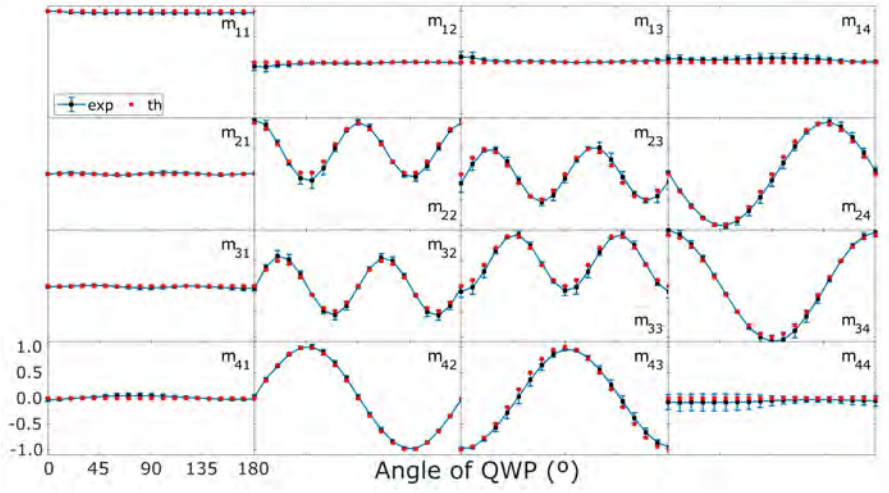

Figure 5.21: Theoretical Mueller matrix values (red dots) and recovered Mueller matrix mean values (blue line) of an achromatic QWP rotated from 0^o to 180^o using ECM with the sample Set I.

Conclusions

After all this analysis of the performances of the different calibration methods, several conclusions can be derived. Firstly, the introduction of the QWP in the measurement set-up adds possible misalignments among itself with the LP axis and the PSA axis. This discrepancy may produce spatial inhomogeneity in the polarization arriving at the detector. Therefore, the upper bound of 0.05 Stokes

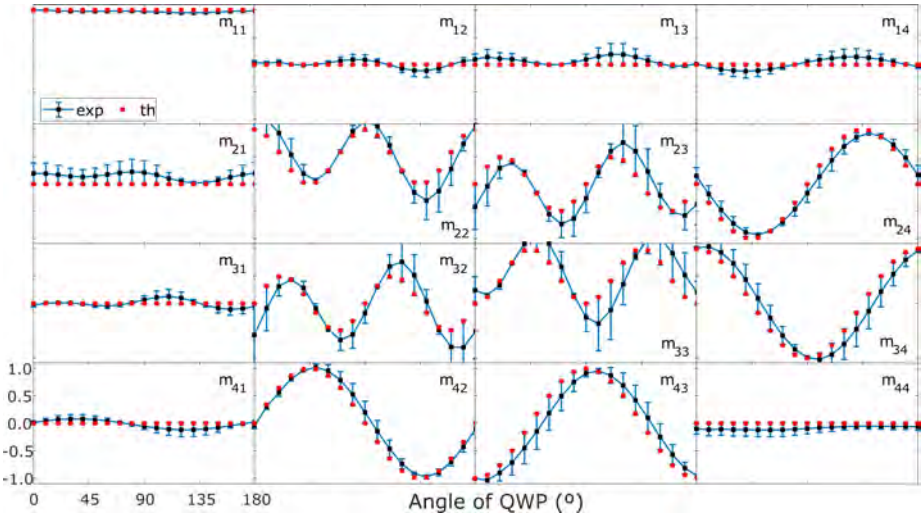

Figure 5.22: Theoretical Mueller matrix values (red dots) and recovered Mueller matrix mean values (blue line) of an achromatic QWP rotated from 0^o to 180^o using PCM with the sample Set I.

error considered in linear polarization, should be relaxed up to 0.10 (normal boundary in experimental results).

Regarding Stokes imaging, the DRM is the best method to recover the full polarization state of a scene. Also, it is the simplest to be implemented and only 4 measurements are required. It is worth mentioning that the statistical figures of all methods when changing from linear to elliptical polarization differ, especially in the standard deviation, being up to two times bigger in the latter case. This can be due to a misalignment of the LP and QWP axis to the axis of the PSA system affecting the homogeneity of the intensity.

Regarding MMI, the best method is the ECM. It allows an accurate measurement of the polarization properties both in partial and full MMI. As well as in the Stokes technique, the error parameters increased a bit from linear to elliptical components, being below the 10% of error in any case.

Part IV

Polarization Results

Dear walker who is wandering through this thesis, the time has finally come. The desired moment, when I share with you the wonders this polarimetric camera can do and our eyes cannot believe, has arrived. Come in and enter the world of Wizardry, [that scientists call Physics].

Chapter 6

Polarimetric imaging using the DoAP camera

In this chapter, the DoAP system measures the polarization state of light are for very distinct scenes for demonstrating its performance. Following the guidelines during this thesis, three types of polarization acquisitions are tested with the DoAP camera: Stokes imaging, active Stokes imaging and Mueller Matrix imaging.

All of them measure the polarization signal of the scene and display it in diverse forms. The simplest option for measuring polarization is the retrieval of the Stokes vector and its derived parameters. This passive mode is presented in Section 6.1 and sets the basis for understanding the polarization concepts. The other two imaging modes do require an active illumination with a controlled polarization. In Section 6.2, the active Stokes imaging studies the change of the signal between entering and returned polarization state of the scene. Section 6.3 shows the capability of the DoAP camera to acquire a 4x4 matrix of images that corresponds to the Mueller matrix and gathers all the polarimetric information about the measured sample. Each section is related to the specific theoretical background already explained in Section Section 2.2.

6.1 Stokes imaging

The most straightforward manner of measuring polarization consists in retrieving the Stokes vector at each pixel of the image. Each vector component has an associated map and the total set provides specific information about the polarization state. For a better comprehension, a brief reminder about the Stokes parameters: the S_0 component represents the intensity image, equivalent to the acquired by a conventional intensity sensor, and ranges from 0 to 1. The S_1 refers to the difference between the vertical and horizontal components of the electrical field and, thus, describes the amount of linear polarization on this perpendicular basis. Alternatively, the S_2 refers to the difference between the $+45^o$ and -45^o axis of the electrical field, and its associated amount of linear polarization in this specific axis. Finally, the S_3 indicates the presence of a shift between electrical field components being its minimum in left-handed circular polarization ($S_3 = -1$) and its maximum in right-handed circular polarization ($S_3 = 1$). Middle values indicate the presence of elliptical polarization states and, when $S_3 = 0$, there exists pure linear polarization. Section 2.2 explains further details.

Apart from Stokes parameters, some other advanced parameters can be derived from the vector components to give more intuitive information. These

are the Degree of Polarization (DOP), Degree of Linear Polarization (DOLP), Degree of Circular Polarization (DOCP), the Angle of Linear Polarization (AOLP) and the ellipticity (ϵ) and they stand for indicating the quantity of polarized light, linear polarized light, circularly polarized light, the angle of the polarization and the associated ellipticity, respectively. The equations for obtaining the Stokes vector and its derived parameters maps were presented in Section 2.2.1.

In previous chapter, Section 5.5 gave the final calibration results of the DoAP system by means of the curves and the maps of well-known laboratory samples like LP and QWP in transmission. However, in this section, the passive Stokes maps of a larger variety samples and compositions are presented.

Validation experiment

In the first place, and continuing with the transmission geometry of calibration results, Figure 6.1 presents a scene composed of four LPs (A-D: EO #86-178) with different optical axis orientations and two CPs (E: EO #88-084 and F: EO #11-047) of different ellipticities placed on a diffuser plate illuminated with unpolarized uniform white light. Since the scene is still under controlled conditions, the optical characteristics of the samples are already known (measured with PAX1000VIS polarimeter) and gathe red in Table 6.1. It serves for validating the performance when scenes are not uniform across the FOV.

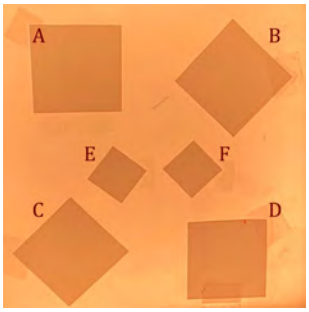

Figure 6.1: Scene composed by four LP (A-D) and two CP (E,F).

	Stokes vector	DOLP	DOCP	AOLP	ϵ
A	[1.0,1.0,0.1,0.0]	0.98	0.20	2.3^o	0.3^o
B	[1.0,0.0,1.0,0.0]	0.99	0.16	45.4^o	0.5^o
C	[1.0,0.1,-1.0,0.0]	1.0	0.03	135.0^o	-0.1^o
D	[1.0,-1.0,0.0,0.0]	0.97	0.26	87.5^o	1.0^o
E	[1.0,0.0,0.2,-0.98]	0.2	0.98	49.1^o	-38.0^o
F	[1.0,0.0,-0.2,0.98]	0.2	0.98	139.5^o	39.0^o

Table 6.1: Polarimetric parameters of the polarizers present in Figure 6.1. DOP is 1.0 in all cases.

The recovered Stokes maps and the related histograms are displayed in Figure 6.2. They come from the measured intensities by the PSA and the obtained calibration matrix **W** using ECM. Results show the ability of the DoAP camera to correctly recover the polarization state of the scene. S_0 map and histogram show the intensity centred around 0.4, being consistent with the transmission of the polarizers ($42 \pm 2\%$). In the S_1 map, polarizers A and D have maximum (0.98) and minimum (-0.99) values, meanwhile, B and C have values of -0.25 and 0.20, respectively. Circular polarizers E and F show values of -0.30 and -0.25. This is reflected in the S_1 histogram where three peaks are visible. In the S_2 map, the roles between A-D and B-C pairs are exchanged

and the histogram show again the three expected peaks. B and C show the maximum (0.96) and minimum (-0.98) values, respectively. Polarizers A and D show errors lower than ± 0.1 from theoretical values. E and F polarizers agree with figures shown in Table 6.1 with 0.21 and -0.2, respectively. Finally, the S_3 map is only relevant for E and F polarizers (-0.93 and 0.93). Values of LPs are around -0.05 ± 0.1, meeting the greatest peak centred at 0^o in histogram.

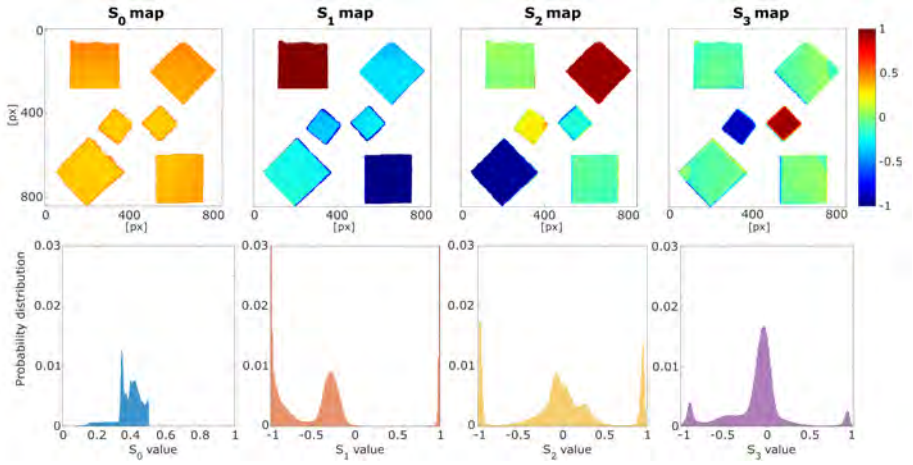

Figure 6.2: (Top) Maps of the Stokes parameters of the scene in Figure 6.1. (Bottom) The associated histograms for each map.

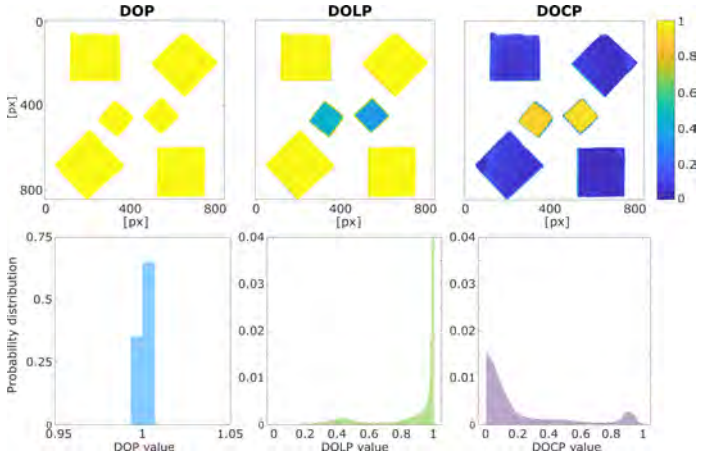

Figure 6.3: (Top) Maps of the DOP, DOLP and DOCP of the scene in Figure 6.1. (Bottom) The associated histograms for each map.

The maps of advanced parameters are recovered pixel-by-pixel using the Stokes maps and they are presented in Figure 6.3 and Figure 6.4. The DOP parameter agrees with the expected value of 1.0. This means that all polarizers provide polarized light, either linear or circular. The DOLP shows that LPs A-D effectively polarize light linearly, meanwhile E and F provide a 0.38 of DOLP demonstrating the non-ideality of a film CP. The DOCP map states again that polarizers A-D do not show elliptical behaviour (0.05 ± 0.15) and the E-F polarizers exhibit a circular behaviour with 0.91 of DOCP.

The maps related to the angle parameters are consistent with the values gathered in Table 6.1. The LPs A-D show values of $(0.02^o, 52.0^o, 128.0^o, 92.0^o) \pm 3^o$ and the CPs E-F values of 72^o and 105^o have a shift from expected. The ellipticity map highlights that E-F polarizers introduce a shift between components of the electrical field yielding the highest absolute value in S_3 and DOCP. Their values are -32^o and 34.5^o, respectively, and the histogram shows them as tiny peaks in the limit values. The central region of the histogram at $\epsilon = 0^o$ corresponds to the LPs A-D with values around $-1^o \pm 4.5^o$.

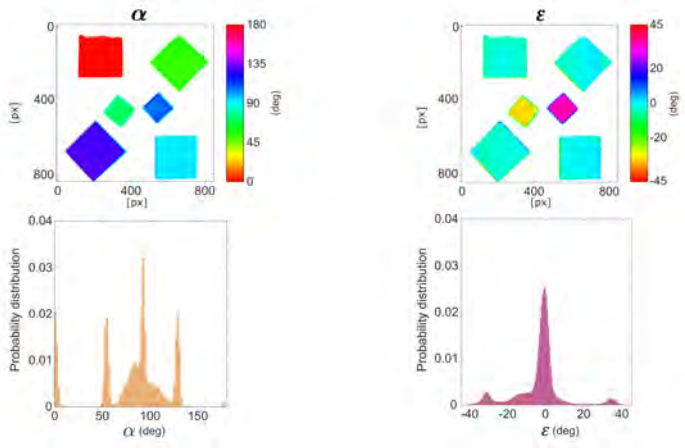

Figure 6.4: (Top) Maps of the AOLP and ϵ of the scene in Figure 6.1. (Bottom) The associated histograms for each map.

The second part of Section 6.1 consists in measuring several types of objects in reflection geometry under natural unpolarized light. For each experiment, the complexity of the scene is increased by adding more objects of distinct materials. The purpose of these studies is to see the performance of the camera in passive mode. Results are recovered images from the DoAP device when measuring the samples illuminated with unpolarized light in reflection geometry. From now on, only Stokes parameters, DOLP, DOCP, AOLP and ϵ maps are present.

Polarizers

The first experiment reproduces the arrangement of the A-F polarizers in the validation scene but using reflection geometry and natural light. When placing the samples, LPs B-C and CPs E-F are interchanged. Figure 6.5 shows the Stokes vector maps together with the advanced polarimetric parameters. They are recovered with the same accuracy as in transmission geometry. The only variations are observed in AOLP and ϵ values which differ a bit in B-C and E-F polarizers from Figure 6.4 because they are not placed in the same orientation. This is also noticed in Figure 6.2, where the S_2 values are higher.

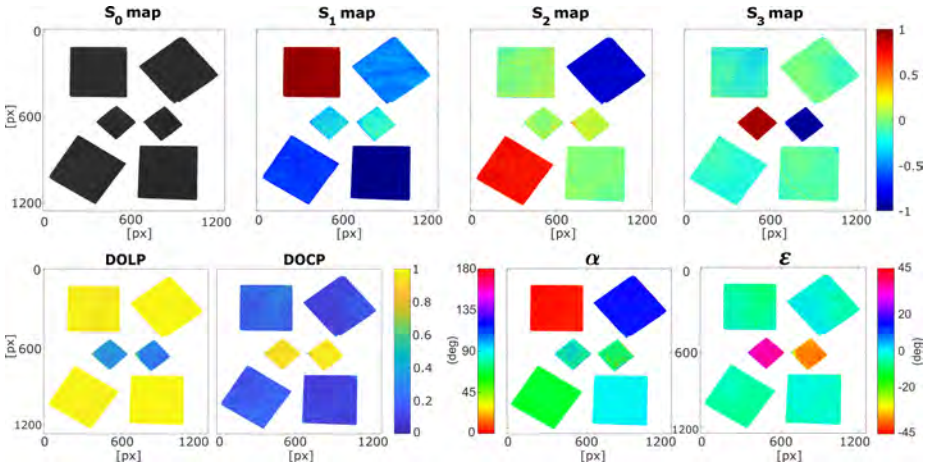

Figure 6.5: (Top) Maps of the Stokes parameters of several polarizers as in Figure 6.1. (Bottom, left) DOLP, and DOCP maps. (Bottom, right) Maps of AOLP and ϵ.

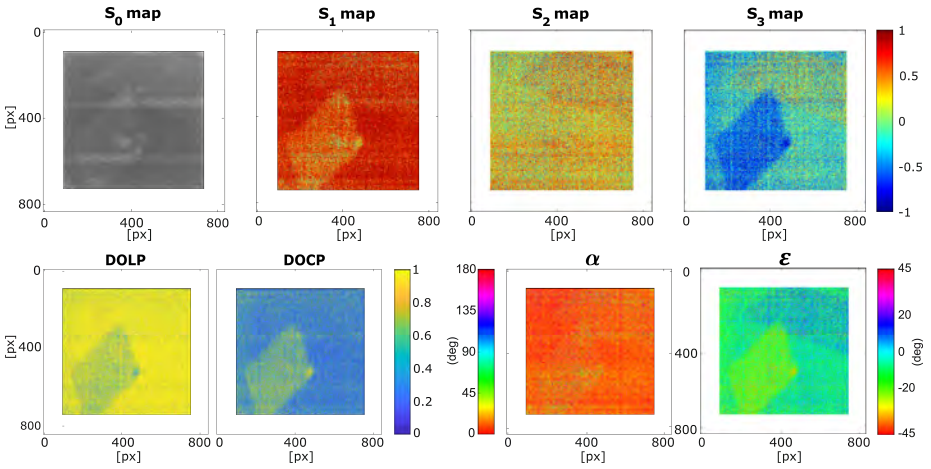

Figure 6.6: (Top) Maps of the Stokes parameters of pieces of tape on a LP. (Bottom, left) DOLP, and DOCP maps. (Bottom, right) Maps of AOLP and ϵ.

Thereafter, another LP at 0^o is completely covered with tape in the horizontal position and then two pieces of tape are placed on it at different orientations. Comparing *a priori* the maps of Figure 6.5 with the LP A of Figure 6.5, it is noticeable a change in the polarization state. Covering the LP with tape changes S_2 and S_3 maps where the mean value of the polarizer passes from 0 and to 0.35 and -0.30, respectively. The tape introduces retardation in the horizontal linear polarization coming out from the LP which becomes elliptically polarized. There are two regions on the LP that can be differentiated in the Stokes maps corresponding to the two pieces of tape at oblique orientations. The bottom left piece of tape has more elliptical polarization than the top right tape. These conclusions are supported by the fact the DOLP of the LP decreases from 1.0 to 0.8 in the background and the bottom left tape goes down up to 0.55. On the contrary, the DOCP of the bottom tape increases to 0.65. The ϵ map suffers a shift in the values due to the tape on the LP. The bottom and top pieces of tape are distinguishable from the background with values of -20^o and 9^o, agreeing with their behaviour as retarders.

Stones

The second experiment consists of a pair of different stones: granite with embedded silver and calcite. Their Stokes maps are retrieved to see if each stone has particular polarimetric characteristics. Figure 6.7 shows the polarimetric information of the granite stone with silver elements embedded and Figure 6.8 displays the polarization information of the calcite stone. It is worth mentioning that the background signal is different from zero in the maps (including the angle maps) since unpolarized incident light gets polarized by the reflection.

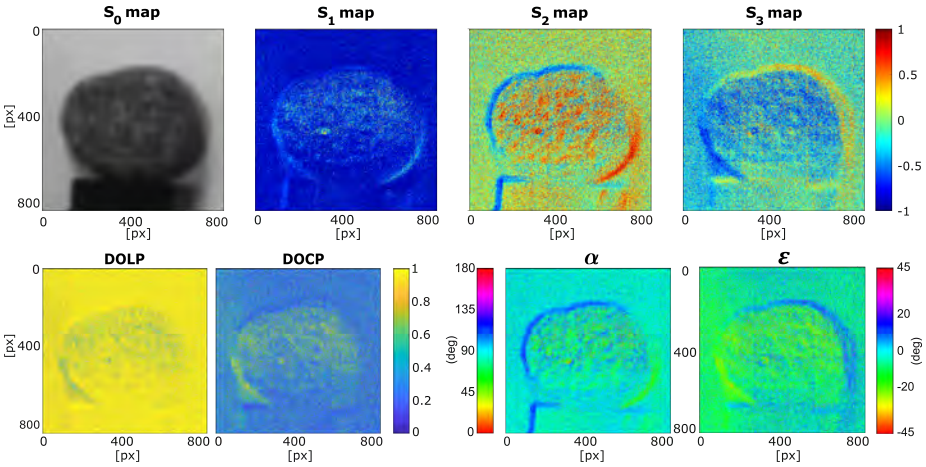

Figure 6.7: (Top) Maps of the Stokes parameters of granite stone with silver elements. (Bottom, left) DOLP, and DOCP maps. (Bottom, right) Maps of AOLP and ϵ.

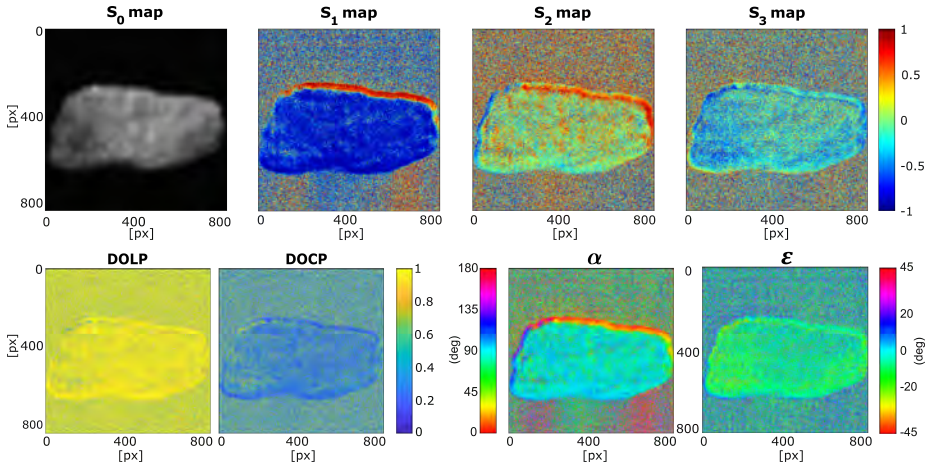

Figure 6.8: (Top) Maps of the Stokes parameters of calcite stone. (Bottom, left) DOLP, and DOCP maps. (Bottom, right) Maps of AOLP and ϵ.

Granite stone seems to have some circular polarization signal in the upper half-part of the stone as seen in S_3, DOLP and DOCP maps. The S_1 map shows a strong signal of the linear component due to the reflection of light from the object towards the camera. In the S_2 map, some points show different values from granite material corresponding to the metallic elements. On the other hand, the calcite stone shows a smoother behaviour although some local changes are appreciated from the surface roughness. Its S_1 map agrees with the polarized reflection from the object. S_2 and S_3 maps have a lower polarization. During registration, the alignment error of the channels is lower than a pixel. Therefore, the false signal from stone borders is due to the different reflection angles to the camera view. DOLP and DOCP show that the stone predominately polarizes the incident light into linear polarization like a dielectric material. The AOLP shows local displacements from the normal angle of the camera view and the ϵ is steadier.

Electronic card

A third experiment is addressed to show the disparity in behaviour between two groups of materials: dielectrics and metals. In this case, the polarization signal of an electronic card is retrieved in Figure 6.9. The S_1 map shows a higher signal of the plastic components of the card and the S_2 map highlights both some plastic and metallic elements, meanwhile last ones are more noticeable in the S_3 maps. The behaviour of metallic structures agrees with the changes in the ellipticity map.

This divergence between plastic and metallic materials is already studied in [130, 131, 175], as explained in Section 2.5. However, they used the intensity-based Fresnel coefficients from measurements through a LP to enhance the algorithm. In this case, since the DoAP camera can acquire full-Stokes images, a

mask can be developed to separate the materials using the circular component (S_3) and the ellipticity. Figure 6.10 displays Stokes maps after applying the mask to separate the metallic components from the dielectric ones. Material classification and quality inspection can be possible applications based on polarization signal detection.

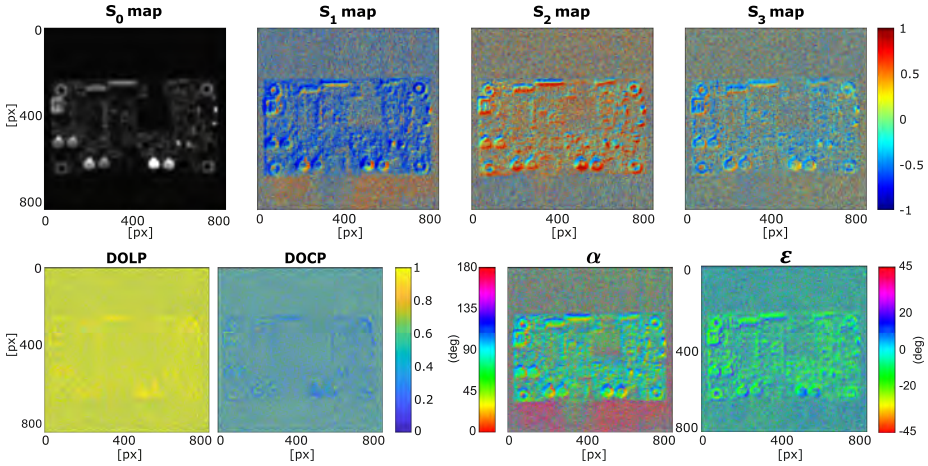

Figure 6.9: (Top) Maps of the Stokes parameters of an electronic card.(Bottom, left) DOLP, and DOCP maps. (Bottom, right) Maps of AOLP and ϵ.

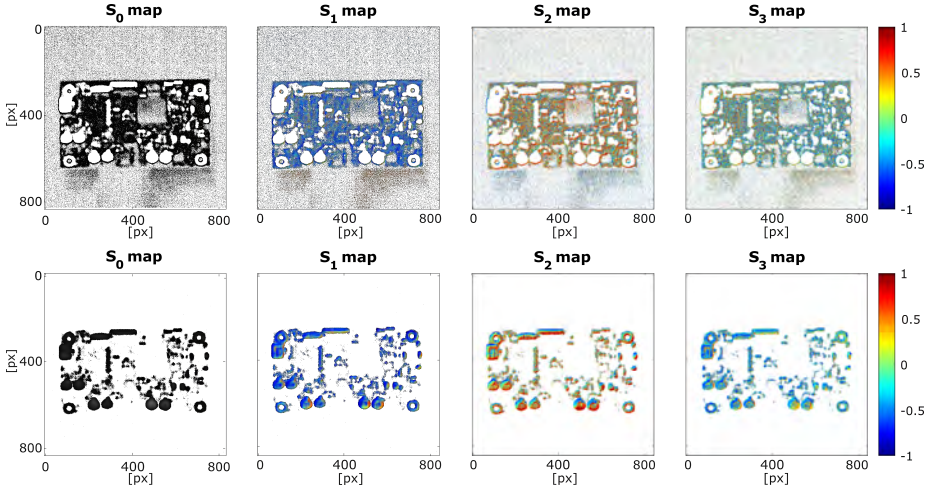

Figure 6.10: (Top) Maps of the Stokes parameters for the dielectric elements of the electronic card. (Bottom) Maps of the Stokes parameters for the metallic components of the electronic card.

Complex scene

The fourth experiment gathers several objects of different natures. From left to right, a rubber, a flash drive with metallic and wooden parts, a silicone Hermione Granger's miniature, a ceramic star and a plastic container. After measuring the scene in passive Stokes imaging, the polarization signal reflected from the materials is presented in Figure 6.11. S_1 shows the polarized reflection of the ambient illumination in all the objects except in the flash drive where its metallic part shows a lower linear signal. S_2 map does not show major changes between materials, only object borders are highlighted. Regarding the S_3 map, the metal part in the flash drive confirms a higher signal and the rubber has a slight circular component. On the contrary, wood, silicone, ceramic and plastic show values around zero. They confirm to have a linear polarized signal since their DOLP is high and AOLP values are around 90^o from reflection. Metal and rubber confirm to have elliptical polarization signals since they show higher values (0.5 and 0.8) in DOCP map and (-15^o and -26^o) in ϵ map, respectively.

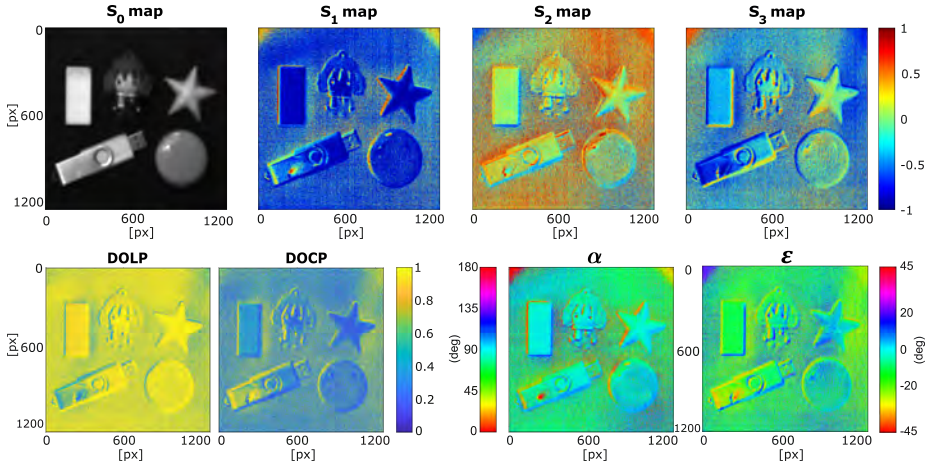

Figure 6.11: (Top) Maps of the Stokes parameters of several objects. From left to right: rubber, flash drive, silicone miniature, ceramic star and plastic container. (Bottom, left) DOLP, and DOCP maps. (Bottom, right) Maps of AOLP and ϵ.

Liquid samples

A fifth experiment is performed using liquid samples. Three vases containing, from left to right, distilled water, sugar dilution of 0.4 g/ml and milk diluted in water. Each dilution has a predominant optical property. Water is set as the reference sample since it does not present any polarization optical activity. Sugar is a chiral particle which interacts with polarized light. And lastly, milk shows scattering due to the presence of big scatterers as lipids in water. Figure 6.12 gathers the polarization information measured from the reflection of white light. It shows the already commented effect of linear polarization due to reflection in

background. As the incident light is unpolarized, the only remarkable information comes from the crystal vases which show a vertical polarization signal. None of the liquids can be differentiated since their optical properties do not interact with unpolarized light.

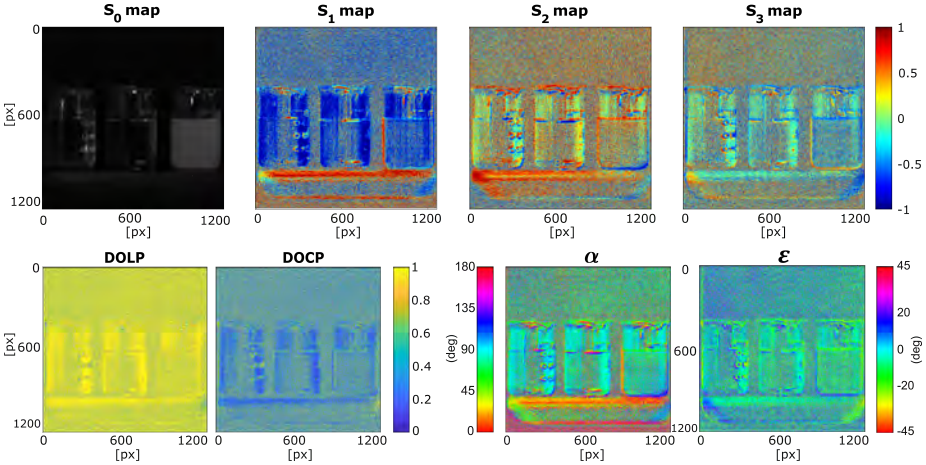

Figure 6.12: (Top) Maps of the Stokes parameters of water, sugar and milk dilutions, from left to right. (Bottom, left) DOLP, and DOCP maps. (Bottom, right) Maps of AOLP and ϵ.

Real-life scenes

Up to now, all the previous experiments were addressed in laboratory. This experiment presents two outdoor scenes measured with passive Stokes imaging. Figure 6.13 displays two parked cars in front of the camera view. Linear polarization is across the scene and tiny circular signal is detected. Crystal of the cars seem to polarized the reflected light coming from the sun changing the AOLP and being distinguished from the rest of the scene. On the contrary, the windows of the building do not contrast except for the borders since the sunlight does not incidence onto them. Combining the information from S_2 and S_3 maybe can distinguish the soil from the cars and the building.

Figure 6.14 contains a more complete scene of a car park. This image is taken rotating 40^o the camera view. This affects the reflected polarization in the maps. The general behaviour of the objects remains the same but the S_2 parameter seems to vary across the FOV, and thus, changing the related AOLP. It is curious how the lateral windows of the car show the same behaviour as the window of the building. They are vertical oriented, meanwhile the front window of the car is tilted horizontally reflecting in a different angle the polarization the incident sunlight to the camera.

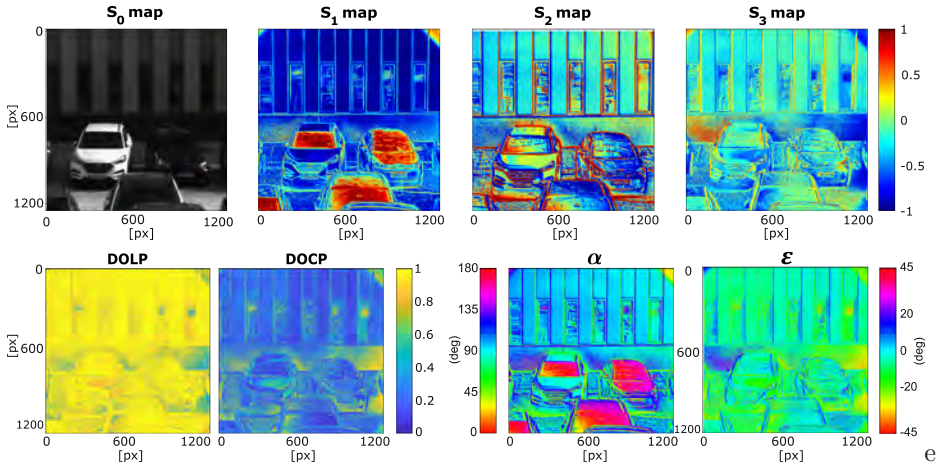

Figure 6.13: (Top) Maps of the Stokes parameters of two cars.(Bottom, left) DOLP, and DOCP maps. (Bottom, right) Maps of AOLP and ϵ.

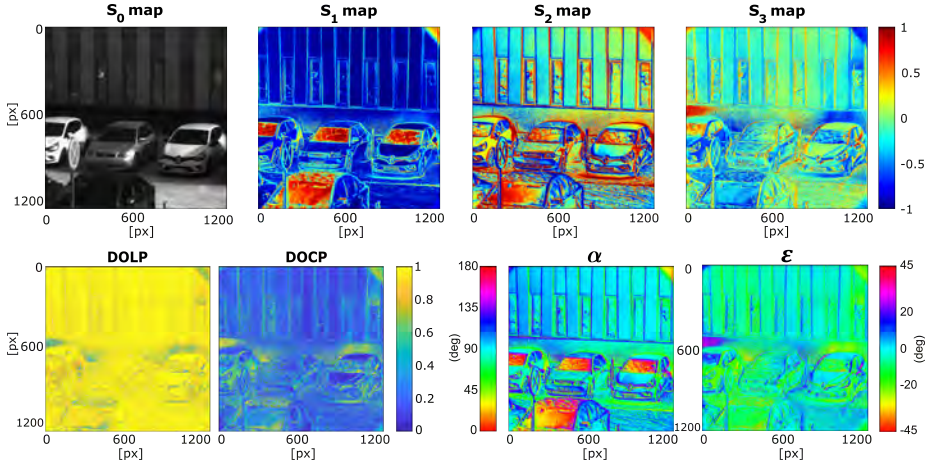

Figure 6.14: (Top) Maps of the Stokes parameters of a car park.(Bottom, left) DOLP, and DOCP maps. (Bottom, right) Maps of AOLP and ϵ.

Summary

In this Section 6.1, DoAP system has demonstrated its capacity of recovering full-Stokes images. The accuracy in the scene of Section 6.1 validates the system performance for the subsequent experiments. From the results, it can be concluded that linear polarization is more present in the scenes. Full-Stokes images show that pure circular polarization is not detected but elliptical one. Feasible applications for passive Stokes imaging can be material differentiation and quality inspection since it detects variation from dielectric and metal. Another application may be object segmentation as seen in the last example.

6.2 Active Stokes imaging

Our DoAP camera has demonstrated to be able to recover full-Stokes images from a scene. As explained in Section 2.5 many studies have been developed to enhance the contrast and the Signal-to-Noise-Ratio (SNR) in imaging using active illumination. In this case, specific types of samples are selected to experiment of active Stokes imaging. The six samples have in common being transparent. Consequently, the measurement is performed in transmission geometry using a polarized uniform illumination. It is applied to detect gradients in material properties. The incident light has a linear polarization state of $\vec{S_{in}} = [1.0, 0.0, -1.0, 0.0]$ with $\alpha_{in} = 135^o$.

Polarized sunglasses

The first sample is sunglasses with polarized crystals. Despite their frame and crystals being dark stained, both translucent plastic and crystal let pass the polarized light through it as appreciated in Figure 6.15. The materials behave similarly but not equally. Both exhibit linear polarization signatures changing the AOLP from 135^o of the illumination to 32^o in the plastic and 6^o in the crystal. Circular polarization signature appears in the inner limits of the crystals showing suffered tensions by the material. Inside the crystal, there is a region with distant behaviour since it is the refracted rays coming from the surface where the sample is placed onto.

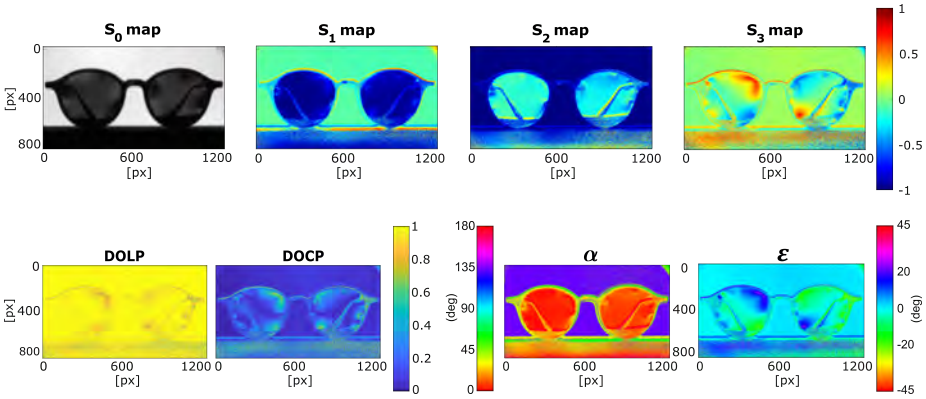

Figure 6.15: (Top) Maps of the Stokes parameters of polarized sunglasses. (Bottom, left) DOLP, and DOCP maps. (Bottom, right) Maps of AOLP and ϵ.

Glasses

The second sample consists of transparent glasses with an angular frame. Figure 6.16 shows that crystals present a stronger presence of a circular component in comparison with sunglasses. Their bigger shape and edgier borders, due to the frame shape, distort the crystal resulting in the stress gradient observed

in the maps. These glasses show elliptical and circular polarization depending on the zone in the crystal and its associated local ellipticity.

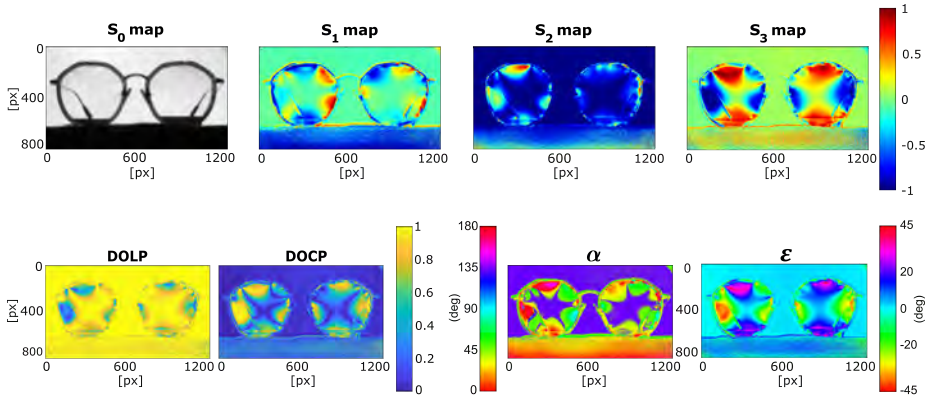

Figure 6.16: (Top) Maps of the Stokes parameters of transparent glasses. (Bottom, left) DOLP, and DOCP maps. (Bottom, right) Maps of AOLP and ϵ.

Plastic fork

The third sample is a plastic fork. Once more, new information is displayed through the polarimetric parameters maps in Figure 6.17 that passive Stokes nor intensity imaging (S_0 map) cannot detect. The background consists of homogeneous active illumination and its polarization agrees with the measured $\vec{S_{in}}$. S_1 and S_3 maps denote the existence of elliptical polarization. This correlates with the ellipticity map whose values do not reach $\pm 45^o$.

Miscellaneous scene

The fourth scene gathers various transparent objects to see their polarization signal. Figure 6.18 presents three plastic items and three pieces of tape at various orientations. Resembling the previous samples, the plastic objects show the same signal. In specific, the vase exhibits evident changes in polarization due to internal tensions. On the other hand, pieces of tape do not vary the active illumination components associated with linear polarization. However, they are only distinguishable from the background in the S_3 map. This leads to conclude that they act as retarders introducing some ellipticity. In addition, it is proof that contrast can be increased thanks to active illumination. Passive Stokes imaging only can retrieve the tape position when a polarizer is placed beneath it, as shown in Figure 6.6. Other experiments were conducted using tape and paper in passive mode and no detectable contrast was measured from the background.

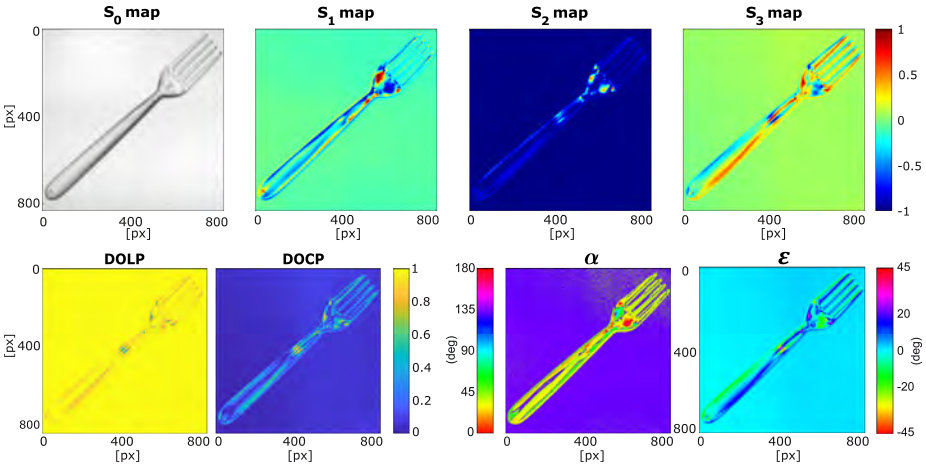

Figure 6.17: (Top) Maps of the Stokes parameters of a plastic fork. (Bottom, left) DOLP, and DOCP maps. (Bottom, right) Maps of AOLP and ϵ.

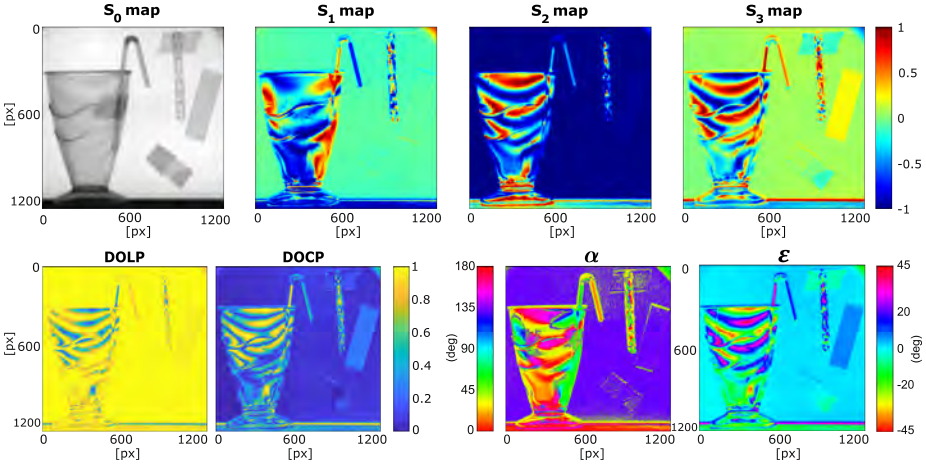

Figure 6.18: (Top) Maps of the Stokes parameters of the scene. (Bottom, left) DOLP, and DOCP maps. (Bottom, right) Maps of AOLP and ϵ.

Liquid samples

The next two pairs of samples are based on liquids. All of them are transparent and they cannot be distinguished through intensity. Firstly, water and 0.4 g/ml sugar dilution are compared in the same scene. This combination was already measured using passive Stokes imaging (Figure 6.12) and both samples are equivalent. Conversely, Figure 6.19 reveals two disparate natures. Water does not change the characteristics of incident polarization. On the other hand, sugar does rotate it from 135^o to 35^o. This is supported by the maps of S_1 and AOLP. The maps regarding circular properties remain invariant. Secondly, salt and

sugar dilutions are competing to see the effects on polarization in Figure 6.20. Once more, sugar dilution out-stands over the salt due to its chirality. However, water and salt from Figure 6.19 and Figure 6.20 are not separable.

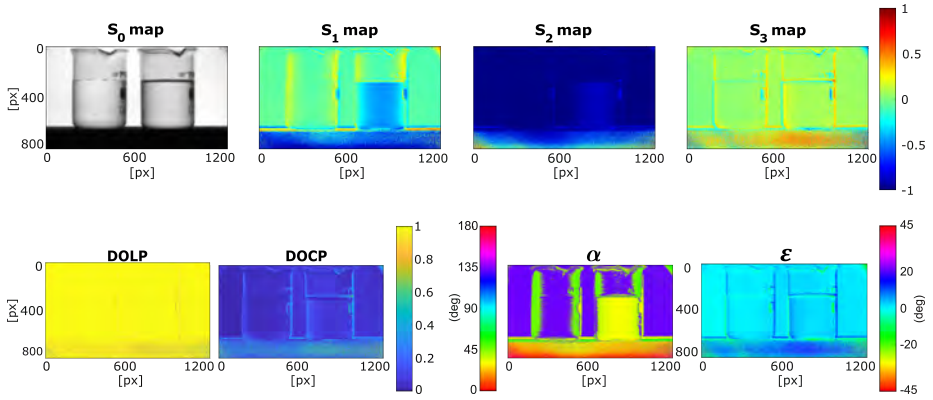

Figure 6.19: (Top) Maps of the Stokes parameters of the water (left) and sugar dissolution (right). (Bottom, left) DOLP, and DOCP maps. (Bottom, right) Maps of AOLP and ϵ.

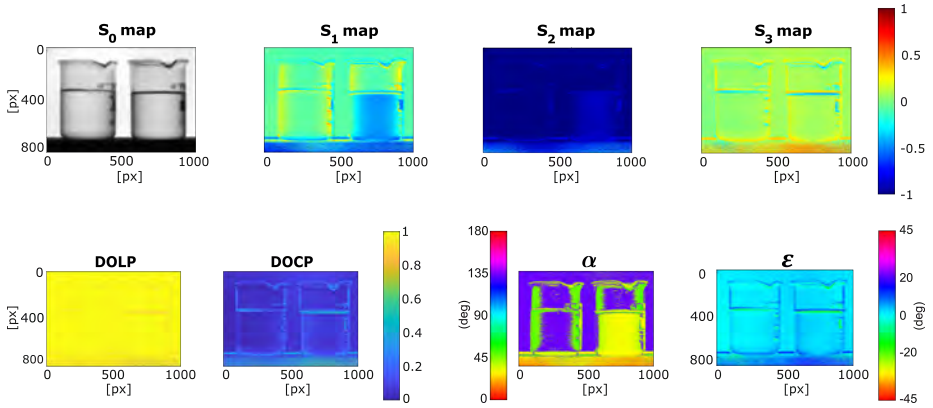

Figure 6.20: (Top) Maps of the Stokes parameters of the salt dilution (left) and sugar dissolution (right). (Bottom, left) DOLP, and DOCP maps. (Bottom, right) Maps of AOLP and ϵ.

Summary

Active Stokes imaging allows for enhancement of the contrast in scenes where passive Stokes do not detect good enough. All these samples have in common being transparent and the main effect of active illumination arises in plastics. Different polarization states from the incident polarization appeared. Stress from temperature and pressure profiles imparts local variations in the refractive

index of the amorphous solids such as glass and plastic. From the maps of active Stokes imaging, the associated refraction index can be calculated [176].

6.3 Mueller matrix imaging

The corresponding scheme detection for a complete determination of polarization properties consists in measuring the Mueller matrix (MM) of the scene. As previously explained in Section 2.1, MM gathers all the polarization properties as a transfer function does with a circuit. This 4x4 matrix represents mathematically all linear interactions the sample performs onto the input Stokes vector. Mueller matrix imaging consists in obtaining this matrix at each pixel of the scene to know its depolarization, scattering and retardance properties.

The MM can be recovered as explained in Section 2.2.2 using Equation (2.23) and broadband active illumination. The optimum four RPS of PSG in Section 5.3 are employed for the recovery of MM together with calibration matrix $\mathbf{W}$ from ECM. Several experiments are addressed in transmission and reflection geometry, ordered in complexity, to study the capability of DoAP for measuring the MM. Firstly, controlled and *a priori* known samples were presented to validate quantitatively the performance in Section 5.5. Then, several materials with uniform surface properties are measured in transmission. Finally, heterogeneous scenes in reflection are presented for a complete evaluation.

Vortex Retarder (VR)

The first sample consists in a Vortex Retarder (VR) (THORLABS WPV10-633), see Figure 6.21 (a). The vortex retarders are half-wave plates with a spatially varying fast axis orientation θ which rotates around its centre following Equation (6.1):

$$\theta = \frac{m}{2}\alpha + \delta \tag{6.1}$$

where m is the order of VR, α is the azimuth angle and δ is the fast axis orientation when $\alpha = 0^o$.

This sample corresponds to order $m = 2$ and it shows four-pattern polarization in the output as displayed in Figure 6.21 (b). The fast axis distribution is mapped in Figure 6.21 (left), where four modulation regions appeared from Equation (6.1). VR of order $m = 2$ is a polarization independent device. Due to its fast axis distribution, it will generate similar polarization distributions regardless of the incident polarization direction of the light. When performing MMI, the same results were obtained independent of the angle of rotation. The VRs are employed with input linear polarization in a single wavelength to generate Laguerre-Gaussian doughnut hole beams. These beams are used to enlarge the trapping region of optical tweezers and create special point spread functions in micro-lithography [177].

Figure 6.22 shows the MM measured in the VIS range. Examining the doctoral thesis about VRs [179], theoretical models and their experimental results agree with the measured MM by DoAP camera. They obtain also a blurred image of the sample, and it is not related to optical aberrations in the system. In our results, the components m_{11} and m_{44} show a circular signal

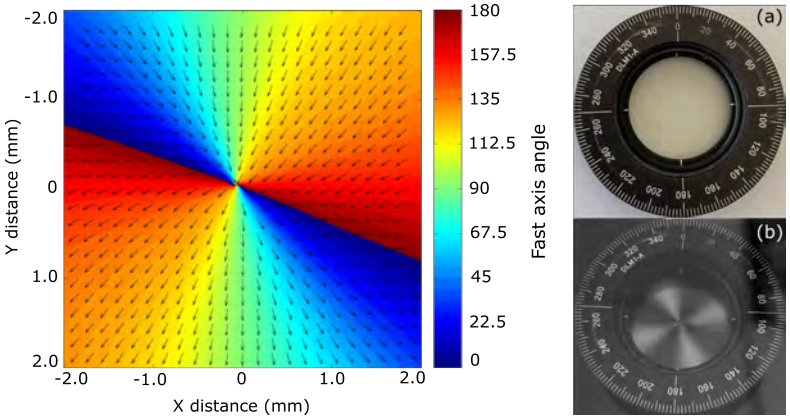

Figure 6.21: (Left) Fast axis angle distribution of the VR [178]. (a) Image of the m = 2 VR. (b) The intensity profile created by the VR when viewed between crossed LPs.

instead the doughnut profile (as expected monochrome wavelengths) since the measurement was carried out under VIS light. In the dissertation, theoretical MM for a $m = 2$ VR does only show signal in the diagonal and the m_{32} and m_{23} components but their experimental results exhibit additional signal in others. This is studied in detail in [179] and they conclude that the fluctuation of linear and circular retardation together with the orientation axis variation from ideal design values during construction originates non-idealities. Therefore, Figure 6.22 shows the MM of a non-ideal VR and gathers all the errors happening in the whole VIS band.

6.3.0.1 Liquid samples

The second experiment comprises measuring the MM of diverse liquid samples in VIS band. Water, ink and milk are tested and results are gathered in Figure 6.23. Water is treated as a reference sample since the resulting MM is almost an identity matrix, where the maximum absolute value of non-diagonal elements is smaller than 0.11. This means water does not depolarise the input light [180]. Ink needs to be very diluted in water to have a signal in transmission geometry. Its MM shows the signal of a non-depolarized light absorber since the diagonal elements show stronger values, and the non-diagonal elements are smaller than 0.06. It is an identity matrix, the ink acts as an absorbent reducing the component m_{43} of the MM of water. This means that the water and very diluted ink can preserve all of the polarization states. Milk is compounded by lipids, which act like scatterers, and water, which is the principal non-sensitive polarization absorption medium. As the concentration of milk is very low, the changes in MM are minor. It shows similar behaviour to ink but with lower values in the diagonal and some noticeable increments in non-diagonal elements. Absorption and scattering processes are present in milk due to the different compositions of the solute.

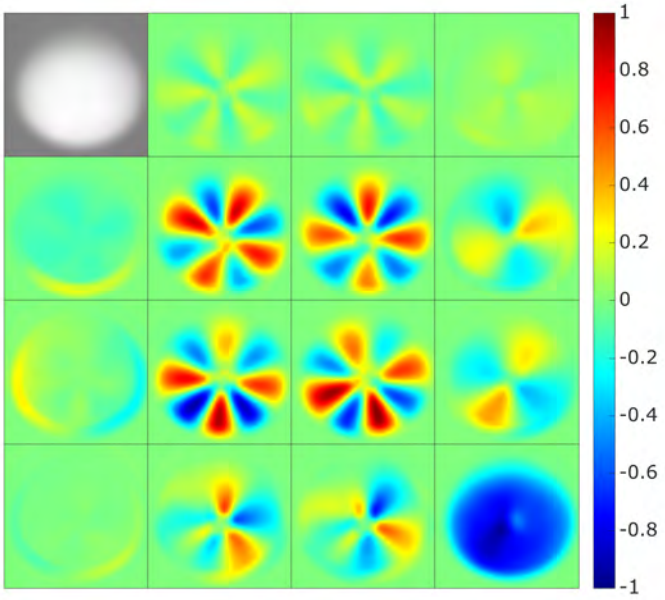

Figure 6.22: MM of a vortex retarder in VIS band. All matrix components are normalized respect to m_{11}. It represents the intensity and is displayed in grey scale.

Major changes in the MM can be appreciated with two different samples: vinegar and oil. Figure 6.24 present their associate MM, which are more complex than previous isotropic samples. Recalling the interpretation and parameters deduced from the MM explained in Section 2.2.2, it can be seen that they have in common first row, corresponding to the depolarization vector $\vec{P} \simeq [1.0, 0.0, 0.0, 0.0]$. The diattenuation vector $\vec{D}$, which is the first column of MM, differs in both cases: vinegar sample has $\vec{D} \neq \vec{P}$ and oil $\vec{D} \sim \vec{P}$. The remaining 3x3 matrix stores the depolarization, diattenuation and retardation information of the samples. It contrasts in both indicating that they possess different polarimetric properties. The respective matrices for each property can be decoded using a decomposition for a deeper analyses and understanding of the optical properties.

Sugar dilutions of distinct concentrations

Finally, the last experiment with liquids is done with sugar dilutions. Different concentrations of sugar are prepared and imaged in transmission using white light. Figure 6.25 shows the MM for six different concentrations: $[0.0, 0.042, 0.17, 0.23, 0.32, 0.40]$ g/ml. Four elements of the matrix m_{22}, m_{23}, m_{32} and m_{33} variate with sugar concentration. These elements refer to interactions in the linear polarization, as previously appreciated in Section 6.2.

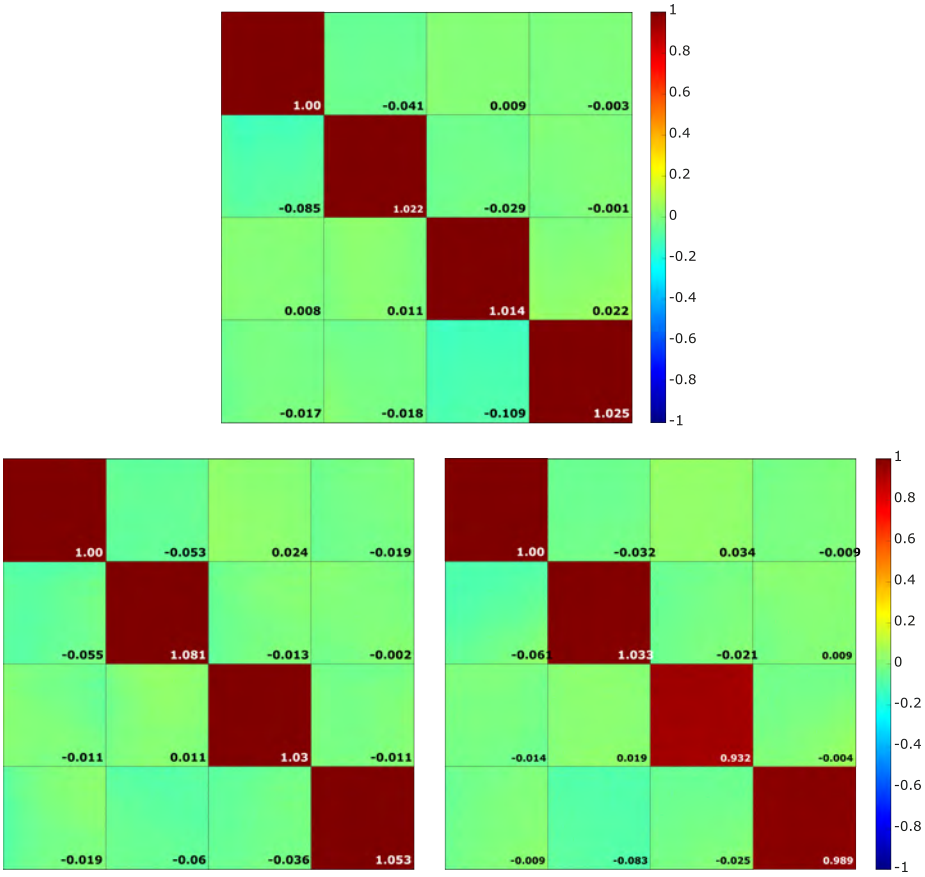

Figure 6.23: MM of water (top), diluted ink (bottom-left) and diluted milk (bottom-right) in visible band. All matrix components are normalized respect to m_{11}.

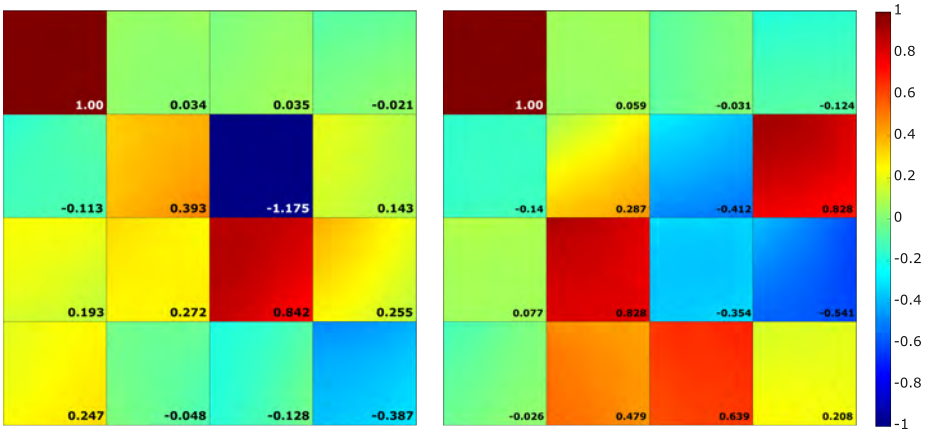

Figure 6.24: MM vinegar (left) and olive oil (right) in visible band. All matrix components are normalized respect to m_{11}.

Sugar has optical activity as stated in Stokes imaging. It is a chiral molecule and it rotates the plane of linear polarization, as demonstrated in S_1 and AOLP maps of Figure 6.19. The retrieved curves by the DoAP camera in Section 6.2 agree with the behaviour of glucose [181]. When increasing the concentration of glucose, the absolute value of m_{23} and m_{32}, which refers to the circular retardance, raises. On the contrary, the values of m_{22} and m_{33} decrease demonstrating the presence of depolarization.

Many studies have studied detecting glucose based on polarization in a non-invasive manner [137, 147]. They measure the polarization signal using MMI and decompose the resulting MM to obtain the optical rotation. The concentration of glucose can be retrieved from a linear relation with the angle of rotation [137, 138].

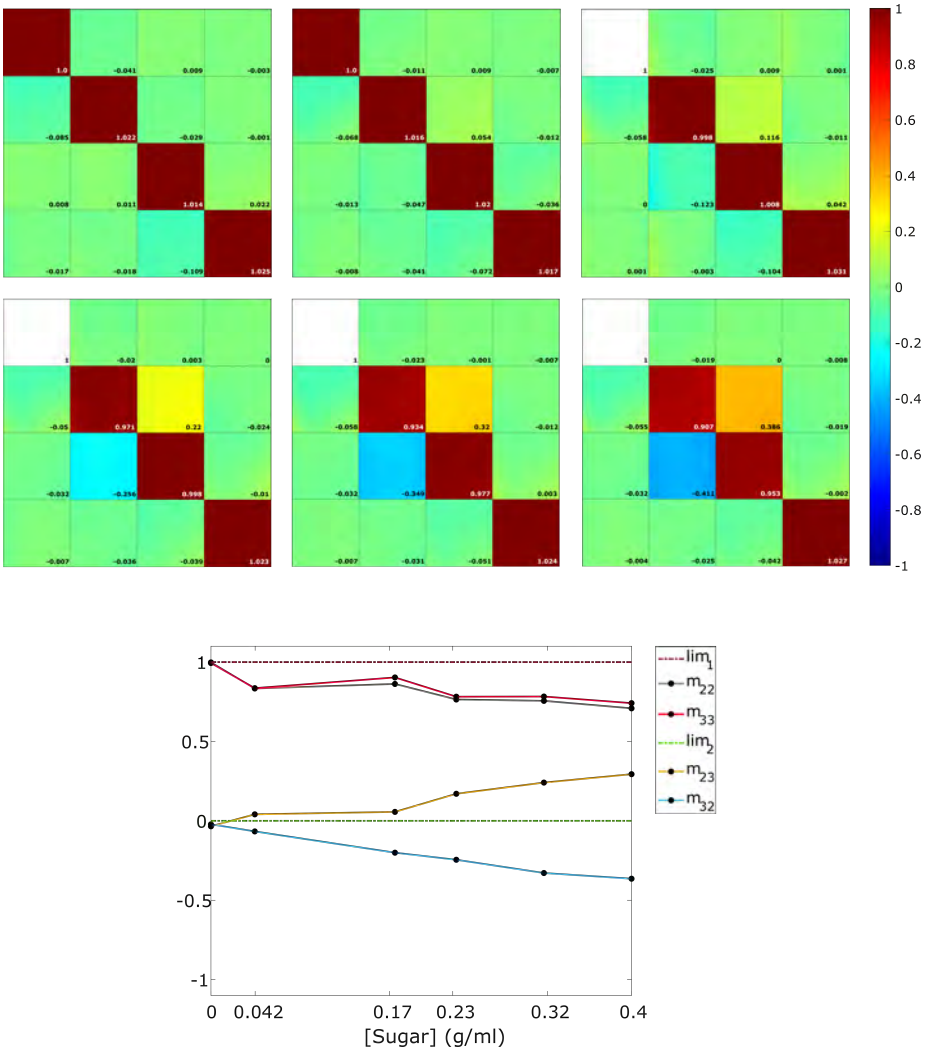

Figure 6.25: (Top and middle) MM of sugar dilutions at different concentrations. They are ordered by higher solute concentration from left to right. All matrix components are normalized respect to their m_{11}. (Bottom) Graphic of the mean value at the four components which vary with sugar concentration. Red dashed line correspond to the ideal value of m_{22} and m_{33}. Green dashed line stands for the ideal value of m_{23} and m_{32}.

The following experiments correspond to objects imaged in Section 6.1 in order to see the differences between Stokes and Mueller matrix imaging when recovering polarization information.

Polarizers

The first set of three measurements reproduces the validation scene composed of different polarizers in Section 6.1, followed by the polarizer with pieces of tape and finishing with a white paper with pieces of tape on it.

MM of validation scene is presented in Figure 6.26. It shows the dependence of each component of the matrix on the different polarization states. The theoretical MM for each polarizer (following the previous A-E notation) are gathered in Table 6.2 for a better comprehension of the image. Since the m_{11} component shows the intensity information and it has the same behaviour for all polarizers, it can be concluded that all polarizers have the same transmission in reflection. The components of rows and columns $1-3$ present dependence on linear polarization, whereas row and column 4 correspond to circular polarization. DoAP demonstrates its ability to reconstruct the MM of a heterogeneous scene by the agreement between the experimental results and the theory.

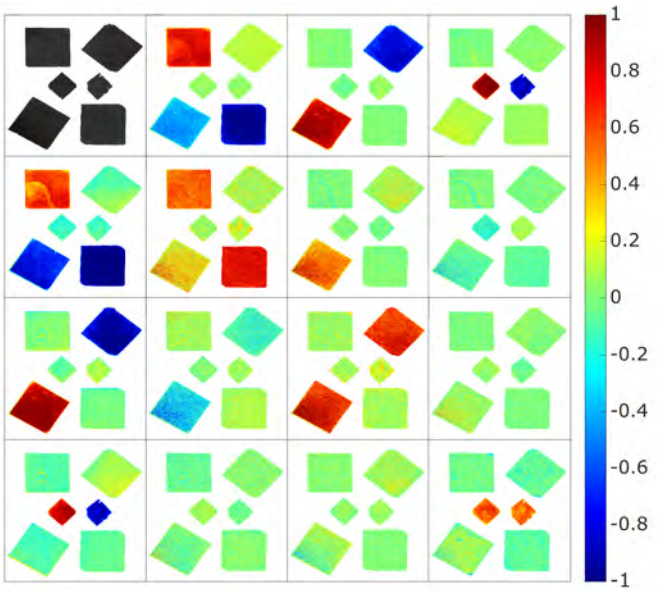

Figure 6.26: MM of several polarizers at different orientations. All matrix components are normalized respect to m_{11}. It represents the intensity and is displayed in grey scale. The polarizers are labeled from A-E. A-D are LPs at 0^o, 135^o, 45^o and 90^o. E is a right-handed CP and F is left-handed.

A	B	C	D
$\begin{pmatrix} 1 & 1 & 0 & 0 \\ 1 & 1 & 0 & 0 \\ 0 & 0 & 0 & 0 \\ 0 & 0 & 0 & 0 \end{pmatrix}$	$\begin{pmatrix} 1 & 0 & -1 & 0 \\ 0 & 0 & 0 & 0 \\ -1 & 0 & 1 & 0 \\ 0 & 0 & 0 & 0 \end{pmatrix}$	$\begin{pmatrix} 1 & 0 & 1 & 0 \\ 0 & 0 & 0 & 0 \\ 1 & 0 & 1 & 0 \\ 0 & 0 & 0 & 0 \end{pmatrix}$	$\begin{pmatrix} 1 & -1 & 0 & 0 \\ -1 & 1 & 0 & 0 \\ 0 & 0 & 0 & 0 \\ 0 & 0 & 0 & 0 \end{pmatrix}$

E	F
$\begin{pmatrix} 1 & 0 & 0 & 1 \\ 0 & 0 & 0 & 0 \\ 0 & 0 & 0 & 0 \\ 1 & 0 & 0 & 1 \end{pmatrix}$	$\begin{pmatrix} 1 & 0 & 0 & -1 \\ 0 & 0 & 0 & 0 \\ 0 & 0 & 0 & 0 \\ -1 & 0 & 0 & 1 \end{pmatrix}$

Table 6.2: Theoretical MM of A-E polarizers present in Figure 6.26. A-D correspond to LPs at different orientations, meanwhile E-F are right and left-handed CPs, respectively.

Then, two pieces of tape are placed onto the LP at 0^o, already covered with tape in the horizontal direction. Again, the intensity measurement does not show contrast among the elements of the scene, meanwhile, the rest of the components can identify the two pieces of tape. This is an improvement from Figure 6.6 where the piece of tape at the top is hardly distinguished. The matrix components related to S_1 and S_3 parameters are different from zero, agreeing with the previous Stokes maps. The presence of tape introduces retardance to the polarizer as seen in m_{33} and m_{44} where the values are different from zero, in comparison with Figure 6.26.

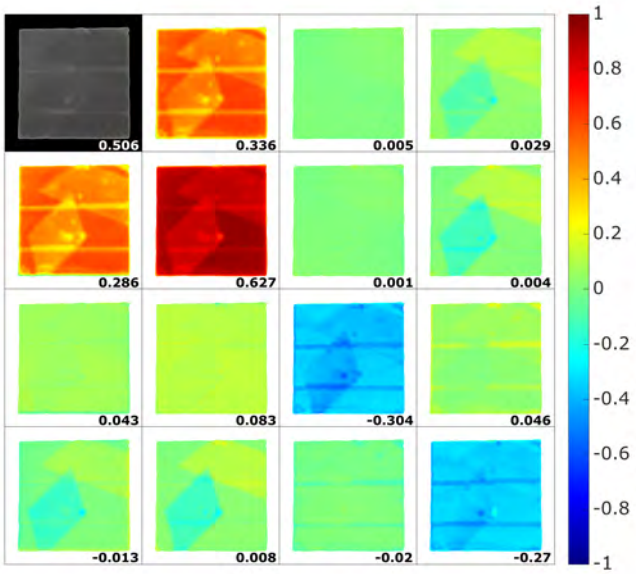

Figure 6.27: MM of pieces of tape in different positions and orientations placed on a LP. All matrix components are normalized respect to their m_{11}. It represents the intensity and is displayed in grey scale.

Finally, two tapes of different materials (one translucent and the other transparent) are placed on white paper. This experiment was not presented in Section 6.1 since no contrast between samples and background was detected. Although the orientation of the crosses where similar, the behaviour between tapes differs. The translucent tape seems to introduce higher retardance than the transparent counterpart. In addition, the white paper seems to behave like a depolarizer since diagonal components of the background possess higher values.

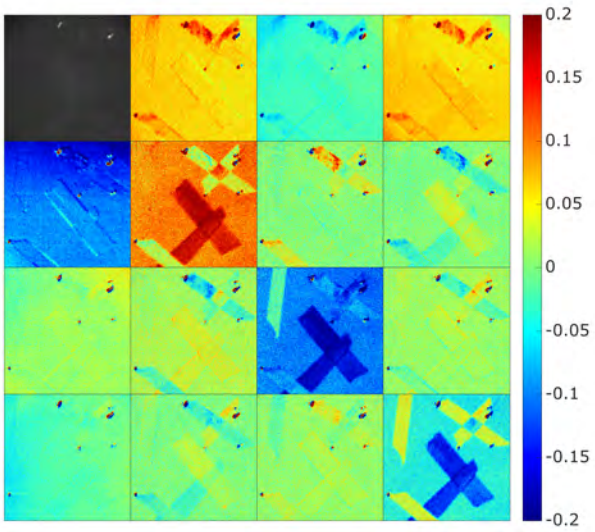

Figure 6.28: MM of pieces of tape in different positions and orientations placed onto a white paper. All matrix components are normalized respect to their m_{11}. It represents the intensity and is displayed in grey scale.

Stones

The second set measures the MM of the granite and calcite stones. In these cases, clear differences arise in this type of imaging. Granite stone (Figure 6.29) and calcite stone (Figure 6.30) show some highlighted elements in the diagonal but they differ in the non-diagonal components where some weak signal is retrieved from the granite stone. This is due to granite stone having silver elements embedded and they are detected in the MM. Stokes imaging does not show with clarity the silver in granite and cannot distinguish it from calcite.

Electronic card

The third set consists in measuring the electronic card to study the complete response to polarization. Figure 6.31 gives the associated MM. Setting again a threshold, as in Stokes imaging, metallic and dielectric parts may be separated but this takes more time that only measuring the Stokes vector.

Complex scene

The fourth experiment gathers several materials in the same FOV. Figure 6.32 displays the obtained MM of (from left to right) a rubber, a flash drive (half metallic, half wood), a polystyrene "S"-letter, a ceramic star and a plastic container are imaged. Their polarization response differs clearly between the metallic parts and dielectric materials, in contrast with Stokes imaging.

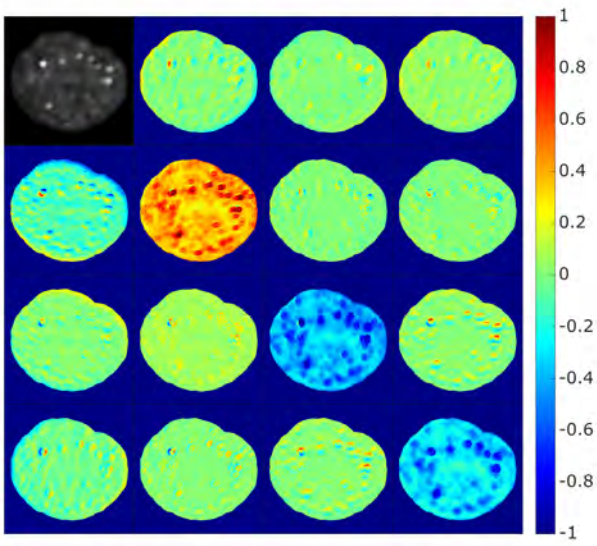

Figure 6.29: MM of granite stone with embedded silver. All matrix components are normalized respect to their m_{11}. It represents the intensity and is displayed in grey scale.

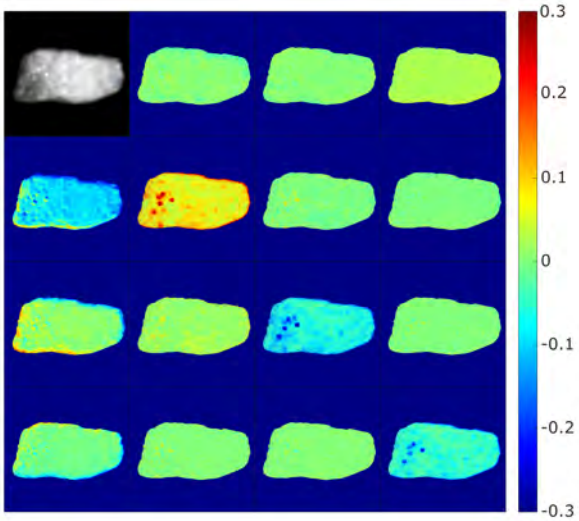

Figure 6.30: MM of calcite stone. All matrix components are normalized respect to their m_{11}. It represents the intensity and is displayed in grey scale.

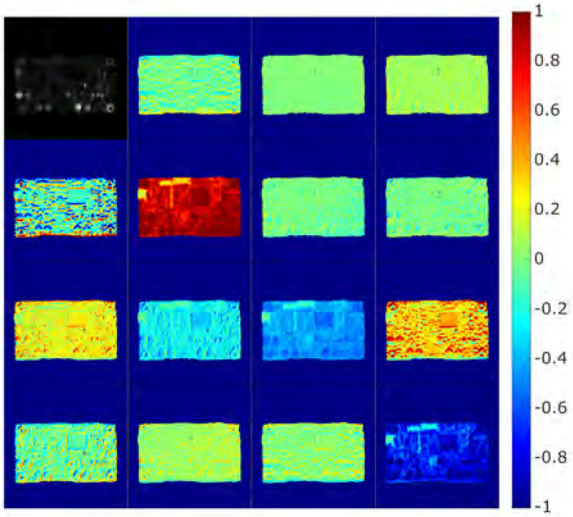

Figure 6.31: MM of an electronic card with plastic and metallic elements. All matrix components are normalized respect to their m_{11}. It represents the intensity and is displayed in grey scale.

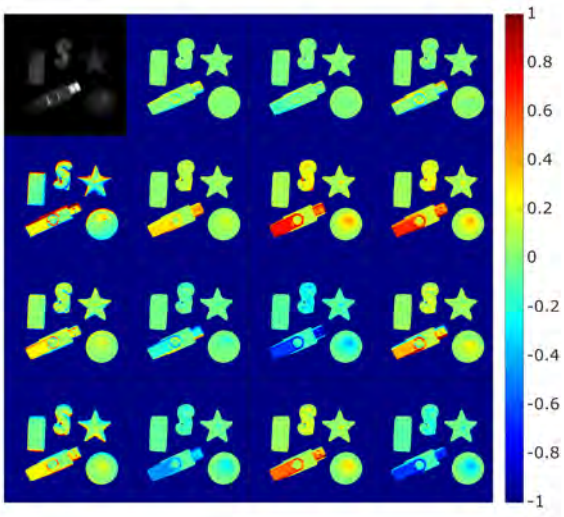

Figure 6.32: MM of several objects with diverse compositions. From left to right: a rubber, a flash drive, a polystyrene "S"-letter, a ceramic star and a plastic container. All matrix components are normalized respect to their m_{11}. It represents the intensity and is displayed in grey scale.

Summary

In this section, several tests are presented to demonstrate the capability of DoAP system to recover the MM of a scene. Quantitative recovery of the MM is done with the achromatic QWP sample, which agrees with theoretical values with errors below 10%. Regardless a more qualitative study is done with the rest of the samples, many of them are contrasted with existing studies in the literature. MMI shows more complete polarization properties in the samples that are not distinguished in Stokes imaging.

Main optical properties of materials: depolarization, diattenuation and retardation appear correlated in the information provided by the MM. A further process is needed to have them independently employing MM decomposition. Several methods are developed in the literature, though the more common is Lu-Chipman decomposition.

Chapter 7

Polarimetric imaging: seeing through fog

A Viking ship is late in its return home from the newly discovered lands far west. Winter is around the corner and the weather will soon turn ugly. It's imperative that the helmsman maintains the course due East. But where exactly is Home? The sky is becoming more cloudy every passing day. Most nights the stars are not visible and even during the day the sun has difficulty breaking through. Daylight is short and during good part the sun illuminates the sky from below the horizon . . . somewhere. Hanging from the top of the knorrship mast a sailor squints his eyes looking for clues in the brightness of the clouds . . . to no avail. Then Leif the Lucky spots an opening in the clouds. He reaches for the pouch hanging from his waist and takes out his Sunstone. Through the crystal he looks at the small patch of blue sky. He turns the rock until it becomes yellow. Next he shouts to the helmsman with his stretched arm pointing starboard . . . towards Home. H. LaFey, "The Vikings," National Geographic, Vol. 137, p.528, 1970

This last chapter addresses the experimental application of polarimetric imaging in a real-world problem: vision through turbid media. The Icelandic sagas tell the story of how the Vikings sailed from Bergen on the coast of Norway to Iceland, continuing to Greenland and, likely, Newfoundland in the American continent. This remarkable sailing achievement was realized between 700 -1100 AC, before the magnetic compass reached Europe from China. How did they steer true course in the long voyages out of land sight, especially in the common bad weather and low visibility of those high latitudes? In 1967, a Danish archaeologist, Thorkild Ramskou, suggested that the Vikings might have used the polarization of the skylight for orientation when clouds hid the sun position [1]. They would have used as polarizers natural crystals available to them, the famous sunstones described in the sagas. Between 2001 and 2007, Horváth and colleagues performed experiments to see if the proposed method worked [182]. The researchers used a device that measures polarization to computed the difference between the angles of sunlight when it was cloudy, clear, foggy and completely overcast. They found that the position of the sun in the sky could be calculated even in clouds and fog. When the sky was completely overcast, though, the sun was harder to find. This issue attracts special interest due to its significance in multi-modal sensors development for remote sensing, surveillance tasks or autonomous vehicles. Theoretical simulations have analysed the behaviour of polarized light and the main conclusion was the behaviour depends on the input polarization state [157–159].

Two different studies are disclosed in this last part of the thesis. In the

first place, the fog polarization signature is studied using a modified DoFP camera to see if polarimetric imaging yields an improvement in SNR in both detection schemes: reflection and transmission. Afterwards, quantitative and qualitative analyses are performed using the DoAPC in reflection to see the capability of active Stokes imaging for detecting embedded objects in fog at different visibilities.

7.1 Fog characterization

Images obtained through scattering media contain information from two separate sources: the signal coming from the object and the scattered light. The luminance coming from the object (L_{obj}) is degraded by the scattering media as a function of the distance to the camera ($T(dist)$). In the case of active illumination, the main scattering source however comes from the backscattering from the illumination system (B) rather than the scattering coming from a background light source (A), although this may not be negligible [166, 183].

$$I = S + B = L_{obj} \cdot Illum \cdot T(dist) + B + A \tag{7.1}$$

According to this model, the signal coming from an object (S) is related to its luminance (L_{obj}) which depends on its polarization response to the active illumination ($Illum$) and its distance to the camera and also on the scattering properties of the medium ($T(dist)$). Figure 7.1 displays a schematic description of the concepts. From the above formula, it is clear that proper illumination is key since it plays an important role in the signal intensity of the object, which is mixed with the scattering of the medium ($T(dist)$), and the backscattering (B) of the media which becomes an extra noise term. Moreover, there can be additional noise from airlight illumination (A). This is the reason why a homogeneous distribution is sought in order to properly detect the objects.

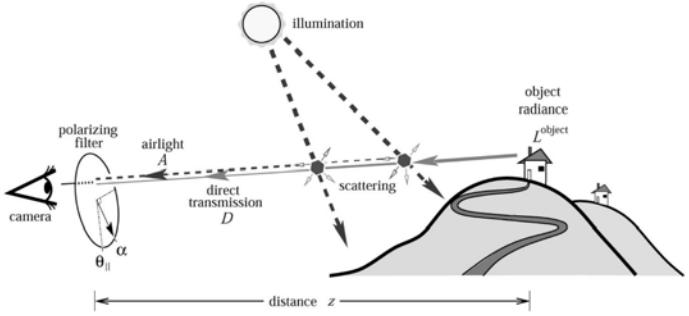

Figure 7.1: Schematic representation of the active illumination imaging model [183].

To understand the issues of imaging through fog, we study the scattering properties of fog when imaging by reflection and transmission for different fog density conditions and distances. Thus, both backscattering (B) and forward scattering ($T(dist)$) will be characterized for both linear and circular polarization illuminations. This is expected to provide conclusions on the polarization mode that yields better performance.

Experimental set-up

Experiments seek to reproduce a real fog environment to introduce the imaging system, composed of a polarimetric camera with active illumination, and obtain relevant data about fog properties. Therefore, a large-scale fog chamber is used to generate the real-fog conditions and a modified DoFP is used as a polarization detector. The different components of the experimental set-up to perform the studies are explained in the following.

Imaging system

The imaging system consists of a combined polarization and colour-sensitive camera, together with an active illumination system composed of white light polarized illumination set as an array. Both systems (camera and illumination) can switch between linear and circular polarization and their housings have been arranged to fulfil the IP68 standard. They are mechanically assembled jointly in order to homogeneously illuminate the whole Angular Field-of-View (AFOV) of the imaging system which is 20x20 degrees (HxV). Each system is explained in detail next.

The detector is a Phoenix 5.0 MP Colour Polarization camera (LUCID Vision Labs) together with an objective of fixed focal length (EO #59-871). It is a DoFP imaging polarimeter that allows measuring the intensity (S_0) and the linear Stokes components of light (S_1 and S_2). The camera incorporates the Sony IMX250MYR CMOS sensor, which consists of an array of linear micro-polarizers oriented at four different angles (0^o, 45^o, 90^o, and 135^o), allowing the recovery of linear Stokes parameters, see Figure 7.2 (left).

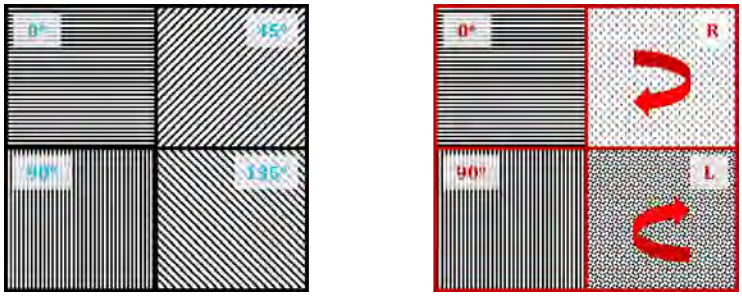

Figure 7.2: (Left) Macro-pixel composed by the four LP with axis at (0^o, 45^o, 90^o, and 135^o). (Right) Macro-pixel after placing the QWP oriented at 0^o. Channels corresponding to the angles 45^o and 135^o are expanded to detect left (LC) and right-handed (RC) circular polarization, respectively. Linear channels 0^o and 90^o remain unchanged.

For measuring simultaneously both linear and circular polarization states, an achromatic QWP (THORLABS, AQWP10M-580) is placed in front of the objective and aligned with the optical axis of the micro polarizer at 0^o to measure the S_3 parameter. In this manner, the DoFP camera is no longer a linear Stokes detector but a snapshot orthogonal state contrast analyser, since the S_2 parameter cannot be detected. This transformation can be observed in Figure 7.2 (right). The former 45^o and 135^o channels can now discriminate right-handed (RC) and left-handed (LC) circular polarization states instead of detecting linearly polarized light. Since the QWP fast axis is parallel to the 0^o linear polarizer, the 0^o horizontal (HL) and 90^o vertical (VL) linearly polarized light remains unaltered as they are eigenvalues of the Mueller matrix of the retarder.

The QWP is placed on a flip-flop mount (TRF90/M - 90° Flip Mount for Ø1" Filters and Optics, M4 Tap) in front of the objective of the camera in order to easily switch between circular and linear polarization states. This slight mechanical modification also enables varying the focal length of the objective for better focusing without affecting the QWP optical fast axis alignment with the axes of the micro polarizers.

In order to assure the correct position of the micro-polarizers, horizontally polarized light is measured using the set-up. The horizontal 0^o channel detected the maximum signal. Afterwards, a radiometric calibration was performed to tackle the non-uniform responses due to variance in pixel detectivity and discrepancy in the transmission of the micro-polarizers at the different orientations. The change in the aperture of the objective does not affect the polarization state, showing the QWP axis is properly aligned with that of the camera.

To achieve waterproof conditions for the camera, required for survival in the fog chamber, the camera is placed inside an aluminium IP68 housing case (Retex, 140 x 140 x 91 mm) with a polarization-maintaining N-BK7 window for the visible range. (WG12012 - Ø2" N-BK7 Broadband Precision Window,

Uncoated, thickness = 12 mm). The whole system is shown in Figure 7.3.

Figure 7.3: (Left) Enclosed camera into an IP68 housing cage to preserve the seal of the inner cavity. (Right) Set-up of the modified DoFP camera together with the QWP aligned to the horizontal axis.

The active illumination needs to be carefully designed to provide uniform illumination to all AFOV, since the variables $Illum$, B and A in Equation (7.1) directly depend on it. The first test showed that using a single light source provided a poor illumination distribution across the FOV, even if using large diameter, long focal length systems. Consequently, an array of 4 active light sources has been designed and built to produce a homogeneous illumination distribution. The change in illumination obtained after the modifications is displayed in Figure 7.4.

Figure 7.4: Backscattering signal of the active illumination under dense fog conditions produced by the illumination distribution. (Left) Inhomogeneous distribution produced by the single light source. (Right) Homogeneous distribution produced by the 2x2 illumination array.

The individual optical design of each light source is the same as the one for MMI but varies the exit aperture diameter. It consists of white light emitted by LEDs followed by a polarizer. The detailed optical design can be revised in Section 3.3 in Figure 3.21. The 2x2 array was mechanically assembled around the camera housing as shown in Figure 7.5. Each light source is placed equidistant from the optical axis of the polarimetric camera. This allowed illuminating all the FOV of the camera with a constant optical power that can be adjusted electrically. The polarization of the emitted light may be linear horizontal or

left-circular by just reversing the circular polarizers, maintaining the optical power for the same electrical inputs.

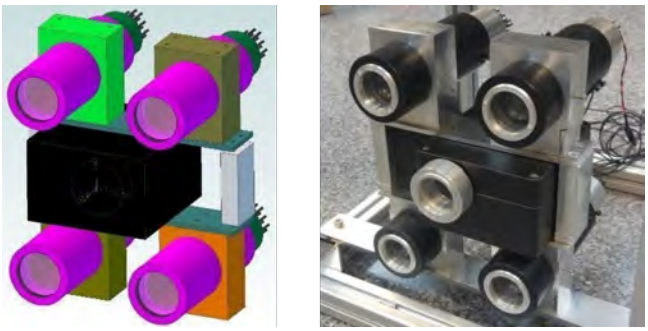

Figure 7.5: (Left) Mechanical design of the system. (Right) Picture of the built unit.

Since the polarization of the illumination can be either linear or circular as well, we define the channels of the camera as co-polarized (CO) for the same polarization state of the active illumination and cross-polarized (CROSS) for its orthogonal polarization state. In this manner, when illuminating with a HL polarization, the CO channel is the 0^o channel whereas the CROSS is the 90^o one. Analogously, when the illumination is set to LC polarization, the CO is the LC channel and the CROSS is the RC one.

Fog facility

Tests are performed in a dedicated indoor facility where it is possible to control and repeat the desired weather conditions, in particular regarding the density of the fog. The selected platform was CEREMA (Centre d'Études et d'expertise sur les Risques, l'Environnement, la Mobilité et l'Aménagement) dependent on the French Ministry of Transportation and infrastructures. The climate chamber is located in Clermont-Ferrand (France).

The facility is composed of two main parts: a control room and the test room. In the control room PCs, dedicated instrumentation and power supplies can be installed and connected to the test room via a small gate. The control room is separated from the test room (where rain and fog are produced) by a wall. This wall is glazed, which allows the monitoring of the test room from inside the control room. The test room is an infrastructure allowing fog, and also rain, to be generated under controlled conditions. It is 31 m-long and includes a 15-m fixed section (tunnel) and a 16-m greenhouse with an opaque cover to simulate nighttime conditions. This platform is 5.5 m wide and 2.3 m high. Fog is produced by nozzles spraying water under high pressure. Therefore, it is possible to produce a fog of different densities by modifying the quantity of water injected, in all temperature and humidity conditions. Visibility (meteorological visibility) is measured by a laser transmissometer and can be kept constant by 10-m increments between 10 m and 100 m.

It is possible to perform two types of fog tests: (1) production of fog until saturation (meteorological visibility < 10m) and then a dissipation to a meteorological visibility of >400 meters; and (2) making meteorological visibility steps from 10 to 80 meters sustained in time. We have used both options. It is also possible to produce two kinds of droplet size distribution for fog, one with small droplets (one mode around 1 micron) and the other one with bigger droplets (two modes with distributions of droplets around 1 and 10 microns). More detailed information about the facility can be found in [184, 185].

Finally, all the measurements are referred to meteorological visibility. The meteorological visibility is measured by a transmissometer placed inside the test room [186]. The transmittance corresponds to the ratio of the luminous flux received to the luminous flux emitted by the source. The meteorological visibility is calculated from the measurement of this magnitude in real-time and it is monitored in the control room.

All the tests are performed using cycles of fog with visibilities ranging from 5 m to 95 m. The particle size of the water corresponds to a Gaussian distribution with a mean diameter of 2 μm, being similar to the statistics of natural radiation fog [185]. The measurements are done in night-time conditions to avoid undesired noise.

Reflection scheme detection

These tests aim to compare the backscattering of the fog under the same illumination conditions but different polarization states at various visibilities. In these experiments, the source and detector are placed in the same plane facing the fog chamber to measure the backscattered light. The chamber does not contain any object in the FOV of the camera to minimize reflection artefacts. The camera is set to 1 second of exposure time and no gain, and the luminous flux emitted in circular and linear polarization illumination is adjusted to be the same. Each image has a size of 1224x1024 pixels. The scheme of the set-up is represented in Figure 7.6.

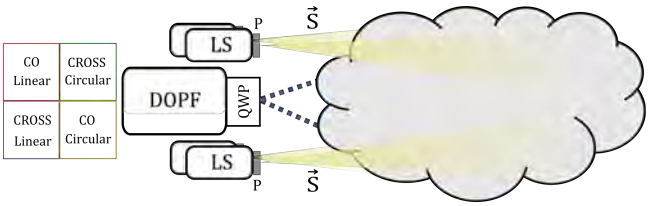

Figure 7.6: Scheme of the set-up for detection in reflection of backscattered light from fog under active illumination. The light source (LS) with the polarizer (P) illuminates the fog with polarization $\vec{S}$ that is backscattered to the modified DoFP camera.

The backscattering signal from active illumination is, in principle, proportional to the density of the fog and inversely proportional to visibility. So, the larger the fog density, and the lower the visibility, the stronger the amount of backscattered light. The intensity registered at the detector coming from the

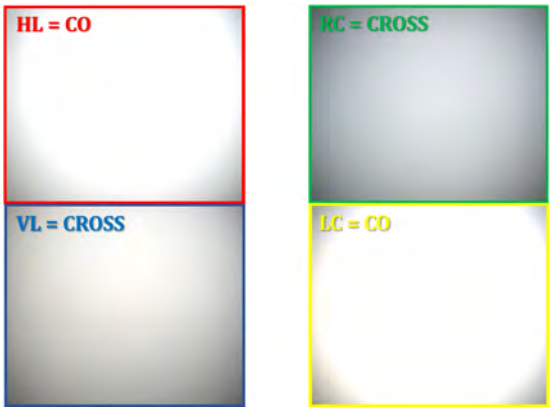

Figure 7.7: Backscattered light signal in respective CO and CROSS channels for HL (left) and LC (right) input polarization. CO channels are saturated for the maintenance of polarization in backscattered light.

backscattered light at extremely low visibilities is the most intense. This can be seen in Figure 7.7 which shows the amount of backscattered light in extremely short visibility conditions (below 10 m) in the CO and CROSS channels for HL and LC input polarizations. In both cases, the most saturated signal coincides with CO channel, hampering the perception of the camera in this channel. On the contrary, CROSS polarization channel is less affected by the backscattered light. This implies that backscattering in extremely dense fog essentially maintains the same polarization state as the illumination since the optical path of the backscattered photons is too short to get depolarized.

This hypothesis must be quantitative contrasted. Illumination conditions are equivalent in circular and linear states, so comparisons among them are valid. Figure 7.8 shows the mean detected intensity of a central ROI as a function of visibility for CO and channels, for both circular and linear illumination-detection. It can be observed that for the circular illumination, intensity in CO/CROSS channels does not meet until large visibility values. This occurs when the initial polarization signature has been completely randomized since orthogonal channels are receiving the same amount of energy. Light with LC polarization is still polarized until 80 m of visibility. It should be stated that below 0.2 in the grey scale (corresponding to 85m of visibility at circular polarization) the amount of backscattered signal is not significant and the discussion is not applicable. On the other hand, for linear input polarization, CO and CROSS channels overlap faster,at around 17m of visibility. This leads to the conclusion that circular polarization is expected to maintain polarization 5 times further than linear illumination. Therefore, the ellipticity shows larger preservation than AOLP and fog's memory effect for circular polarization appears.

It can also be appreciated that circular CROSS channel values are significantly lower than the linear ones at low visibilities, suggesting it receives less backscattering signal. This fact, together with the disparity between circular

CO and CROSS channels, demonstrates the superiority of circular polarization for contrast enhancement in imaging.

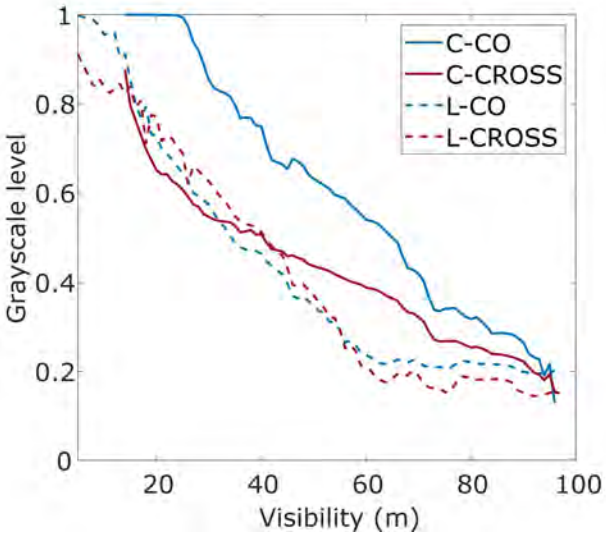

Figure 7.8: Mean intensity value of the backscattered light by fog for circular (C) and linear (L) polarization CO and CROSS channels as a function of the visibility.

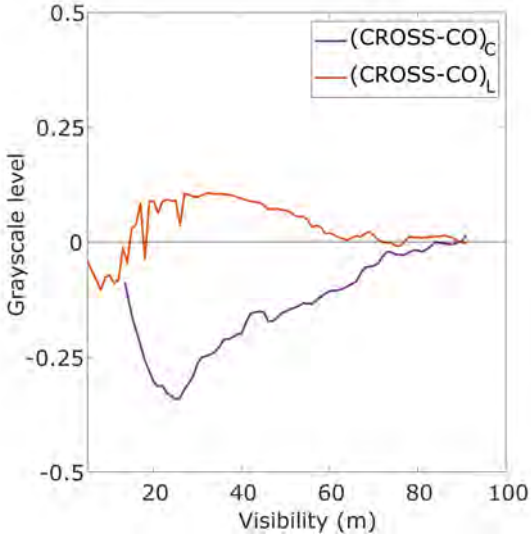

Figure 7.9: Difference between CO/CROSS channels of the backscattered light as a function of visibility.

Another way to compare the persistence of circularly over linearly polarized light is to compute the difference between the CO/CROSS channels, corresponding to the S_1 parameter for linear polarization and the $(-S_3)$ parameter for circular one. Having a larger distance from zero involves a higher contrast between the orthogonal channels and the possibility of improving contrast in detection. Negative values demonstrate the superiority of CROSS channel in both polarizations, although circular illumination shows always a greater performance than the linear one. The optimum visibility distance is at 25m where the circular CROSS channel is affected the least by backscattering. These results align with the previous statements supporting the argument circular polarization is more stable to depolarization in turbid media than linear polarization.

Formerly, the test scene was an empty fog environment to understand the behaviour of backscattered polarized light. Now, the scene contains embedded objects in fog, with known properties, to study the contrast capability of our system for their detection. The test scene comprises calibrated diffusive panels placed at three different distances (10 m, 15 m and 20 m) from the illumination-camera system over a whole visibility cycle. The scene is presented in Figure 7.10 with the two panels of interest highlighted: a black panel of 0% reflectance in orange and a white panel of 100% reflectance in blue. The chosen active illumination is LC based on the previous test results and the camera settings remain the same.

Figure 7.10: Calibrated diffusive panels for embedded object detection in fog. The two panels of interest are highlighted: a black panel of 0% reflectance in orange and a white panel of 100% reflectance in blue.

The contrast between the black and white diffusive panels is defined as a figure of merit for quantifying the ability of the system to discriminate between the objects. Several ways of computing contrast are described in literature [187], but the most extended, even in the presence of different materials in the scene, is Michelson contrast (C_M) [188]. This contrast is defined as:

$$C_M = \frac{I_{max}(x_b, y_b) - I_{min}(x_d, y_d)}{I_{max}(x_b, y_b) + I_{min}(x_d, y_d)} \tag{7.2}$$

It is calculated by subtracting the average pixel value in the dark area, $I_{min}(x_d, y_d)$, from the average pixel value in the bright area $I_{max}(x_b, y_b)$, divided by the sum of the average value in these respective areas. This standard contrast ranges from 0 to 1, where 1 stands for maximum contrast and is obtained when no turbid media is present or when the applied algorithm greatly reduces the influence of haze.

Figure 7.11 shows the evolution of the contrast calculated between the ROIs corresponding to the white and black diffusive panels at the three distances. As already mentioned, the S_0 signal corresponds to the intensity signal of a conventional RGB camera. The CO and CROSS signals correspond to the same channels of the polarimetric system under circular illumination.

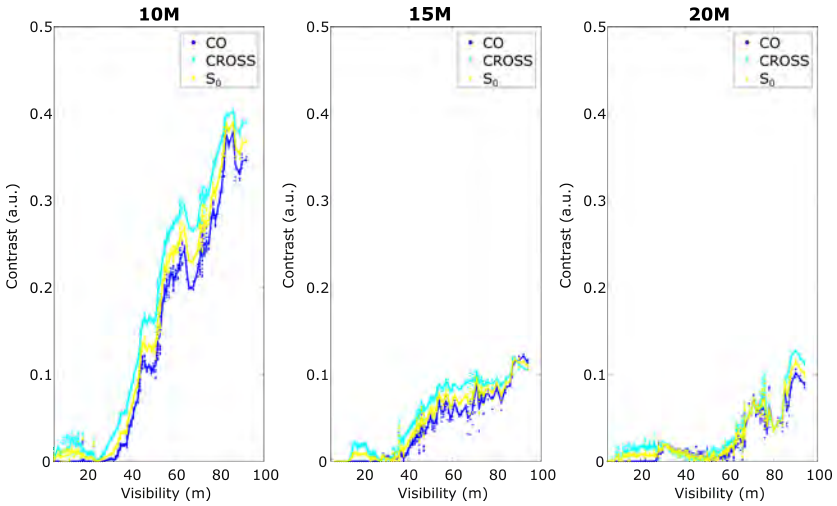

Figure 7.11: Contrast between the black and white diffusive panels at distances of 10 m, 15 m and 20 m under circular active illumination. Contrast is calculated directly on the measured intensity images: S_0, CO and CROSS.

CROSS channel outperforms in all distances over the CO and intensity channels as inferred from previous results. Fog is the principal source of the backscattered signal. Detecting with the CROSS channel allows filtering the photons coming back from the fog, which maintain the initial polarization, and differentiating between the panels. The arriving photons to the CROSS are the ones that changed their polarization in the reflection on the diffusive plate. Simultaneously, an active LiDAR system measured the same scene using a circularly polarized beam and provided the same conclusions in the infrared wavelength of 1064nm [164]. These results agree with the work of [189] where distinct materials embedded in fog are measured under active illumination and CROSS circular channel outperforms in dielectric materials.

Summary

These experiments confirm that circular polarization is more likely to be maintained than linear polarization through a turbid media such as fog, confirming the so-called polarization memory effect. Consequently, using circular polarization may improve image contrast under fog conditions since the backscattering effect can be damped using the CROSS polarization channel and the detection range can be extended. In addition, the difference between CO/CROSS appears as a useful additional tool to improve contrast in images under backscattering conditions.

Transmission scheme detection

Many models about the transmission of polarised light through scattering environments have been developed based on Monte Carlo simulations, as presented in Section 2.5.1. All of them drive to the memory effect light property. Other authors have tested experimentally these theoretical results though restricted to linear polarization [160] and they demonstrate the depolarization of the beam is proportional to the optical depth. In this experiment, a long-distance measurement of the transmission of a polarised beam under real fog conditions is addressed to compare the efficiency of both circular and linear polarization.

In similarity with the previous backscattering experiment, the forward scattering effects that polarized light suffers are evaluated in transmission with the fog chamber empty of objects in order to avoid undesired interactions with such objects. The disposition of set-up is displayed in Figure 7.12.

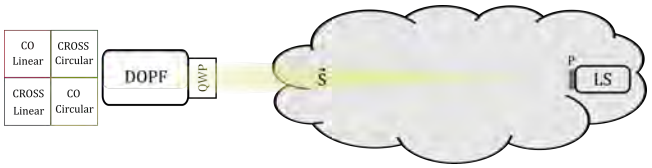

Figure 7.12: Scheme of the set-up for detection in the transmission of forward-scattered light from fog under active illumination. The light source (LS) with the polarizer (P) illuminates the fog with polarization $\vec{S}$ that is forward scattered to the modified DoFP camera at 28 m.

Now, the source and detector are facing each other inside the fog chamber and the light source had a divergence of $\pm 6.65^o$ and is aligned pointing towards the camera at a distance of 28 m. In this case, only the illumination is changed between linear and circular polarization, controlling electrically the output optical power. The camera is set again to 1 second of exposure time and no gain, having the same conditions as the previous experiments.

It may be observed in Figure 7.13 how the CO channels present a circle of saturation at the position of the light source for both input polarization states HL and LC. Initially, we aimed to study at which depth polarized light could penetrate through the fog and reach the detector as a function of the visibility

for both linear and circular polarization. Nonetheless, the light source is visible even for low visibilities with the lowest optical power at the furthest possible distance. Only under extremely dense fog (visibility < 5 m), all channels are completely obscured by fog. Despite this, as the visibility increases, so does the dominance of CO-channel detected photons.

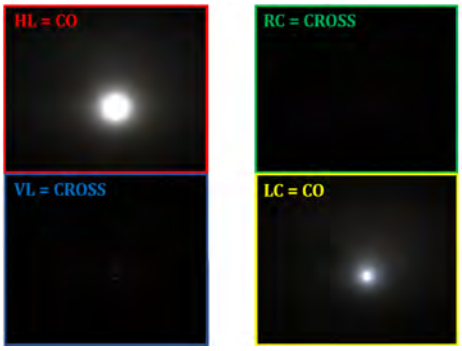

Figure 7.13: Forward light signal (visibility < 10 m) in respective CO and CROSS channels for HL (left) and LC (right) input polarization. CROSS channels filter the incoming light remarking the prevalence of the input polarized light through fog

The saturation radius in the CO channels is directly proportional to the source divergence and the visibility of the turbid media. The light source radius is reduced at low visibilities because a higher probability of single and multiple scattering events exists which randomize the photon directions preventing them to arrive at the detector. As the fog gets lighter, the saturation beam radius starts to grow because the probability of being scattered is reduced. The radius will tend to achieve the initial width when there was no fog in the chamber.

Alternatively, it is noticed that visibility affects too the saturation radii on the CROSS images obtained. The denser the fog, the smaller the radii of the saturation circle as in the CO channel. However, as the visibility increases, so does the saturation radii of CROSS channel. This effect is due to light undergoing multiple scattering getting more diffused, and thus, depolarized. These photons with changed polarization from the initial one, arrive at the orthogonal channel.

Thus, the next step is to compare the ability of both linear and circular polarizations to maintain their initial properties based on the radius of the circle in the saturation veil [190, 191]. Quantitative measurements of the size of the saturation veil are shown below in Figure 7.14.

Comparing the polarization signals of the CO channels, the radii on the LC channel are always smaller (0.78 times) than the ones on the HL channel. This confirms that circular polarization can penetrate deeper in fog without depolarizing as more ballistic photons are detected than in the case of linear polarization. This behaviour is consistent with the Mie scattering phase functions of linear and circular polarization. The phase function in the circular case possesses a marked forward lobule which permits the photons to propagate around the beam axis with higher probability than the linear case [157]. In

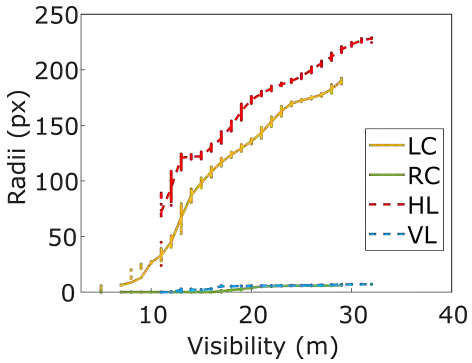

Figure 7.14: Comparison of the saturation veil radii in pixels for the CO and CROSS channels for circular and linear polarization as a function of the visibility.

addition, the radii of the CROSS channels, RC and VL, denote the presence of multiple scattering that change the initial polarization of the photons and the off-axis illumination coming from the divergence of the source.

To confirm the results beyond the use of the saturation radius, the evolution of the radii at 15 equally spaced points, non-saturated intensity levels, in the beam profile imaged at the sensor is evaluated to improve the accuracy of the method. Three different visibilities 12 m, 18 m, and 24 m (plotted as three colours) are included to further generalize the analysis. Figure 7.15 shows the signal ratio of the CO and CROSS channels relative to the S_0 parameter plotted against the radii of the section of the intensity profile at those 15 values of intensity. Circular (solid lines) and linear (dashed lines) polarization cases are included for comparison.

The curves show that the smallest radius in the CO channel corresponds to ballistic photons with unchanged polarization and trajectory, being the lesser as shown in the ratio at the 3 visibilities and both polarizations. When increasing the radii, so does the CO signal level, since it corresponds to photons that do not change the polarization state but suffered more scattering in the propagation direction.

The contrary behaviour is observed in the CROSS channel. The smallest radius has the highest signal value, as these photons are the ballistic ones which suffered depolarization without changing the direction. The sum of both minimum radii signal values from the CO and CROSS channels gives the total ratio. This time as the radii broaden, the signal decreases as the probability of depolarization and change in direction is reduced for all visibilities and both input polarizations.

In addition, the curves demonstrate how the beam broadens as visibility is reduced in both CO and CROSS, due to the increase of multiple scattering processes. The curves show that the lower visibility and, thus, a broader intensity profile, at the CROSS channel (larger values of radius), the faster the beam gets depolarized and the signal increases. Moreover, circular polarization has a higher

signal level and lower radii in the CO channel and a lower signal in the CROSS channel for all visibilities in comparison with linear polarization. This implies that circular polarization has a larger signal-to-noise ratio in transmission at deeper layers, whereas the signal of the linearly polarized light carries some noise due to its higher depolarization ratio when propagating in scattering media.

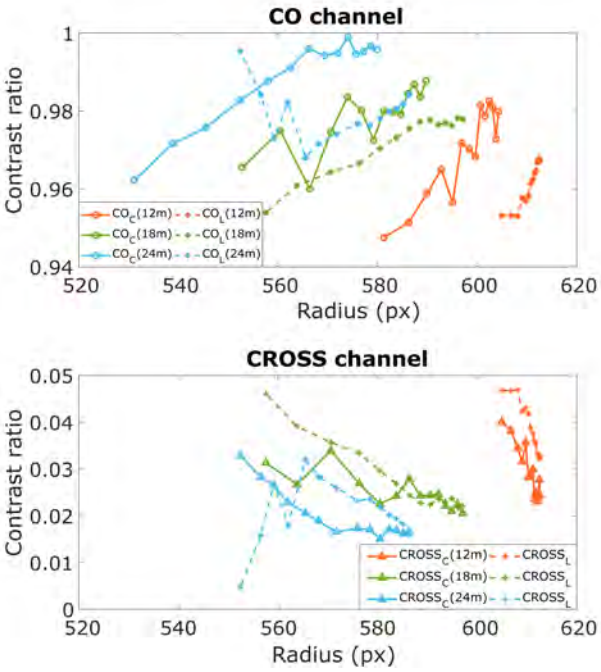

Figure 7.15: Comparison of the ratio between CO (top) and CROSS (bottom) respect to the S_0 signal as a function of the radius of the intensity profile of the source image in the circular (solid lines) and linear (dashed lines) polarizations at three visibilities: 12 m, 18 m and 24 m, using different colours.

Summary

The presented results show the dependence of the optical light penetration and the sensing range on the input polarization illumination in scattering environments. Its maximum is obtained with circularly polarized light since it is detected in deeper optical layers at the same radius of scattering as in the linear polarization case. On the other hand, circular polarization permits the detection of the location of the point source embedded in the scattering media with better accuracy getting rid of the depolarized diffused photons. This may be useful for surveillance applications such as detecting the light from a beacon, for example.

7.2 Active imaging Full-Stokes DoAPC

The previous study threw relevant results about the superiority of circular polarization against linear when measuring through fog based on detecting the CO and CROSS polarizations of the active light. Many studies have been performed to see in turbid media using polarization property as introduced in Section 2.5.1, but the majority of them perform their studies applying the physical filtering of measuring with specific polarization states in the camera to detect embedded objects, as previously done with the modified DoFP. Other research have shown the usefulness of linear combinations between channels of the PSA such as difference between CO and CROSS to improve detection [166, 189], in the same manner as in Figure 7.9. Based on this last evidence, the next step in the analysis of detection through turbid media is to employ the DoAPC to acquire the full Stokes images and see the complete polarization response of the scattering media.

DoAPC is a full-Stokes Division of Aperture Polarimeter (DoAP) camera that has the ability, as already demonstrated in Chapter 6, to recover the maps of the Stokes vector and its related parameters of the scene. By definition, the Stokes parameters come from the difference between orthogonal polarization states, see Equation (2.7), which is exactly studied in Figure 7.9 and similar studies in literature [166, 189].

The two main singularities of our system are the ability to acquire the Stokes vector in a single shot, providing a fast measurement, and the elliptical states compounding the PSA. These states are the optimum polarization states for a polarimetric device with a PSA of 4 analyzers to minimize the noise influence in the measurement. Theoretical studies for the optimization of polarimetric systems claim that this arrangement of polarization states has immunity to Gaussian and Poisson noise, simultaneously. On one side, having immunity to Gaussian noise supposes an improvement in signal acquisition in scattering media, where the signal is strongly affected by this kind of noise. On the other side, being immune to Poisson noise reduces the influence on the input polarization of the signal to the noise, making the system suitable for active Stokes imaging.

Figure 7.16: (Left) DoAPC with the active illumination in the fog chamber. (Right) Camera-illumination system working during a fog cycle inside the chamber.

In order to analyse the complete polarization signal when imaging through fog with the DoAPC, two experiments in reflection geometry are addressed using active Stokes imaging mode. The set-up is maintained from Figure 7.6 but using the DoAPC system with the active illumination 2 x 2 array adapted to it. The camera is placed inside a mild steel IP68 housing cage (RS PRO, 400 x 500 x 150 mm) with the polarization maintaining N-BK7 window for the VIS range, as shown in Section 7.2. The details of the re-design of the system for the experiments has been presented in Chapter 3 in Section 3.2.

Firstly, it is sought to quantify the difference between signals coming from the panels under linear or circular active illumination. Hence, the previous experiment is replicated using the same diffusive black and white panels but instead of detecting with the modified DoFP camera, the DoAPC is used. In addition, three different distances (5 m, 8.5 m and 12.5 m) are evaluated this time through a complete fog cycle from 5 m of visibility to 95m, see Figure 7.17. Both linear and circular polarization are placed in the active illumination to study differences in behaviour with complete Stokes information.

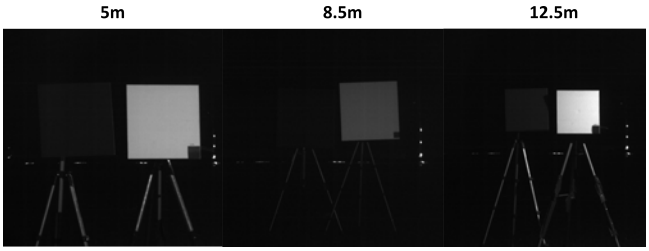

Figure 7.17: Black and white panel measured at the three distances (5 m, 8.5 m and 12.5 m) by the DoAPC for detection.

The Stokes parameters and the angle parameters are measured for a complete cycle using linear (HL) and circular (LC) polarization. Their mean values for the black panel region, the white panel region and the background signal are displayed in the following. DOPs parameters do not show any relevant information since they come from the Stokes parameters and the S_0 signal, very affected by the fog.

The intensity S_0 channel shows the signals of the white panel concerning the black panel and the background. Here, it is shown that for low visibilities this parameter is affected by backscattered light. The black panel and background show similar behaviour. For the closest distance, the white paper is more detectable thanks to its reflectance property as the signal is maintained through visibility changes. For all panels, the circular polarization is preserved better at a 5 m distance. For higher distances, the signal is lost when the visibility increases since no scattering medium is present.

The linear and circular illuminations show variations in their Stokes parameters when fog is present. Initially, despite HL is set as illumination, observing Figures 7.19 to 7.21 can be appreciated that Stokes parameters differ from the value [1.00.00.0]. The same effect occurs with circular illumination.

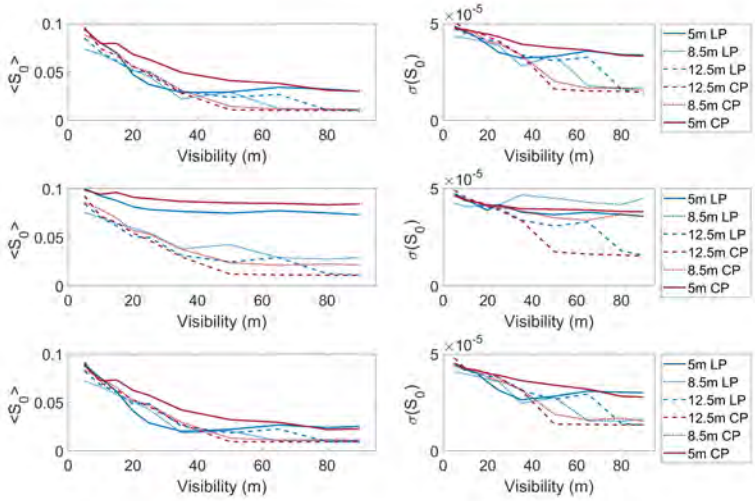

Figure 7.18: Mean intensity signal and its associate variance in a complete fog cycle for both linear (LP) and circular (CP) polarizations of (Top) the black panel, (middle) the white panel, (bottom) the background at three distances of the panel (5 m, 8.5 m and 12.5 m).

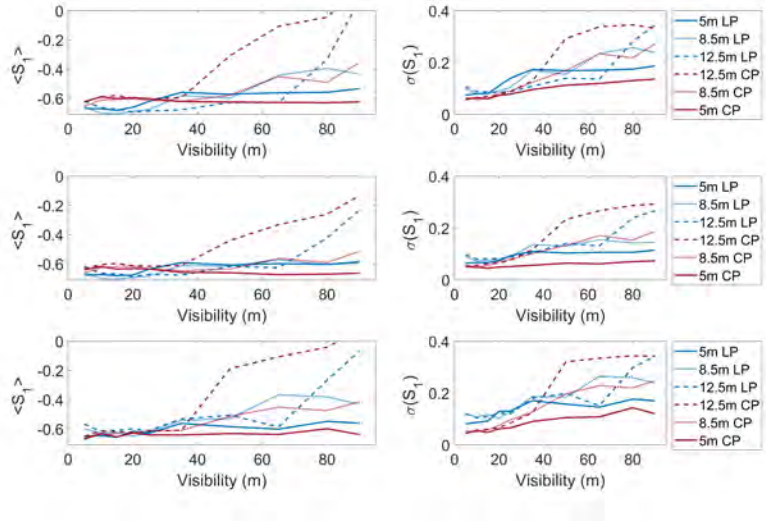

Figure 7.19: Mean S_1 parameter signal and its associate variance in a complete fog cycle for both linear (LP) and circular (CP) polarizations of (Top) the black panel, (middle) the white panel, (bottom) the background at three distances of the panel (5 m, 8.5 m and 12.5 m).

However, in this case, the illumination is not completely circularly polarized from the beginning and tends to an elliptical state since the CPs of the light sources cannot provide a pure circular state. This can be confirmed in Figure 7.23 where the ϵ starts with values higher than -45^o, the ϵ of an LC state.

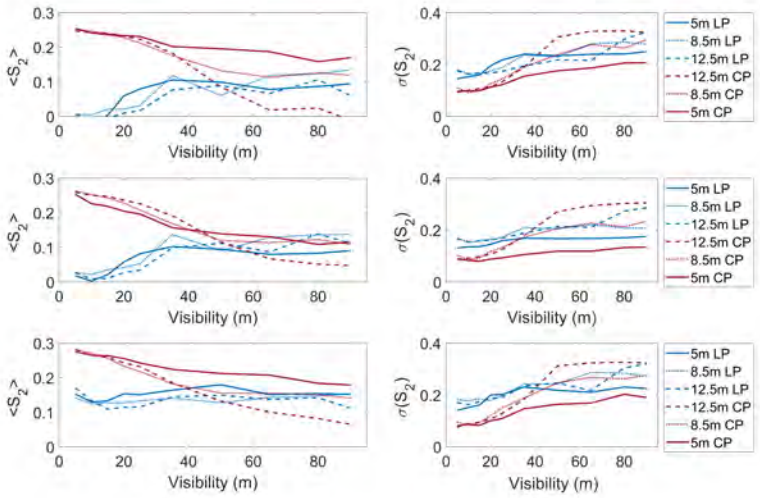

Figure 7.20: Mean S_2 parameter signal and its associate variance in a complete fog cycle for both linear (LP) and circular (CP) polarizations of (Top) the black panel, (middle) the white panel, (bottom) the background at three distances of the panel (5 m, 8.5 m and 12.5 m).

At 5 m and 8.5 m, the Stokes parameters of both illuminations tend to have the same polarization state at the panels at higher visibilities. This means that the diffusive nature of the panels makes the active polarization depolarized and, then, it reflects a specific polarization state.

At 12.5 m the white panel starts to be differentiated from the black one and background at medium visibilities under circular polarization since the strongly elliptical initial polarization passes to be almost linearly polarized. This is noticed in the Figures 7.22 and 7.23 where AOLP has different values for the white panel from 45 m of visibility. The signal of linear polarization changes too with visibility in the same trend for all panels and the background being indistinguishable. This is the furthest distance of the objects from the camera and only circular input polarization can distinguish the white panel from the other one and the background despite the depolarization being higher in this situation than in closer distances.

The second experiment consists in measuring a complex scene to observe the ability of imaging objects of distinct natures. Given the former conclusions regarding circular polarization for this application, the last test is restricted to circular polarization as long as the previous studies showed improved performance

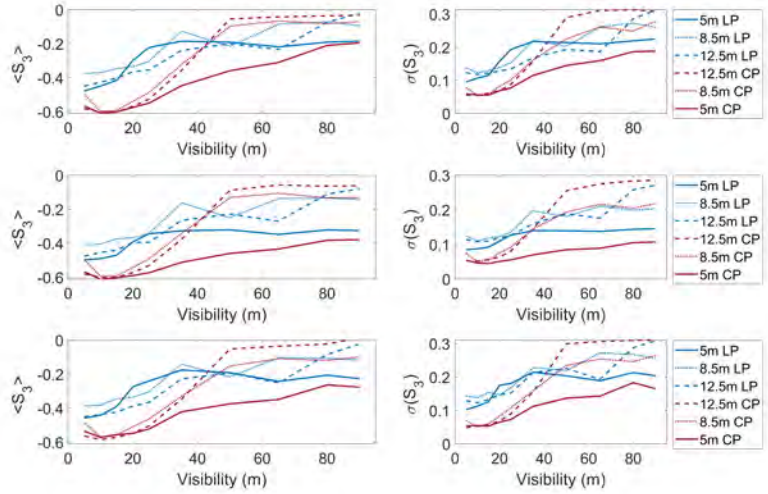

Figure 7.21: Mean S_3 parameter signal and its associate variance in a complete fog cycle for both linear (LP) and circular (CP) polarizations of (Top) the black panel, (middle) the white panel, (bottom) the background at three distances of the panel (5 m, 8.5 m and 12.5 m).

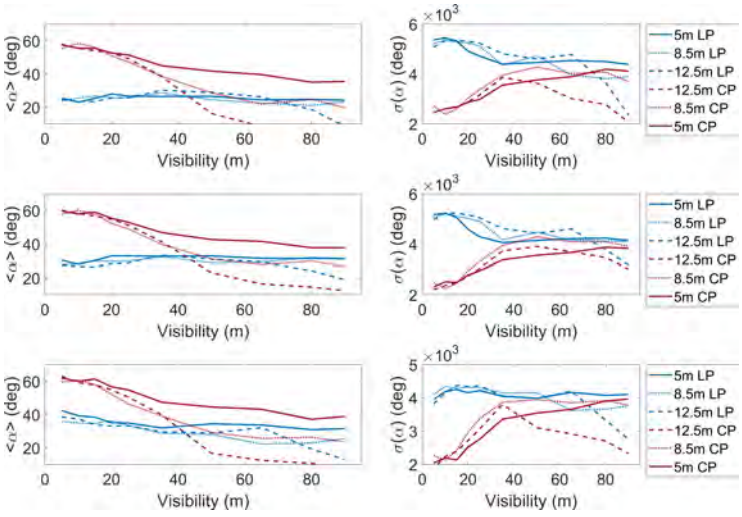

Figure 7.22: Mean AOLP parameter signal and its associate variance in a complete fog cycle for both linear (LP) and circular (CP) polarizations of (Top) the black panel, (middle) the white panel, (bottom) the background at three distances of the panel (5 m, 8.5 m and 12.5 m).

in backscattering and transmission Section 7.1. Another acquisition with only

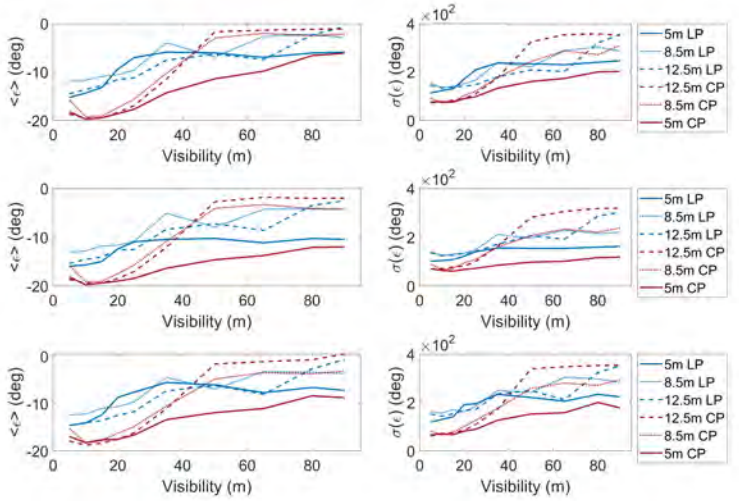

Figure 7.23: Mean ϵ parameter signal and its associate variance in a complete fog cycle for both linear (LP) and circular (CP) polarizations of (Top) the black panel, (middle) the white panel, (bottom) the background at three distances of the panel (5 m, 8.5 m and 12.5 m).

the LEDs without any polarizer is done just for comparison. The scene contains a car with retro-reflective tapes, a bicycle and a manikin.

Figure 7.24 gathers the Stokes parameters maps at four visibilities: 5 m, 15 m, 35 m and 65 m. LED illumination does linearly polarize light as displayed in the maps. Objects start to be detectable at 15 m where the retro-reflective tapes are shown in the S_0 map. In this case, polarization illumination and detection do not improve the range detection in imaging. All polarimetric channels do show the car and the bike (both metallic objects) presence but only the linear maps do inform about the presence of the manikin (a dielectric object). This is reinforced by the fact that AOLP map does even show a contrast between the different parts of the manikin in Figure 7.25.

When illuminating with the light sources with the CPs, again elliptical state is measured in the Stokes parameters under extreme fog (5 m) in Figure 7.26. This time the retro-reflective parts of the car are further differentiated from the fog in the S_3 channel changing its signature from negative to positive values, as well as in the ellipticity maps in Figure 7.27, meaning a flip in polarization during reflection. As the visibility increases, so does the signal coming from the retro-reflective parts of the car. The bicycle is partially differentiated in comparison with LED illumination since only the frontal part shows remarkable contrast. The manikin is only appreciated in the S_2 map.

Two conclusions can be derived from these measurements. Firstly, under linear illumination, the linear Stokes parameters yield higher contrast in objects,

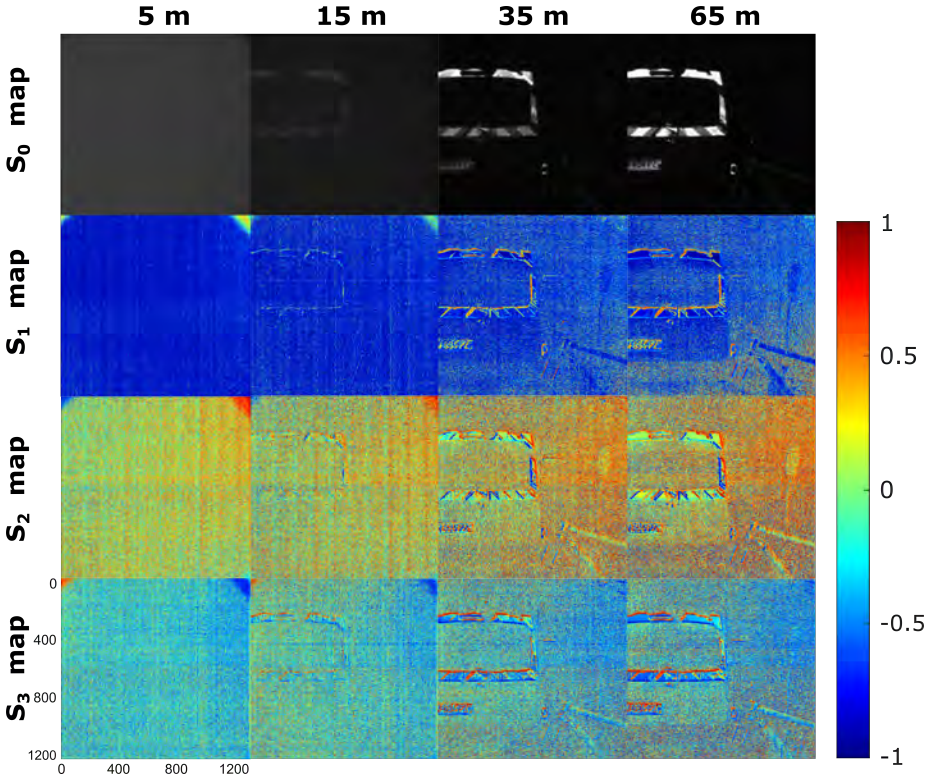

Figure 7.24: Maps of the Stokes parameters of a complex scene under LED polarized illumination at four visibilities: 5 m, 15 m, 35 m and 65 m.

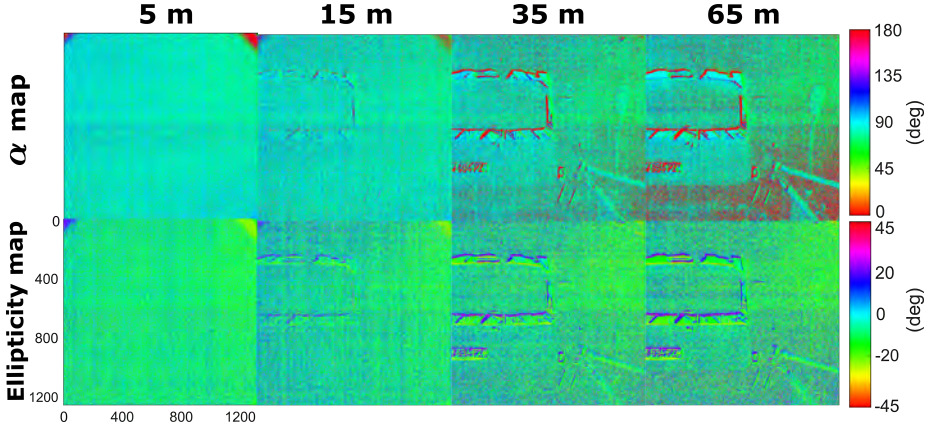

Figure 7.25: Maps of the Stokes parameters of a complex scene under LED illumination at four visibilities: 5 m, 15 m, 35 m and 65 m.

especially in the dielectric ones. The bicycle was painted, so it can be considered to be composed of dielectric material. Secondly, although linear illumination can distinguish some car parts, they cannot be differentiated from other objects. Meanwhile, the retro-reflective materials under circular (elliptical) polarization, show the largest contrast to the background and they flip the handedness of the input state ellipticity allowing them to identify its nature.

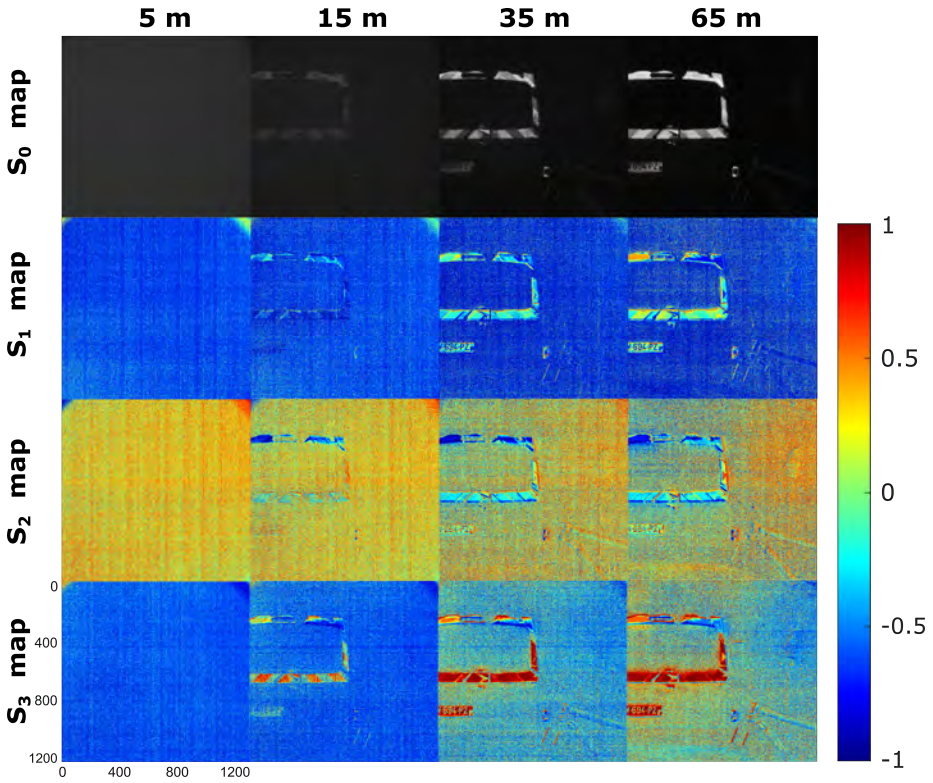

Figure 7.26: Maps of the Stokes parameters of a complex scene under circular illumination at four visibilities: 5 m, 15 m, 35 m and 65 m.

These experiments show that measuring the Stokes vector and its associated angles (as the DOPs do not bring relevant information) allows following the changes in the polarization state of the scene during a fog cycle. However, despite the difference between CO/CROSS channels is suggested to aid in the representation of the contrast in the reflection experiments using the modified DoFP system, detecting diffusive panels under active polarization based on Stokes vector do not improve the contrast. In this case, the DoAPC contains elliptical states in the PSA, and they are not orthogonal to the active illumination, as in the modified DoFP device. Therefore, they compute the Stokes vector but cannot have the capacity of using its polarization images (intensity images from each PSA channel) to filter out completely the backscattering light of one

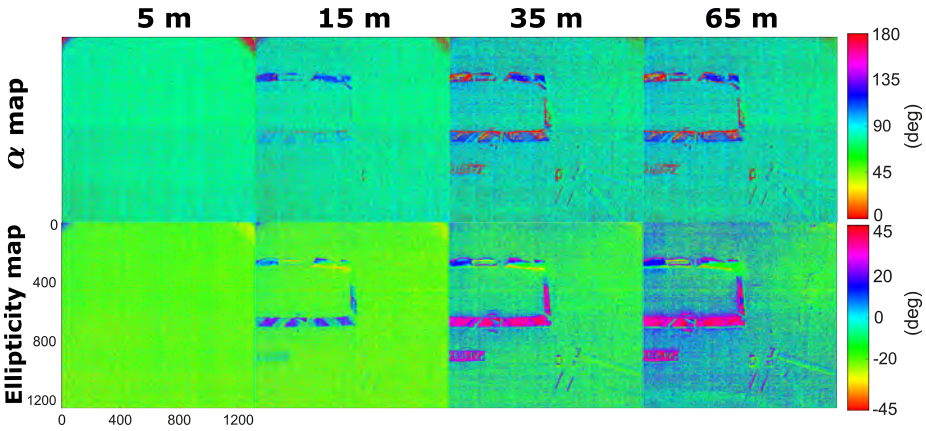

Figure 7.27: Maps of the Stokes parameters of a complex scene under circular illumination at four visibilities: 5 m, 15 m, 35 m and 65 m.

channel, since an amount of circular (linear) polarization will pass through them when illuminating with linear (circular) polarization will pass through them.

Nevertheless, the ability to retrieve the Stokes vector and its associated parameters opens several paths to explore the improvement of the detection in scattering media. One may be using the Stokes parameters maps and the angle's maps to calculate the optimum illumination state to get rid of the fog backscattered signal when measuring with the DoAPC. This needs the implementation of adaptable polarization in the light sources in a close loop together with the polarization maps. Another path can be the study of different visualizations of the polarization maps and the application of some noise filtering in the images.

This last proposal is being studied during these last years and it has been applied to the images measured under active circular polarization. Figure 7.28 presents a 3-channel polarimetric image (3-OSC) formed by the stack of the S_1, S_3 and ϵ maps, as it is an RGB image, at different visibilities. Conversely, Figure 7.29 is composed by the S_1, S_3 and α maps. Both images highlight different parts of the scene and this type of representation can be used for a more understandable evaluation of the images.

Besides this new representation of polarimetric information, denoising the polarization maps can be studied and tested for enhancement of vision in dispersive media. Figure 7.30 shows the difference between 3-OSC image and the same after applying a Gaussian filter in order to minimize the influence of fog.

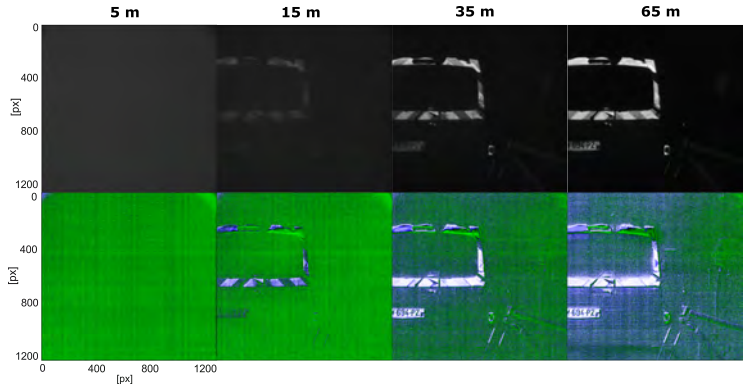

Figure 7.28: Images of (top) the S_0 parameter and (bottom) the 3-OSC composed by S_1, S_3 and ϵ maps of a complex scene under circular illumination at four visibilities: 5 m, 15 m, 35 m and 65 m.

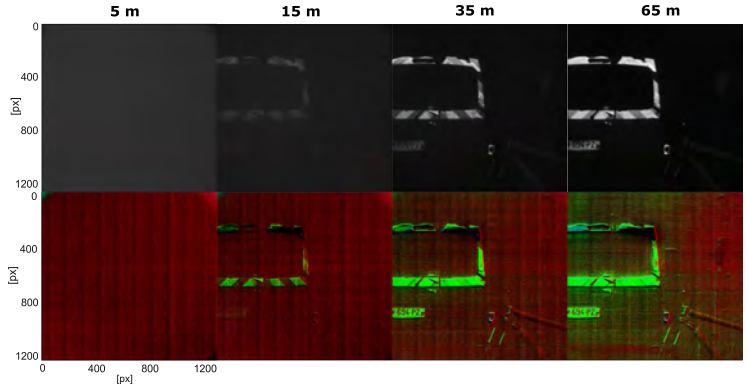

Figure 7.29: Images of (top) the S_0 parameter and (bottom) the 3-OSC composed by S_1, S_2 and S_3 maps of a complex scene under circular illumination at four visibilities: 5 m, 15 m, 35 m and 65 m.

Summary

Measuring the Stokes vector under active illumination promises to serve as a useful tool to detect through turbid media. However, the relation between the active polarization and the states composing the PSA of the system must be studied in detail in order to get the optimum results. For that, the full-Stokes vector maps and their associated angles can be served to its development. Differences in behaviour between linear and circular active illumination are observed, especially in retro-reflective and dielectric materials. Moreover, using different visualization options and noise filtering may help in the processing of the scene to enhance detection.

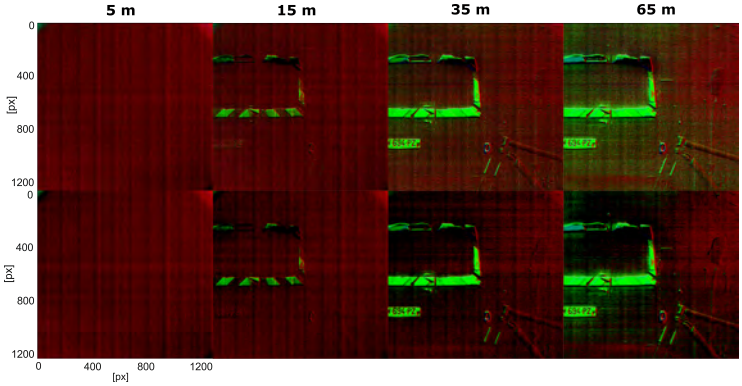

Figure 7.30: Comparison between (top) 3-OSC image of the complex scene before and (bottom) after a Gaussian filter under circular illumination at four visibilities: 5 m, 15 m, 35 m and 65 m.

Conclusions

"All we have to decide is what to do with the time that is given us."

The Fellowship of the Ring
J.R.R. Tolkien

In the Chapter 1, we proposed to develop a snapshot polarimetric camera in the VIS waveband. Based on quantitative and qualitative analyses, it has been demonstrated that our DoAPC can measure the complete polarization information, obtaining full-Stokes images and MM images, in the VIS range. Extension to other wavelength ranges is a matter only of optomechanical design and availability of components. Moreover, a balance between speed and optimum performance is accomplished by having a snapshot polarimetric camera immunized to Gaussian and Poisson noises by using of optimal polarization states. Subsequently, the DoAPC is applied to study the enhancement of detection under scattering media using the polarization property of light.

Along this Thesis, all the steps to achieve these general objective have been explained in detail. In the first place, during the design stage, different alternatives for the optical design were presented. The architecture of DoAP using a stack of an array of minilenses and polarizing elements has demonstrated to be the best choice combining performance, price and availability of components. In such configuration, movement artefacts are minimized and calibration can account for geometrical and polarimetric aberrations. Besides, this design employs a unique sensor and shares optics revealing to be more economical than others. The division of the active area of the sensor in four images is not critical as long as the number of pixels in imaging arrays is constantly growing. Thanks to the DoAP architecture, the polarization calculation requires less time for acquiring the full-Stokes vector in a single measurement (instead of the usual need of 4 images) and the MM in four mesurements (instead of 16). However, some limitations are noticed during experiments like the narrow FOV, which only allows medium-long distance measurements, the monochrome sensor, which measures the incoming white light so a potential spectral signature vanishes, and the sensor detectivity, which demands high gain in low light conditions. All these constraints can be improved through further optimization of the optomechanical design. Some natural follow-up ideas are given in Future work.

Beyond this, using the optimal states in the 2x2 array of the PSA showed good agreement with theoretical studies in the literature that demonstrated that this combination of polarization states in the PSA allows the minimum noise transmission during the whole polarization image acquisition. So, these elliptical

states were used in the PSA in both full-Stokes and Mueller matrix imaging together with the complementary optimum states in the PSG of the MMI.

Further, a complete calibration procedure for DoAPC systems has been proposed and implemented using the information available form the state of the art. The calibration algorithm proposed for the system intends to be generic so other researchers can take advantage of the details offered in this research and help them to perform and check the correctness during the calibration of their own systems. Our calibration algorithm is differentiated into three different steps addressing the distinct parts of the design: the sensor, the optical design and the polarizing elements inside the system. The radiometric calibration is based on a very standardised algorithm and procedure to account for offset signal from the sensor and non-uniformity in pixel detectivity. The geometric calibration employs computer vision algorithms based on feature detection instead of using interpolation algorithms or custom-developed functions to match the four intensity sub-images of the sensor and establish a pixel to pixel correspondence between them. These two calibration steps are a quite general approach and do not require a specific calibration sample. In this last case, both SURF and ORB functions in Matlab are employed since they complement themselves when not enough inliers are present within the scene. Although they achieve small errors in matching, they are quite time-consuming. Further study in an optimal programming of this functions should be done to provide a good ratio for assuring fast computation of the polarization images in case the scene is very dynamic.

Finally, our third step is the polarimetric calibration that relies on the ECM algorithm, which is indeed one of the conclusions from the Thesis we want to highlight. After studying three general calibration algorithms, ECM showed to be the broadest algorithm when any polarimetric imaging mode is required. Detailed comparisons of the performance of three polarimetric calibration methods both for Stokes and MM imaging were analyzed and we concluded that the desirable method for a DoAP system relies on the constraints of the experiment. On the one hand, the DRM can be applied when time and budget are compromised only being able to recover with confidence the Stokes vector of the scene.The PCM can be used in Stokes vector estimation when there is not available a good retarder for calibration, or if there is no possibility of a good alignment of the retarder. In the rest of the situations, the ECM shows the best validation results for measuring the full polarization state of the scene with errors lower the 10% in broadband for all imaging modes. It can be performed only once and the system can be used in both Stokes and Mueller matrix imaging modes without extra calculations.

The DoAPC, in addition, has shown its capabilities to porperly measure both full-Stokes and MM polarimetric measurements that become significantly simplified because of the simultaneous acquisitions of four polarimetric images including the circular components, which is one of the main advantages of DoAP cameras. The ability of acquiring in a single-shot the Stokes vector allows the fast calculation of all related polarimetric parameters such as the DOPs, AOLP and ϵ helped in the understanding of the information.

In particular, and as another main conclusion of this work, the DoAPC

system has been shown to be able to detect polarization from scenarios of diverse complexity. Some conclusions about polarization behaviour can be extracted from the studied samples. It is widely said that circular polarization is rare in nature and linear polarization is predominant. This affirmation is partially supported by the obtained results. Linear polarization prevails in the reflections of the dielectric background and samples, but some changes in polarization occur in the process allowing to detect elliptical polarization states. This superposition between circular and linear components is unequally weighted since the AOLP and the low ϵ in the samples still hold that belief. Passive full-Stokes imaging can be thus useful in material classification, object inspection, removal of reflections and remote sensing for object detection, in a faster way than the state of the art as four images are simultaneously acquired.

Nonetheless, this type of imaging is not effective with all samples. Those which do not reflect the incoming light or do not introduce a change in the unpolarized illumination are not distinguishable from a polarimetric point of view. In this situation, results are equivalent to obtaining intensity images. However, the implementation of active full-Stokes imaging may introduce new information since changes in *a priori* known polarization can be detected shining new polarimetric information in the scene. This behaviour prevails, for instance, on most transparent amorphous materials. Active full-Stokes imaging can measure the local polarization changes in the material due to stress going beyond the information which may be extracted from linear polarization states. This type of imaging mode can be used to quantify this stress related to local variations of the refractive index, and also refractive index can be calculated from the polarization measurement. The DoAPC can be used as a polariscope that can work under any polarization state in the illumination.

The other imaging mode that DoAPC can implement is the determination of the MMI in the full VIS waveband from only 4 image acquisitions, significantly reducing the acquisition time.

Experimental results allow also to conclude the potential of MMI for different applications in particular related to polarimetric properties of materials, performed in reflection and transmission geometry, have shown the capability of calculating correctly the MM of the scene in a pixel by pixel basis, providing 16 maps of polarization information from only 4 image acquisitions,significantly speeding up the time of current experimental approaches. The main optical properties of materials, including in particular depolarization, diattenuation and retardation, appear in these 16 maps. For this reason, MMI shows details of the samples that go unnoticed in Stokes imaging. MMI employing broadband detection facilitates the material classification or object inspection in finer detail than Stokes imaging. Since the given time for a PhD thesis to be executed is limited, further analyses on the obtained MM results are planned to better understand the implications of these results in the future due to lack of time. More details are disclosed in Future work.

In the Thesis objectives at Introduction, we claimed that the DoAPC was developed to be applied in a specific real application. The optimization of the states in the PSA to be immune to Gaussian and Poisson noise, the broadband

detectivity in the VIS range and the possibility of fast acquisition of Stokes vector and Mueller Matrix images makes the developed DoAPC a feasible polarimetric system to measure the polarization signature of fog and other scattering media.

We quantified experimentally for the first time using an orthogonal contrast imager and active Stokes imaging [S. Peña-Gutiérrez *et al.* 2022] that circular polarization is maintained further than linear polarization through the fog. This polarization memory effect can be used to improve contrast in detection by filtering the backscattered CO polarization, which contains the fog reflection. From the same effect, optical light penetration is dependent on light polarization. It was observed that using circular polarization can enlarge the sensing range of an active polarimetric device. This can be useful for surveillance applications, or in mobility applications to detect light sources embedded in foggy scenarios with higher accuracy.

As another relevant conclusion of the work, DoAPC can measure the Stokes vector coming from the foggy scene under active illumination. The Stokes vector carries the mixed signal of the embedded objects and the polarimetric signature of the fog. Some limitations appeared in detecting the polarization signal of low-polarizing materials due to the sensor characteristics. In low-light scenes, the sensor required to increase the gain since long exposure time was not possible due to the dynamic nature of the fog, and this increased the noise in the signal. Therefore, differentiating depolarizing materials embedded in fog can be a difficult task using Stokes detection. On the contrary, objects with strong polarized reflection signal can be detected, like retro-reflective materials. This sets the path to conclude that active polarized light sources could be detected without matching the PSA (as it happens with the orthogonal contrast imager) since the device has a full range for detecting any polarization state. Once more, further research is needed to optimize the active polarization imaging for object detection and it is described in Future work.

The current development and commercial success of linear Stokes cameras based on the SONY IMX250MZR/MYR chip reveals the need for different types of polarimetric cameras in several applications which expand conventional computer vision cases. The extension of linear Stokes cameras to full-Stokes cameras maintaining the same resolution for circular polarization states is one of the present challenges in the sector nowadays. This Thesis thus makes a first step by accomplishing the development and optimization of a full polarization camera in VIS waveband, to enhance acquisition time and noise equalization while reducing movement and registration artefacts. The existing literature in the polarization field and the possible new applications of the technology have led us to the study, development and construction of the DoAPC in the visible range based on a DoAP configuration.

The current optical designs based on DoAP architectures implement very basic polarization measurement states, usually basic linear polarization states combination $(0^o, 45^o, 90^o, 135^o)$ in the MWIR range, while some others perform full-Stokes by exchanging 135^o polarizer by a circular one. A minority implement six states including both circular polarization states is done by T.Mu *et al.* However, only some of them have been applied to perform dehazing without

implementing an optimized PSA nor measuring the full Stokes vector of the haze.

In this Thesis, we have taken into account the optimization studies and implemented a full polarization DoAPC. Our camera has been demonstrated to work accurately in passive and active Stokes imaging, as well as in Mueller matrix imaging modes. The final application of this Thesis consists in pushing the limits in computer vision as addressed here. Vision through turbid media is a field of great interest since it affects a wide variety of applications ranging from a more technical field, like surveillance tasks and autonomous vehicles, to a more healthcare field, such as tissue characterization and cancer diagnosis. Through this work, the fog polarization signal has been experimentally characterized and, for the first time, the full-Stokes vector signal under active imaging is analysed for different fog densities. This opens the door to the DoAPC for contributing to boosting the ongoing research in imaging polarimetry.

Future work

"For even the very wise cannot see all ends."

The Fellowship of the Ring
J.R.R. Tolkien

Based on previous conclusions, some recommendations can be highlighted for further research in two main scopes.

Design of the camera

For example, the optomechanical design of the DoAPC could be optimized to be more compact so as to make it more manipulable. Experiments at different distance ranges, including short-distance, can be addressed by using a suitable objective in the camera. Since the sensor is monochrome, it can be interesting to place a variable colour filter to study the polarimetric signal in a specific waveband. In this manner, our DoAPC can be transformed into a spectropolarimetric camera in the VIS band.

Other improvements to the design can be done for the automation of the acquisition. For the sake of speed, the PSG of the calibration, as well as, the active illumination in active Stokes imaging and MMI can be performed using electronically controlled liquid variable retarders (LCVRs). In addition, a specific algorithm between the frame grabber software and Matlab can be developed. This will make the process more user-friendly and faster to achieve a real-time calculation of the polarization information.

Applications of the DoAPC

Polarization is known for having a wide range of uses. The DoAPC can be employed to enlarge the list of applications presented in this Thesis.

Stokes imaging can be applied to diverse outdoor scenarios in daylight and night conditions. The recovered full Stokes vectors can be merged with an IR camera to improve signal contrast in outdoor conditions without active illumination.

Mueller matrix imaging requires a deeper analysis of the measured matrix to understand its meaning and the relation between the different properties that occur simultaneously when interacting with the sample. To do this, the MM should be decomposed into the matrices of the fundamental properties. Several methods are developed in literature [28, 34, 37], although the most common is the Lu-Chipman decomposition [30]. In specific, the decomposition of the

MMs of the measured sugar dilution at different concentrations is a valuable case of study. Retrieving the polarization properties using 2D imaging can be a substantial contribution towards the development of a non-invasive estimation of glucose concentration for diabetes disease.

Further research in fog media is still pending. Starting from passive Stokes imaging, the DoAPC can be tested in dehazing applications taking the profit of retrieving the full Stokes vector of the scene. Following the experiments of this Thesis, using an automatic active illumination with LCVRs will allow searching for the optimum polarization state to achieve the best contrast in Stokes imaging. Besides, implementing a modulation in the active light can help to isolate the polarization signal coming from a light source embedded in turbid media increasing the detection range. This could be of interest in surveillance tasks.

Up to now, only fog was measured but the study of polarization in different adverse conditions like smoke is suggested to be the next step. Smoke is a dispersive media but the particles have a bigger size, thus obeying a different scattering law.

Finally, some experiments can be done applying the MMI to measure the MM in VIS broadband of dispersive media, like fog, smoke or turbid water. The Mueller matrix has been demonstrated to provide more detailed information on the polarimetric properties of the sample. This can be used for the benefit of investigating a different approach to detection enhancement in dispersive media.

And last but not least, artificial intelligence is becoming a very useful tool of computer vision for many transversal applications. Scientists are using them for very broad fields to improve object detection or image classification. In the specific case of turbid media, some researchers have applied it with active systems like LiDar [192]. I propose to develop and apply AI algorithms on the polarization information or a set of fused data to recover better contrast imaging for remote sensing applications in hazardous environments.

Dissemination

The scientific results of current research have been disseminated in reference publications in journals in the fields of Optics, Biophotonics, Optical Engineering and Sensors from the main scientific societies (OSA, EOS, SPIE, IEEE) and in international conferences across Europe, e.g. the team routinely attends the SPIE Optical Metrology and IEEE Sensors series, and is permanently exploring novel relevant conferences. Advances of the thesis have been disseminated in journals and conferences from Spanish societies like the National Optics Meeting and the Optoel series, and in seminars organized by industrial clusters and technology platforms.

10.1 Journal publications

- **Sara Peña-Gutiérrez** and Santiago Royo, "Polarization calibration assessment for a broadband imaging polarimeter based on a division of aperture architecture", Opt. Express (2022) (Accepted).
- Maria Ballesta-Garcia, **Sara Peña-Gutiérrez**, Ana Rodríguez-Aramendía, Pablo García-Gómez, Noel Rodrigo, Aleix R. Bobi, and Santiago Royo, "Analysis of the performance of a polarized LiDAR imager in fog," Opt. Express 30, 41524-41540 (2022).
- **Sara Peña-Gutiérrez**, Maria Ballesta-Garcia, Pablo García-Gómez and Santiago Royo, "Quantitative demonstration of the superiority of circularly polarized light in fog environments," Opt. Lett. 47, 242-245 (2022).
- **Sara Peña-Gutiérrez**, Maria Ballesta-Garcia and Santiago Royo, "Activities in imaging through fog at CD6: polarimetric imaging," 2021 13th International Conference on Electromagnetic Wave Interaction with Water and Moist Substances (ISEMA), 2021, pp. 1-4, doi: 10.1109/ISEMA49699.2021.9508284.
- Maria Ballesta-Garcia, **Sara Peña-Gutiérrez** and Santiago Royo, "Activities in imaging through fog at CD6: polarized light propagation modelling," 2021 13th International Conference on Electromagnetic Wave Interaction with Water and Moist Substances (ISEMA), 2021, pp. 1-4, doi: 10.1109/ISEMA49699.2021.9508301.
- **Sara Peña-Gutiérrez**, María Ballesta and Santiago Royo, "A full Stokes imaging polarimeter based on a consumer CMOS camera," Proc. SPIE 11059, Multimodal Sensing: Technologies and Applications, 1105913 (21 June 2019); https://doi.org/10.1117/12.2525706

- Laura Rey-Barroso, **Sara Peña-Gutiérrez**, Carlos Yáñez, Francisco J. Burgos-Fernández, Meritxell Vilaseca and Santiago Royo, "Optical Technologies for the Improvement of Skin Cancer Diagnosis: A Review," Sensors 21, 252 (2021).

- Maria Ballesta-Garcia, **Sara Peña-Gutiérrez**, Aina Val-Martí and Santiago Royo, "Polarimetric Imaging vs. Conventional Imaging: Evaluation of Image Contrast in Fog," Atmosphere 12, 813 (2021).

10.2 Papers in submission

- Design and construction of an imaging Mueller matrix polarimeter based on DoAP architecture. *Opt. Express*

- Applications of Mueller matrix polarimeter based on DoAP architecture. *Opt. Express*

10.3 Oral presentations in conferences

- **Sara Peña-Gutiérrez**, Maria Ballesta-García and Santiago Royo, "Activities in imaging through fog at CD6: polarimetric imaging", *2021 13th International Conference on Electromagnetic Wave Interaction with Water and Moist Substances (ISEMA)*, 2021, 1-4, doi: 10.1109/ISEMA49699.2021.9508284.

- Maria Ballesta-García, **Sara Peña-Gutiérrez**, and Santiago Royo, "Activities in imaging through fog at CD6: polarized light propagation modelling", *2021 13th International Conference on Electromagnetic Wave Interaction with Water and Moist Substances (ISEMA)*, 2021, 1-4, doi: 10.1109/ISEMA49699.2021.9508301.

- J. Riu, N. Rodrigo, F. Sanabria, **S. Peña**, M. Ballesta, S. Royo; Cámaras lidar para imagen 3D de alta resolución a tiempo real In the XII Reunión Nacional de Óptica (RNO) Castellón, España, 3-6 July 2018; ISBN (digital ed.): 978-84-09-03559-5

10.4 Poster presentations in conferences

- **Sara Peña-Gutiérrez**, Paula Maynou-Ribas, Maria Ballesta-García and Santiago Royo. "Medida de superficies 3D mediante imagen polarimétrica", *"XII Reunión Española de Optoelectrónica: OPTOEL 2021 , 30 of June, 1-2 of July 2021 (online event), Valencia*, 2021, p. 1-6. ISBN 978-84-18471-75-9.

- Miguel Ares, Sara Peña, Isidre Rivero, "3D skin tumour analyzer." *XIII Reunión Nacional de Óptica 2021, 22-24 Novembre 2021 (online event), Valencia*, 2021, pp.37-38.

- Maria Ballesta-García, **Sara Peña-Gutiérrez**, Aina Val and Santiago Royo. "Evaluación de modos de imagen polarimétrica en una cámara de niebla mediante el uso del contraste de imagen". *"XII Reunión Española de Optoelectrónica: OPTOEL 2021 , 30 of June, 1-2 of July 2021 (online event)*, 2021, p. 1-5. ISBN 978-84-18471-75-9.

- L. Rey *et al.* "Polarized multispectral imaging for the diagnosis of skin cancer". *Color and Imaging Conference. Twenty-seventh Color and Imaging Conference* (CIC27) held October 21-25, 2019, in Paris, France". Society for Imaging Science and Technology (IST), 2019, p. 381-385.

- L. Rey *et al.* "Polarized multispectral imaging for the diagnosis of skin cancer", *Congreso Nacional de Color* 2019, 26 of September 2019, Linares, Jaen, Spain 2019.

- **Sara Peña-Gutiérrez**, Maria Ballesta-García and Santiago Royo, "Método de calibración de una cámara CMOS comercial para su uso como cámara polarimétrica", *Optoel 2019: XI Reunión Española de Optoelectrónica, 3-5 of July 2019, Zaragoza*, 2019, p. 1-6.

- Maria Ballesta-Garcia, **Sara Peña-Gutiérrez** and Santiago Royo, "Detección de luz en medios turbios: simulaciones de Monte-Carlo para imagen activa usando luz polarizada o detección resuelta en el tiempo". *Optoel 2019: XI Reunión Española de Optoelectrónica, 3-5 of July 2019, Zaragoza*, 2019, p. 1-6.

- **Sara Peña-Gutiérrez**, María Ballesta, Santiago Royo, "A full Stokes imaging polarimeter based on a consumer CMOS camera," Proc. SPIE 11059, Multimodal Sensing: Technologies and Applications, 1105913 (21 June 2019); https://doi.org/10.1117/12.2525706

10.5 Patents

- S.Royo, N. Rodrigo, **S. Peña-Gutiérrez**, J. Riu, J. Kallhammer, "Lidar imaging apparatus for a motor vehicle." Brief description: Improvement in LiDAR imaging systems. Registration number: 19161075.7. Invention patent. Data of registration: 06/03/2019. Country of registration: Institutions of the European Union. Ambit: European. Titular entity: Veoneer Sweden AB.

10.6 Awards

The work presented here has also been awarded as winner of:

- "Beca de Recerca per estudiants universitaris 2018", granted from Ajuntament de Terrassa.
- "Beca de Recerca per estudiants universitaris 2021", granted from Ajuntament de Terrassa.
- "Beca de Recerca per estudiants universitaris 2022", granted from Ajuntament de Terrassa.

Bibliography

[1] T. Ramskou, "Solstenen," *Skalk*, vol. 2, pp. 16–17, 1967.

[2] E. Collett, *Polarized Light: Fundamentals and Applications*, 1st Ed. Marcel Dekker Inc., 1993.

[3] J. S. Tyo, D. L. Goldstein, D. B. Chenault, and J. A. Shaw, "Review of passive imaging polarimetry for remote sensing applications," *Appl. Opt.*, vol. 45, no. 22, pp. 5453–546, 2006.

[4] F. S. et al., "An overview of polarimetric sensing techniques and technology with applications to different research fields," *Proceedings of SPIE - SPIE Sensing Technology + Applications*, vol. 9099, 9099B, 2014.

[5] G. D. Lewis, D. L. Jordan, and P. J. Roberts, "Backscattering target detection in a turbid medium by polarization discrimination," *Appl. Opt.*, vol. 38, pp. 3937–3944, 1999.

[6] J. Fade, S. Panigrahi, and A. C. et al., "Long-range polarimetric imaging through fog," *Appl. Opt.*, vol. 53, pp. 3854–3865, 2014.

[7] S. Sudarsanam, J. Mathew, S. Panigrahi, J. Fade, M. Alouini, and H. Ramachandran, "Real-time imaging through strongly scattering media: Seeing through turbid media, instantly," *Sci. Rep.*, vol. 6, pp. 1–9, 2016.

[8] P. Y. Deschamps *et al.*, "The polder mission: Instrument characteristics and scientific objectives," *IEEE Trans. Geosci. Remote Sens.*, vol. 32, pp. 598–615, 1994.

[9] T. Novikova, A. Pierangelo, and A. D. Martino, "Polarimetric imaging for cancer diagnosis and staging," *Opt. Photonics News*, vol. 23, pp. 26–33, 2012.

[10] A. Pierangelo *et al.*, "Polarimetric imaging of uterine cervix: A case study," *Opt. Express*, vol. 21, pp. 14 120–14 130, 2013.

[11] *Astrophysical Spectropolarimetry*. Cambridge University Press, 2001.

[12] J. T. Bueno, E. L. Degl'Innocenti, and M. C. *et al.*, "Selective absorption processes as the origin of puzzling spectral line polarization from the sun," *Nature*, vol. 415, pp. 40–406, 2002.

[13] J. T. Bueno, T. D. P. Alemán, and L.Belluzzi, "Atomic scattering polarization. observations, modeling, predictions," *Proceedings of the International Astronomical Union*, vol. 10, no. S305, pp. 127–135, 2014.

[14] V.V.Tuchin, "Polarized light interaction with tissues," *J. Biomed. Opt.*, vol. 21, no. 7, p. 071 114, 2016.

[15] B. Saleh and M. Teich, *Fundamentals of Photonics*, 1st Ed. John Wiley & Sons Inc., 1991.

[16] G. G. Stokes, "Composition and resolution of streams of polarized light from multiple sources," *Trans. Cambridge Philos. Soc.*, vol. 9, pp. 399–416, 1852.

[17] E. Collett, "The description of polarization in classical physics," *Am. J. Phys.*, vol. 36, no. 8, pp. 713–725, 1968.

[18] M. Bass *et al.*, *Handbook of Optics, Volume I: Geometrical and Physical Optics, Polarized Light, Components and Instruments*, 3rd Ed. McGraw-Hill, Inc., 2009.

[19] D. H. Goldstein, *Polarized Light*, 1st Ed. Taylor & Francis Group, 2011.

[20] R. A. Chipman, *"Polarimetry"*, 2nd Ed. Mc Graw-Hill, 1995.

[21] M. Born and E. Wolf, *Principles of optics: electromagnetic theory of propagation, interference and diffraction of light*, 7th expanded Ed. Cambridge University Press, 1999.

[22] W. A. Shurcliff, *Polarized Light*. Harvard University Press, 1962.

[23] L. Wolff, "Polarization-based material classification from specular reflection," *IEEE Trans. Pattern Anal. Mach. Intell.*, vol. 12, no. 11, pp. 1059–1071, 1990.

[24] L. Rey-Barroso *et al.*, "Visible and extended near-infrared multispectral imaging for skin cancer diagnosis," *Sensors*, vol. 18, p. 1441, 2018.

[25] C. M. Persons, M. Jones, and C. F. *et al.*, "A proposed standard method for polarimetric calibration and calibration verification," *Proc. of SPIE*, vol. 6682, pp. 1–12, 2007.

[26] M. Bass, *Handbook of Optics Volume II Devices, Measurements, and Properties*, 2nd Ed. Mc Graw-Hill, 1995.

[27] F. Kenny, "Introduction to polarization and polarimetry," in *Astronomical Polarisation from Infrared to Gamma Rays*, 1st Ed. Springer Nature Switzerland, 2019.

[28] R. M. A. Azzam, "Propagation of partially polarized light through anisotropic media with or without depolarization: A differential 4x4 matrix calculus," *J. Opt. Soc. Am.*, vol. 68, pp. 1756–1767, 1978.

[29] J. Gil and E. Bernabeu, "Depolarization and polarization indices of an optical system," *Opt. Acta*, vol. 32, pp. 185–189, 1985.

[30] S. Y.Lu and R. A. Chipman, "Interpretation of mueller matrices based on polar decomposition," *Opt. Soc. Am.*, vol. 13, pp. 1106–1113, 1996.

[31] N. Ortega-Quijano, B. Haj-Ibrahim, E. García-Caurel, J. L. Arce-Diego, and R. Ossikovski, "Experimental validation of mueller matrix differential decomposition," *Opt. Express*, vol. 20, no. 2, pp. 1151–1163, 2012.

[32] R. Ossikovski, M. Anastasiadou, S. B. Hatit, E. Garcia-Caurel, and A. D. Martino, "Depolarizing mueller matrices: How to decompose them," *Phys. Status Solidi (A)*, vol. 205, no. 4, pp. 720–727, 2008.

[33] W. Gao, "Mueller matrix decomposition methods for tissue polarization tomography," *Optics and Lasers in Engineering*, vol. 147, pp. 106 735–, 2021.

[34] S. R. Cloude, "Group theory and polarisation algebra," *Optik (Stuttg.)*, vol. 75, pp. 26–36, 1986.

[35] S. R. Cloude, "Conditions for the physical realisability of matrix operators in polarimetry," *Proc. SPIE*, vol. 1166, pp. 177–185, 1989.

[36] J. Gil and E. Bernabeu, "Obtainment of the polarizing and retardation parameters of a non-depolarizing optical system from the polar decomposition of its mueller matrix," *Optik (Stuttg.)*, vol. 76, pp. 67–71, 1987.

[37] N. Ortega-Quijano and J. L. Arce-Diego, "Mueller matrix differential decomposition," *Opt. Lett.*, vol. 36, no. 10, pp. 1942–1944, 2011.

[38] R. Sridhar and R. Simon, "Normal form for mueller matrices in polarization optics," *J. Mod. Opt.*, vol. 41, no. 10, pp. 1903–1915, 1994.

[39] R. Ossikovski, "Analysis of depolarizing mueller matrices through a symmetric decomposition," *J. Opt. Soc. Am. A*, vol. 26, no. 5, pp. 1109–1118, 2009.

[40] C. Fallet, A. Pierangelo, R. Ossikovski, and A. D. Martino, "Experimental validation of the symmetric decomposition of mueller matrices," *Opt. Express*, vol. 18, no. 2, pp. 831–842, 2010.

[41] J. S. Tyo, "Noise equalization in stokes parameter images obtained by use of variable-retardance polarimeters," *Opt. Lett.*, vol. 25, pp. 1198–1200, 2000.

[42] J. S. Tyo, "Design of optimal polarimeters: Maximization of signal-to-noise ratio and minimization of systematic error," *Appl. Opt.*, vol. 41, pp. 619–630, 2002.

[43] D. S. Sabatke, M. R. Descour, E. Dereniak, W. C. Sweatt, S. A. Kemme, and G. S. Phipps, "Optimization of retardance for a complete stokes polarimeter," *Opt. Lett.*, vol. 25, pp. 802–804, 2000.

[44] J. C. del Toro Iniesta and M. Collados, "Optimum modulation and demodulation matrices for solar polarimetry," *Appl. Opt.*, vol. 39, no. 10, pp. 1637–1642, 2000.

[45] F. Goudail, "Noise minimization and equalization for stokes polarimeters in the presence of signal-dependent poisson shot noise," *Opt. Lett.*, vol. 34, no. 5, pp. 647–649, 2009.

[46] A. Peinado, A. Lizana, J. Vidal, C. Iemmi, and J. Campos, "Optimization and performance criteria of a stokes polarimeter based on two variable retarders," *Opt. Express*, vol. 18, pp. 9815–9830, 2010.

[47] M. R. Foreman, A. Favaro, and A. Aiello, "Optimal frames for polarization state reconstruction," *Phys. Rev. Lett.*, vol. 115, no. 26, p. 263 901, 2015.

[48] J. Dai, F. Goudail, M. Boffety, and J. Gao, "Estimation precision of full polarimetric parameters in the presence of additive and poisson noise," *Opt. Express*, vol. 26, pp. 34 081–34 093, 2018.

[49] F. Goudail, "Equalized estimation of stokes parameters in the presence of poisson noise for any number of polarization analysis states," *Opt. Lett.*, vol. 41, pp. 5772–5775, 2016.

[50] J. Dai and F. Goudail, "Precision analysis of arbitrary full-stokes polarimeters in the presence of additive and poisson noise," *J. Opt. Soc. Am.*, vol. 36, pp. 1229–1240, 2019.

[51] A. Ambirajan and D. C. Look, "Optimum angles for a polarimeter: Part i," *J. Opt. Eng.*, vol. 34, no. 6, pp. 1651–1655, 1995.

[52] A. Ambirajan and D. C. Look, "Optimum angles for a polarimeter: Part ii," *J. Opt. Eng.*, vol. 34, no. 6, pp. 1656–1658, 1995.

[53] S. Shibata, T. Onuma, and Y. Otani, "Real-time birefringence mapping by full-stokes polarization camera," *6th International Conference on Spectroscopic Ellipsometry (ICSE VI)*, 2013.

[54] D. Lara and C. Paterson, "Stokes polarimeter optimization in the presence of shot and gaussian noise," *Opt. Express*, vol. 17, pp. 21 240–21 249, 2009.

[55] J. Zallat, S. Aïnouz, and M. P. Stoll, "Optimal configurations for imaging polarimeters: Impact of image noise and systematic errors," *J. Opt. A: Pure Appl. Opt.*, vol. 8, pp. 807–814, 2006.

[56] T. Mu, C. Zhang, and R. Liang, "Demonstration of a snapshot full-stokes division-of-aperture imaging polarimeter using wollaston prism array," *J. Opt. (UK)*, vol. 17, p. 125 708, 2015.

[57] T. Mu, Z. Chen, C.Zhang, and R. Liang, "Optimal configurations of full-stokes polarimeter with immunity to both poisson and gaussian noise," *J. Opt.*, vol. 18, no. 5, pp. 055 702–055 712, 2016.

[58] T. Mu, C.Zhang, and R. Liang, "Optimal design and performance metric of broadband full-stokes polarimeters with immunity to poisson and gaussian noise," *Opt. Express*, vol. 24, pp. 29 691–29 704, 2016.

[59] T. Mu, C. Zhang, Q. Li, and R. Liang, "Achromatization of waveplate for broadband polarimetric system," *Opt. Lett.*, vol. 40, pp. 2485–2488, 2015.

[60] N. Hagen and Y. Otani, "Stokes polarimeter performance: General noise model and analysis," *Appl. Opt.*, vol. 57, pp. 4283–4296, 2018.

[61] J. S. Tyo, "Extending optimization to active mueller polarimeters," *Proc. SPIE, Polarization Measurement, Analysis, and Applications V*, vol. 4819, 2002.

[62] G. Anna and F. Goudail, "Optimal mueller matrix estimation in the presence of poisson shot noise," *Opt. Express*, vol. 20, pp. 21 331–21 340, 2012.

[63] F. Goudail, "Optimal mueller matrix estimation in the presence of additive and poisson noise for any number of illumination and analysis states," *Opt. Lett.*, vol. 42, pp. 2153–2156, 2017.

[64] X. Li, F. Goudail, H. Hu, Q. Han, Z. Cheng, and T. Liu, "Optimal ellipsometric parameter measurement strategies based on four intensity measurements in presence of additive gaussian and poisson noise," *Opt. Express*, vol. 26, pp. 34 529–34 544, 2018.

[65] T. Mu, D. Bao, C. Zhang, Z. Chen, and J. Song, "Optimal reference polarization states for the calibration of general stokes polarimeters in the presence of noise," *Opt. Comm.*, vol. 418, pp. 120–128, 2018.

[66]]. J. S. Tyo and H. Wei, "Optimizing imaging polarimeters constructed with imperfect optics," *Appl. Opt.*, vol. 45, pp. 5497–5503, 2006.

[67] T. Mu, C. Zhang, Q. Li, and R. Liang, "Error analysis of single-snapshot full-stokes division-of-aperture imaging polarimeters," *Opt. Express*, vol. 23, p. 10 822, 2015.

[68] A. Lizana, J. Campos, A. V. Eeckhout, and A. Márquez, "Misalignment error analysis in polychromatic division of focal plane stokes polarimeters," *OSA Continuum*, vol. 18, pp. 1565–1575, 2019.

[69] M. Vedel, N. Lechocinski, and S. Breugnot, "Compact and robust linear stokes polarization camera," *EPJ Web Conf.*, vol. 5, p. 01 005, 2010.

[70] Q. Cao, C. Zhang, and E. DeHoog, "Snapshot imaging polarimeter using modified savart polariscopes," *Appl. Opt.*, vol. 51, no. 24, pp. 5791–5796, 2012.

[71] M. W. Kudenov, M. J. Escuti, E. L. Dereniak, and K. Oka, "White-light channeled imaging polarimeter using broadband polarization gratings," *Appl. Opt.*, vol. 50, no. 15, pp. 2283–2293, 2011.

[72] M. Kudenov, E. Dereniak, L. Pezzaniti, and G. R. Gerhart, "2-cam lwir imaging stokes polarimeter," *Proc. SPIE 6972, Polarization: Measurement, Analysis, and Remote Sensing VIII, 69720K (2 April 2008)*, 6972–69720K, 2008.

[73] M. E. Ketara, M. Vedel, and S. Breugnot, "Acquisition method improvement for bossa nova technologies' full stokes, passive polarization imaging camera salsa," *Proc. of SPIE*, vol. 26, 98530A, 2016.

[74] G. F. J. Garlick, G. A. Steigmann, and W. E. Lamb, "Differential optical polarization detectors," U.S. patent 3,992,571, Nov. 16, 1976.

[75] C. Farlow, D. B. Chenault, J. L. Pezzaniti, K. Spradley, and M. Gulley, "Imaging polarimeter development and applications," *Proc. SPIE*, vol. 118, p. 4481, 2002.

[76] "Fluxdata imaging polarimeter, fd-1665." (Mar. 10, 2018), [Online]. Available: http://www.fluxdata.com/.

[77] T. Mu, S. Pacheco, Z. Chen, C. Zhang, and R. Liang, "Snapshot linear-stokes imaging spectropolarimeter using division-of-focal-plane polarimetry and integral field spectroscopy," *Sci. Rep.*, vol. 1, pp. 1–11, 2017.

[78] W. Hsu, G. Myhre, K. Balakrishnan, N. Brock, M. Ibn-Elhaj, and S. Pau, "Full-stokes imaging polarimeter using an array of elliptical polarizer," *Opt. Express*, vol. 22, no. 3, pp. 3063–3074, 2014.

[79] "Sony imx250mzr/myr." (Sep. 24, 2018), [Online]. Available: https://www.sony-semicon.co.jp/products_en/new_pro/september_2018/%20imx250mzr_myr_e.html.

[80] "Sony imx250mzr/myr." (Oct. 20, 2022), [Online]. Available: https://www.sony-semicon.com/files/62/flyer_industry/IMX250_264_253MZR_MYR_Flyer_en.pdf.

[81] J. Pezzaniti and D. Chenault, "A division of aperture mwir imaging polarimeter," *Proc. Of SPIE 5888*, vol. Polarization Science and Remote Sensing II, Belligham, WA, 2005, p. 58880V, 2005.

[82] X. Huang, Y. Jin, and Z. Zhao, "Optical design of an aperture-divided mwir imaging polarimeter," *3rd International Symposium of Space Optical Instruments and Applications, Springer*, vol. 192, pp. 73–80, 2016.

[83] H. Wang and J. Liang, "Optimization and calibration of a snapshot medium-wave infrared full-polarization-imaging system," *Opt. Commun.*, vol. 421, pp. 56–65, 2018.

[84] K. Oka and T. Kato, "Spectroscopic polarimetry with a channeled spectrum," *Opt. Lett.*, vol. 24, pp. 1475–1477, 1999.

[85] M.Dubreuil, S. Rivet, B. L. Jeune, and J. Cariou, "Snap-shot mueller matrix polarimeter by wavelength polarization coding," *Opt. Express*, vol. 15, no. 21, pp. 13 660–13 668, 2007.

[86] N. A. Hagen *et al.*, "Compact methods for measuring stress birefringence," *Proc. SPIE*, vol. 5158, pp. 45–53, 2003.

[87] A. S. Alenin, I. J. Vaughn, and J. S. Tyo, "A nine-channeled partial mueller matrix polarimeter," vol. 10407, p. 104070L, 2017.

[88] J. Song, I. J. Vaughn, A. S. Alenin, and J. S. Tyo, "Imaging dynamic scenes with a spatio-temporally channeled polarimeter," *Opt. Express*, vol. 27, no. 20, pp. 28 423–28 436, 2019.

[89] N. A. Rubin, G. D'Aversa, P. Chevalier, Z. Shi, W. T. Chen, and F. Capasso, "Matrix fourier optics enables a compact full-stokes polarization camera," *Science*, vol. 365, no. 6448, eaax1839, 2019.

[90] N. A. Rubin, P. Chevalier, M. Juhl, R. C. M. Tamagnone, and F. Capasso, "Imaging polarimetry through metasurface polarization gratings," *Opt. Express*, vol. 30, no. 6, pp. 9389–9412, 2022.

[91] Y. Shah *et al.*, "An all-dielectric metasurface polarimeter," *ACS Photonics*, vol. 9, 2022.

[92] G. E. Healey and R. Kondepudy, "Radiometric ccd camera calibration and noise estimation," *IEEE Transactions on a Pattern Analysis and Machine Intelligence*, vol. 6, no. 3, pp. 267–276, 1994.

[93] A. Ortiz and G. Oliver, "Radiometric calibration of ccd sensors: Dark current and fixed pattern noise estimation," *IEE International on Robotics and Automation*, vol. Proc. ICRA 5, pp. 4730–4735, 2004.

[94] H. Gu, S. Liu, X. Chen, and C. Zhang, "Calibration of misalignment errors in composite waveplates using mueller matrix ellipsometry," *Appl. Opt.*, vol. 54, pp. 648–693, 2015.

[95] O. Morel, R. Seulin, and D. Fofi, "Handy method to calibrate division-of-amplitude polarimeters for the first three stokes parameters," *Opt. Express*, vol. 24, pp. 13 634–13 646, 2016.

[96] A. Bénière, M. Alouini, F. Goudail, and D. Dolfi, "Design and experimental validation of a snapshot polarization contrast imager," *Appl. Opt.*, vol. 48, pp. 5764–5773, 2009.

[97] D. G. Lowe, "Distinctive image features from scale-invariant keypoints," *Int. J. Comput. Vis.*, vol. 60, pp. 91–110, 2004.

[98] H. Bay, T. Tuytelaars, and L. V. Gool, "Surf: Speeded up robust features," *Computer Vision-ECCV 2006, Springer*, pp. 404–417, 2006.

[99] M. Guizar-Sicairos, S. T. Thurman, and J. R. Fienup, "Efficient subpixel image registration algorithms," *Opt. Lett.*, vol. 33, no. 2, pp. 156–158, 2008.

[100] J. P. Allebach, "Image scanning, sampling, and interpolation," in *Handbook of Image and Video Processing*, A. Bovik, Ed., 2nd Ed., Academic Press, 2005.

[101] M. Brown and D. Lowe, "Invariant features from interest point groups," *BMC*, 2002.

[102] D. Mistry and A. Banerjee, "Comparison of feature detection and matching approaches: Sift and surf.," *Global Res. Dev. J. Eng.*, vol. 2, pp. 1–7, 2017.

[103] E. Rosten and T. Drummond, "Machine learning for high speed corner detection," *9th European Conference on Computer Vision*, vol. 1, pp. 430–443, 2006.

[104] M. C. et al., "Brief: Binary robust independent elementary features," *11th European Conference on Computer Vision (ECCV), Heraklion, Crete. LNCS Springer, September 2010*, 2010.

[105] E. Rublee, V. Rabaud, K. Konolige, and G. R. Bradski, "Orb: An efficient alternative to sift or surf," *2011 International Conference on Computer Vision*, pp. 2564–2571, 2011.

[106] C. M. et al., "Improved orb algorithm using three-patch method and local gray difference," *Sensors (Basel)*, vol. 20, no. 4, p. 975, 2020.

[107] D. H. Goldstein and E. Collett, *Polarized Light*, 2nd. Ed. Marcel Dekker, 2003.

[108] D. H. Goldstein, "Mueller matrix dual-rotating retarder polarimeter," *Appl. Opt.*, vol. 31, pp. 6676–6683, 1992.

[109] R. M. A. Azzam, "A simple fourier photopolarimeter wit rotation polarizer and analyser for measuring jones and mueller matrices," *Opt. Commun.*, vol. 25, pp. 137–140, 1978.

[110] O. Rodríguez-Núñez, J. López-Téllez, O. Rodríguez-Herrera, and N. C. Bruce, "Calibration and data extraction in nonoptimized mueller matrix polarimeters," *Appl. Opt.*, vol. 56, pp. 4398–4404, 2017.

[111] Y. Zhang, H. Zhao, and N. Li, "Polarization calibration with large apertures in full field of view for a stokes imaging polarimeters based on liquid-crystal variable retarder," *Appl. Opt.*, vol. 52, pp. 1284–1292, 2013.

[112] M. Liu, X. Zhang, T. Liu, G. Shi, L. Wang, and Y. Li, "On-orbit polarization calibration for multichannel polarimetric camera," *Appl. Sci.*, vol. 9, p. 1424, 2019.

[113] Y. Quéau, F. Leporcq, and A. Alfalou, "Design and simplified calibration of a mueller imaging polarimeter for material classification," *Opt. Lett.*, vol. 43, pp. 4941–4944, 2018.

[114] I. Montes-González, N. Bruce, O. Rodríguez-Herrera, and O. Rodríguez-Núñez, "Method to calibrate a full-stokes polarimeter based on variable retarders," *Appl. Opt.*, vol. 58, pp. 5952–5957, 2018.

[115] F. Han, T. Mu, and D. B. *et al.*, "Iterative reconstruction for general linear imaging polarimetry without polarimetric calibration," *Opt. Lett.*, vol. 45, pp. 57–60, 2020.

[116] S. Powell and V. Gruev, "Calibration methods for division-of-focal-plane polarimeters," *Opt. Express*, vol. 21, pp. 21 039–21 055, 2013.

[117] Y. Giménez, P. Lapray, A. Foulonneau, and L. Bigué, "Calibration for polarization filter array cameras: Recent advances," *Proc. SPIE 11172, 14th International Conference on Quality Control by Artificial Vision*, p. 1 117 216, 2019.

[118] B. Boulbry, J. Ramella-Roman, and T. Germer, "Improved method for calibrating a stokes polarimeter," *Appl. Opt.*, vol. 46, pp. 8533–41, 2007.

[119] E. Compain, S. Poirier, and B. Drevillon, "General and self-consistent method for the calibration of polarization modulators, polarimeters, and mueller-matrix ellipsometers," *Appl. Opt.*, vol. 38, pp. 3490–3502, 1999.

[120] R. Ossikovski, B. A. Bugami, E. Garcia-Caurel, and S. R. Cloud, "Polarizer calibration method for mueller matrix polarimeters," *Appl. Opt.*, vol. 59, pp. 10 389–10 395, 2020.

[121] H. Holst, "Comparison of different calibration methods suited for calibration problems with many variables," *Appl. Spectrosc.*, vol. 46, pp. 1780–1784, 1992.

[122] R. Meng, Z. Chen, X. Wang, Y. Liu, H. He, and H. Ma, "Comparison of different calibration methods for mueller matrix microscopy of cells," *Appl. Opt.*, vol. 60, pp. 1380–1386, 2021.

[123] S. Peña-Gutiérrez and S. Royo, "Polarization calibration assessment for a broadband imaging polarimeter basedon a division of aperture architecture," *Opt. Express*, 2022.

[124] A. De Martino, E. Garcia-Caurel, B. Laude, and B. Drevillon, "General methods for optimized design and calibration of mueller polarimeters," *Thin Solid Films*, vol. 455-456, pp. 112–119, 2004.

[125] H. Hu, E. Garcia-Caurel, G. Anna, and F. Goudail, "Simplified calibration procedure for mueller polarimeter in transmission configuration," *Opt. Lett.*, vol. 39, pp. 418–420, 2014.

[126] J. Qi, D. S. Elson, and S. Stoyanov, "Eigenvalue calibration method for 3x3 mueller polarimeters," *Opt. Lett.*, vol. 44, pp. 2362–2365, 2019.

[127] K. K. *et al.*, "The aerosol characterization from polarimeter and lidar (acepol) airborne field campaign," *Earth System Science Data*, vol. 12, no. 3, pp. 2183–2208, 2020.

[128] D. Li *et al.*, "Study on polarization scattering applied in aerosol recognition in the air," *Opt. Express*, vol. 27, no. 3, A581–A595, 2019.

[129] E. Hecht, *Optics*, 5th Ed. Pearson, 2017.

[130] S. Tominaga and A. Kimachi, "Polarization imaging for material classification," *Opt. Eng.*, vol. 47, no. 12, p. 123 201, 2008.

[131] L. Zhang and E. R. Hancock, "Robust estimation of shape and polarisation using blind source separation," *Patt. Rec. Lett.*, 2013.

[132] G. A. Atkinson and E. R. Hancock, "Recovery of surface orientation from diffuse polarization," *IEEE Trans. Image Process.*, vol. 15, pp. 1653–1664, 2006.

[133] N. M. Garcia, I. de Erausquin, C. Edmiston, and V. Gruev, "Surface normal reconstruction using circularly polarized light," *Opt. Express*, pp. 14 391–14 406, 2015.

[134] J. Fade, M. Roche, and M. Alouini, "Computational polarization imaging from a single speckle image," *Opt. Lett.*, vol. 37, no. 3, pp. 386–388, 2012.

[135] J. Dupont, X. Orlik, A. Ghabbach, M. Zerrad, G. Soriano, and C. Amra, "Polarization analysis of speckle field below its transverse correlation width : Application to surface and bulk scattering," *Opt. Express*, vol. 22, no. 20, pp. 24 133–24 141, 2014.

[136] T. Gehrels, *Planets, Stars, and Nebulae Studied with Polarimetry*. 1974.

[137] V. V. Tuchin, *Handbook of Optical Sensing of Glucose in Biological Fluids and Tissues*, 1st Ed. CRC Press, 2018.

[138] S. Manhas, M. K. Swami, P. Buddhiwant, N. Ghosh, P. K. Gupta, and K. Singh, "Mueller matrix approach for determination of optical rotation in chiral turbid media in backscattering geometry," *Opt. Express*, vol. 14, no. 1, pp. 190–202, 2006.

[139] Y. L. Lo and T. C. Yu, "A polarimetric glucose sensor using a liquid-crystal polarization modulator driven by a sinusoidal signal," *Opt. Commun.*, vol. 259, pp. 40–48, 2006.

[140] P. Mukherjee, N. Hagen, and Y. Otani, "Glucose sensing in the presence of scattering by analyzing a partial mueller matrix," *Optik*, vol. 180, pp. 775–781, 2019.

[141] C. Eduardo, F. do Amaral, and B. Wolf, "Current development in non-invasive glucose monitoring," *Med. Eng. & Phys.*, vol. 30, pp. 541–549, 2008.

[142] Q. H. Phan and Y. L. Lo, "Stokes-mueller matrix polarimetry system for glucose sensing," *Opt. Las. Eng.*, vol. 92, pp. 120–128, 20106.

[143] N. Ghosh, "Tissue polarimetry: Concepts, challenges, applications, and outlook," *J. Biom. Opt.*, vol. 16, no. 11, p. 110 801, 2011.

[144] M. Menzel, J. Reckford, D. Weigand, H. Köse, K. Amunts, and M. Axer, "Diattenuation of brain tissue and its impact on 3d polarized light imaging," *Biom. Opt.*, vol. 8, pp. 1106–1113, 2017.

[145] M. Menzel, M. Axer, K. Amunts, H. D. Raedt, and K. Michielsen, "Diattenuation imaging reveals different brain tissue properties," *Sci. Rep.*, vol. 9, pp. 1–12, 2019.

[146] J. Qi and D. Elson, "Mueller polarimetric imaging for surgical and diagnostic applications: A review," *J. Bioph.*, vol. 10, pp. 950–982, 2017.

[147] N. Ghosh, J. Soni, M. Wood, M. A. Wallenberg, and I. Vitkin, "Mueller matrix polarimetry for the characterization of complex random medium like biological tissues," *Pramana - J Phys*, vol. 75, pp. 1071–1086, 2011.

[148] D. Layden, N. Ghosh, and A. Vitkin, "Quantitative polarimetry for tissue characterization and diagnosis," *Advanced Biophotonics: Tissue Optical Sectioning*, vol. 5, pp. 73–108, 2013.

[149] M. R. Antonelli *et al.*, "Mueller matrix imaging of human colon tissue for cancer diagnostics: How monte carlo modeling can help in the interpretation of experimental data," *Opt. Express*, vol. 18, no. 10, pp. 10 200–10 208, 2010.

[150] V. A. U. *et al.*, "Diattenuation of brain tissue and its impact on 3d polarized light imaging," *Sci. Rep.*, vol. 11, pp. 1–12, 2021.

[151] L. Rey-Barroso, S. Peña-Gutiérrez, C. Yañéz, F. Burgos-Fernández, M. Vilaseca, and S. Royo, "Optical technologies for the improvement of skin cancer diagnosis: A review," *Sensors*, vol. 21, p. 252, 2021.

[152] K. M. Yoo and R. R. Alfano, "Time-resolved coherent and incoherent components of forward light scattering in random media," *Opt. Lett.*, vol. 15, pp. 320–322, 1990.

[153] C. Gonatas, M. Ishii, J. Leigh, and J.C.Schotland, "Optical diffusion imaging using a direct inversion method," *Physical Review*, vol. 52, p. 4361, 1995.

[154] M. Duncan, R. Mahon, L. Tankersley, and J. Reintjes, "Time-gated imaging through scattering media using stimulated raman amplification," *Opt. Lett.*, vol. 16, no. 23, pp. 1868–1870, 1991.

[155] H. Horinaka, K. Hashimoto, K. Wada, Y. Cho, and M. Osawa, "Extraction of quasi- straightforward-propagating photons from diffused light transmitting through a scattering medium by polarization modulation," *Opt. Lett.*, vol. 20, pp. 1501–1503, 1995.

[156] S. Panigrahi, J. Fade, and M. Alouini, "Adaptive polarimetric image representation for contrast optimization of a polarized beacon through fog," *J. Opt.*, vol. 17, no. 6, p. 065 703, 2015.

[157] J. C. Ramella-Roman, S. A. Prahl, and S. Jacques, "Three monte carlo programs of polarized light transport into scattering media: Part i," *Opt. Express*, vol. 13, pp. 4420–4438, 2005.

[158] T. H. et al., "Broad-band transmission characteristics of polarization in foggy environments," *Atmosphere*, vol. 10, p. 342, 2019.

[159] J. D. van der Laan, J. B. Wright, S. A. Kemme, and D. A. Scrymgeour, "Superior signal persistence of circularly polarized light in polydisperse, real-world fog environments," *Appl. Opt.*, vol. 57, pp. 5464–5473, 2018.

[160] J. Ryan and A. Carswell, "Laser beam broadening and depolarization in dense fog," *J. Opt. Soc. Am.*, vol. 68, pp. 900–908, 1978.

[161] J. Liang, L. Ren, H. Ju, W. Zhang, and E. Qu, "Polarimetric dehazing method for dense haze removal based on distribution analysis of angle of polarization," *Opt. Express*, vol. 23, no. 20, p. 16 146, 2015.

[162] J. H. et al., "Resolution enhancement in active underwater polarization imaging with modulation transfer function analysis," *Appl. Opt.*, vol. 54, pp. 3294–3302, 2015.

[163] S. Peña-Gutiérrez, M. Ballesta-Garcia, P. García-Gómez, and S. Royo, "Polarization calibration assessment for a broadband imaging polarimeter basedon a division of aperture architecture," *Opt. Lett.*, vol. 47, no. 2, pp. 242–245, 2022.

[164] M. Ballesta-Garcia *et al.*, "Analysis of the performance of a polarized lidar imager in fog," *Opt. Express*, vol. 30, no. 23, pp. 41 524–41 540, 2022.

[165] F. C. MacKintosh, J. X. Zhu, D. J. Pine, and D. A. Weitz, "Polarization memory of multiply scattered light," *Phys. Rev. B*, vol. 40, p. 9342, 1989.

[166] R. E. Nothdurft and G. Yao, "Applying the polarization memory effect in polarization-gated subsurface imaging," *Appl. Opt.*, vol. 45, pp. 5532–5541, 2018.

[167] R. Ragazzoni, "Pupil plane wavefront sensing with an oscillating prism," *J. Mod. Opt.*, vol. 43, pp. 289–293, 1996.

[168] T. Y. Chew, R. M. Clare, and R. G. Lane, "A comparison of the shack-hartmann and pyramid wavefront sensors," *Opt. Commun.*, vol. 267, pp. 189–195, 2006.

[169] R. Ragazzoni, A. Ghedina, and A. Baruffolo, "Testing the pyramid wavefront sensor on the sky," *Proc. SPIE*, vol. 4007, pp. 423–430, 2000.

[170] A. Tozzi, P. Stefanini, E. Pinna, and S. Esposito, "The double pyramid wavefront sensor for lbt," *Proc SPIE*, vol. 7015, p. 701 558, 2008.

[171] J. M. Bennet, *Handbook of Optics Volume I Fundamentals, Techniques, and Design*, 2nd Ed. Mc Graw-Hill, 1995.

[172] W. Zhou, A. C. Bovik, H. R. Sheikh, and E. P. Simoncelli, "Image quality assessment: From error visibility to structural similarity," *IEEE Transactions on Image Processing*, vol. 13, no. 4, pp. 600–612, 2004.

[173] R. Datteri and B. Dawant, *Med Image Comput Assist Interv.*, vol. 15, no. 3, pp. 139–146, 2012.

[174] M. Mujat and A. Dogariu, "Real-time measurement of the polarization transfer function," *Appl. opt.*, vol. 40, pp. 34–44, 2001.

[175] L. Wolff, "Polarization methods in computer vision," Columbia University, 1991.

[176] D. A. Holmes, "Formula for calculating the refractive index of a thin transparent plate from polarization-state transmission measurements," *J. Opt. Soc. Am.*, vol. 57, no. 4, pp. 544–545, 1967.

[177] R. Chipman, W. Lam, and G. Young, *Polarized Light and Optical Systems*, 1st Ed. CRC Press, 2018.

[178] "Thorlabs wpv10-633." (Sep. 19, 2022), [Online]. Available: https://www.thorlabs.com/newgrouppage9.cfm?objectgroup_id=9098.

[179] S. McEldowney, "Vortex retarders," The University of Arizona, 2008.

[180] S. Zhao *et al.*, "Experimental investigation of quantum key distribution over a water channel," *Appl. Opt.*, vol. 58, no. 14, pp. 3902–3907, 2019.

[181] H. Arwin *et al.*, "Optical chirality determined from mueller matrices," *Appl. Sci.*, vol. 11, p. 6742, 2021.

[182] G. Horváth *et al.*, "On the trail of vikings with polarized skylight: Experimental study of the atmospheric optical prerequisites allowing polarimetric navigation by viking seafarers," *Phil. Trans. R. Soc.*, vol. 366, pp. 772–782, 2011.

[183] Y. Y. Schechner, S. G. Narasimhan, and S. K. Nayar, "Polarization-based vision through haze," *Appl. Opt.*, vol. 42, pp. 511–525, 2003.

[184] M. Colomb, H. Khaled, P. André, P. L. J. Boreux, and J. Dufour, "An innovative artificial fog production device improved in the european project fog," *Atmos. Res.*, vol. 87, 2008.

[185] P.Duthon, M. Colomb, and F. Bernardin, "Fog classification by their droplet size distributions: Application to the characterization of cerema's platform," *Atmosphere*, vol. 11, 2020.

[186] P.Duthon, M. Colomb, and F. Bernardin, "Light transmission in fog: The influence of wavelength on the extinction coefficient," *Appl. Sci.*, vol. 9, p. 2843, 2019.

[187] E.Peli, "Contrast in complex images," *J. Opt. Soc. Am. A*, vol. 7, pp. 2032–2040, 1990.

[188] P. Bex and W. Makous, "Spatial frequency, phase, and the contrast of natural images," *J. Opt. Soc. Am. A*, vol. 19, pp. 1096–1106, 2002.

[189] M. Ballesta-Garcia, S. Peña-Gutiérrez, A. Val, and S. Royo, *Atmosphere*, vol. 30, no. 23, 2021.

[190] S. Rehn, A. Planat-Chrétien, M. Berger, J. Dinten, C. Deumié-Raviol, and A. D. Silva, "Depth probing of diffuse tissues controlled with elliptically polarized light," *J. Biomed. Opt.*, vol. 18, p. 016 007, 2013.

[191] S. Sridhar and A. D. Silva, "Enhanced contrast and depth resolution in polarization imaging using elliptically polarized light," *J. Opt. Soc. Am. A*, vol. 21, p. 071 107, 2016.

[192] N. A. Rawashdeh, J. P. Bos, and N. J. Abu-Alrub, "Camera–lidar sensor fusion for drivable area detection in winter weather using convolutional neural networks," *Optical Engineering*, vol. 62, no. 3, p. 031 202, 2022.